199(4), 2024

COMBUSTION ENGINES

PTNSS

Silesian University of Technology

XI INTERNATIONAL

CONGRESS ON COMBUSTION ENGINES

POWERTRAINS TECHNOLOGIES AND ALTERNATIVE FUELS

POLISH SCIENTIFIC SOCIETY
OF COMBUSTION ENGINES

23rd-25th June 2025

congress.ptnss.pl

Silesian University of Technology
Faculty of Transport and Aviation Engineering
Zygmunta Krasinskiego str. 8, 40-019 Katowice, Poland

Due to the dynamic development of machine and vehicle powertrains, the "Combustion Engines" scientific journal, while retaining its historical title, currently publishes works related not only to internal combustion engines, but also other powertrains, including hybrid drives, electric drives and fuel cells.

PTNSS Supporting Members
Członkowie wspierający PTNSS

BOSMAL Automotive Research and Development Institute Ltd
Instytut Badań i Rozwoju Motoryzacji BOSMAL Sp. z o.o

Motor Transport Institute
Instytut Transportu Samochodowego

Institute of Aviation
Sieć Badawcza Łukasiewicz – Instytut Lotnictwa

Automotive Industry Institute
Sieć Badawcza Łukasiewicz – Przemysłowy Instytut Motoryzacji

Sieć Badawcza Łukasiewicz – Poznański Instytut Technologiczny

AVL List GmbH

Air Force Institute of Technology
Instytut Techniczny Wojsk Lotniczych

Military Institute of Armoured & Automotive Technology
Wojskowy Instytut Techniki Pancernej i Samochodowej

Toyota Motor Poland Ltd. Sp. z o.o.

RADWAG Balances and Scales
RADWAG Wagi Elektroniczne

MS Mechatronic Solutions Group

FOGO Sp. z o.o.

Horus Energia Sp. z o.o.

COMBUSTION ENGINES

A Scientific Magazine

2024, 199(4)

Year LXIII

PL ISSN 2300-9896
PL eISSN 2658-1442

Publisher:

Polish Scientific Society of Combustion Engines
60-965 Poznan, pl. M. Skłodowskiej-Curie 5, Poland
tel.: +48 61 6475966, fax: +48 61 6652204
E-mail: sekretariat@ptnss.pl
WebSite: http://www.ptnss.pl
Papers available on-line: http://combustion-engines.eu

Contents

Publisher:

Polish Scientific Society of Combustion Engines
60-965 Poznan, pl. M. Sklodowskiej-Curie 5, Poland
tel.: +48 61 6475966, fax: +48 61 6652204
E-mail: sekretariat@ptnss.pl
WebSite: http://www.ptnss.pl

Subscriptions
Send subscription requests to the Publisher's address.
Cost of a single issue PLN 100.

Preparation for print
ARS NOVA Publishing House
60-782 Poznan, ul. Grunwaldzka 17/10A

Circulation: 160 copies

Printing and binding

Zakład Poligraficzny Moś i Łuczak, sp. j.,
Poznań, ul. Piwna 1

The journal is under the patronage of the Transport Committee and the Machine Building Committee of the Polish Academy of Sciences

The journal is registered and listed in the Polish and international database

Papers published in the
Combustion Engines
quarterly receive 70 points as stated by the Notification of the Minister of Science dated 5 January 2024.

Declaration of the original version
The original version of the Combustion Engines journal is the printed version.

Cover

I – 2.0-litre GAC and Toyota ammonia engine *(www.bloomberg.com)*; background *(Virtual abstract industrial factory with wireframe mesh and glowing objects – freepick.com)*

IV – Cummins – variable geometry turbocharger *(cummins.com)*

Article citation info:
Aoyagi T, Wakasugi T, Tsuru D, Tashima H. Analysis of effects of pre-chamber orifices on torch flame behaviours in lean-burn gas engines. Combustion Engines. 2024;199(4), 3-14. https://doi.org/10.19206/CE-188112

Takahide AOYAGI
Takuya WAKASUGI
Daisuke TSURU
Hiroshi TASHIMA

Combustion Engines
Polish Scientific Society of Combustion Engines

Analysis of effects of pre-chamber orifices on torch flame behaviours in lean-burn gas engines

ARTICLE INFO

Received: 5 March 2024
Revised: 31 March 2024
Accepted: 29 April 2024
Available online: 9 July 2024

Fuel conversion from heavy oil to natural gas is favoured as a quick remedy for GHG reduction from industrial engines in ship propulsion and power generation fields thanks to fewer carbon contents in natural gas. In medium-speed gas engines, the ejection of torch flame from a pre-chamber is often used to promote flame propagation within a main combustion chamber. Although orifice specifications affect the ejection behaviour of the torch flame and the following combustion in the main chamber, the effects are difficult to fully understand. Some of the authors developed a constant-volume combustion vessel that simulated the combustion chamber around the top dead centre of a pre-chamber type gas engine and observed the effects of orifice specifications on the torch flame ejection and the combustion in the main chamber. Still, the correlation was not concluded due to the lack of physical examination. In the paper, the above measurement results were confirmed by using RANS-type CFD considering the larger scale of the target engines, and the physical background of the effects of orifice specifications was successfully reproduced.

Key words: *gas engine*, *pre-chamber, torch flame, CFD simulation, combustion visualization*

1. Introduction

Many countries that are signatories to the Paris Agreement have set their action plans to achieve carbon neutrality (CN) by 2050, and progress is being made in the development of electrification [6] and e-fuels [11] to decarbonize prime movers in the field of land transportation. More generous GHG reduction targets have been set for off-road power sources, such as industrial engines and marine engines, because of their long continuous operating time, and high average engine load, which results in the difficulty in electrification. However, IMO/MEPC80 in 2023 [12] declared GHG reductions in the marine sector should be in line with other sectors. Since internal combustion engines will account for the majority even when CN is achieved, it is essential to shift to non-carbon-containing fuels such as ammonia and hydrogen by 2050. Due to the difference in combustion characteristics, long-term development is still necessary for practical application, and toward the short-term goal of halving GHG emissions by 2030, gas engines purely running on natural gas (NG) should be introduced on a large scale. After the widespread use of hydrogen fuel, continuous usage of gas engines with e-gas obtained from methanation could be the next option [1].

The mainstream of current marine gas engines burns a lean premixture of NG/air preferring the potential for reducing NO_x emissions without additional after-treatments and improving thermal efficiency thanks to the high degree of constant volume [10]. However, due to the lower combustion speed of the lean premixture, it is not easy to complete combustion in a combustion chamber of a larger scale, therefore a smaller ignition source or lower ignition energy may increase slippage of unburned methane and cycle-to-cycle variations [8]. For this reason, various enhanced ignition measures have been used for lean-burn gas engines instead of a usual open chamber with a spark plug. In medium-speed engines, so-called “precombustion chamber (PC) ignition” has been widely studied [14, 15, 20]. In the PC ignition, torch flames ejected through orifices bored at the tip of a PC are expected to promote the combustion in a main combustion chamber (MC) of the lean-burn gas engines, to shorten the distance for the premixed flame to propagate toward an end-gas zone, and to expand the stable combustion range free from misfire and knocking [5].

PC ignition systems are divided into passive PC ignition mainly used in lean-burn gas engines of ca. 200 mm or less in the bore, and active PC ignition so in lean-burn gas engines of more than 200 mm in the bore. The former is essentially a small dome-shaped cap attached over an electrode gap of a spark plug. There is no active scavenge of the inner PC gas, and the combustible MC mixture is the only fuel source that comes in through orifices drilled in the cap during a compression stroke. The latter has a PC of larger volume and an independent fuel supply path that realises the local stratification of the mixture concentration from PC to MC and strengthens the ignition potential and penetration of the torch flame. The active PC ignition is sometimes applied to small high-speed SI (Spark Ignition) engines and is named TJI (Turbulent Jet Ignition). It has been eagerly studied to promote combustion in small high-speed SI engines [3, 16, 25] and some extreme-performance engines [19].

Marine lean-burn gas engines, however, have significant geometric differences, such as a cylinder bore that exceeds the knock limit (ca. 100 mm in bore) of small SI engines, a smaller volume ratio of PC to MC and a multi-orifice layout in the PC tip. In addition, marine lean-burn gas engines are highly supercharged to keep the mean effective pressure compatible with their diesel substitutes under lean mixture conditions. These factors push the marine lean-

burn gas engines to have an independent fuel supply device in their PC. Even so, their stable operation range is strictly limited between a knocking limit on the richer mixture side and a misfiring limit on the leaner mixture side [21], and the active PC ignition for marine lean-burn gas engines [7, 13, 18] has been investigated and studied separately from the TJI for high-speed SI engines.

In general, because of high cost for experiments and measurements in large-scale engines, CFD simulation is intentionally utilized to support the development and design process of large lean-burn gas engines [2, 9, 24]. For example, in-cylinder phenomena such as the mixture formation in a PC [17] and pre-ignition initiated by lubricant oil droplets were numerically reproduced [23], although the validity of those simulations cannot be secured because of the lack of measurements including actual visualization of the torch flame in the whole of a MC. There are very few cases in which the validity of numerical predictions was examined by tracing back the effects of PC orifice specifications on the torch flame behaviours in the MC. Moreover, the validity of the simulation should be examined by comparing it with actual visualization data in consideration of the unsteady nature of lean-burn gas engine's in-cylinder phenomena such as mixture formation and two-stage ignition and combustion process.

Wakasugi et al. [22] developed a CVCV (Constant Volume Combustion Vessel) that simulated the combustion chamber around the top dead centre of a PC-type gas engine and observed the effects of orifice specifications on the torch flame ejection and the combustion process in the main chamber. Still, the correlation between them was not concluded due to the lack of physical examination.

In the study, the above measurement results were numerically confirmed by RANS-type CFD considering the larger scale of the target engines, and the mechanism of the effects of the orifice specification was successfully reproduced and extensively examined in non-combustible ambient conditions of the MC.

2. Experimental apparatuses and procedures

As mentioned, the measurement results acquired by Wakasugi et al. [22] were fully adopted for comparison with the CFD simulation, since they can be said to be rare attempts to investigate the effects of orifice specifications by visualizing ejection behaviour of the torch flame from a pre-chamber and the following combustion process in a main chamber. Although the duplication with the source literature is inevitable, the main points for measurement are described below.

Figure 1 and Table 1 show the cross-sectional views of the CVCV and its main specifications, respectively. The CVCV has a simple pancake-shaped internal volume as a Main combustion Chamber (MC) of ϕ240 mm in bore and 30 mm in height. The MC is nearly equivalent to the clearance volume of a typical medium-speed natural gas engine. A Pre-Chamber (PC) with orifices near its bottom is mounted on the centre of the CVCV top lid, and the configuration of the PC, such as orifice diameter and the number of orifices, can be changed by exchanging a PC tip attached to the bottom of the PC. The details of tested PC tips will be explained later. The PC and MC have independent air/fuel mixture intake paths, and each can supply air/fuel mixture of different compositions. The bottom wall of the MC is entirely made of quartz glass, and the inner surface of the MC top lid is mirror-polished. The layout realizes full optical access to in-chamber combustion phenomena from the bottom window and double-path type shadowgraph optics.

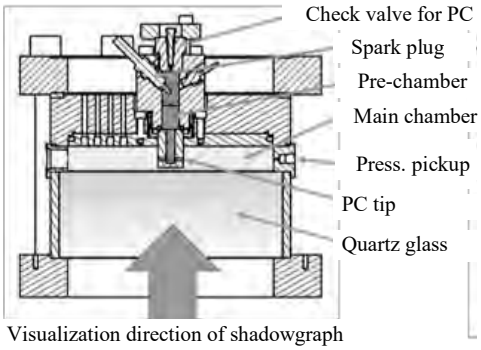

Fig. 1. Cross-sectional views of the CVCV

Table 1. Main specifications of CVCV

Main chamber ($D_{MC} \times H_{MC}$)	∅240 mm × 30 mm
Pre-chamber ($D_{PC} \times H_{PC}$)	∅20 mm × 65 mm (upper part w/o PC tip)
Optical window ($D_w \times t$)	∅260 mm × 100 mm Fused quartz glass
Max. in-chamber press.	10 MPa
Ignition device in PC	Spark plug
Mixture supply system	PC and MC separated

3. CFD setup and procedures

The 3D-CFD simulation by CONVERGE was tried to reproduce the above experimental results in the CVCV simulating combustion phenomena in a PC-type gas engine. Considering the larger scale of target medium-speed engines and the practical CFD usage in the design phase of future gas engines, a RANS turbulence scheme was adopted to save computational load and time. The details of the calculation setup and procedures are as follows.

The SAGE detailed chemical kinetics solver by Senecal [13] was adopted as the combustion model, and the spark ignition was modelled by the energy source model. The RNG k-ε model was adopted as a typical turbulence model in RANS simulation. In general, the SAGE combustion model calculates the elementary reaction rate while CFD solves the transport equation. However, to reduce the computational expense, this detailed chemistry was only activated in cells that passed the minimum temperature, and HC mole fraction specified in CONVERGE. In addition, the multi-zone chemistry model by Babajimopoulos [24] was used to expedite the detailed chemistry calculations. The reduced primary reference fuel mechanism was used to make efficient calculations. The standerd reaction mechanism in CONVERGE was used, and it consists of the reduced version of GRI-Mech1.2 by Andrei [9] with an enhanced Zeldvich mechanism embedded and consists of 26 species and 107 reactions for methane.

Figure 2 shows the initial meshing of the computational domain that models the internal volume of the CVCV. The PC and the MC of the CVCV are reproduced with cubic cells according to a rectangular Cartesian coordinate. In the case of the figure, the reference PC tip is set on the PC bottom. As shown in the figure, the orifices of the tested PC tips are horizontally bored.

The cell size was uniformly minimized at 1.0 mm in the internal space of the PC including the orifices. Considering the unburned gas and the torch flame ejection from the PC orifices, groups of cells of a truncated-cone shape were attached to the exit of orifices with a minimum diameter of about 8 mm and with a spread angle of about 30 degrees as shown in the figure. The initial number of cells was set to about 275,000. After the start of combustion in the MC, however, the Adaptive Mesh Refinement (AMR) was activated based on the local gradient in temperature and velocity between the cells, and the AMR automatically contracted the minimum cell size to 0.5 mm and increased the number of cells to a maximum of 150 million. All the wall temperatures surrounding the CVCV combustion chambers were set to 300 K. The heat loss to the wall surfaces was predicted by the turbulent heat transfer model based on the boundary layer treatment using the nondimensional distance y+ and the turbulent kinetic energy.

For a better understanding of the calculation results, preceding jets of unburned PC mixture and following torch flames should be distinguished from the ambient gas or the mixture in the MC. In the study, the gas components originating from the PC mixture were identified as marker gas.

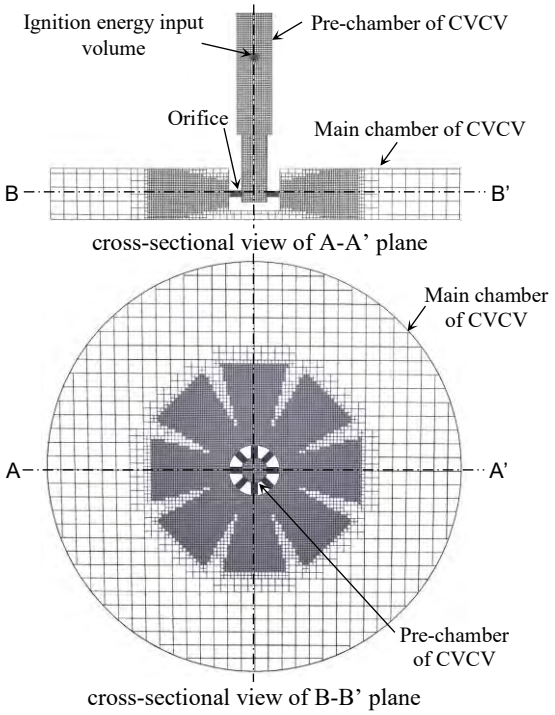

Fig. 2. Schematic view of initial meshing of the computational domain for the CVCV inner volume with a reference PC tip (Tip #1, see Table 3 and Fig. 3)

The jets of the unburned PC mixture were identified by setting the boundary concentration of marker gas to 1.0 mass%, and the torch flames including the ignited MC mixture were identified by setting the boundary cell temperature to 350 K or higher.

4. Experimental conditions

Table 2 lists the experimental conditions both for combustion tests and numerical simulations. Photographing setups for the combustion tests are also included in the lower lines of the table. Following the mixture formation in actual PC-type gas engines, the PC is always filled with a stoichiometric (λ_{PC} = 1.0) CH_4/air mixture to secure stable ignition and strong torch flame ejection. MC gas conditions, however, were determined by the experimental considerations. In the case of non-combustible MC gas, the MC is filled with pure nitrogen by shutting off both an oxygen valve for artificial air preparation in the primary supply line and a CH_4 valve in the secondary supply line. In the case of MC mixture gas, both the valves are open to prepare a CH_4/air mixture of an equivalence ratio of λ_{MC} = 1.7.

Table 2. Experimental conditions

Gas charging state	1.0 MPa, 300 K
Fuel gas in PC	CH_4/air premixture, λ_{PC} = 1.0
Ambient gas in MC	N_2 (non-combustible) CH_4/air premixture, λ_{MC} = 1.7
PC tips	#1~#8 on Table 3
Frame rate	20,000 fps
Resolution	1024×1024 pixels
Exposure time	10.0 μs

Figure 3 shows a cross-sectional view of the reference PC tip: Tip #1. As mentioned above, PC orifices are horizontally bored to make it easy to measure the penetration and spread cone angle of the torch flame from the visualized torch flame images through a quartz glass window covering the whole bottom surface of the MC.

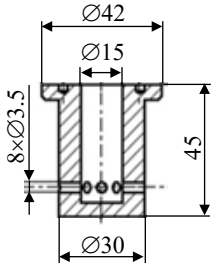

Fig. 3. Cross-sectional view of the reference PC tip (Tip #1, see Table 3)

Table 3 shows a specification list of eight PC tips identified as Tip ID: #1~#8. Tip #1 is selected as the reference PC tip, in which the orifice diameter; D_{ori} is ∅3.5 mm, and the number of orifices; N_{ori} is set to 8. Tips #2 and #3 have N_{ori} of 6 and 10, respectively, and their D_{ori} is determined so that the total orifice opening area is almost the same as that of Tip #1. For Tips #4 and #5, N_{ori} is set constant at 8 and D_{ori} is set to ∅2.5 mm and ∅5.0 mm, respectively.

Table 3. Main specifications of the PC tips

PC tip ID	Orifice specifications					Tip throat diameter D_{trt} [mm]	Chamber vol. ratio V_{PC}/V_{MC} [%]
	Diameter D_{ori} [mm]	Length L_{ori} [mm]	Aspect ratio $(L/D)_{ori}$ [-]	Number of holes N_{ori} [-]	Total opening area A_{ori} [cm^2]		
#1	∅3.5	7.5	2.14	8	0.770	∅15	2.3
#2	∅4.0	7.5	1.86	6	0.754	∅15	2.3
#3	∅3.1	7.5	2.42	10	0.755	∅15	2.3
#4	∅2.5	7.5	3.00	8	0.393	∅15	2.3
#5	∅5.0	7.5	1.50	8	1.571	∅15	2.3
#6	∅3.5	5.0	1.43	8	0.770	∅10	2.0
#7	∅3.5	7.5	2.14	8	0.770	∅10	2.0
#8	∅3.5	10.0	2.86	8	0.770	∅10	2.0

Each nozzle tip has a different orifice aspect ratio; $(L/D)_{ori}$ ranging from 1.43 to 3.00 and two variations of relative PC volume; V_{PC}/V_{MC} at 2.3% (Tips #1~#5) or 2.0% (Tips #6 ~#8).

5. Results and discussion

5.1. Analysis methodology

In a PC-type gas engine, combustion in an MC progresses due to the combination of the forced ignition by the torch flames and their mixing/combustion promotion effect on the MC mixture. To identify the above effects, the CVCV can switch the MC ambience to non-combustible pure nitrogen or methane-air premixture. Wakasugi et al. [22] carried out visualization measurements of the torch flame with the MC ambience under both non-combustible and combustible conditions.

In this study, however, as a first step in investigating the combustion process of PC-type gas engines, the reproducibility of numerical predictions regarding the influence of orifice specifications on torch flame ejection behaviour was evaluated by comparing measurement results in non-combustion conditions with numerical prediction results. Moreover, the preceding ejection process of unburned gas from the PC, which is difficult to observe with visualization experiments was numerically examined.

5.2. Effects of orifice aspect ratio

As explained, eight PC tips with different specifications were prepared to investigate the influence of orifice specifications, but changing only certain factors is not always easy and requires careful consideration of measurement results. First, the effects of the orifice aspect ratio; $(L/D)_{ori}$ were examined as an example of changing a single specific factor of a PC.

Figure 4 compares the temporal change of the penetration length and the spreading (cone) angle of the torch flame between the measurement results and the simulation results when only the aspect ratio was varied in a range of $(L/D)_{ori}$ = 1.43, 2.14, and 2.86 by changing L_{ori} = 5.0 mm (Tip #6), 7.5 mm (Tip #7), and 10.0 mm (Tip #8) respectively while keeping N_{ori} = 8, D_{ori} = ∅3.5 mm. Both values are averaged over the 8 torch flames from each orifice. The displayed time unit: ASOE represents the elapsed time since the torch flame started ejecting from the PC. Increasing the aspect ratio extends the penetration of torch flames and suppresses their spreading angle. Compared to diesel spray, a major feature of torch flame is that there is a high inverse correlation between ejection velocity and spread angle, but the tendency was relatively small in these cases because the ejected momentum was kept the same. It should be noted the discrepancy between measurements and numerical predictions is large in the early stage of the torch flame ejection, and the order of the penetration between $(L/D)_{ori}$ = 2.14 and 2.86 is reversed. It may be caused by the difficulty in determining the ignition of the unburned methane-air premixture preceding torch flames. In the visualization, the determination depends on how to distinguish the boundary between the unburned mixture and the torch flame based on the brightness of the shadowgraph image, and in the CFD calculation, it depends on the evaluation of the dilution effect by atmospheric nitrogen. Although the difference between the two decreases in the late stage of ejection as the momentum of the torch flame decreases, the influence of underestimation of the measurement seems more dominant (See arrows B and C in Fig. 5). As for the spreading angle of the torch flame, its trends versus $(L/D)_{ori}$ are said to be well reproduced both qualitatively and quantitatively.

Figure 5 compares the shadowgraph images of the torch flame and the visualized results of the numerical prediction. The black circle in the centre of the shadowgraph image corresponds to the bottom of the PC. The prediction results show the area where the temperature surpassed the threshold level in the horizontal cross-section B-B' in Fig. 2. Due to the insufficient adjustment of the optical system, false information was often superimposed in the shadowgraph images as a darkened area of about twice the PC radius around the PC (See arrow A in the figure). In addition, because of dividing the cylindrical combustion chamber of the CVCV with cubic cells, the predicted penetration and the shape of the torch flames tend to be different whether the direction of mesh division is perpendicular or oblique to the torch flame ejection.

5.3. Effects of throat diameter of nozzle tip

Second, the effects of the throat diameter of a nozzle tip; D_{trt} were checked as another example of changing a near single PC specification by replacing the reference PC Tip #1 (D_{trt} = ∅15 mm) with Tip #7 (∅10 mm). With this exchange, a PC/MC volume ratio; V_{PC}/V_{MC} was also reduced from 2.3 % to 2.0 % and the stored energy in the PC by 15%, and some throttling effect was given at the same time during the flame propagation from a main part of the PC to the PC tip.

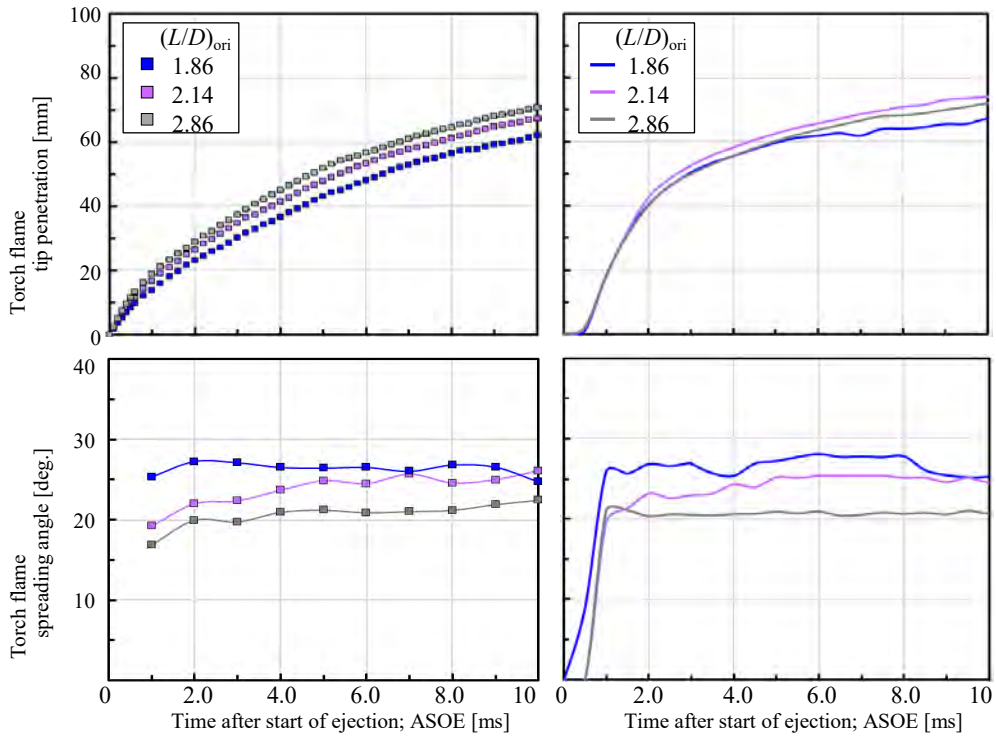

Fig. 4. Effects of $(L/D)_{ori}$ on torch flame penetration and its spreading angle by PC Tip #6 ($(L/D)_{ori}$ = 1.43), #7 (2.14), and #8 (2.86) respectively with N_{ori} = 8 and D_{ori} = ∅3.5 mm in common, measurement results (left half), and simulation results (right half)

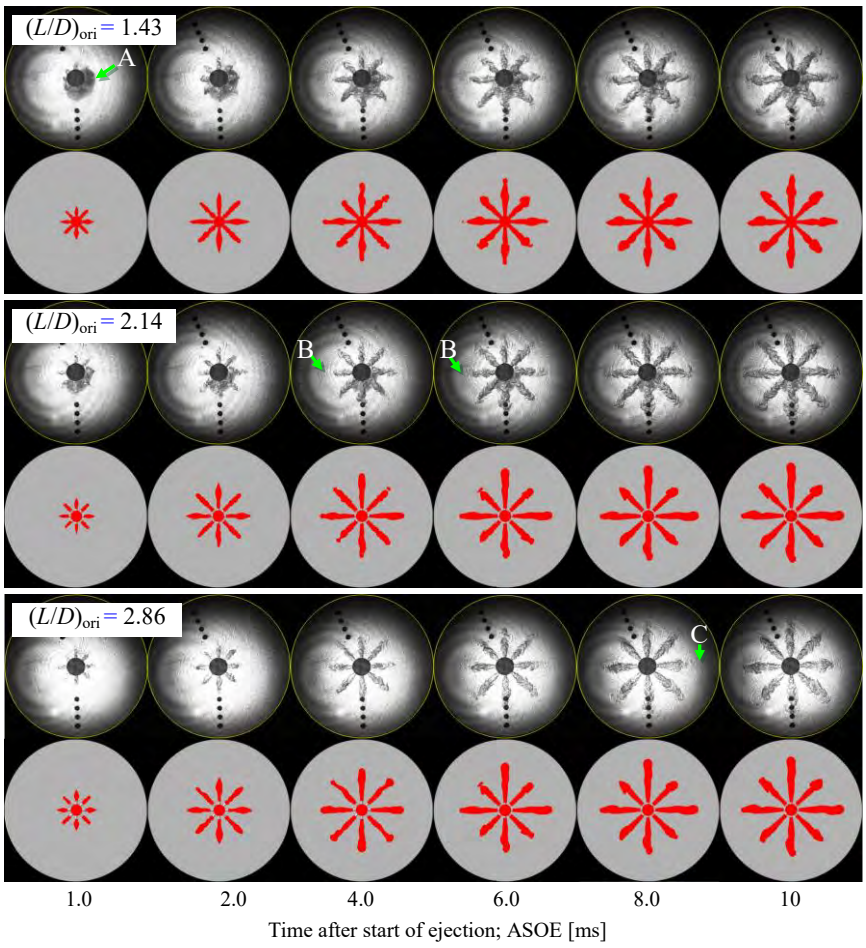

Fig. 5. Effects of orifice aspect ratio; $(L/D)_{ori}$ on ejection behaviour of torch flame by PC Tip #6 ($(L/D)_{ori}$ = 1.43), #7 (2.14), and #8 (2.86) respectively with N_{ori} = 8 and D_{ori} = ∅3.5 mm in common, shadowgraph images (upper row of island), and simulation results (lower row)

Figure 6 shows the temporal change of the penetration length and the spreading angle of the torch flame comparing the measurement and simulation results. All in all, the decrease in D_{trt} was observed to cause a slower ejection speed from the PC orifice and a wider spreading angle of the torch flame. The agreement of both results was qualitatively good in these aspects, but the torch flame penetration was overestimated especially in the jet-developing process of the D_{trt} = ∅10 mm (V_{PC}/V_{MC} = 2.0%) case. The numerical simulation in the study may overestimate the heat release rate in the PC and the exaggeration of the throttling effect. These suggest that not only the stored energy in the PC but also the combustion process and the cross-sectional shape are important for predicting the ejection behaviour of torch flame.

5.4. Effects of number of orifices

Third, the effects of N_{ori} on torch flame behaviour were preferentially explored because the number of orifices is an important design factor in a PC-type gas engine. It directly affects the torch flame distribution and the ignition area in the MC mixture. In the study, N_{ori} was set to 6 (Tip #2), 8 (Tip #1), and 10 (Tip #3) with the total orifice opening area; A_{ori} and the PC volume; V_{PC} kept almost constant. So, D_{ori} changed to ∅4.0 mm, ∅3.5 mm, and ∅3.1 mm, and $(L/D)_{ori}$ changed to 1.86, 2.18, and 2.42 for the N_{ori} = 6, 8, and 10 orifice cases, respectively.

Figure 7 and 8 summarize the measurement and simulation results in the same manner as the previous case. The false information was superimposed again in the shadowgraph images of the N_{ori} = 10 case (See arrow A). Since the momentum of a single torch flame is inversely proportional to N_{ori}, the N_{ori} = 6 case shows the longest penetration and the N_{ori} = 10 shows the shortest. However, the torch flame penetration showed little difference until about 1 ms ASOE in all cases, then the growth gradient for the 10-orifice case got slower around the timing, and the 6-orifice case showed a similar behaviour at about 6 ms ASOE. This trend can be attributed to the momentum of the individual torch flames. The torch flame led by unburned gas in the PC has a sharper tip than two-phase diesel sprays. It suggests the preceding unburned PC mixture could assist the torch flame penetration before slowing down claimed by Zhou et al. [25].

The overall reproducibility of the torch flame behaviour by the CFD of the study shows good agreement with these characteristics of the torch flame. Moreover, prediction results for 2 ms ASOE with N_{ori} = 6 hinted that the torch flames located in up and down directions in Fig. 6 partially quenched at their tip and an unburnt region remains in the centre of the tip even after flame development, indicating that the ejection intensity of the torch flame can affect the combustion process in the MC (See arrow B). Although the prediction results successfully reproduce effects on the penetration and spreading angle of the torch flame, as well as their order among the tested N_{ori}s, the predictions overestimate the penetration up to around 2 ms ASOE in the early

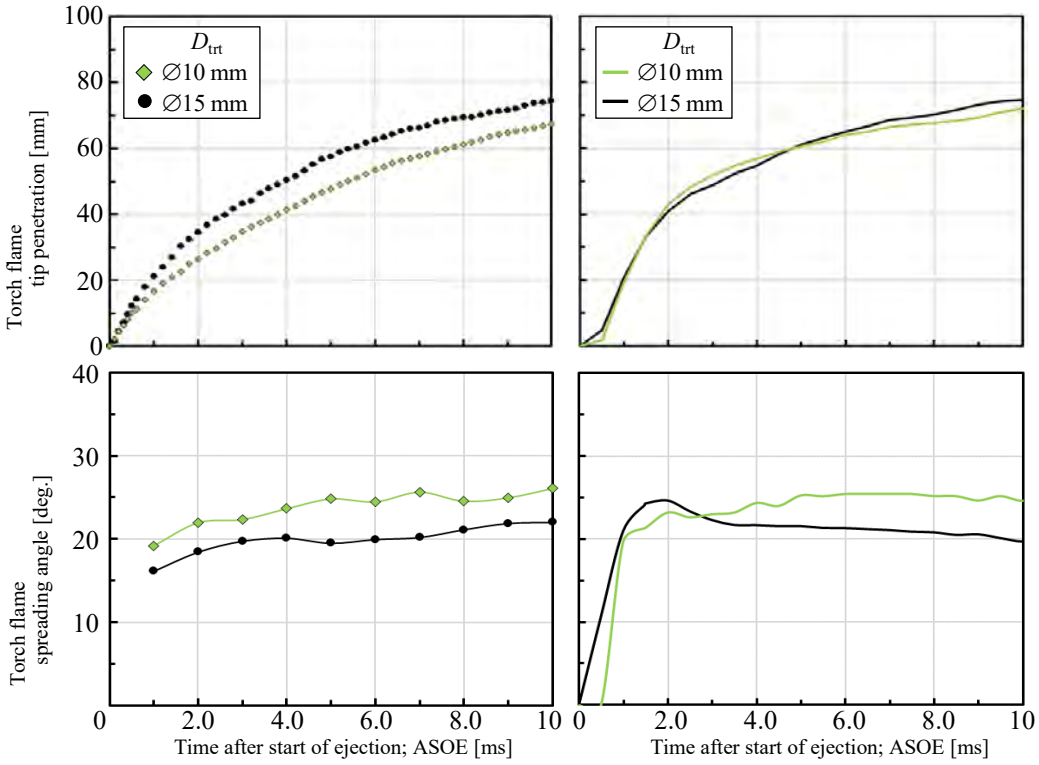

Fig. 6. Effects of D_{trt} n torch flame penetration and its spreading angle by PC Tip #1 (D_{trt} = ∅15 mm, V_{PC}/V_{MC} = 2.3%) and #7 (∅10 mm, 2.0%) respectively with N_{ori}(= 8) and L_{ori}(= 7.5 mm) in common, measurement results (left half), and simulation results (right half)

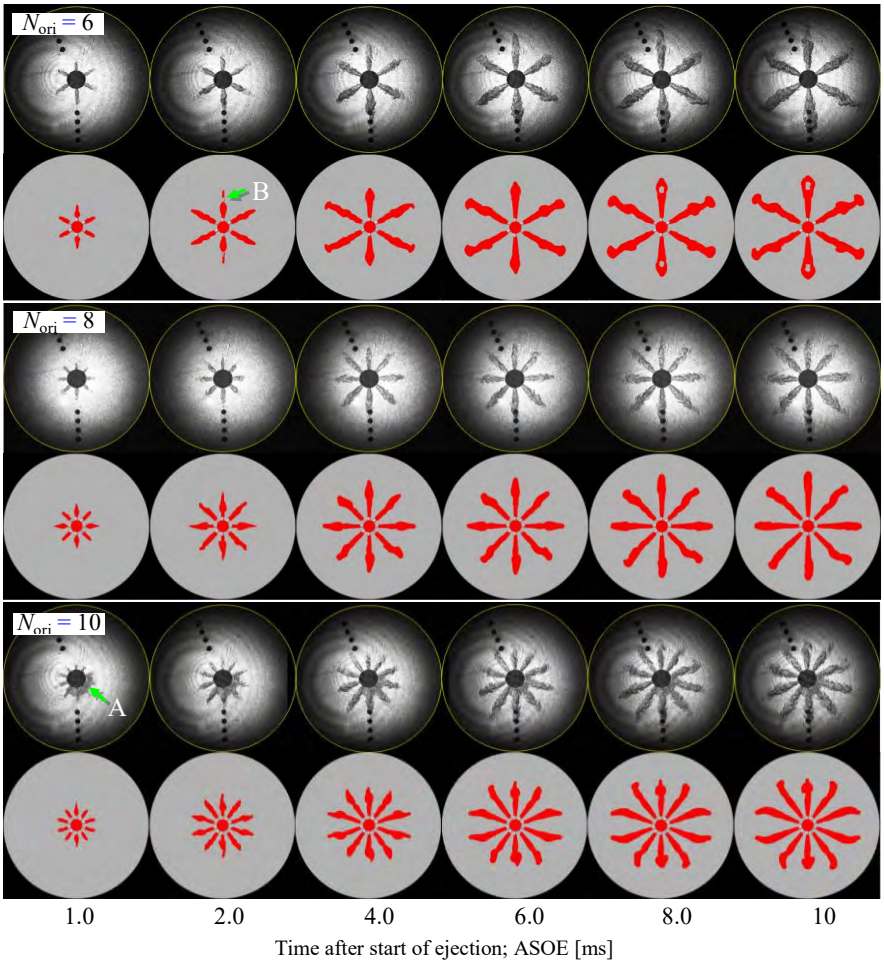

Fig. 7. Effects of number of orifices; N_{ori} on ejection behaviour of torch flame by PC Tip #2 (N_{ori} = 6, D_{ori} = ∅4.0 mm), #1 (8, ∅3.5 mm), and #3 (10, ∅3.1 mm) respectively, with ca. same A_{ori}, measurement results (upper row of island), and simulation results (lower row)

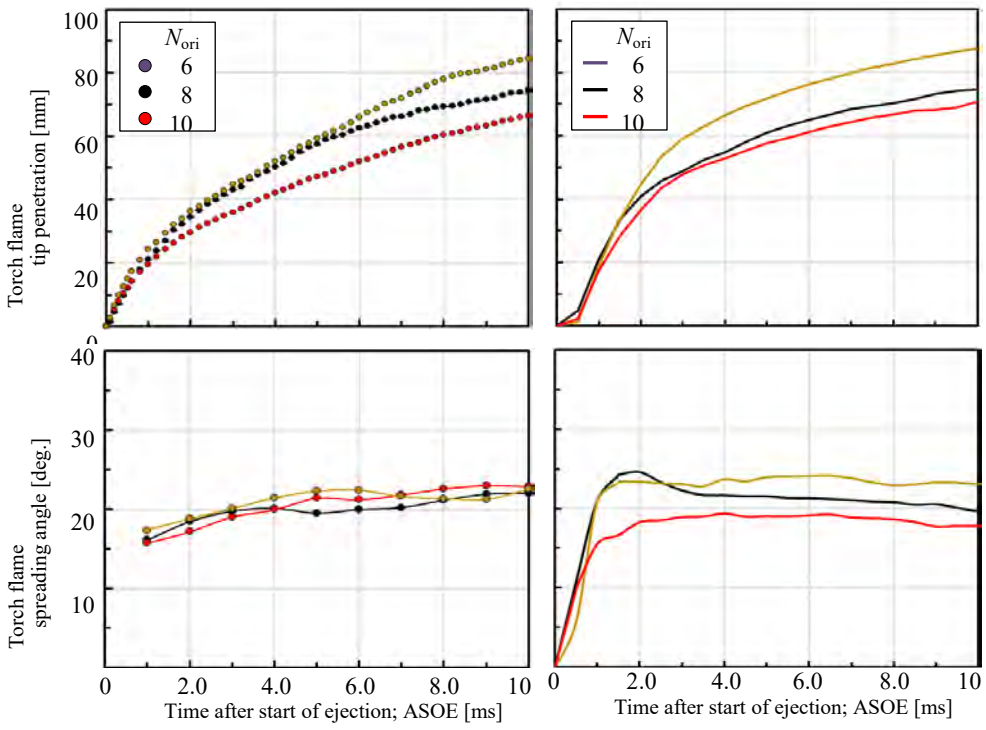

Fig. 8. Effects of N_{ori} on torch flame penetration and its spreading angle by PC Tip #2 (N_{ori} = 6, D_{ori} = ∅4.0 mm), #1 (8, ∅3.5 mm), and #3 (10, ∅3.1 mm) respectively, with ca. same A_{ori}, measurement results (left half), and simulation results (right half)

images that as D_{ori} increases, the penetration of the torch flame decreases and the spreading angle after the torch development increases. Unlike the previous experiments with almost constant A_{ori}, there was a clear difference among the penetrations of the three cases immediately after the ejection. This can be explained by the fact that the ejection speed of the torch flame from orifices could be roughly in inverse proportion to A_{ori} or square of D_{ori}, since the combustion process in the PC is thought to be the same regardless of the nozzle tip specifications.

5.5. Effects of orifice diameter

Finally, the effects of the orifice diameter: D_{ori} were investigated by changing the reference Tip #1 to Tip #4 or Tip #5. D_{ori} was ∅2.5 mm in Tip #4, ∅3.5 mm in Tip #1, and ∅5.0 mm in Tip #5 keeping N_{ori}(= 8), L_{ori}(= 7.5 mm), and V_{PC}/V_{MC}(= 2.3%) at their reference values. The ratio of A_{ori} among these PC tips was about 1: 2: 4, and $(L/D)_{ori}$ changed from 3.00 through 2.14 to 1.50. So, the effects of $(L/D)_{ori}$ should be counted when considering both experimental results.

Figure 9 and 10 summarize the measurement and simulation results. Again, arrow A in a shadowgraph image of the D_{ori} = ∅5.0 mm case shows that the false information was include. It can be seen in the shadowgraph stage of ejection and the effects of N_{ori} on the spreading angle. The latter may reflect the larger flame contour variation with jetting momentum in the spread angle.

Both the measurement and simulation results showed good qualitative agreement with the above behaviour, but they do not match quantitatively very well except for the reference case of Tip #1. The penetration length was unignorably underpredicted in the D_{ori} = ∅2.5 mm case and overestimated in the D_{ori} = ∅5.0 mm case while the spreading angle was underestimated in the latter case. The reason may be that the prediction in this study does not accurately reflect the stretching and misfiring of a reaction zone varied on the ejection speed of the torch flame. In other words, in the D_{ori} = ∅2.5 mm case, the ignitability of the preceding PC mixture may be underestimated compared to the measurement results. In contrast, it may be overestimated in the D_{ori} = ∅5.0 mm case. All of these imply the importance of investigating the behaviour of unburned gas that precedes the torch flame. This will be discussed in detail later.

5.6. Effects of unburned PC mixture ejection

Figure 11 is an example of the PC configuration of 4-stroke-cycle lean-burn gas engines. Since the 4-valve layout is necessary for high-power-density engines, the PC should be in the centre of the combustion chamber, have a funnel shape expanding upward, and locate the fuel supply port and the spark plug on its top surface. This means the ignited flame in the PC always propagates from top to bottom and a considerable portion of the methane-air mixture inside the PC is discharged being unburned before the torch flame ejection. This preceding PC mixture can be the origin of the difference between the measured torch flame penetration and the predicted one.

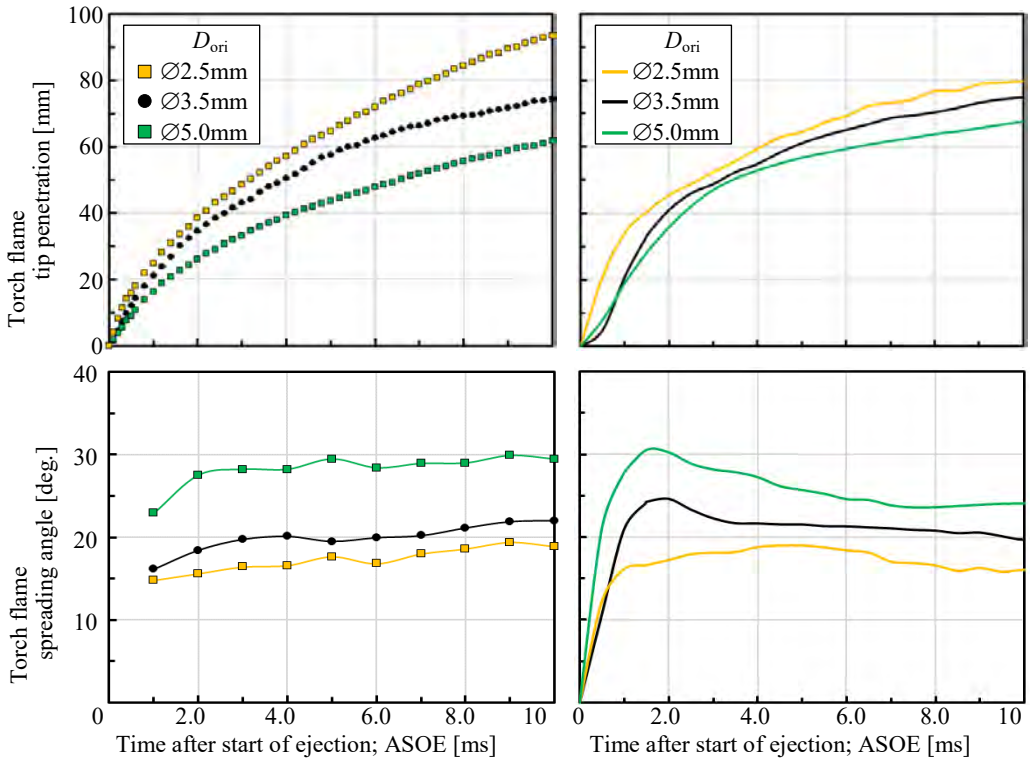

Fig. 9. Effects of D_{ori} = ∅2.5 mm, ∅3.5 mm, and ∅5.0 mm on torch flame penetration and its spreading angle by PC Tip #4, #1, and #5 respectively with N_{ori}(= 8) and V_{PC} in common, measurement results (left half), and simulation results (right half)

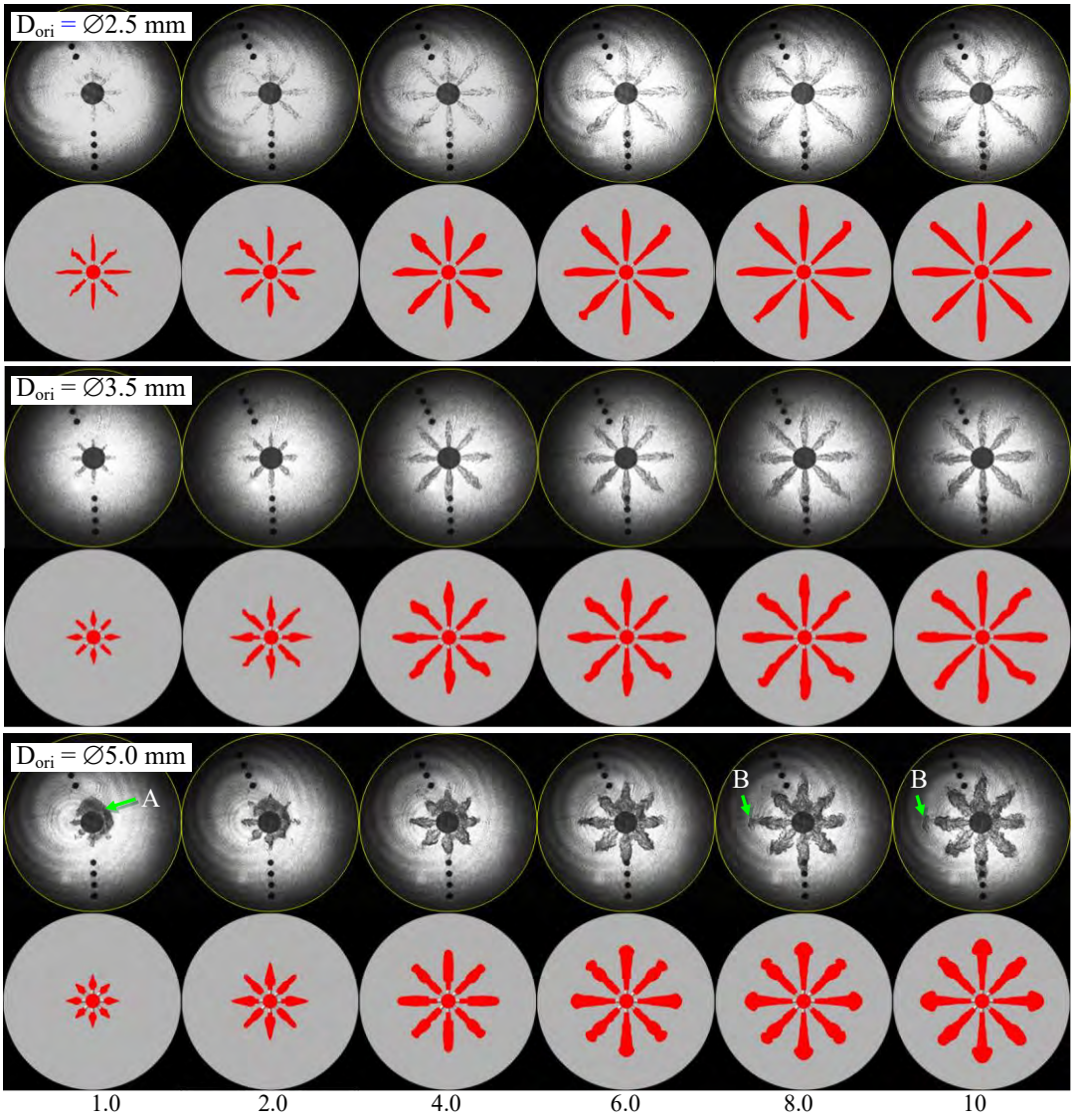

Fig. 10. Effects of orifice diameter; D_{ori} on ejection behaviour of torch flame by PC Tip #4 (∅2.5 mm), #1 (∅3.5 mm), and #5 (∅5.0 mm), respectively with N_{ori} = 8 and V_{PC} in common, in the shadowgraph images (upper row of island) and simulation results (lower row)

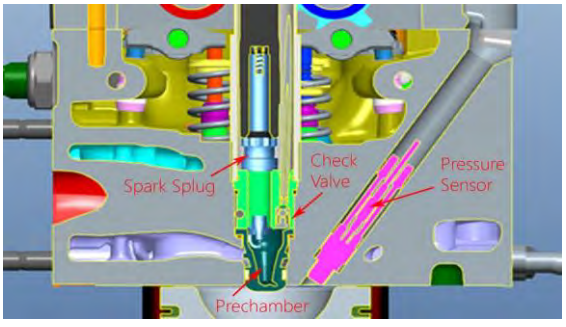

Fig. 11. Example of cross-sectional view of pre-chamber assembly [4]

Figure 12 compares enlarged views of observed plumes of unburned PC mixture in the N_{ori} = 10 case with corresponding ones predicted by the CFD. The latter was visualized as the light yellow iso-surface of 1 mass% of the PC mixture (marker gas). The arrows in the shadowgraph images indicate the position of the visible jet tips of the unburned PC mixture. The capture timings of the two are not the same due to the difference in storage period. The CFD gave so quick diffusion of the PC mixture into the MC in advance that the mixture surrounded the outer circumference of the PC before the ejection was captured in the shadowgraph at 16.0 ms ASOE. After the true ejection started, however, penetrations of both experiments seemed the same, and their variation among the orifices seemed small. Since the diffusion to the MC ambient means dilution of the preceding PC mixture with inert nitrogen, it is expected to affect the ignitability of the mixture by the following torch flame.

Figure 13 collects the predicted behaviours of torch flame from the investigation for the effect of D_{ori} with light yellow iso-surfaces of the PC mixture superimposed. As mentioned in Fig. 11, there was a discrepancy in penetration length between the observed and predicted torch flame, which is presumably due to the lack of reproducibility in the entrainment of MC ambient by the ejected PC mixture

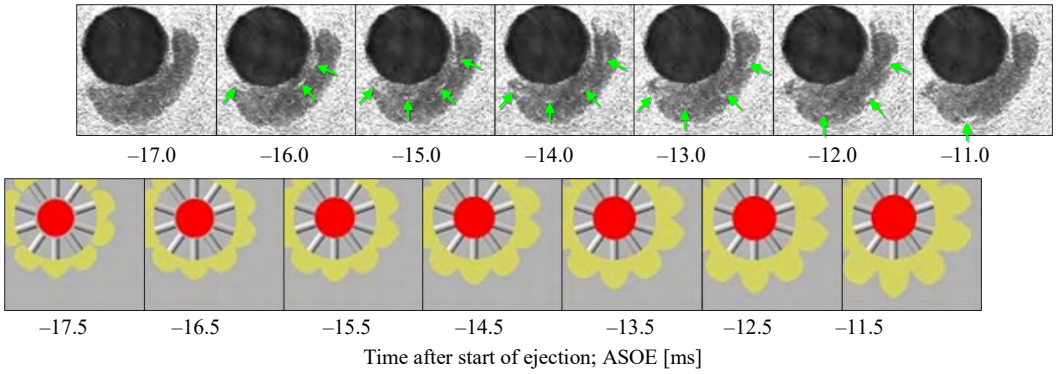

Fig. 12. Enlarged view of the ejection process of the unburned PC premixture by PC Tip #3 (N_{ori} = 10, D_{ori} = ∅3.1 mm), measurement results (upper row), and simulation results (lower row), arrows in the shadowgraph images

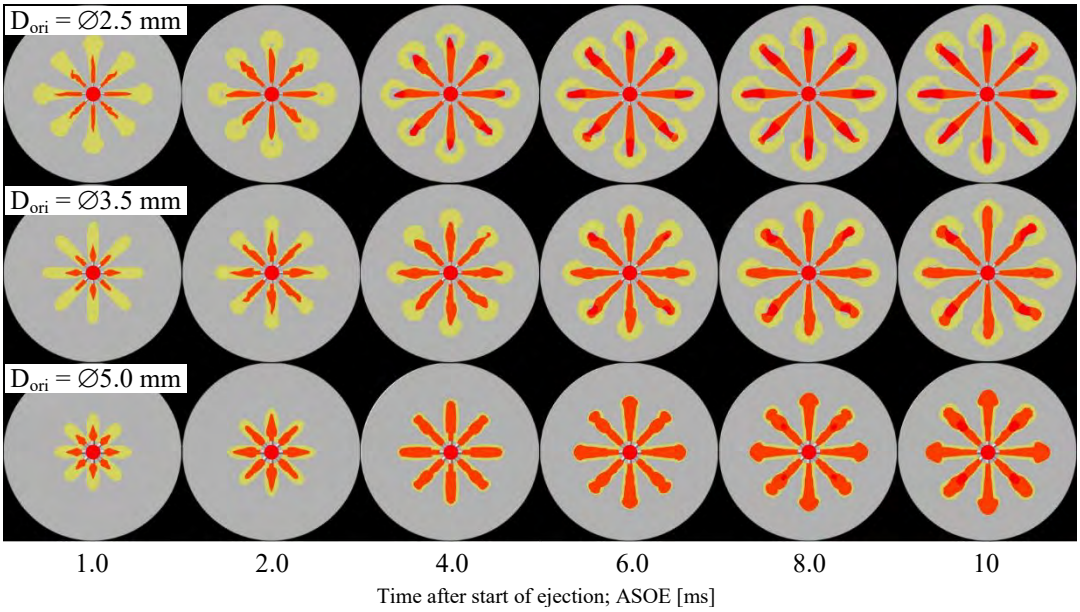

Fig. 13. Predicted relation between the preceding plumes of unburned premixture and the following torch flames by PC Tip #4 (D_{ori} = ∅2.5 mm), #1 (∅3.5 mm), and #5 (∅5.0 mm), respectively with N_{ori} = 8 and V_{PC} in common

and in the ignition occurrence from the torch flame. In general, the higher ejection speed enhances the MC nitrogen entrainment of the PC mixture and the stretch of the torch flame, and results in the deterioration of the ignitability of the torch flame to the plume of the PC mixture. In the D_{ori} = ∅2.5 mm case, the preceding PC mixture has the highest ejection velocity of the three cases, and its entrainment of MC nitrogen progresses since the tip of the premixture decelerates and expands because of the entrainment by the time the torch flame starts ejection. The torch flame also decelerates significantly as the torch flame travels through the unburned premixture, but no ignition of the premixture occurs from the torch flame.

On the other hand, in the D_{ori} = ∅5.0 mm case, the unburned premixture is ignited as early as 2 ms after the torch flame ejection, and the flame length increases rapidly, after which the torch flame progresses almost entirely into the premixture. By Comparing with the combustion visualization by the shadowgraph, it is thought that the ignitability of the premixture by the torch flame was underestimated in the former case and overestimated in the latter.

6. Conclusions

In this study, the effects of specifications of a pre-chamber (PC) tip were numerically examined in detail based on the comparison with measurement results in a constant-volume combustion vessel (CVCV) that simulated the combustion chamber configuration of a medium-speed PC-type gas engine. As a first step in investigating the combustion process of PC-type gas engines, the reproducibility of CFD predictions regarding the influence of PC tip specifications on torch flame ejection was evaluated under non-combustion conditions by charging pure nitrogen in the main chamber (MC). Moreover, the preceding ejection process of unburned premixture from the PC was discussed in some cases succeeding in its visualization. The following conclusions were obtained.

1. The reproducibility of the CFD simulation that considers the reduction of calculation load for the application to a medium-speed gas engine was successfully evaluated based on measurement results of the torch flame behaviour in a constant-volume combustion vessel (CVCV) with the same scale as a PC-type medium-

speed gas engine under non-combustible ambient conditions in an MC.

2. If other specifications of the PC tips are the same, the penetration length of torch flames of a PC-type gas engine is proportional to the ejection velocity or the ejection momentum of a torch flame, while their spreading angle changes inversely. The trends were qualitatively and quantitatively reproduced by the applied CFD frame. Although the increase in the orifice aspect ratio and the decrease in the PC tip throat diameter also give similar but relatively weaker trends, the reproducibility of the numerical simulation got worse with these parameters.
3. The numerical predictions consistently tended to overestimate the penetration of the torch flame in the early stage of the ejection. The discrepancy is probably attributed to the unburned premixture ejection from the PC preceding the torch flame. For the applied shadowgraph optics in the measurements, it was difficult to identify the ignited region of the unburned premixture by the torch flame, and for the applied numerical prediction, it was difficult to reproduce the entrainment of the MC ambient and the ignition process of the unburned premixture.
4. The investigation of the effects of a PC orifice diameter showed that the ignition potential of the torch flame tended to be overestimated in the larger orifice case of a slower ejection speed and less MC ambient entrainment, but it was reversed in the smaller orifice case of a higher ejection speed. As for the tip penetration of the unburned premixture, detailed observation of the shadowgraph images and the visualized prediction results were in good agreement, but the simulated penetration was somewhat obscure because of the excessive numerical diffusion of the premixture from the orifice into the MC ambient and the evaluation uncertainty in the ignitability of the nitrogen-diluted unburned premixture by the torch flame.

As a next step, it is necessary to simulate the whole combustion process numerically with the MC charged with a lean premixture of CH_4/air. By comparing with the experimental results in the MC combustion cases by Wakasugi et al. [22], essential flame propagation from the torch flame surface into the MC premixture would be numerically clarified, and then a novel and practical index for the combustion-promoting potential of the torch flame such as so-called “jet intensity” could be formulated based on the PC tip specifications.

Nomenclature

A_{ori}	total opening area of PC tip orifices
AMR	adaptive mesh refinement
ASOE	after the start of ejection
CFD	computational fluid dynamics
CN	carbon neutrality
CPU	central processing unit
CVCV	constant volume combustion vessel
D_{ori}	diameter of PC orifice
D_{trt}	throat diameter of PC tip
GHG	greenhouse gas
GRI	Gas Research Institute
IMO	International Maritime Organization
L_{ori}	length of PC orifice
$(L/D)_{ori}$	aspect ratio of PC tip orifice
MC	main combustion chamber
MEPC	Marine Environment Protection Committee
N_{ori}	the number of PC tip orifices
NG	natural gas
NO_x	nitrogen oxides
PC	pre-combustion chamber
RANS	Reynolds-Averaged Navier-Stokes equations
SAGE	structural adaptive grid embedding
SI	spark ignition (forced ignition)
t	tickness of oprical window
TJI	turbulent jet ignition
V_{MC}	capacity volume of MC
V_{PC}	capacity volume of PC
λ_{PC}	global air excess ratio in PC
λ_{MC}	global air excess ratio in MC

Bibliography

[1] Aakko-Saksa T, Lehtoranta K, Kuittinen N, Järvinen A, Jalkanen J, Johnson K et al. Reduction in greenhouse gas and other emissions from ship engines: current trends and future options. Prog Energ Combust. 2023;94:101055. https://doi.org/10.1016/j.pecs.2022.101055

[2] Abdelhameed E, Tsuru D, Tashima H, Sako T, Consideration of combustion improvements of lean-burn gas engine with pre-combustion chamber. 30th CIMAC World Congress, Busan 2023.

[3] Atis C, Chowdhury SS, Ayele Y, Stuecken T, Schock H, Voice AK. Ultra-lean and high EGR operation of dual mode, turbulent jet ignition (DM-TJI) engine with active pre-chamber scavenging. SAE Technical Paper 2020-01-1117. 2020. https://doi.org/10.4271/2020-01-1117

[4] Bach C. Record efficiency for a gas engine. Empa HP. https://www.empa.ch/web/s604/gason

[5] Badr O, Alsayed N, Manaf M. A parametric study on the lean misfiring and knocking limits of gas-fueled spark ignition engines. Appl Therm Eng. 1998;18(7):579-594. https://doi.org/10.1016/S1359-4311(97)00029-X

[6] Falkner R. The Paris Agreement and the new logic of international climate politics. Int Aff. 2016;2(5):1107-1125. https://doi.org/10.1111/1468-2346.127086

[7] Guo H, Zhou S, Shreka M, Feng Y. Effect of pre-combustion chamber nozzle parameters on the performance of a marine 2-stroke dual fuel engine. Processes. 2019;7(12):876. https://doi.org/10.3390/pr7120876

[8] Keenan M, Pickett R, Tronconi E, Nova I, Kinnunen N, Suvanto M et al. The catalytic challenges of implementing a Euro VI heavy duty emissions control system for a dedicated lean operating natural gas engine. Top Catal. 2019;62:273-281. https://doi.org/10.1007/s11244-018-1127-7

[9] Kim J, Scarcelli R, Som S, Shah A, Biruduganti MS, Longman DE. Numerical investigation of a fueled pre-chamber spark-ignition natural gas engine. Int J Engine Res. 2022; 23(9):1475-1494. https://doi:10.1177/14680874211020180
[10] Korakianitis T, Namasivayam AM, Crookes RJ. Natural-gas fueled spark-ignition (SI) and compression-ignition (CI) engine performance and emissions. Prog Energ Combust. 2011;37(1):89-112. https://doi.org/10.1016/j.pecs.2010.04.002
[11] Kulzer AC. Sustainability & powertrain systems: from electrification to hydrogen and eFuels (updated). Proc. JSAE PEL Int Meeting, Technical Challenges for a Carbon Neutral Society by 2050. Kyoto 2023.
[12] IMO HP MEPC80. https://www.imo.org/en/MediaCentre/PressBriefings/pages/Revised-GHG-reduction-strategy-for-global-shipping-adopted-.aspx
[13] Liyan F, Jun Z, Bo L, Lei C, Weiyao W, Long W et al. Research on the characteristics of enrichment fuel injection process in the pre-chamber of a marine gas engine. SAE Technical Paper 2015-01-1961. 2015. https://doi.org/10.4271/2015-01-1961
[14] Matla J, Kaźmierczak A, Haller P, Trocki M. Hydrogen as a fuel for spark ignition combustion engines – state of knowledge and concept. Combustion Engines. 2024;196(1): 73-79. https://doi.org/10.19206/CE-171541
[15] Sadanandan R, Markus D, Schießl R, Maas U, Olofsson J, Seyfried H et al. Detailed investigation of ignition by hot gas jets. P Combust Inst. 2007;31(1):719-726. https://doi.org/10.1016/j.proci.2006.08.027
[16] Senecal PK, Pomraning E, Richards KJ. Multi-dimensional modeling of direct injection diesel spray liquid length and flame lift-off length using CFD and parallel detailed chemistry. SAE Technical Paper 2003-01-1043. 2003. https://doi.org/10.4271/2003-01-1043
[17] Shapiro E, Tiney N, Kyrtatos P, Kotzagianni M, Bolla M, Boulouchos K et al. Experimental and numerical analysis of pre-chamber combustion systems for lean burn gas engines. SAE Technical Paper 2019-01-0260. 2019. https://doi.org/10.4271/2019-01-0260
[18] Tashima H, Kunimitsu M, Sugiura K, Tsuru D. Development of high-efficiency gas engine through observation and simulation of knocking phenomena. 26th CIMAC World Congress, Bergen 2010.
[19] Trombley G, Toulson E. A fuel-focused review of pre-chamber initiated combustion. Energ Convers Manage. 2023; 298:117765. https://doi.org/10.1016/j.enconman.2023.117765
[20] Validi AA, Schock H, Jaberi F. Turbulent jet ignition assisted combustion in a rapid compression machine. Combust Flame. 2017;186:65-82. https://doi.org/10.1016/j.combustflame.2017.07.032
[21] Valladolid PG, Tunestål P, Monsalve-Serrano J, García A, Hyvönen J. Impact of diesel pilot distribution on the ignition process of a dual fuel medium speed marine engine. Energ Convers Manage. 2017;149:192-205. https://doi.org/10.1016/j.enconman.2017.07.023
[22] Wakasugi T, Tsuru D, Tashima H. Influences of the pre-chamber orifices on the combustion behavior in a constant volume chamber simulating pre-chamber type medium-speed gas engines. Combustion Engines. 2022;191(4):66-76. https://doi.org/10.19206/CE-148171
[23] Yasueda S, Takasaki K, Tashima H. The abnormal combustion affected by lubricating oil ignition in premixed gas engine, Proceedings of the ASME 2012 Internal Combustion Engine Division Spring Technical Conference. 2012:29-36. https://doi.org/10.1115/ICES2012-81042
[24] Ye Y, Yue Z, Wang H, Liu H, Wu C, Yao M. A mapping approach for efficient CFD simulation of low-speed large-bore marine engine with pre-chamber and dual-fuel operation. Energies. 2021;14(19):6126. https://doi.org/10.3390/en14196126
[25] Zhou L, Song Y, Hua J, Liu F, Liu Z, Wei H. Effects of different hole structures of pre-chamber with turbulent jet ignition on the flame propagation and lean combustion performance of a single-cylinder engine. Fuel. 2022;308: 121902. https://doi.org/10.1016/j.fuel.2021.121902

Takahide Aoyagi, MEng. – Energy Conversion Group, Technology Platform Center, Technology & Intelligence Integration, IHI Corporation, Japan.
e-mail: *t.jr.aoyagi@gmail.com*

Daisuke Tsuru, DEng., Ass. Prof. – Shipping Technology Department, National Institute of Technology Oshima College, Japan.
e-mail: *tsuru.daisuke@oshima.kosen-ac.jp*

Takuya Wakasugi, MEng. – Interdisciplinary Graduate School of Engineering Sciences, Kyushu University, Japan.
e-mail: *wakasugi.takuya.875@s.kyushu-u.ac.jp*

Hiroshi Tashima, DEng., Ass. Prof. – Faculty of Engineering Sciences, Kyushu University, Japan.
e-mail: *tajima.hiroshi.539@m.kyushu-u.ac.jp*

Article citation info:
Stępień Z. Vehicle related non exhaust particle emissions – Euro 7 requirements. Combustion Engines. 2024;199(4):15-29. https://doi.org/10.19206/CE-190606

Zbigniew STĘPIEŃ

Combustion Engines
Polish Scientific Society of Combustion Engines

Vehicle related non exhaust particle emissions – Euro 7 requirements

ARTICLE INFO

Received: 6 April 2024
Revised: 28 June 2024
Accepted: 28 June 2024
Available online: 10 July 2024

The article is a multi-directional review of the current knowledge in the field of particulate matter emissions from motor vehicles, but not related to the combustion process in piston combustion engines. A summary of the research results available in the literature was provided regarding the size and composition of particulate emissions from abrasive wear of working elements of brake systems and tires. The mechanisms of particulate matter formation related to the wear processes of brake pads, discs, and tires were described. Reference was made to currently available research results regarding the harmful, toxicological impact on the health of chemical components contained in particulate matter, in particular on diseases of the respiratory and cardiovascular systems. A critical analysis of various, previously unstandardized measurement and assessment methods for the emissions of this particulate matter category was carried out, pointing to future needs. Relating, in particular, to the requirements of the new Euro 7 standard.

Key words: *particulate matter, brake system emissions, tire wear emissions, methods of particulate matter measurement, Euro 7*

1. Introduction

Current epidemiological and experimental research on environmental pollution related to road traffic more commonly focuses on particulate matter (PM). These particles range in diameter from a few nanometers to hundreds of microns. The evidence obtained in the studies clearly indicated a harmful, toxicological health impact of chemical components contained in particulate matter, in particular on diseases of the respiratory and cardiovascular systems [2, 22, 47, 51]. Among all critical risk factors for mortality, exposure to ambient fine particulate matter ranks seventh (OECD 2017). According to OECD studies, the contribution of NEE (non-exhaust emissions) to traffic-induced particulate matter concentrations in local hotspots may exceed 50% [50, 122], which highlights the importance of NEE in urban environments.

PM emitted from motor vehicles are classified based on two main sources of origin, i.e. exhaust emissions, which represent PM resulting from incomplete combustion of fuel and lubricating oil in the combustion chamber, and PM emissions not related to the combustion process in the engine resulting from braking processes, tire wear as well as the resuspension of particles generated by road traffic [59, 138, 139, 142]. Non-combustion emissions (NEE) from road traffic refer to particles released into the air as a result of the wear of the friction elements of the braking system, tires, road surface, and road dust re-suspension during vehicle use on the road [10, 39, 42, 46, 110]. The size, chemical composition, and emission rate of particles from such sources affect the concentration of particles in the atmosphere and how harmful they are to human health. Such particles have a chemical composition and size different from particulate matter in exhaust gases.

NEE arises regardless of the type of vehicle and the type of its drive unit (power source). With the implementation of the vehicle exhaust emission control policy and the successive reduction of permissible emission limits for regulated exhaust gas components, the emission of particulate matter arising from the combustion process in engines has gradually decreased, and the relative share of particulate matter emissions from brake and tire wear has therefore grown unchecked. The concentration of airborne particulate matter is often referred to as PM_{10}. These are particles with a diameter of less than 10 µm expressed per unit volume. In certain conditions, car brake materials also emit ultrafine particles (with diameters below 0.1 µm), and their numerical concentration is several orders of magnitude greater than the concentration of fine particles (PM_{10}) [8, 84, 129, 155].

It was noted in other studies that particulate emissions from brake wear in Europe are made up of 30% ($PM_{2.5}$) and 40% (PM_{10}) for emissions from sources unrelated to combustion in engines [18, 32, 45, 53]. PM emissions not related to the combustion process accounted for a share ranging from 30% ($PM_{2.5}$) and 45% (PM_{10}) in 2010 to 54% ($PM_{2.5}$) and 69% (PM_{10}) in 2020 (after the introduction of DPF filters), and will probably exceed 90% in 2040 (Fig. 1) [18]. Research results indicate that particles originating from the wear of brake friction elements may constitute up to 21% of the total amount of PM10 emitted by motor vehicles in large urban areas, of which approximately 35-55% is suspended in the air, the remaining portion is usually deposited on the brake system elements. or on the road surface [52, 71, 79, 87, 142, 162]. The tire wear process generates and releases particles that consist of degraded tire tread compound (elastomer) mixed with minerals from the road surface. These particles are often called tire and road wear particles (TRWP) [56, 83, 134, 152]. Studies conducted over the last 10 years show that tire particulate matter emissions range from 0.2 kg/year/capita in countries with low vehicle numbers to 5.5 kg/year/capita in countries with high vehicle numbers. Therefore, the average is approximately 0.8 to 1 kg/year/inhabitant [14, 15, 81, 148]. Tire wear causes the formation and emission of microplastics, which constitute a huge environmental pollution problem.

Electric vehicles have been gaining increasing popularity for over a dozen years now [13, 78, 126]. The research results from various sources regarding the particulate matter

emission produced from the wear of brakes and tires vary. Some studies indicate that these emissions may be greater than the total PM emissions from an internal combustion engine vehicle (ICEV) [16, 143]. Many researchers indicate that electric vehicles are about 20% heavier than ICEVs due to the mass of their batteries, which would be expected to cause particulate emissions from increased brake wear, tire wear, road wear, and road dust resuspension [1, 131].

a)

b)

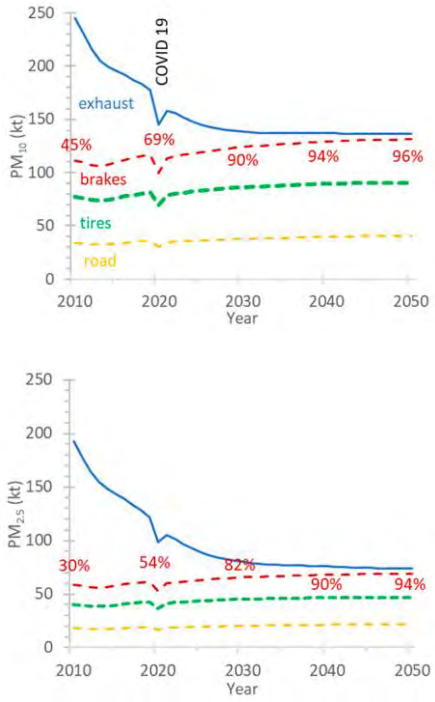

Fig. 1 Changes and forecasts of emissions from exhaust gases and other sources (brake, tire, and road wear) and total PM emissions from road transport in the EU27: (a) PM10; (b) PM2.5 [32]

On the other hand, it should be noted that the amount of braking done in battery electric vehicles is typically several times lower due to the use of a regenerative braking system. Despite this, recent studies based on updated emission analyzes have shown that the high mass of electric vehicles can offset the positive effect of regenerative braking on reducing particulate emissions [16, 63, 143]. The results of other studies state that electric vehicles' particulate emissions are comparable to conventional ICEVs' emissions [150]. Consequently, further research is needed to better understand the overall impact of vehicle electrification on emissions primarily related to braking and tire wear.

Emissions of regulated substances, including PM, from combustion engines have been restricted based on emission limit values for more than 30 years. There are no legal restrictions on non-exhaust emissions relating to particulate matter emissions and their resuspension. Already, NEEs have supplanted exhaust emissions as the largest source of PM emissions from road traffic. The growing trend in NEE emissions is also indicated by data from EU vehicle emissions analyzes done up to the year 2021 [28, 106] and after [6]. Most importantly, this major source of PM emissions from road traffic is currently not subject to any legislative process. It is therefore essential that future regulations introduce restrictions on NEEs and their contribution to total PM emissions. Taking this into account, the European Union has proposed that the standard currently being developed for limiting emissions of harmful components from motor vehicles – Euro 7 – should include reductions in particulate emissions not only from ICE exhaust gases [51, 142, 149]. However, the biggest problem that remains to be solved before the introduction of the new Euro 7 standard is the development of a standardized method for measuring NEE PM that will ensure obtaining reliable, repeatable measurement results.

The measurement of particulate emissions from NEE is a complicated challenge due to the open configuration of the vehicle brake system and the tires operating in the area of significant air flow influence. As a result, the particles are immediately diluted and dispersed by the surrounding air. This means that making repeatable measurements becomes a complex and difficult task. Moreover, measurement conditions on the road are greatly influenced by a set of highly variable parameters. In this regard, performing emission measurements in real operating conditions (RDE) becomes essential for a better understanding of the actual emission behavior and its reliable assessment. This led to the establishment of a dedicated Working Group on Particle Measurement Program (PMP) for the United Nations Economic Commission for Europe (UNECE) to develop a dedicated PM measurement methodology for NEE sources. Overall, further detailed investigation of PM from NEEs is necessary to reduce road traffic-related PM emissions and assess future health risks [1, 51, 142, 149].

The aim of this article was to perform a broad literature review, systematize the existing knowledge and to critically analyze it in the field of NEE.

2. Particulate emissions from brakes and tires

Non-combustion emissions (NEE) refer to particulate emissions released as a result of wear of brake friction elements, corrosion processes [52, 53, 162], tire-road surface interactions [69], and particle resorption [106, 127]. The vast majority of the brake and tire mass that becomes particles is released as the result of abrasion processes. Moreover, it has been shown that both sources can emit ultra-fine particles through thermochemical processes [157]. When assessing the emission of particulate matter, it is necessary to take into account not only their mass distribution but also their size distribution, as well as their quality (e.g., chemical composition and biological effect). The amount of emissions and the composition of PM from the wear of brake components can vary depending on many factors, the most important of which are:

– composition of the brake pad friction material, which may be organic or metallic. When specifying the materials from which brake pads can be made, the following should be mentioned: organic pads without asbestos (NAO – non-asbestos organics), low-alloy steel, carbon and aluminum [41, 155]. Metallic pads are divided into low-metallic (LM) or low-alloy, semi-metallic (SM) and fully metallic (rare). The Economic Commission for Europe (ECE) typically refers to the most representative

brake pads for Europe, which are either LM or SM [20, 26, 105, 132]. The results of previous research have shown that replacing ECE pads with NAO pads can reduce PM emissions from brakes [84, 129, 140, 159, 160]. The reduction was approximately 62% for PM10, 55% for PM2.5, and 64% for PN. It was also shown that brake disc wear can be easily reduced by replacing LM brake pads with NAO pads [155]. Brake pads described as NAO are popular in the USA, Japan, and Korea, while brake pads described as ECE are the most popular in Europe. Brake discs made of grey cast iron (GCI) are often used because of their high melting point, high heat storage capacity, as well as damping. Their other advantages are good castability and machinability [12, 105]. It is estimated that for brake discs made of grey cast iron, cooperating with high emission brake pads of the ECE type, the disc contributes to the emission of approximately 60% of the total PM mass [60, 64, 130, 136], while when using ceramic discs, this share can be reduced to < 5% [130]. When drum brakes were used, the brake drum with GCI contributed approximately 37% of the total mass of PM emissions [64]

- type of brake assembly, including discs, drums, their sizes, surface structure, and groove depths [41]
- vehicle operating conditions, including initial speed, deceleration rate, fluid pressure acting on the brake pistons, torque, and brake temperatures [41, 75, 128].

Generally speaking, the processes of brake wear and changes in kinetic energy or energy dissipated from the brakes are all related [35, 61, 103, 159]. Therefore, in the case of specific, identical braking cycles, the wear of brake friction elements should be correlated with the load (vehicle mass) [33, 143]. Reliably estimated emission factors are necessary to calculate with the required precision the contribution of PM emissions to the total PM emissions of a vehicle, as well as to estimate the emission reduction potential of different brake technologies and materials. To determine the emission factors, the required measurements shall be carried out both under laboratory conditions (e.g. PoD on dynamometer) and in the vehicle (chassis dynamometer, road measurements). In practice, measurements can be made using different equipment and test methods (most often gravimetric filtration method, optical and electrical meters, etc.) using different driving cycles [99, 146]. Therefore, in the past, various tests were used in which different test conditions were expected (ambient temperature, simulated vehicle mass), and the tests used different methods of determining the emission factors. Therefore, due to differences in methodology, test formulae and measurement instrumentation used, a direct, reliable comparison of the emission factors thus obtained may be subject to significant error [38, 52, 57, 93, 95, 116, 119, 122, 125, 132, 153, 158]. It will not be until the introduction of the EU – Global Technical Regulation (GTR 24) on PM emissions from the brakes of light motor vehicles that it will become possible to standardize measurement procedures. This regulation specifies the test procedure, the necessary system requirements, the test conditions, and the method and scope of equipment preparation for the WLTP-B test cycle using brake dynamometers. Table 1 summarizes the mass-dependent emission factors (mg/km/B) or particulate emissions (#/km/B) from different sources measured according to the requirements of GTR 24 for light vehicles, i.e. according to the WLTP-B test cycle. [45].

Not the entire mass of the worn brake pad and disc ends up suspended in the air as the so-called total suspended fraction. It usually constitutes 30–42%, with the majority of the airborne fraction being PM10 (usually ≫ 80%) [4, 48, 60, 62, 68, 95, 116]. The results of the tests showed that from a theoretical point of view, about 43% of the fraction corresponded to a median mass with a particle diameter of approximately 6.3 μm [81]. PM size distributions measured in the same study showed that the mass peak was expected in the PM range of 3–6 μm [15, 82]. From the analysis of the results of many tests carried out in accordance with the GTR 24 standard, WLTP-B test cycle [38, 52, 57, 93, 95, 116, 119, 122, 125, 132, 153, 158], of which some are shown in Table 1, the PM2. 5 to PM10 ratio was found to be 40% for ECE brake pads, 45% for NAO brake pads, 59% for CC and HMC brake discs and 60–100% for drum brakes [54, 160].

The constantly growing share of electrified (hybrid) and fully electric vehicles means that more attention ends up being paid to measuring their NEEs. On the one hand, it is assumed that the NEE value for such vehicles will increase due to their higher mass (between 15 and 25%) but on the other hand, it should also be assumed that it will decrease due to the high rate of regenerative braking and thus the lower actual use of friction brakes [16, 67, 133, 143]. So far, the number of available research results, based on which PM emission factors from brakes in electrified vehicles were determined, is limited [33, 61, 103, 143, 159]. Selected results are included in Table 2. In this case, the emission factors, which are absolute values, were lower than those given in Table 1, where the results were based solely on total frictional braking. As a result, compared to ICE equivalents, the reductions obtained are usually > 60% (Table 2) [45].

The emission factors described apply only to particulates (i.e. those that do not evaporate at 350°C) and to total particles, without a separate nucleation mode. The volatile nucleation mode occurs when the brake friction elements exceed the permissible (critical) temperature, usually within the range of 165 to 240°C [16, 48, 49, 94, 119, 126]. In such cases, the increase in emissions may be several orders of magnitude higher and is dependent on local supersaturation rates. Therefore, further tests in accordance with the GTR 24 protocol are necessary to confirm the repeatability of the results in such cases of brake operation.

Moreover, in accordance with the current version of GTR24, the PM10 emission factors for electrified vehicles shall be calculated using the PM emission factor of the internal combustion engine vehicle (ICV) using the so-called friction braking contribution coefficients [55]. For plug-in hybrid vehicles (PHEV), the friction braking contribution factor is set at 0.3 and for fully electric vehicles at 0.15. In practice, both electrification variants have slightly higher measured PM emission factors than those used in the above calculation method. Properly selected factors are a good first approximation for a typical mid-size electrified

Table 1. Particle matter emission factors of friction brakes related to vehicle mass (mg/km/B) or number of particulates emitted (#/km/B) measured according to the light vehicle brakes procedure GTR 24, i.e. with the WLTP-B braking cycle, unless otherwise specified

Year	Reference	Type	Pad	Mass kg	PM_{10} mg/km/B	$PM_{2.5}$ mg/km/B	PN × 10^9 #/km/B	Comments
2021	[97, 98]	Disc	ECE	1700	8.5	4.5	3.5	Medium sedan
2021	[77]	Disc	LM	2250	4.7	2.4	1.0	Class J
2021	[77]	HMC	LM	2250	2.1	1.2	1.3	Class J
2021	[77]	CC	LM	2250	1.4	0.9	0.8	Class J
2022	[99]	Disc	ECE	1800	4.5	1.45	3.4	Luxury sedan
2023	[88, 100]	Disc	ECE	1600	6.0	2.0	2.2	Class C
2023	[88, 100]	Disc	NAO	1600	2.3	0.7	1.0	Class C
2023	[88, 100]	Disc	ECE	1668	10.7	3.8	8.6	Class J
2023	[88, 100]	Disc	ECE	2623	9.1	3.1	3.3	SUV
2023	[88, 100]	Drum	n/a	1253	0.5	0.3	1.7	Super mini
2023	[101]	Disc	LM	1660	5.3	2.8	4.3	Class C
2023	[101]	Disc	NAO	1660	3.9	2.2	1.8	Class C
2023	[101]	Disc	ECE	1660	1.5	0.9	5.1	Class C
2023	[101]	Drum	LM	2041	1.1	0.8	2.8	Class C
2023	[101]	Drum	NAO	2041	0.3	0.3	0.5	Class C
2023	[101]	Disc	ECE	2113	7.6	3.5	3.9	Class J
2023	[101]	Disc	ECE	2027	4.1	1.2	2.1	Luxury sedan
2023	[94]	Disc	ECE	1840	6.5	1.8	0.5	Japanese market

B – brake; CC – carbon ceramic; D – disc (GCI); ECE – Economic Commission for Europe; GCI – grey cast iron; HMC – hard metal coated discs; LACT – Los Angeles City Traffic; LCV – light-commercial vehicle; LM – low metallic; NAO – non-asbestos organic; SUV – sports utility vehicle.

Table 2. Particulate emission factors from electric vehicle brakes related to vehicle mass (mg/km/V) or number of particulates emitted (#/km/V), percentages in brackets include emission reductions compared to electric vehicles with their ICE counterparts with friction brake only (i.e. regenerative braking disabled)

Year	Reference	Type	Pad	Vehicle or Mass	PM_{10} mg/km/V	$PM_{2.5}$ mg/km/V	PN × 10^9 #/km/V	Comments
2020	[89]	Disc	NAO	1600	2.0–2.3	1.0–1.4	1.3–8.9	PHEV
2021	[102]	Disc	n/a	1800	0.9	–	–	BEV
2023	[101]	Disc	ECE	1660	5.7 (–62%)	3.4 (–57%)	7.3 (–40%)	PHEV
2023	[101]	Disc	ECE	1660	3.1 (–79%)	2.3 (–71%)	2.1 (–82%)	BEV
2023	[103]	Disc	ECE	1350	10.5	4.5	141	HEV, Chassis, WLTP-E
2023	[104]	Disc	ECE	1228	–	–	0.5* (–4%)	Chassis, WLTP-B
2023	[104]	Disc	ECE	1228	–	–	0.5* (–65%)	Chassis, WLTP-E
2023	[104]	Disc	ECE	1228	–	–	4* (< 90%)	Chassis, RDE
2023	[80]	Disc	NAO	1553	0.3 (–86%)	0.14 (–78%)	0.05 (–84%)	PHEV, WLTP-B**

* back-calculated for emissions without regenerative braking and multiplied by 2,83/0,83 to be converted into total emissions related to the brakes of the rear axle; ** multiplied by 2.83 to convert to vehicle emissions. n/a = not available.

.

vehicles. However, given the multitude of different topologies and performance capabilities of electrified powertrains, a single factor per vehicle group will never reliably compare emissions from conventionally powered vehicles to electrified vehicles. Therefore, a suitable, dedicated method for determining vehicle-specific coefficients is already in development and will be added to GTR at a later stage.

The tire structure includes the following elements: tread, tire shoulder, tire side, belt ply, cord ply, inner lining, etc.

The tire wear process is quite complex, but it can be reduced to three main factor groups that influence it:

- related to the tire (structure, material, wear resistance, etc.)
- related to the vehicle (suspension parameters, load, speed, driving force, etc.)
- related to the environment (road conditions, temperature, method of operation, etc.).

The wear mechanism for rubber is very important for the tire wear particle generation process, which needs to be investigated. In the field of tribology, research on the rubber wear mechanism is relatively mature, including fatigue wear, friction wear, adhesive wear, and chemical erosion wear [92, 162]. While driving (accelerating, braking, turning), the tires have direct contact with the ground and support the vertical, lateral, and tangential load and reversing, capsizing, and rolling resistance moments. When tires contact the ground, direct friction and slippage occur, which causes micro-cutting and tearing of tires and the road surface. The wear process then progresses between the tires and the ground. When the cumulative friction energy in the relevant contact area reaches the critical energy, the tire surface is damaged; some of this surface is removed in the form of abrasive chips [1], and wear occurs. Tire wear usually manifests itself in the form of mixed tire and road surface wear, each accounting for approximately 50% [34].

The share of tire and road wear particles (TRWP) in PM emissions was estimated at 5–30%, up to 10% of the tire wear weight emits particulate matter in the air with a size of < 10 μm [36]. The literature [152] has collected and analysed data on PM size distribution, including tire wear particles (TWP) and TRWP. The test results included particle sizes from 1 μm up to hundreds of μm for road simulators, from about 0. 4 to 20 μm for road tests and above 1 μm up to 200 μm from road run-off. The results discussed in [34] placed the diameter of TRWP in the range of 4 to 350 μm, with an average diameter of 100 μm and a particle density

of 1.8 g/cm^3. Similar results were presented in [24, 52, 88, 89, 98]. As in the case of particle size testing from brake friction wear, differences in TWP and TRWP measurement results occur due to different testing procedures, sampling systems, and particle size measurement systems. The research described in [162] showed that the number of particles consists mainly of ultrafine particles with a maximum concentration of 100 nm. The particle mass was mainly represented by fine and coarse particles with a maximum concentration of 0.5 μm and 1.3–2.5 μm.

Table 3 compares the degree of tire tread wear and the PM emission factor (EF) for cars equipped with different drive systems operating in different road conditions. "Total," in this case, indicates the ratio of total tire tread loss and the total vehicle traveled distance. The obtained research results have shown that the degree of tire tread wear of electric vehicles was 1.2 times greater than that of vehicles powered by combustion engines due to their 20% greater weight [94, 161]. At the same time, the degree of wear of the tire tread of a vehicle powered by a compression-ignition engine was 5% higher than in the case of a vehicle powered by a spark-ignition engine due to the slightly (~2%) greater mass and greater (~20%) engine torque. Analyzing the effect of road type, tire tread wear rates were 10% and 50% higher on rural roads and highways, respectively, than in urban areas due to the increased wear occurring when travelling at high speed. Generally, tire tread wear rates have been found to be highest in urban areas, followed by highways and rural roads [43, 94]. The research did not take into account the impact of braking events on tire wear because each tested vehicle moved on an asphalt surface at a constant speed, without changing the direction of movement and without braking. Based on the PM_{10} and $PM_{2.5}$ tire wear EFs, it was estimated that tire tread wear was responsible for 5% of PM_{10} particle emissions, 16% of which were classified as airborne $PM_{2.5}$ particles [67, 161]. The EF values of PM_{10} for the SI vehicle, the CI vehicle and the electric vehicle were 7.9, 8.4 and 10.1 mg/V·km, respectively, and the EF for $PM_{2.5}$ was 1.3, 1.3 and 1.6 mg/V·km respectively. Typically, the degree of tire tread wear was strongly related to the weight of the vehicle and the maximum torque of the drivetrain. In the case of the tested vehicles, the maximum torque values of the vehicle powered by a spark ignition engine, a compression ignition engine and an electric vehicle were 265 Nm, 320 Nm and 395 Nm, respectively [43, 94, 161]. However, since the vehicles travelled on the test track at a constant speed, the effect of the torque difference on tire wear was negligible. Differences in PM EF tire wear depending on vehicle type resulted primarily from the difference in vehicle weight [161].

3. Formation mechanisms of particulate matter not related to the combustion process

Non-combustion particles arise from a variety of vehicle-related sources. The main sources are:

- Wear of brake friction elements. Emissions resulting from brake wear arise both as a result of mechanical processes, due to the impact of friction on brake linings and discs during braking, as well as volatilization processes of brake pad materials as a result of very high local temperatures [156]. PM emissions from brakes depend on the type and geometry of the brakes, the wheels and the rim. The flow of air through the rims to cool the brakes and discs also plays a key role in the wear characteristics. Emissions are also sensitive to the driving style of the driver. Studies have shown that PM emissions caused by mechanical processes are usually larger and contain particles with larger diameters, and are therefore decisive for the volume of PM mass emissions. Emissions resulting from thermal processes include much smaller particles, they are strongly correlated with brake temperature and constitute the vast majority of PN concentrations [99, 114, 122, 142, 156, 164]. The contribution of $PM_{2,5}$ typically accounts for about one third of the total PM_{10} emissions from wear of friction brake components [53].
- Tire wear. The surface of the tire in contact with the road surface is gradually abraded. This leads to the formation of large amounts of small rubber particles that cover a wide range of sizes below 10 micrometers, thus contributing to the formation of PM_{10} and $PM_{2.5}$. Generally, emissions from tire wear arise mechanically as a result of friction between the tire tread and the road surface or as a result of the volatilization of substances [53, 99]. Studies show that ultrafine PM concentrations are generally low [52, 99] and usually correlate with "abnormal" or "extreme" driving conditions [98].
- Road surface wear. Friction between the tire surface and the road surface not only leads to tire abrasion, but also to the abrasion of the road surface.
- Suspended road dust. Dust from various sources, including abrasion products of various vehicle elements, settles on road surfaces. Road dust studies have shown that much of it falls within the particle size range $PM_{2,5}$ and PM_{10}.

The mechanical interactions between the brake pad and the disc generates brake wear particles (BWP) of various sizes during the braking process [154]. Most studies indicate a unimodal mass distribution of BWP sizes with diameters in the range of 1–10 μm [59, 75, 76, 84, 88, 112]. The quantitative distribution of BWP depends on factors such as

Table 3. EFs of non-exhaust tire wear PM emitted from the ICEVs and EV according to road type [161]

Model	Tire tread wear rate (g/V·km)				Tire wear PM EF (mg/V·km)							
	Urban areas	Rural roads	Motorways	Total	Urban areas		Rural roads		Motorways		Total	
					PM10	PM2.5	PM10	PM2.5	PM10	PM2.5	PM10	PM2.5
Gasoline ICE	123.3	135.6	200.0	158.9	6.2	1.0	6.8	1.1	10.0	1.6	7.9	1.3
Diesel ICE	132.7	141.9	209.5	167.4	6.6	1.1	7.1	1.1	10.5	1.7	8.4	1.3
EV	160.7	178.1	246.8	201.7	8.0	1.3	8.9	1.4	12.3	2.0	10.1	1.6

brake pad material [115, 128] and operation history [35]. Moreover, the brake temperature may influence the BWP size distribution above the critical brake temperature in the range ($140°C < T_{crit} < 240°C$) when the smallest BWPs are generated [8, 9, 35, 107]. The research has shown that at temperatures $T > 185°C$, particles with a size of 0.011–0.029 μm were numerically predominant [110]. Other studies [8] found that the emission of particles with a size of 0.011–0.034 μm increased for temperatures in the range of 165–190°C. It was also found that the average density of the particle material slightly depended on the aerodynamic diameter of the particle in the range of 0.06–10 μm, which means that the mass fraction of ultrafine particles in PM_{10} can be assumed to be equal to the volume fraction [8]. To sum up, the following statements could be made:

- The temperature of the brake friction elements has a significant influence on the number and mass fractions of ultrafine particles [110].
- At temperatures below 200°C, ultrafine particles have no measurable mass contribution to PM_{10} [110].
- At temperatures above 200°C, the mass share of ultrafine particles in PM_{10} reached several dozen percent. This fraction generally increased with temperature and decreased with slip duration [110].

During the production process, after the pressing machine, the brake pads are heat treated by scorching. In this process, the surface of the blocks is exposed to high temperature (usually above 700°C) for a short time (from several dozen seconds to several minutes) [25, 97]. This results in the removal of the less thermally stable phenolic resin as a result of the carbonization reaction, and its absence increases the brittleness of the surface, which becomes more abrasive than the surface of brake pads that were not scorched. Higher abrasiveness of the friction surface results in faster smoothing of both new pads and new friction surfaces of discs, but on the other hand it is responsible for greater wear of pads and discs, and therefore increased PM emissions when they start to be used. Due to carbonization reactions, the friction surface of new brake pads may consist of more condensed organic substances, including volatile and semi-volatile organic compounds. These compounds can evaporate from the friction surface when braking and be released in the form of ultrafine particles smaller than 0.1 μm. A more adhesive nature of the friction phenomenon begins to take place as the contact surfaces become smoother as a result of abrasive polishing accompanied by the formation of a stable friction layer. The presence of stable primary and secondary contact surfaces is believed to be crucial to maintaining the desired friction parameters without excessive wear due to abrasion caused by the movement of loose abrasive particles [25, 96, 120].

Tire wear particulates are produced mechanically as a result of shear forces occurring between the tire tread and the road surface. The physical properties of such particles vary depending on driving style, tire material, road condition, the weather, etc. [69]. Tribological mechanisms of rubber wear are known and understood, including fatigue wear, friction wear, adhesive wear, and chemical erosion wear [1, 34, 36, 89, 118, 123, 152, 162]. As a result of friction and slip, micro-cracks and cracks in the tire and the road surface are formed, causing continuous, increasing wear. Particulate formation occurs when the accumulated local friction energy in the area of contact reaches enough energy to damage (critical energy) the tire surface in the area of contact with the road surface. Tire wear typically occurs simultaneously in different forms, as a mixture of tire wear and road surface wear, accounting for about 50% of each type of wear. Variable factors influencing tire wear include tire characteristics (e.g., its composition, construction), road surface characteristics and operating method, and vehicle characteristics (e.g., speed, cornering method, vehicle weight, and power) [11]. The tire operating temperature and the interaction of the tire surface with the road surface material are also important [3, 56, 83]. BWP sampling and TRWP (tire and road wear particles) measurements in road conditions may be carried out according to various methodologies [30, 66, 121]. Research carried out in accordance with the TRAKER method showed that particles collected behind the front wheels of a car have a PM size distribution reaching 2–3 μm, with a high content of earth's crust elements, which indicates a high share of PM from road wear and dust [17, 88, 90].

4. Composition of solid particles not related to the combustion process

Friction elements materials of the braking systems must meet several basic requirements, the most important of which are high wear resistance, high coefficient of friction, and limited noise and vibration [20, 26, 45]. These materials can be broadly divided into organic and metallic. Other categories that are usually rarely used are ceramics, carbon (only for high brake heating temperatures), and aluminum (only for light vehicles and rear brakes) [26]. Brake pads consist of various components, the most important of which are binders, fillers, friction enhancers, reinforcing fibers and lubricants, while the brake disc is usually made of grey cast iron with additional coatings to improve performance. Fibrous ingredients play a key role in strengthening the friction material. Since the ban on asbestos, many different new fibers have been developed for use in brake friction materials. Among them, organic fibers are based on cellulose, aramid, or natural plants, while inorganic fibers are made of metals or minerals. Fibers improve the strength and tribological properties of friction materials [45, 132, 159]. The synergistic effect of different fibers is often sought to improve the performance of friction materials [45, 159].

Grey cast iron (GCI) is the most commonly used material for brake discs used in cars [12, 105, 135]. However, GCI has poor corrosion resistance and excessive wear, which results in high particulate emissions from the brakes. The results of the tests have shown that corrosion of brake discs reduces the braking performance by reducing the coefficient of friction and, at the same time, significantly increases both the number and the mass of particulates emitted (between 2 and 30 times compared to a non-corroded disc under the same test conditions) [44]. Various technological processes and conditioning forms (e.g. cryogenic, thermal) are used to improve tribological parameters and reduce brake disc wear [117, 135]. Another preferred solution that may be employed is to apply a special abra-

sion resistant coating to the disc surface, e.g. a hard metal coating (HMC), using tungsten carbide, cobalt or chromium carbide [12, 151]. Another option would be to use carbon-ceramic (CC) brake discs. Despite the high costs, CC and HMC discs are becoming an increasingly popular method of reducing the amount of particles produced [44, 58, 130].
Tires typically consist of rubber/elastomers, fillers, additives, reinforcing agents and vulcanizing agents, which vary depending on the tire type and application [152]. For example, truck tires contain about 80% natural rubber, while passenger car tires contain only about 15% [21]. Some of these can be used as markers for tire wear in the environment. Such examples include components used in the vulcanization process, such as 2-(4-morpholinyl)-benzothiazole [86] and Zn, [67] or those originating from thermal decomposition of tire tread polymers [147] such as styrene, isoprene, dipentene, butadiene, vinylcyclohexene, and benzothiazole. Benzothiazoles are used in the ISO standard to determine TRWP (tire and road wear particles) [77]. Compared to particles from tires themselves, TRWPs also include metals from brake linings and road surface materials and contain lower concentrations of polymers [3, 83].

The large variety in the compositions of currently used brake pads causes large differences in the chemistry and morphology of the emitted particulates [84, 95, 104, 155]. The composition of particulate matter from brakes and the degree of their emission are also influenced by the conditions in which braking occurs (pad pressure on the disc during braking, disc/pad temperature, and environmental conditions, etc.) [41, 75, 84, 88, 104, 111, 127]. Brake operations are primarily related to the emission of particulate matter Fe, Cu, Zn, Ba, and Sb, which are used as indicators of brake wear [23, 27, 70]. Moreover, gasification of the resins contained in brake pads often occurs, and hydrocarbon particles are formed [27, 41, 128]. In turn, metal oxides may be formed as a result of metal oxidation [75]. The particle size distribution from brake wear is usually homogeneous, with peak particle size ranging from 1 μm to 6 μm [16, 32, 39, 85, 87]. At the same time, many researchers, e.g. [23, 27, 41, 52, 70, 102, 124, 128] note the possibility of bi- or even multimodal PM size distribution with at least one peak in the fine and/or ultrafine fraction and increased particulate mass in the $PM_{2.5}$ range. It is believed that these particles are formed by the evaporation, condensation, and aggregation of primary particles and are the result of high braking forces and high brake disc temperature [27, 59].

The most important factors affecting the intensity, degree of wear, and the formation of particles emitted by tire abrasion are the design and structure of the tire, the chemical composition of the tire material, wear resistance, tire pressure, the size of the contact area with the road surface and the tire temperature. Vehicle-related factors include driving speed, longitudinal/lateral acceleration, vehicle weight and load distribution, suspension type, braking frequency and force, and cornering frequency and sharpness. Factors related to the road surface are also important, including surface structure, micro and macro texture, porosity, road dust load, and surface binder (bitumen, cement). [36, 52, 69, 91, 98].

The chemical composition of PM emitted from tires depends on the composition of rubber/elastomers and fillers (black carbon, silica, silanes), the additives used (preservatives, antioxidants), the type of textile and metal reinforcements, and vulcanizing agents (ZnO, S, Se, Te, thiazoles, organic peroxides, nitro compounds) and process oils. The morphology of particles emitted from tires would classify them as circular/dendritic particles [36, 52, 69, 91, 98].

5. Methods of particle emission measurement

Measuring non-exhaust particulate emissions from ICE posed a new technological and logistical challenge. The reason for this was the complexity of the vehicle and its operation as a whole and the difficulty of dynamically measuring PM resulting from wear and tear of mechanical components of the vehicle's braking system and running gear. [74, 99, 100]. It is necessary to develop a unified method for sampling particulate matter emitted from the wear of brake and tire friction elements in order to obtain representative, reliable, accurate, and repeatable results. So far, various researchers have used different, non-standardized methods to sample and measure PM emissions unrelated to the engine combustion process [35, 61, 99, 103, 143, 146, 159, 164]. However, each of the methodologies used so far has its own set of drawbacks. Laboratory simulations of the brake friction elements wear are most often based on standard test cycle conditions, but the main disadvantage of such measurements is the inability to simulate the course of brake activation encountered during real driving conditions on the road. In turn, laboratory tests on tire wear do not yet use a unified standard test cycle, which makes it difficult to analyze the emission characteristics resulting from tire wear. Chassis dynamometer tests provide good control of the measurement process, but are limited by the possibility of obtaining an appropriate sample size and are not representative of real braking processes. [37, 74, 100]. Standardized emission factors for each particulate source are used to calculate emissions (Table 1). In the case of tires, specific emission factors for each vehicle type (car, truck, motorcycle, etc.) are combined with distance travelled statistics to generate an emitted mass estimate. Emission factors are expressed in mg/vehicle/km with different values for PM_{10} and $PM_{2.5}$. Most countries use the methodology provided in the 2016 version of the EMEP/EEA Air Pollutant Emissions Inventory Guidebook (EMEP/EEA, 2016) for estimating PM emissions from tire and brake wear and road surface wear. This provides a fairly simple approach that combines PM emission factors in milligrams emitted per kilometer (mg/km) for passenger cars, light trucks, heavy goods vehicles and two-wheelers with the number of vehicle-kilometers travelled per year. For Europe, all emission factors are collected in the Guidebook [109]. Current emission factors are based on studies published between 1990 and 2000 [109], with conclusions based on indirect measurements. Hence, many publications admit that emission factors are imprecise, even in the DEFRA report [7]. The values given in the guides are indirect measurements, resulting from the total loss of the tire mass (tire weight lost is the data being measured, not the mass of airborne particles specifically). As a result, in 2021, the Working Party on Energy and Pollution (GRPE) entrusted the Particle

Measurement Programme Informal Working Group (PMP-IWG) to develop a global technical regulation (GTR) covering the sampling PM and measurement of PM emissions from brake wear of light vehicle (LDV) friction brake components for vehicles up to 3.5 t [20, 45, 129]. Similarly, in 2022, a joint task force was established within the Working Party on Noise and Tires (GRBP) and the GRPE to develop a procedure for measuring tire wear and assessing the PM wear performance of a wide range of tires available on the market [19, 129]. These two activities were carried out on the basis of the United Nations Economic Commission for Europe World Forum for Harmonization of Vehicle Regulations (UNECE WP.29). As part of the work on the GTR, PMP-IWG developed the first version of a test methodology comprising a set of technical procedures for measuring brake PM emissions on dynamometers [129]. These specifications include provisions for the conduct of the test [45, 129], the methodology for regulating the cooling process, the procedure for preparing the brake pads, the measurement of PM and PN emissions and the presentation of the results [45, 97, 99]. Throughout this process, it was found that the losses of emitted particles between the brake and the sampling point must be kept as low as possible. To ensure this, isokinetic sampling is necessary, where the volume flow used to cool the brake must be precisely matched to the extraction or sampling rate of the measuring device. This ensures that the measured particle mass values are reliable. To ensure that the measurement results can be related to actual conditions encountered during vehicle operation on the road, the standardized WLTP-B braking test cycle has been successfully developed [45, 74, 129]. The cycle was established using actual vehicle data, and it maps different brake application points over the required period of time. This guarantees the repeatability of the recorded PM emission resulting from the abrasion of brake friction elements. It was assumed that the measurements of PM emissions from brakes carried out on the test stand will be standardized in the future in the developed WLTP braking cycle. Due to the fact that a given vehicle model must be accurately reproduced on a test bench, the combination of the working assembly of brake pads and brake disc with the vehicle mass and its distribution has a significant impact on the observed wear patterns. These parameters must be programmed on a test bench, except for brakes used in electric vehicles. In this case, under real operating conditions, regenerative braking ensures that the friction brake is used less frequently and therefore PM emissions are lower. In September 2021, PMP-IWG organized the first Inter-Laboratory Study (ILS) to evaluate the newly developed methodology. The main ILS results were presented to the IWG in March 2022 in the form of six different presentations [155]. In June 2022, GRPE adopted GTR 24 on a broad methodology for measuring PM emissions from brakes [53, 69, 74, 95, 145]. The Global Technical Regulation (GTR 24) on PM emissions from brakes of light commercial vehicles includes harmonized measurement procedures. GTR 24 is the world's first regulation that systematizes and establishes procedures for measuring particulate emissions from sources other than ICE exhaust gases. GTR 24 will be implemented as part of the Euro 7 exhaust emissions regulation, which aims to reduce PM and PN emissions from road transport, both for particulate matter from the combustion process in ICE and for particulate matter from NEE, and to improve air quality in Europe.

6. Euro 7 – particles not related to the combustion process

The scope of the proposed Euro 7 standard goes beyond the current vehicle type approval requirements contained in Euro 6 [45, 74, 129]. The Euro 7 standard extends regulatory requirements to the type approval of braking systems and tires, in particular with regard to particulate emissions and the occurring abrasion process. The regulation applies to tires of classes C1 (passenger cars and commercial vehicles), C2 (light commercial vehicles) and C3 (heavy commercial vehicles), in accordance with UN Regulation 117. As a result, the Euro 7 standard will include a requirement to limit the maximum emissions of PM_{10} particulate matter from brake pads and tires. Generally speaking, for electric cars it will be 3 mg/km, for combustion passenger cars, hybrids and hydrogen cars 7 mg/km, and for large vans and delivery vehicles 11 mg/km [7, 27]. The Euro 7 emission standard will apply for the first time to the type approval of new models of light vehicles and their braking systems 2.5 years after the regulation enters into force – Fig. 2. A year later, all newly registered vehicles will have to meet the new Euro 7 requirements. Euro 7 heavy goods vehicles will apply to new vehicle models 4 years after entry into force, and after 5 years to all new vehicles.

Fig. 2 Schedule for the rollout of the Euro 7 standard for vehicles of various categories [27]

Regardless of the final date of introduction of the Euro 7 standard (currently set for July 1, 2030), brake particle limits for heavy goods vehicles will only begin to apply from 2030. In the case of tires, abrasion limits will be introduced in July 2028 for class C1 tires, in April 2030 for class C2 tires, and in April 2032 for class C3 tires [27].

Compared to ICE-powered vehicles, electric and electrified vehicles can reduce PM emissions from brakes by using regenerative braking. In practice, this means that instead of brakes, an electric motor operating in generator mode is used to slow the vehicle down. This technological difference was reflected in the requirements of the Euro 7 standard by establishing lower particulate limits for electric vehicles compared to other types of drive systems – Table 4 [27].

In the first step, Euro 7 lists particulate matter emission limits for passenger cars and light commercial vehicles N_1 until the end of 2029. Starting in 2030, the regulation also provides particulate emission limits extended to buses and trucks of categories M_2, M_3, and N_2, N_3. Particulate emissions from braking systems for M_1 and N_1 vehicles will be tested in accordance with UN Global Technical Regulation No. 24.8.

A test procedure for PM measurements from truck braking systems has not been developed yet (Table 4) [27].

Table 4 Particulate matter emission limits during braking for Euro 7 [27]

Date	Powertrain type	Vehicle categories		
		M_1/N_1 class I & II	N_1 class III	M_2/N_2 and M_3/N_3
Until December 2029	Battery electric vehicles	3 mg/km	5 mg/km	none
	Other powertrain types	7 mg/km	11 mg/km	none
January 2030 – December 2034	Battery electric vehicles	tbd	tbd	tbd
	Other powertrain types	tbd	tbd	tbd
From January 2035	All powertrain types	3 mg/km	tbd	tbd

Fig. 3. Dates of introducing tire wear limits through the Euro 7 standard [27]

The Euro 7 standard will also introduce limits on PM emissions from tire abrasion. As a consequence, only tires with abrasion rates below the Euro 7 limits will receive type approval. The required testing procedure and emission limits are currently being developed by the United Nations Economic Commission for Europe (UNECE) and will be introduced as an amendment to the Euro 7 regulations. If the UNECE regulation is not adopted in time, the Commission will be given the authority to develop a procedure for assessing PM emissions from tires and setting limits on this emission. As shown in Fig. 3, the Euro 7 requirements will cover different tire classes at different times – first, C1 tires from July 2028, then C2 tires from April 2030, and finally, C3 tires from April 2032. The order of introduction will be same for all categories. In the first stage, the Euro 7 standard will apply to new tire models that receive type approval for the first time. A year later, new vehicles placed on the market will have to be equipped with Euro 7 approved tires, and a year later all tires placed on the market must meet Euro 7 requirements.

7. Conclusions

- Emissions of particulate matter not related to the engine combustion process (resulting from wear of brake friction elements and tire friction processes with the road surface) are currently unregulated both in terms of measurement methodology as well as emission limits.
- Non exhaust PM vehicle emissions have already exceeded PM emissions from exhaust gases as the main source of particulate matter emissions from road traffic. Despite this, this major source of PM emissions from road traffic is currently not covered by any legal regulation to control and limit these emissions.
- The health risks posed by particulate matter emitted from braking systems and tire abrasion are not yet clearly understood in their entirety. This requires multidisciplinary research efforts to adopt effective and appropriate evidence-based emissions reduction legislation and strategies to protect human health.
- When taking action to reduce particulate emissions resulting from the wear of brake friction elements and tire abrasion, the chemical profile of the emissions, as well as the total mass and number of particles, should be taken into account.
- With the growing popularity of alternative vehicle powertrains, NEEs are increasingly contributing to air pollution. This is reflected in mitigation strategies through new requirements that will be introduced by the Euro7 emissions standard, which plans to take into account non-combustion emissions for the first time.
- Measuring particulate emissions not related to the combustion process in the engine presents a new technological challenge. This is due to the complexity of the vehicle and its operation as a whole and to the difficulty of dynamically measuring particulate emissions caused by the wear of both friction brake components and tires.
- One of the main reasons for the observed inconsistencies in the particulate matter measurements (PM and PN) is the lack of a unified, standardized methodology for sampling and measuring both particulate matter caused by brake elements abrasion and tire wear.
- Realistic PM coefficients with NEE are necessary to reliably calculate the contribution of PM emissions from brake and tire wear to air pollution, but also to estimate the reduction potential of these emissions through the use of new or existing technologies and improved formulae for brake and tire friction components.

Nomenclature

BWP	brake wear particles
CC	carbon ceramic
ECE	Economic Commission for Europe
EF	emission factor
EU	European Union
GCI	grey cast iron
GTR	global technical regulation
HMC	hard metal coated discs
ICE	Internal Combustion Engine
ILS	inter-laboratory study
LACT	Los Angeles City Traffic
LDV	light duty vehicles
LM	low-metallic
NAO	non-asbestos organics
NEE	non exhaust emissions
OECD	Organisation for Economic Co-operation and Development
PHEV	plug-in hybrid electric vehicles
PM	particle matter
PMP	particle measurement programme

PMP-IWG Particle Measurement Programme Informal Working Group
PoD pin-on- disc
RDE real driving emission
SM semi-metallic
SUV sports utility vehicle
TRWP tire and road wear particles
TWP tire wear particles
UNECE United Nations Economic Commission for Europe
WLTP Worldwide Light duty Test Procedure

Bibliography

[1] Aatmeeyata DSK, Sharma M. Traffic generated non-exhaust particulate emissions from concrete pavement: a mass and particle size study for two-wheelers and small cars. Atmos Environ. 2007;43(35):5691-5697. https://doi.org/10.1016/j.atmosenv.2009.07.032

[2] Adamiak B, Szczotka A, Woodburn J, Merkisz J. Comparison of exhaust emission results obtained from Portable Emissions Measurement System (PEMS) and a laboratory system. Combustion Engines. 2023;195(4):128-135. https://doi.org/10.19206/CE-172818

[3] Adachi K, Tainosho Y. Characterization of heavy metal particles embedded in tire dust. Environ Int. 2004;30(8): 1009-1017. https://doi.org/10.1016/j.envint.2004.04.004

[4] Adamczak L. At source brake dust active filtering system EB2023-EFA-008. Proceedings of the EuroBrake 2023. Barcelona 12-14 September 2023.

[5] Agudelo C, Vedula RT, Collier S, Stanard A. Brake particulate matter emissions measurements for six light-duty vehicles using inertia dynamometer testing. SAE Int J Adv&Curr Prac in Mobility. 2021;3(2):994-1019. https://doi.org/10.4271/2020-01-1637

[6] Air Quality Expert Group (AQEG) non-exhaust emissions from road traffic. UK 2019 (accessed on 7 January 2024).

[7] Air Pollution in the UK 2019. September 2020. https://uk-air.defra.gov.uk/library/annualreport/ (accessed on 1 March 2024).

[8] Alemani M, Nosko O, Metinoz I, Olofsson U. A study on emission of airborne wear particles from car brake friction pairs. SAE Int J Mater Manuf. 2016;9(1):147-157. https://doi.org/10.4271/2015-01-2665

[9] Alemani M, Wahlström J, Olofsson U. On the influence of car brake system parameters on particulate matter emissions. Wear. 2018;396-397:67-74. https://doi.org/10.1016/j.wear.2017.11.011

[10] Amato F, Cassee FR, van der Gon HAC, Gehrig R, Gustafsson M et al. Urban air quality: the challenge of traffic non-exhaust emissions. J Hazard Mater. 2014;275:31-36. https://doi.org/10.1016/j.jhazmat.2014.04.053

[11] Amato F. An urban air quality problem for public health; impact and mitigation measures. Elsevier 2018. https://doi.org/10.1016/B978-0-12-811770-5.01001-3

[12] Aranke O, Algenaid W, Awe S, Joshi S. Coatings for automotive gray cast iron brake discs: a review. Coatings. 2019; 9:552. https://doi.org/10.3390/coatings9090552

[13] Axsen J, Wolinetz M. Reaching 30% plug-in vehicle sales by 2030: modeling incentive and sales mandate strategies in Canada. Transport Res D-Tr E. 2019;65:596-617. https://doi.org/10.1016/j.trd.2018.09.012

[14] Baensch-Baltruschat B, Kocher B, Stock F, Reifferscheid G. Tyre and road wear particles (TRWP) – a review of generation, properties, emissions, human health risk, ecotoxicity, and fate in the environment. Sci Total Environ. 2020;733: 137823. https://doi.org/10.1016/j.scitotenv.2020.137823

[15] Baensch-Baltruschat B, Kocher B. Kochleus C, Stock F, Reifferscheid G. Tyre and road wear particles – a calculation of generation, transport and release to water and soil with special regard to German roads. Sci Total Environ. 2021; 752: 141939. https://doi.org/10.1016/j.scitotenv.2020.141939

[16] Beddows DCS, Harrison RM. PM10 and PM2.5 emission factors for non-exhaust particles from road vehicles: dependence upon vehicle mass and implications for battery electric vehicles. Atmos Environ. 2021;244:117886. https://doi.org/10.1016/j.atmosenv.2020.117886

[17] Beji A, Deboudt K, Khardi S, Muresan B, Lum L. Determinants of rear-of-wheel and tire-road wear particle emissions by light-duty vehicles using on-road and test track experiments. Atmos Pollut Res. 2021;12(3):278-291. https://doi.org/10.1016/j.apr.2020.12.014

[18] Belis CA, Karagulian F, Larsen BR, Hopke PK. Critical review and meta-analysis of ambient particulate matter source apportionment using receptor models in Europe. Atmos Environ. 2013;63:94-108. https://doi.org/10.1016/j.atmosenv.2012.11.009

[19] Bondorf L, Kohler L, Grein T, Epple F, Philipps F, Aigner M et al. Airborne brake wear emissions from a battery electric vehicle. Atmosphere. 2023;14:488. https://doi.org/10.3390/atmos14030488

[20] Borawski A. Conventional and unconventional materials used in the production of brake pads – review. Sci Eng Compos Mater. 2020;27:374-396. https://doi.org/10.1515/secm-2020-0041

[21] Camatini M, Crosta G, Dolukhanyan T, Sung C, Giuliani G, Corbetta G et al. Microcharacterization and identification of tire debris in heterogeneous laboratory and environmental specimens. Mater Charact. 2001;46:271-283. https://doi.org/10.1016/S1044-5803(00)00098-X

[22] Czerwinski J, Mayer A, Stepien Z, Oleksiak S, Andersen O. Reduction of emissions and unregulated components with DPF + SCR. Conference DEXFIL 2009;11.

[23] Dall'Osto M, Querol X, Amato F, Karanasiou A, Lucarelli F, Nava S et al. Hourly elemental concentrations in PM2.5 aerosols sampled simultaneously at urban background and road site during SAPUSS – diurnal variations and PMF receptor modelling. Atmos Chem Phys. 2013;13:4375-4392. https://doi.org/10.5194/acp-13-4375-2013

[24] Dall'Osto M, Beddows DC, Gietl JK, Olatunbosun O, Yang X, Harrison RM. Characteristics of tyre dust in polluted air: studies by single particle mass spectrometry (ATOFMS). Atmos Environ. 2014;94:224-230. https://doi.org/10.1016/j.atmosenv.2014.05.026

[25] Dante RC. Handbook of friction materials and their application. Elsevier 2016. https://doi.org/10.1016/C2015-0-00634-7

[26] Day A, Bryant D. Braking of road vehicles. 2nd ed. Butterworth-Heinemann, Kidlington, Cambridge 2022. https://doi.org/10.1016/B978-0-12-822005-4.00064-0

[27] Dornoff J, Rodríguez F. Euro 7: the new emission standard for light- and heavy-duty vehicles in the European Union. ICCT policy update | Euro 7: emission standard for light- and heavy-duty vehicles in the EU. https://theicct.org/wp-content/uploads/2024/03/ID-116-%E2%80%93-Euro-7-standard_final.pdf (accessed on 21 March 2024).

[28] EEA EIONET Central Data Repository, 2023. https://cdr.eionet.europa.eu (accessed on 7 January 2024).

[29] EPA. Brake and tire wear emissions from onroad vehicles in MOVES3. Report EPA-420-R-20-014, 2020. https://www.epa.gov/sites/default/files/2020-11/documents/420r20014.pdf (accessed on 7 January 2024).
[30] Etyemezian V. Vehicle-based road dust emission measurement: I methods and calibration. Atmos Environ. 2003; 37(32):4559-4571. https://doi.org/10.1016/S1352-2310(03)00528-4
[31] Euro 7 vehicle emission standards: a European Green Deal proposal. Technical studies for the development of Euro 7: testing, pollutants and emission limits. 2022. https://doi.org/10.2873/97170 (accessed on 1 March 2024).
[32] European Commission. Directorate general for internal market, industry, entrepreneurship and SMEs. In Euro 7 impact assessment study. Publications Office: Luxembourg 2022.
[33] European Commission; EEA Climate and Energy in the EU. Country Comparison. 2023. https://climate-energy.eea.europa.eu/topics/transport/emissions-cars/data (accessed on 7 January 2024).
[34] Faino. 48th PMP IWG meeting tyre and road wear particles: the tyre industry perspective UN WP29 GRPE PMP-48-13. ISPRA – November 8, 2018 (accessed on 1 March 2024).
[35] Farwick zum Hagen FH, Mathissen M, Grabiec T, Hennicke T, Rettig M, Grochowicz J et al. Study of brake wear particle emissions: impact of braking and cruising conditions. Environ Sci Technol. 2019;53(9):5143-5150. https://doi.org/10.1021/acs.est.8b07142
[36] Feißel T, Kunze M, Hesse D, Ivanov V, Augsburg K, Gramstat S. On-road vehicle measurement of tire wear particle emissions and approach for emission prediction. Proceedings of the 40th Annual Meeting of the Tire Society. Akron 2 September 2021 (accessed on 1 March 2024).
[37] Feißel T, Hesse D, Ricciardi V, Schiele M, Augsburg M. Novel approaches for measuring and predicting particulate emissions from automotive brakes and tires. 12th International Munich Chassis Symposium 2021:708-728 (accessed on 1 March 2024).
[38] Feo ML, Torre M, Tratzi P, Battistelli F, Tomassetti L, Petracchini F et al. Laboratory and on-road testing for brake wear particle emissions: a review. Environ Sci Pollut Res. 2023;30:100282-100300. https://doi.org/10.1007/s11356-023-29229-7
[39] Furusjö E, Sternbeck J, Cousins AP. PM10 source characterization at urban and highway roadside locations. Sci Total Environ. 2007;387(1-3):206-219. https://doi.org/10.1016/j.scitotenv.2007.07.021
[40] Fussell JC, Franklin M, Green DC, Gustafsson M, Harrison RM, Hicks W et al. A review of road traffic-derived non-exhaust particles: emissions, physicochemical characteristics, health risks, and mitigation measures. Environ Sci Technol. 2022;56:6813-6835. https://doi.org/10.1021/acs.est.2c01072
[41] Garg BD, Cadle SH, Mulawa PA, Groblicki PJ. Brake wear particulate matter emissions. Environ Sci Technol. 2000;34: 4463-4469. https://doi.org/10.1021/es001108h
[42] Gasser M, Riediker M, Mueller L, Perrenoud A, Blank F, Gehr P et al. Toxic effects of brake wear particles on epithelial lung cells in vitro. Part Fibre Toxicol. 2009;6:30. https://doi.org/10.1186/1743-8977-6-30
[43] Geilenkirchen G, Hulskotte J, Dellaert S, Ligterink N, Sijstermans M, Roth K et al. Methods for calculating the emissions of transport in the Netherlands. 2021 PBL Netherlands Environmental Assessment Agency. https://www.pbl.nl/en/publications/ methods-for-calculating-the-emissions-of-transport-in-the-netherlands-2021 (accessed on 1 March 2024).
[44] Ghouri I, Barker R, Brooks P, Kosarieh S, Barton D. The effects of corrosion on particle emissions from a grey cast iron brake disc. SAE Technical Paper 2022-01-1178. 2022. https://doi.org/10.4271/2022-01-1178
[45] Giechaskiel B, Grigoratos T, Dilara P, Karageorgiou T, Ntziachristos L, Samaras Z. Light-duty vehicle brake emission factors. Atmosphere. 2024;15:1-20. https://doi.org/10.3390/atmos15010097
[46] Gietl JK, Lawrence R, Thorpe AJ, Harrison RM. Identification of brake wear particles and derivation of a quantitative tracer for brake dust at a major road. Atmos Environ. 2010; 44(2):141-146. https://doi.org/10.1016/j.atmosenv.2009.10.016
[47] Goel A, Kumar P. A review of fundamental drivers governing the emissions, dispersion and exposure to vehicle-emitted nanoparticles at signalised traffic intersections. Atmos Environ. 2014;97:316-331. https://doi.org/10.1016/j.atmosenv.2014.08.037
[48] Gramstat S, Mertens T, Waninger R, Lugovyy D. Impacts on brake particle emission testing. Atmosphere. 2020;11: 1132. https://doi.org/10.3390/atmos11101132
[49] Gramstat S, Mertens T, Waninger R, Augsburg K, Hamatschek C, Hesse D. Functional coatings of gray-cast iron brake discs – impact on the tribology. Mayer R. (ed). Berichte aus dem µ-Club 2020. Springer Berlin/Heidelberg 2021:162-170. https://doi.org/10.1007/978-3-662-63028-0_10
[50] Grange SK, Fischer A, Zellweger C, Alastuey A, Querol X, Jaffrezo J-L et al. Switzerland's PM10 and PM2.5 environmental increments show the importance of non-exhaust emissions. Atmos Environ. 2021;12:100145. https://doi.org/10.1016/j.aeaoa.2021.100145
[51] Grigoratos T, Martini G. Non-exhaust traffic related emissions. Brake and tyre wear PM. Literature review. Report EUR 26648 EN. European Union, Luxembourg 2014.
[52] Grigoratos T, Martini G. Brake wear particle emissions: a review. Environ Sci Pollu. Res. 2015;22:2491-2504. https://doi.org/10.1007/s11356-014-3696-8
[53] Grigoratos T, Mathissen M, Vedula R, Mamakos A, Agudelo, C, Gramstat S et al. Interlaboratory study on brake particle emissions – part I: particulate matter mass emissions. Atmosphere. 2023;14:498. https://doi.org/10.3390/atmos14030498
[54] Grigoratos T, Mamakos A, Vedula R, Arndt M, Lugovyy D, Hafenmayer C et al. Characterization of laboratory particulate matter (PM) mass setups for brake emission measurements. Atmosphere. 2023;14:516. https://doi.org/10.3390/atmos14030516
[55] GRPE-2023-4e. Clean-(PMP) proposal to amend ECE/TRANS/WP.29/GRPE/2023/4. Proposal for a New UN GTR on laboratory measurement of brake emissions for light-duty vehicles. https://unece.org/transport/documents/2023/01/informal documents/clean-pmp-proposal-amend-ecetranswp29grpe20234 (accessed on 1 March 2024).
[56] Gunawardana C, Goonetilleke A, Egodawatta P, Dawes L, Kokot S. Source characterisation of road dust based on chemical and mineralogical composition. Chemosphere. 2012;87(2):163-170. https://doi.org/10.1016/j.chemosphere.2011.12.012
[57] Guo D, Wei H, Guo Y, Wang C, Yin Z. Non-exhaust particulate matter emission from vehicles: a review. E3S Web Conf. 2021;268:01015. https://doi.org/10.1051/e3sconf/202126801015
[58] Güney B, Mutlu I. Tribological properties of brake discs coated with Cr2O3 – 40% TiO2 by plasma spraying. Surf Rev Lett. 2019;26:1950075. https://doi.org/10.1142/S0218625X19500756

[59] Hagino H, Oyama M, Sasaki S. Laboratory testing of airborne brake wear particle emissions using a dynamometer system under urban city driving cycles. Atmos Environ. 2016;131:269-278. https://doi.org/10.1016/j.atmosenv.2016.02.014
[60] Hagino H, Iwata A, Okuda T. Iron oxide and hydroxide speciation in emissions of brake-wear particles from different friction materials using X-ray absorption fine structure. Atmosphere. 2023;15:49. https://doi.org/10.3390/atmos15010049
[61] Hagino H. Brake wear particle emission measurements based on real driving cycles in several urban areas in a laboratory testing. EB2023-TST-009. Proceedings of the Euro Brakes 2023. Barcelona 12-14 September 2023.
[62] Hagino H. Investigation of brake-wear particle emissions from regenerative-friction brake coordination systems via dynamometer testing. Atmosphere. 2024;15:75. https://doi.org/10.3390/atmos15010075
[63] Hall TJ. A comparison of braking behavior between an IC engine and pure electric vehicle in Los Angeles city driving conditions. SAE Technical Paper 2017-01-2518. 2017. https://doi.org/10.4271/2017-01-2518
[64] Hamatschek C, Hesse D, Augsburg K, Gramstat S, Stich A. Comparison of the particle emission behaviour of automotive drum and disc brakes. 12th International Munich Chassis Symposium 2021. Springer Berlin/Heidelberg, Germany 2022:541-563.
[65] Hamatschek C, Augsburg K, Schobel D, Gramstat S, Stich A, Gulden F et al. Comparative study on the friction behaviour and the particle formation process between a laser cladded brake disc and a conventional grey cast iron disc. Metals. 2023;13:300. https://doi.org/10.3390/met13020300
[66] Han S, Jung YW. A study on the characteristics of silt loading on paved roads in the Seoul metropolitan area using a mobile monitoring system. J Air Waste Manag Assoc. 2012; 62(7):846-862. https://doi.org/10.1080/10962247.2012.686892
[67] Harrison RM, Jones AM, Gietl J, Yin J, Green DC. Estimation of the contributions of brake dust, tire wear, an resuspension to nonexhaust traffic particles derived from atmospheric measurements. Environ Sci Technol. 2012;46;6523-6529. https://doi.org/10.1021/es300894r
[68] Hesse D, Hamatschek C, Augsburg K, Weigelt T, Prahst A, Gramstat S. Testing of alternative disc brakes and friction materials regarding brake wear particle emissions and temperature behavior. Atmosphere. 2021;12:436. https://doi.org/10.3390/atmos12040436
[69] Hesse D, Feißel T, Kunze M, Bachmann E, Bachmann T, Gramstat S. Comparison of methods for sampling particulate emissions from tires under different test environments. Atmosphere. 2022;13:1262. https://doi.org/10.3390/atmos13081262
[70] Hinrichs R, Soares MRF, Lamb RG, Soares MRF, Vasconcellos MAZ. Phase characterization of debris generated in brake pad coefficient of friction tests. Wear. 2011;270:515-519. https://doi.org/10.1016/j.wear.2011.01.004
[71] Hoffmann B, Moebus S, Möhlenkamp S, Stang A, Lehmann N, Dragano N et al. Residential exposure to traffic is associated with coronary atherosclerosis. Circulation. 2007;116: 489-496. https://doi.org/10.1161/CIRCULATIONAHA.107.693622
[72] Hooftman N, Oliveira L, Messagie M, Coosemans T, Van Mierlo J. Environmental analysis of petrol, diesel and electric passenger cars in a Belgian urban setting. Energies. 2016;9: 84. https://doi.org/10.3390/en9020084
[73] Huber MP, Fischer P, Mamakos A, Steiner G, Klug A. Measuring brake wear particles with a real-driving emissions sampling system on a brake dynamometer. SAE Technical Paper 2022-01-1180. 2022. https://doi.org/10.4271/2022-01-1180
[74] Huber MP, Murg J, Steiner G, Wanek-Rüdiger C, Weidinger C, Huemer-Kals S et al. Assessing a vehicle's real-world brake wear particle emissions on public roads. Eurobrake Conference 2023. https://doi.org/10.46720/eb2023-tst-002
[75] Iijima A, Sato K, Yano K, Tago H, Kato M, Kimura H et al. Particle size and composition distribution analysis of automotive brake abrasion dusts for the evaluation of antimony sources of airborne particulate matter. Atmos Environ. 2007; 41:4908-4919. https://doi.org/10.1016/j.atmosenv.2007.02.005
[76] Iijima A, Sato K, Yano K, Kato M, Kozawa K, Furuta N. Emission factor for antimony in brake abrasion dusts as one of the major atmospheric antimony sources. Environ Sci Technol. 2008;42:2937-2942. https://doi.org/10.1021/es702137g
[77] ISO, ISO/TS 21396:2017 Rubber determination of mass concentration of tire and road wear particles (TRWP) in soil and sediments Pyrolysis-GC/MS method, 2017.
[78] Jeong CH, Wang JM, Hilker N, Debosz J, Sofowote U, Su Y et al. Temporal and spatial variability of traffic-related PM2.5 sources: comparison of exhaust and non-exhaust emissions. Atmos Environ. 2019;198:55-69. https://doi.org/10.1016/j.atmosenv.2018.10.038
[79] Kim HS, Na HW, Jang Y, Kim SJ, Kee NG, Shin DY et al. Integrative analysis to explore the biological association between environmental skin diseases and ambient particulate matter. Sci Rep. 2022;12:9750. https://doi.org/10.1038/s41598-022-13001-x
[80] Kolbeck K, Schroder T, Schlichting M, Bacher H. Evaluation of different influencing parameters on the result of brake particle emission measurements. EB2022-FBR-011. Proceedings of the EuroBrake 2022. 17-19 May 2022.
[81] Kole PJ, Löhr AJ, Van Belleghem FGAJ, Ragas AMJ. Wear and tear of tyres: a stealthy source of microplastics in the environment. Int J Environ Res Public Health. 2017;14(10): 1265. https://doi.org/10.3390/ijerph14101265
[82] Koupal J, Den Bleyker A, Kishan S, Vedula R, Agudelo C. Brake wear particulate matter emissions modelling. Eastern Research Group, Boston 2021. https://rosap.ntl.bts.gov/view/dot/60273/dot_60273_DS1.pdf (accessed on 9 February 2024).
[83] Kreider ML, Panko JM, McAtee BL, Sweet LI, Finley BL. Physical and chemical characterization of tire-related particles: comparison of particles generated using different methodologies. Sci Total Environ. 2010;408(3):652-659. https://doi.org/10.1016/j.scitotenv.2009.10.016
[84] Kukutschová J, Moravec P, Tomášek, Matějka V, Smolik J, Schwarz V et al. On air-borne nano/micro-sized wear particles released fromlow-metallic automotive brakes. Environ Pollut. 2011;159(4):998-1006. https://doi.org/10.1016/j.envpol.2010.11.036
[85] Kumar P, Pirjola L, Ketzel M, Harrison R.M. Nanoparticle emissions from 11 non-vehicle exhaust sources – a review. Atmos Environ. 2013;67:252-277. https://doi.org/10.1016/j.atmosenv.2012.11.011
[86] Kumata H, Sanada Y, Takada H, Ueno T. Historical trends of n-cyclohexyl-2-benzothiazolamine, 2-(4-morpholinyl)-benzothiazole, and other anthropogenic contaminants in the urban reservoir sediment core. Environ Sci Technol. 2000; 34(2):246-253. https://doi.org/10.1021/ES990738K
[87] Kunze M, Feißel T, Ivanov V, Bachmann T, David Hesse D, Gramstat S. Analysis of TRWP particle distribution in urban and suburban landscapes, connecting real road measure-

ments with particle distribution simulation. Atmosphere. 2022;13;1204. https://doi.org/10.3390/atmos13081204
[88] Kwak J-H, Kim H, Lee J, Lee S. Characterization of non-exhaust coarse and fine particles from on-road driving and laboratory measurements. Sci Total Environ. 2013;458-460: 273-282. https://doi.org/10.1016/j.scitotenv.2013.04.040
[89] Kwak J, Lee S, Lee S. On-road and laboratory investigations on non-exhaust ultrafine particles from the interaction between the tire and road pavement under braking conditions. Atmos Environ. 2014;97:195-205. https://doi.org/10.1016/j.atmosenv.2014.08.014
[90] Lee S, Kwak J, Kim H, Lee J. Properties of roadway particles from interaction between the tire and road pavement. Int J Auto Tech. 2013;14(1):163-173. https://doi.org/10.1007/S12239-013-0018-Y
[91] Liati A, Schreiber D, Lugovyy D, Gramstat S, Eggenschwiler PD. Airborne particulate matter emissions from vehicle brakes in micro-and nano-scales: morphology and chemistry by electron microscopy. Atmos Environ. 2019; 212:281-289. https://doi.org/10.1016/j.atmosenv.2019.05.037
[92] Liu J. Experimental investigation on the morphology of the tire wear particles and its generation mechanism. Tribology. 2017;37(5):587-593. https://doi.org/10.16078/j.tribology.2017.05.004
[93] Liu Y, Wu S., Chen H, Federici M, Perricone G, Li Y et al. Brake wear induced PM10 emissions during the World Harmonised Light-Duty Vehicle Test Procedure-brake cycle. J Clean Prod. 2022;361;132278. https://doi.org/10.1016/j.jclepro.2022.132278
[94] Liu Y, Chen H, Li Y, Gao J, Dave K, Chen J et al. Exhaust and non-exhaust emissions from conventional and electric vehicles: a comparison of monetary impact values. J Clean Prod. 2022;331:129965. https://doi.org/10.1016/j.jclepro.2021.129965
[95] Mamakos A, Arndt M, Hesse D, Augsburg K. Physical characterization of brake-wear particles in a PM10 dilution tunnel. Atmosphere. 2019;10:639. https://doi.org/10.3390/atmos10110639
[96] Matejka V, Metineoz I, Alemani M, Wahlstr€om J, Bonfanti A, Oloffson U et al., Dependency of PM10 particles emission on stability of friction coefficient and character of friction surface. Proceeding EuroBrake 2016, EB2016-MDS-009, Milano 2016.
[97] Matejka V, Metinoz I, Wahlstromb J, Alemani M, Perricone G. On the running-in of brake pads and discs for dyno bench tests. Tribol Int. 2017;115:424-431. https://doi.org/10.1016/j.triboint.2017.06.008
[98] Mathissen M, Scheer V, Vogt R, Benter T. Investigation on the potential generation of ultrafine particles from the tire–road interface. Atmos Environ. 2011;45:6172-6179. https://doi.org/10.1016/j.atmosenv.2011.08.032
[99] Mathissen M, Grochowicz J, Schmidt C, Vogt R, Farwick zum Hagen FH, Grabiec T et al. A novel real-world braking cycle for studying brake wear particle emissions. Wear. 2018;414-415:219-226. https://doi.org/10.1016/j.wear.2018.07.020
[100] Mathissen M, Grigoratos T, Lahde T, Vogt R. Brake wear particle emissions of a passenger car measured on a chassis dynamometer. Atmosphere. 2019;10:556. https://doi.org/10.3390/atmos10090556
[101] Mathissen M, Grigoratos T, Gramstat S, Mamakos A, Vedula R, Agudelo C et al. Interlaboratory study on brake particle emissions. Part II: particle number emissions. Atmosphere. 2023;14:424. https://doi.org/10.3390/atmos14030424
[102] Maynard D, Coull BA, Gryparis A, Schwartz J. Mortality risk associated with short-term exposure to traffic particles and sulfates. Environ Health Perspect. 2007;115:751-755. https://doi.org/10.1289/ehp.9537
[103] Men Z, Zhang X, Peng J, Zhang J, Fang T, Guo Q et al. Determining factors and parameterization of brake wear particle emission. J Hazard Mater. 2022;434:128856. https://doi.org/10.1016/j.jhazmat.2022.128856
[104] Mosleh M, Blau PJ, Dumitrescu D. Characteristics and morphology of wear particles from laboratory testing of disk brake materials. Wear. 2004;256;1128-1134. https://doi.org/10.1016/j.wear.2003.07.007
[105] Mulani SM, Kumar A, Shaikh HNEA, Saurabh A, Singh PK, Verma PC. A review on recent development and challenges in automotive brake pad-disc system. Mater Today: Proc. 2022; 56:447-454. https://doi.org/10.1016/j.matpr.2022.01.410
[106] National Emissions Reported to the Convention on Long-range Transboundary Air Pollution (LRTAP Convention). https://www.eea.europa.eu/ds_resolveuid/f54753b5901e4a8591060bb4ba23c497 (accessed on 1 March 2024).
[107] Niemann H, Winner H, Asbach C, Kaminski H, Frentz G, Milczarek R. Influence of disc temperature on ultrafine, fine, and coarse particle emissions of passenger car disc brakes with organic and inorganic pad binder materials. Atmosphere. 2020;11:1060. https://doi.org/10.3390/atmos11101060
[108] Nosko O, Vanhanen J, Olofsson U. Emission of 1.3–10 nm airborne particles from brake materials. Aerosol Sci Technol. 2017;51(1):91-96. https://doi.org/10.1080/02786826.2016.1255713
[109] Ntziachristos L, Boulter P. EMEP/EEA air pollutant emission inventory guidebook 2019 – road transport: automobile tyre and brake wear. EEA Report No 13/2019.
[110] Oberdörster G, Maynard A, Donaldson K, Castranova V, Fitzpatrick J, Ausman K et al. Principles for characterizing the potential human health effects from exposure to nanomaterials: elements of a screening strategy. Part Fibre Toxicol. 2005; 2:8. https://doi.org/10.1186/1743-8977-2-8
[111] Olofsson U, Olander L. On the identification of wear modes and transitions using airborne wear particles. Tribol Int. 2013;59:104-113. https://doi.org/10.1016/j.triboint.2012.01.013
[112] Oroumiyeh F, Zhu Y. Brake and tire particles measured from on-road vehicles: Effects of vehicle mass and braking intensity. Atmos Environ. 2021;12:100121. https://doi.org/10.1016/j.aeaoa.2021.100121
[113] Panko J, Hitchcock K, Fuller G, Green, D. Evaluation of tire wear contribution to PM2.5 in urban environments. Atmosphere. 2019;10:99. https://doi.org/10.3390/atmos10020099
[114] Pant P, Harrison RM. Estimation of the contribution of road traffic emissions to particulate matter concentrations from field measurements: a review. Atmos Environ. 2013;77:78-97. https://doi.org/10.1016/j.atmosenv.2013.04.028
[115] Park J, Joo B, Seo H, Song W, Lee JJ, Lee WK et al. Analysis of wear induced particle emissions from brake pads during the Worldwide Harmonized Light Vehicles Test Procedure (WLTP). Wear. 2021;466-467:203539. https://doi.org/10.1016/j.wear.2020.203539
[116] Perricone G, Alemani M, Metinöz I, Matějka V, Wahlström J, Olofsson U. Towards the ranking of airborne particle emissions from car brakes – a system approach. P I Mech Eng D-J Aut. 2017;231:781-797. https://doi.org/10.1177/0954407016662800

[117] Perricone G, Matejka V, Alemani M, Valota G, Bonfanti A, Ciotti A et al. A Concept for Reducing PM 10 emissions for car brakes by 50%. Wear. 2018;396-397:135-145. https://doi.org/10.1016/j.wear.2017.06.018
[118] Perricone G, Matejka V, Alemani M, Wahlström J, Olofsson U. A test stand study on the volatile emissions of a passenger car brake assembly. Atmosphere. 2019;10:263. https://doi.org/10.3390/atmos10050263
[119] Perricone G, Alemani M, Wahlstrom J, Olofsson U. A proposed driving cycle for brake emissions investigation for test stand. P I Mech Eng D-J Aut. 2020;234:122-135. https://doi.org/10.1177/0954407019841222
[120] Piras J, Pini F, Di Girolamo P. PM10 emissions from tires: a disruptive estimate questioning present pollution mitigation strategies. Atmos Pollut Res. 2024;15:101939. https://doi.org/10.1016/j.apr.2023.101939
[121] Pirjola L, Kupiainen KJ, Perhoniemi P, Tervahattu H, Vesala H. Non-exhaust emission measurement system of the mobile laboratory SNIFFER. Atmos Environ. 2009;43(31): 4703-4713. https://doi.org/10.1016/j.atmosenv.2008.08.024
[122] Piscitello A, Bianco C, Casasso A, Sethi, R. Non-exhaust traffic emissions: sources, characterization, and mitigation measures. Sci Total Environ. 2021;766:144440. https://doi.org/10.1016/j.scitotenv.2020.144440
[123] Plachá D, Vaculík M, Mikeska M, Dutko O, Peikertová P, Kukutschová J et al. Release of volatile organic compounds by oxidative wear of automotive friction materials. Wear. 2017;376-377:705-716. https://doi.org/10.1016/j.wear.2016.12.016
[124] Pope CA, Burnett RT, Thun MJ, Calle EE, Krewski D, Ito K et al. Lung cancer, cardiopulmonary mortality, and long-term exposure to fine particulate air pollution. J Am Med Assoc. 2002;287:1132-1141. https://doi.org/10.1001/jama.287.9.1132
[125] Rahimi M, Bortoluzzi, D, Wahlstrom J. Input parameters for airborne brakewear emission simulations: a comprehensiv review. Atmosphere. 2021;12:871. https://doi.org/10.3390/atmos12070871
[126] Rexeis M, Hausberger S. Trend of vehicle emission levels until 2020 – prognosis based on current vehicle measurements and future emission legislation. Atmos Environ. 2009; 43:4689-4698. https://doi.org/10.1016/j.atmosenv.2008.09.034
[127] Rienda IC, Alves CA. Road dust resuspension: a review. Atmos Res. 2021;261:105740. https://doi.org/10.1016/j.atmosres.2021.105740
[128] Sanders PG, Xu N, Dalka TM, Maricq MM. Airborne brakewear debris: size distributions, composition, and a comparison of dynamometer and vehicle tests. Environ Sci Technol. 2003; 37(18):4060-4069. https://doi.org/10.1021/es034145s
[129] Semadeni-Davies A, Coulson G, Gadd J, Somervell E, Longely I, Olivares G. Determining the ecological and air quality impacts of particulate matter from brake and tyre wear and road surface dust: Stage 1: Literature review and recommendations for developing new emission factors for New Zealand. Kotahi W. (ed.). Transport Agency: Wellington 2021. https://www.nzta.govt.nz/resources/research/reports/683/
[130] Seo H, Park J, Kim YC, Lee JJ, Jang H. Effect of disc materials on brake emission during moderate-temperature braking. Tribol Int. 2021;163:107185. https://doi.org/10.1016/j.triboint.2021.107185
[131] Simons A. Road transport: new life cycle inventories for fossil-fuelled passenger cars and non-exhaust emissions in ecoinvent v3. Int J Life Cycle Assess. 2016;21:1299-1313. https://doi.org/10.1007/s11367-013-0642-9
[132] Sinha A, Ischia G, Menapace C, Gialanella S. Experimental characterization protocols for wear products from disc brake materials. Atmosphere. 2020;11:1102. https://doi.org/10.3390/atmos11101102
[133] Smit R. Non-exhaust PM emissions from battery electric vehicles (BEVs) – does the argument against electric vehicles stack up? TER (Transport Energy/Emission Research Pty Ltd.). Australia 2020. https://www.transport-e-research.com/_fles/ugd/d0bd25_029571fc6c8a4d80a46adc23dd74ebfd.pdf (accessed on 7 January 2024).
[134] Sommer F, Dietze V, Baum A, Sauer J, Gilge S, Maschowski C et al. Tire abrasion as a major source of microplastics in the environment. Aerosol Air Qual Res. 2018; 18(8):2014-2028. https://doi.org/10.4209/aaqr.2018.03.0099
[135] Song W, Park J, Choi J, Lee JJ, Jang H. Effects of reinforcing fibers on airborne particle emissions from brake pads. Wear. 2021;484-485. https://doi.org/10.1016/j.wear.2021.203996
[136] Steege R, Welp D, Lange J. The contribution of brake emissions to the total vehicle emissions. 6th International Munich Chassis Symposium 2015. Pfeffer P. (ed.). Proceedings; Springer: Wiesbaden 2015:585-603.
[137] Stępień Z, Czerwinski J, Comte P, Oleksiak S. Nanoparticle and non-legislated gaseous emissions from a gasoline direct-injection car with ethanol blend fuels and detergent additives. Energy&Fuels. 2016;30(9):7268-7276. https://doi.org/10.1021/ACS.ENERGYFUELS.6B00583
[138] Stępień Z, Czerwinski J. Cold start with ethanol-blend fuels and influences on non-legislated emissions of a GDI flex fuel vehicle. Pol J Environ Stud. 2017;26/5:2223-2229. https://doi.org/10.15244/pjoes/69282
[139] Stępień Z. Significance of petrol composition in the formation of fuel injector deposits in direct injection engines. Nafta-Gaz. 2023;3:213-222. https://doi.org/10.18668/NG.2023.03.07
[140] Stojanovic N, Abdullah OI, Grujic I, Boskovic B. Particles formation due to the wear of tires and measures for the wear reduction: a review. P I Mech Eng D-J Aut. 2022;236:3075-3089. https://doi.org/10.1177/09544070211067879
[141] Storch L, Hamatschek C, Hesse D, Feist F, Bachmann T, Eichler P et al. Comprehensive analysis of current primary measures to mitigate brake wear particle emissions from light-duty vehicles. Atmosphere. 2023;14:712. https://doi.org/10.3390/atmos14040712
[142] Thorpe A, Harrison RM. Sources and properties of non-exhaust particulate matter from road traffic: a review. Sci Total Environ. 2008;400:270-282. https://doi.org/10.1016/j.scitotenv.2008.06.007
[143] Timmers VRJH, Achten PAJ. Non-exhaust PM emissions from electric vehicles. Atmos Environ. 2016;134:10-17. https://doi.org/10.1016/j.atmosenv.2016.03.017
[144] Tonegawa Y, Sasaki S. Investigation of analytical methods for tire wear particles. JARI Res J. 2012. 12. J-GLOBAL ID: 201302290885047702. Ref. number: 13A0555596.
[145] Tonegawa Y, Sasaki S. Development of tire-wear particle emission measurements for passenger vehicles. Emission Control Science and Technology. 2021;7:56-62. https://doi.org/10.1007/s40825-020-00181-z
[146] Tutuianu M, Bonnel P, Ciuffo B, Haniu T, Ichikawa N, Marotta A et al. Development of the World-Wide Harmonized Light Duty Test Cycle (WLTC) and a possible pathway for its introduction in the European legislation. Transport Res D-Tr E. 2015;40:61-75. https://doi.org/10.1016/j.trd.2015.07.011
[147] Unice KM, Kreider ML, Panko JM. Use of a deuterated internal standard with pyrolysis-GC/MS dimeric marker

analysis to quantify tire tread particles in the environment. Int J Environ Res Public Health. 2012;9(11):4033. https://doi.org/10.3390/ijerph9114033
[148] Unice KM, Weeber MP, Abramson MM, Reid RCD, van Gils JAG, Markus AA et al. Characterizing export of land-based microplastics to the estuary – part I: application of integrated geospatial microplastic transport models to assess tire and road wear particles in the seine watershed. Sci Total Environ. 2019;646:1639-1649. https://doi.org/10.1016/j.scitotenv.2018.07.368
[149] Van Der Gon HD, Hulskotte J, Jozwicka M, Kranenburg R, Kuenen J, Visschedijk A. Chapter 5 – European emission inventories and projections for road transport non-exhaust emissions: analysis of consistency and gaps in emission inventories from EU member states. Non-Exhaust Emissions. Amato F. (ed.). Academic Press: Cambridge 2018:101-121. https://doi.org/10.1016/B978-0-12-811770-5.00005-4
[150] Van Zeebroek B, De Ceuster G, Elektrische wagens verminderen fijn stof nauwelijks. Transp Mobil Leuven. https://www.tmleuven.be/uploads/navigationtree/files/belang_ niet-uitlaat_fijn_stof_emissies_lang.pdf
[151] Vasiljević S, Glišović J, Stojanović B, Vencl A. Review of the coatings used for brake discs regarding their wear resistance and environmental effect. P I Mech Eng J-J Eng. 2022;236:1932-1949. https://doi.org/10.1177/13506501211070654
[152] Wagner S, Hüffer T, Klöckner P, Wehrhahn M, Hofmann T, Reemtsma T. Tire wear particles in the aquatic environment – a review on generation, analysis, occurrence, fate and effects. Water Res. 2018;139:83-100. https://doi.org/10.1016/j.watres.2018.03.051
[153] Wahid SMS. Automotive brake wear: a review. Environ Sci Pollut Res. 2018;25:174-180. https://doi.org/10.1007/s11356-017-0463-7
[154] Wahlström J, Söderberg A, Olofsson U. Simulation of airborne wear particles from disc brakes. SAE Technical Paper 2009-01-3040. 2009. https://doi.org/10.4271/2009-01-3040
[155] Wahlström J, Olander, l, Olofsson U. A pin-on-disc study focusing on how different load levels affect the concentration and size distribution of airborne wear particles from the disc brake materials. Tribol Lett. 2010;46(2):195-204. https://doi.org/10.1007/s11249-012-9944-5
[156] Wakeling D., Murrells T, Carslaw D, Norris J, Jones L. The contribution of brake wear emissions to particulate matter in ambient air. VDA 2017. http://worldcat.org/issn/21927863 (accessed on 5 March 2024).
[157] Wik A, Dave G. Occurrence and effects of tire wear particles in the environment – a critical review and an initial risk assessment. Environ Pollut. 2009;157(1):1-11. https://doi.org/10.1016/j.envpol.2008.09.028
[158] Wang Y, Yin H, Yang Z, Su S, Hao L, Tan J et al. Assessing the brake particle emissions for sustainable transport: a review. Renew Sustain Energy Rev. 2022;167:112737. https://doi.org/10.1016/j.rser.2022.112737
[159] Woo S-H, Kim Y, Lee S, Choi Y, Lee S. Characteristics of brake wear particle (BWP) emissions under various test driving cycles. Wear. 2021;480-481:203936. https://doi.org/10.1016/j.wear.2021.203936
[160] Woo S-H, Jang H, Na MY, Chang HJ, Lee S. Characterization of brake particles emitted from non-asbestos organic and low-metallic brake pads under normal and harsh braking conditions. Atmos Environ. 2022;278:119089. https://doi.org/10.1016/j.atmosenv.2022.119089
[161] Woo S-H, Jang H, Lee S-B, Lee S. Comparison of total PM emissions emitted from electric and internal combustion engine vehicles: an experimental analysis. Sci Total Environ. 2022;842:156961. https://doi.org/10.1016/j.scitotenv.2022.156961
[162] Zemlik M, Dziubek M, Pyka D, Konat Ł, Grygier D. Case study of accelerated wear of brake discs made of grey cast iron characterized by increased thermal stability. Combustion Engines 2022;190(3):45-49. https://doi.org/10.19206/CE-146698
[163] Zhang X, Chen P, Liu F. Review of tires wear particles emission research status. IOP Conf Ser: Earth Environ Sci. 2020;555:012062. https://doi.org/10.1088/1755-1315/555/1/012062
[164] Ziółkowski A, Fuć P, Jagielski A, Bednarek M. Analysis of emissions and fuel consumption from forklifts by location of operation. Combustion Engines. 2022;189(2):30-35. https://doi.org/10.19206/CE-141741

Prof. Zbigniew Stępień, DSc., DEng. – Performance Testing Department, Oil and Gas Institute – National Research Institute, Poland.
e-mail: *stepien@inig.pl*

Article citation info:
Jakuszko W, Bryk K, Gallas D, Stobnicki P, Tarnawski P. Selection of energy storage systems for a special purpose rail vehicle based on simulation analysis. Combustion Engines. 2024;199(4):30-36. https://doi.org/10.19206/CE-188113

Wojciech JAKUSZKO
Karol BRYK
Dawid GALLAS
Paweł STOBNICKI
Piotr TARNAWSKI

Combustion Engines
Polish Scientific Society of Combustion Engines

Selection of energy storage systems for a special purpose rail vehicle based on simulation analysis

ARTICLE INFO

Received: 17 August 2023
Revised: 14 February 2024
Accepted: 29 April 2024
Available online: 24 May 2024

The issue of power supply to electric rail vehicles leads to a separation of the rail network into electrified and unelectrified portions, where the sections lacking electrification exclude the operation of electric rail vehicles powered from the overhead lines. The potential solution to this problem was found in adding energy storage systems to electric rail vehicles to allow them some range of travel beyond the electrified lines. A simulation analysis of a special-purpose rail vehicle traveling across a non-electrified section of a railway line was conducted to assess the energy consumption rate and the necessary energy storage capacity. Three energy storage solutions were simulated, showing the travel range they can provide, with the aim of finding the lowest battery capacity solution that would still allow the vehicle to safely complete the simulated drive. The final selection of energy storage system capacity was done based on the assumed expected range outside the electrified railway weighed against the mass and cost of the extra energy storage system added to the vehicle. For a vehicle with a mass of 65 tons, a battery system with a capacity of 600 Ah was found to be sufficient.

Key words: *rail vehicle, energy storage, battery, simulation, drive system*

1. Introduction

As countries continue to pursue increasingly more pro-ecological solutions for their industry in an effort to minimize their environmental impact, particularly their carbon footprint, solutions based on electrification have become the new goal [24]. This solution has not been widely adopted in road transport before. However, it has been widely present in the past for the rail transport sector [1]. The aspect of electrification of railway lines has been, so far, subdued in line with their perceived economic viability [19]. Due to the high cost associated with electrifying and maintaining electrified rail lines, conventional solutions based on combustion engines have been provided a wide range of applications for rail transport. This cost-to-value equation has changed with the increasing pressure to decarbonize the industry, however [2]. As a result, new solutions are needed to fulfill the role of the aging and replaceable conventional rail vehicles, especially given the increased focus on limiting the exhaust emissions and fuel consumption of rolling stock [6, 12, 14, 20].

In the case of Poland, the UTK (Office of Rail Transport) concluded in its 2022 report that a total of 17.6% of the total track length in Poland is prepared for travel at the speed of 160 km/h (15.5% at 120–160 km/h and 2.1% at speeds exceeding 160 km/h) [26]. Although new investments were expected for the year 2022, reaching the value of almost 11 billion PLN, a portion of which was to be spent constructing an additional 789 km of railway lines. In the year 2022, a notable lowering of the mean age of passenger rolling stock was observed. This was a reduction in mean age compared to 2021 for electric locomotives from 33.76 to 32.16 years, for diesel locomotives from 43.81 down to 41.94 years, and for EMUs from 25.79 to 24.43 years. The youngest group was the dual-drive multiple units, at a mean age of 0.82 years. This helps visualize the recent rise in popularity of dual-drive systems and other vehicles that are neither strictly diesel nor electric. A similar continued trend was observed for freight rolling stock, where the mean age of electric locomotives decreased from 36.57 to 33.82 years, while for diesel locomotives, the mean age lowered significantly from 38.31 down to 33.51 years. Most importantly, the report notes that about 62.5% of the total track length was electrified (12,126 km of track), leaving the remaining 37.5% (or 7267 km) non-electrified. This means that over a third of all track length in Poland did not have an overhead catenary. This poses a real problem in adjusting the plans of purchasing new rolling stock to the realities of the Polish railway network. Especially given the low rate of growth of electrified railway length in Poland. Between the years 2020 and 2021, it increased by just 210 km (from 11,946 km to 12,156 km).

Since the easiest solution, of buying more conventional vehicles to replace the old ones, would stand in conflict with the environmental goals set by most developed countries, other solutions need to be considered. This problem could be solved by simply expanding on the already existing solutions, such as electric vehicles driving on electrified railway lines. This, however, would require substantial investment in infrastructure improvement. In order to avoid the costs of electrification where possible, the concept of a battery powered rail vehicle was introduced. It is a solution that allows a rail vehicle to partially or temporarily operate outside of the overhead power network using its on-board energy storage systems [7, 17]. This has often been introduced in parallel with other solutions based on ultracapacitors or hydrogen fuel cells [16]. Many solutions for locomotive energy storage systems have been proposed. Spiryagin et al. have concluded that a flywheel system in a diesel locomotive could reduce fuel consumption in heavy haul operations by as much as 12.4% [22]. For light rail

systems, Gee et al. predicted a flywheel solution to offer energy savings of 21.6% [10], while Rupp et al. estimated 31% [18]. Despite these results the flywheel technology has many limitations and, along with the further development of battery technology, seems to be increasingly less competitive to battery solutions, as noted already back in 2015 by Spiryagin in [21]. As a result, battery-based energy storage was considered the more modern solution. The addition of a battery energy storage system on rail vehicles opens the option of also integrating supercapacitors into the system to allow for braking energy recovery. The energy loss on braking represents a large energy waste in rail transport. Many studies have been performed, claiming various levels of efficacy of such a solution. Mayet et al. claimed a 25% fuel consumption reduction when using a battery/supercapacitor energy storage system in a diesel-electric locomotive [13], while Steiner et al. from Bombardier have recorded 30% energy traction savings in a light rail vehicle using a similar system [23]. Teymourfar et al. reported an even greater 44% energy savings for a stationary supercapacitor system on a metro line [27]. Despite all of these encouraging results, supercapacitors remain heavy and expensive, thus making their use more feasible in power substations and stationary systems rather than mounting them onto rail vehicles themselves. Ultimately, creating Multi-Purpose Vehicles (MPV) that don't rely primarily on a diesel engine has proven difficult. Some examples do exist, such as the first fully electric MPV operating on Citybanan in Stockholm created by company Railcare AB.

The solution discussed in the article is that of a special-purpose rail vehicle, designed for track maintenance, equipped with a diesel engine and a lithium-ion battery system that enables it to travel through non-electrified sections of railway lines. This is done to effectively extend the vehicle range beyond the electrified portions of the rail network. Effective use of such a power supply system in rail vehicles can result in a significant reduction of its carbon footprint while eliminating its exhaust emissions [4]. The selection of the technological solutions and devices that are to provide this ability is a key factor in increasing the overall efficiency of rail vehicles. These solutions, the type of energy storage systems used, their capacity and properties, energy recovery systems [15], and additional safety systems all need to be selected with the expected parameters in mind, as well as the intended type of operations the vehicle is to be used for. This can prove particularly difficult for MPVs, as they are often expected to perform a diverse range of tasks. Depending on the solution and technology used, further optimization of energy management (called the Energy Management Strategy or EMS) can further magnify the benefit of the chosen technological solution [5, 11]. This further complicates attempts to assess the overall vehicle efficiency or energy consumption. Furthermore, optimization of the overhead supply system, the substations, timetable organization, and driving speed [9] can also significantly impact the potential level of energy consumption of rail vehicles and maximize the efficiency of braking energy recovery up to even 95% [28]. Unfortunately, these solutions each come with their own drawbacks, whether in the form of additional mass or increased cost. This means that whatever solutions are considered for any given vehicle should be highly contextualized and specific to that vehicle's expected operating conditions and types of tasks performed. Minimizing the cost and size of newly added technological solutions is the key aspect of finding the right balance and maximizing vehicle efficiency.

Increasing the efficiency of rail vehicles is additionally helpful in fulfilling the goals of the Green Rail program (Zielona Kolej), which aims to reduce the CO_2 emissions of rail transport by 85% by the year 2030. It's initiatives like these that promote the development of new energy-saving and energy-recovery technologies while also promoting the use of electric drive systems in rail vehicles to be powered by renewable energy. Similarly, the rail infrastructure is also planned to be modernized. Aiming to increase the total length of electrified railway lines to 14 000 km by 2030. Thus increasing the total share of electrified lines from 62.5% in 2020, to over 72% by 2030. This would classify Poland as the European country with the 7th highest share of electrified railway length, behind Bulgaria at 74.4% and ahead of Austria at 71.9% (as of 2021) [26]. Due to its decreasing ecological impact, rail transport could significantly contribute to reducing greenhouse gas emissions whenever rail is chosen as the transit method instead of road transport. The same report estimated that in 2022, about 342.2 million passengers contributed to reducing CO_2 emissions by 2.6 million tons by opting to travel by rail instead of using road transport. Further electrification of railway lines, along with the modernization of the rolling stock operated, especially for vehicles in the dual drive or electric categories, should lead to steady improvement in the environmental impact of human transport activities.

2. Aim

The main goal of the article was to assess the necessary energy capacity of an on-board battery system for a proprietary special purpose vehicle. The new vehicle was designed as part of a project to be an innovative special hybrid drive MPV improved with independent power storage designed to transport equipment for the construction, diagnosis and measurement of rail infrastructure. The vehicle was expected to have three independent drive systems: a catenary line, a battery system, and an emergency power generator. It should reach a travel speed of 160 km/h with a catenary line power supply. In case of grid failure or lack of catenary lines, it could use its batteries, which can be charged from catenary lines while driving or from a charging station when parked. The main advantages of the vehicle include being able to operate with zero-emissions and a functional braking energy recovery system. The energy is to be stored and used for propulsion to prolong its operation supported by power supplied by batteries. One of the key assumptions of the designed vehicle was to ensure it could travel at a speed of 60 km/h for at least 30 minutes powered by its battery systems alone. This was to ensure emission-free transit from one work location to the next, irrespective of whether the line is electrified or not. Assessing the viability of meeting all the goals and assumptions for the prospective vehicle required a number of tests and simulations. 3 drives were simulated for different variants of the vehicle. These

variants were based on the energy storage capacity of the on-board batteries. The battery system was a set of 4, 6, or 8 batteries for each of the 3 variants, respectively, where each battery had a capacity of 100 Ah, nominal voltage of 666 V DC, max. voltage of 770 V DC, charging current of 80 A, discharging current of 100 A, and a nominal energy of 66.6 kWh.

3. Data and methods

The theoretical test drive was designed based on a proprietary program created in the Matlab environment described in this section. To solve the vehicle motion equation, the program operated using the vehicle characteristics, the route profile data, the speed limit, and the timetable as input provided by the user. The simulation relied on the CBTK formula for multiple units and the Röckel formula for calculating the resistance in the track curvature in a similar process as described in previous research [3]. The intended vehicle specifications were also listed (Table 1), and the selection and implementation of its drive system was discussed in previous research [8, 25].

Table 1. The target technical specification of the proposed 501EH vehicle

Parameter	Value
Service mass	65 t
Max. speed (self-propelled)	160 km/h
Tractive power	65 kW electric motor; 340 kW combustion engine; 100 kWh batteries
Max track gradient	30‰
Gauge	1435 mm
Max track cant value	180 mm

The three performed simulation drives were labeled as drives 1, 2, and 3 for the three vehicle variants having 400 Ah, 600 Ah, and 800 Ah capacity battery systems, respectively. The three battery sizes were selected based on the assertion that the battery's reserve energy should not drop below 300 kWh. Thus the first variant used was given a battery system with only 100 kWh excess power to use, which was shown to be the approximate power needed to travel the distance, based on preliminary calculations. Further variants had their battery capacity increased in 200 Ah increments. The route selected was based on the driving profile of a real rail line often used for testing, which included slope, stops, and a gap in catenary in between for a length of 30 km of track out of the total of 40 km (Fig. 1). The selection of the size of the battery system was to be based on which smallest battery system was able to meet the requirements set for the new vehicle in the project, while ensuring that the vehicle still operates effectively. The general problem was to assess the tradeoff between a larger energy storage system with greater capacity and range, and reducing the vehicle curb weight and cost as much as possible. Simulation tests were used to measure several parameters, such as: vehicle speed, vehicle acceleration, power at the wheels, sum of motion resistances, main circuit power, energy flow through the pantograph system, energy balance at the battery system, battery state of charge (SoC), and traction force for each of the tested vehicle variants. The simulated system was described in block form (Fig. 2) using known properties and parameters of the systems and devices used in the design. This assumes inverter efficiency of 98%, transformer efficiency of 98%, and traction engine efficiency of 94%. The battery system was assumed to have a 92% overall efficiency of charging and discharging for the purposes of the simulation. It should be noted that the choice of battery system brand and type may cause these parameters to vary.

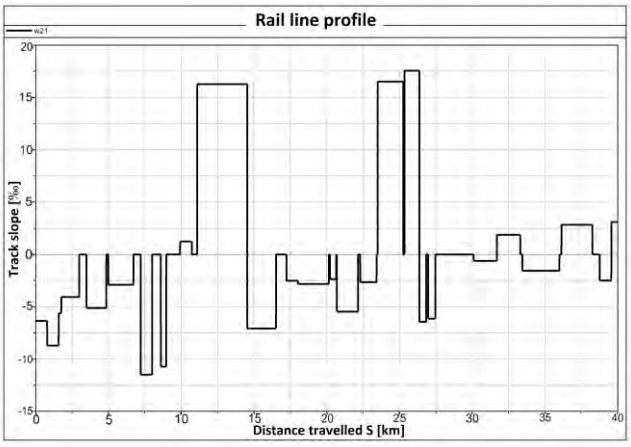

Fig. 1. Track incline profile for the test route

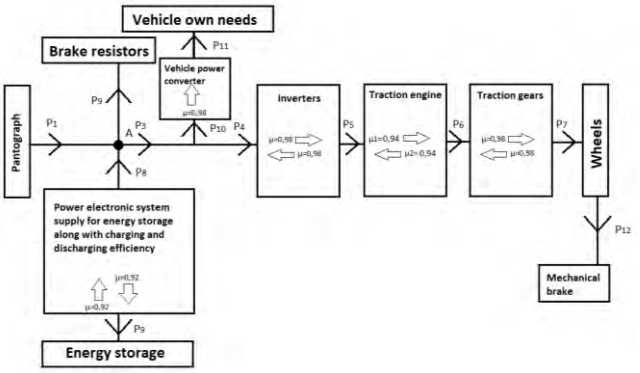

Fig. 2. Schematic of the energy flow in the vehicle drive system

4. Simulation results and discussion

The obtained results indicated that while even the lowest capacity battery system (of 400 Ah) could successfully travel the required 30 minutes at 60 km/h, the depletion of the battery SoC had a more significant impact on the available power output, thus affecting the vehicle traction properties (Fig. 3). This can be seen in the greater values of Power generated at the wheels for drive 3 as compared to drive 1, which also resulted in the motion resistance peaks correlating with uphill climbs to be shorter, as they were being overcome quicker. This also reduced the overall drive time from about 44 minutes for drive 1 down to about 41 minutes for drive 3. It was found that the minimum amount of battery energy needed to travel the 30 km distance without overhead supply was slightly less than 100 kWh for the simulated track profile (Fig. 4). For each of the drives the battery system expended the necessary energy to arrive at the other side of the non-electrified track section, and began to draw power from the overhead catenary again once it became available. This was in line with the expectations, as

the vehicle was to be able to recharge purely from the catenary-supplied power. The rate of power drawn and used need to be monitored by the BMS, so as not to overheat or overload the batteries. This was the side effect of deciding to forgo using supercapacitors for their ability to rapidly store large quantities of charge and equally rapidly release that charge when needed. It was decided that batteries alone, although less effective in that regard, would suffice if properly managed.

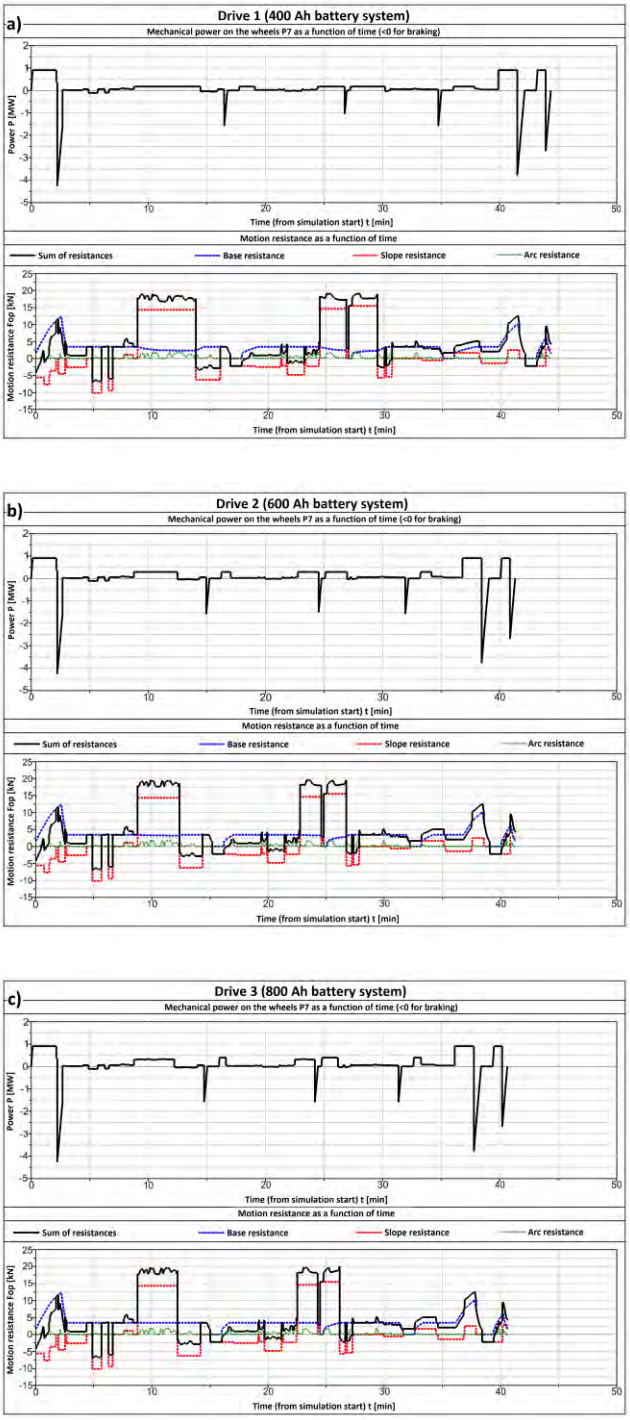

Fig. 3. Vehicle power at the wheels and movement resistance of the simulation drive for each vehicle variant: a) drive 1, b), drive 2, c) drive 3

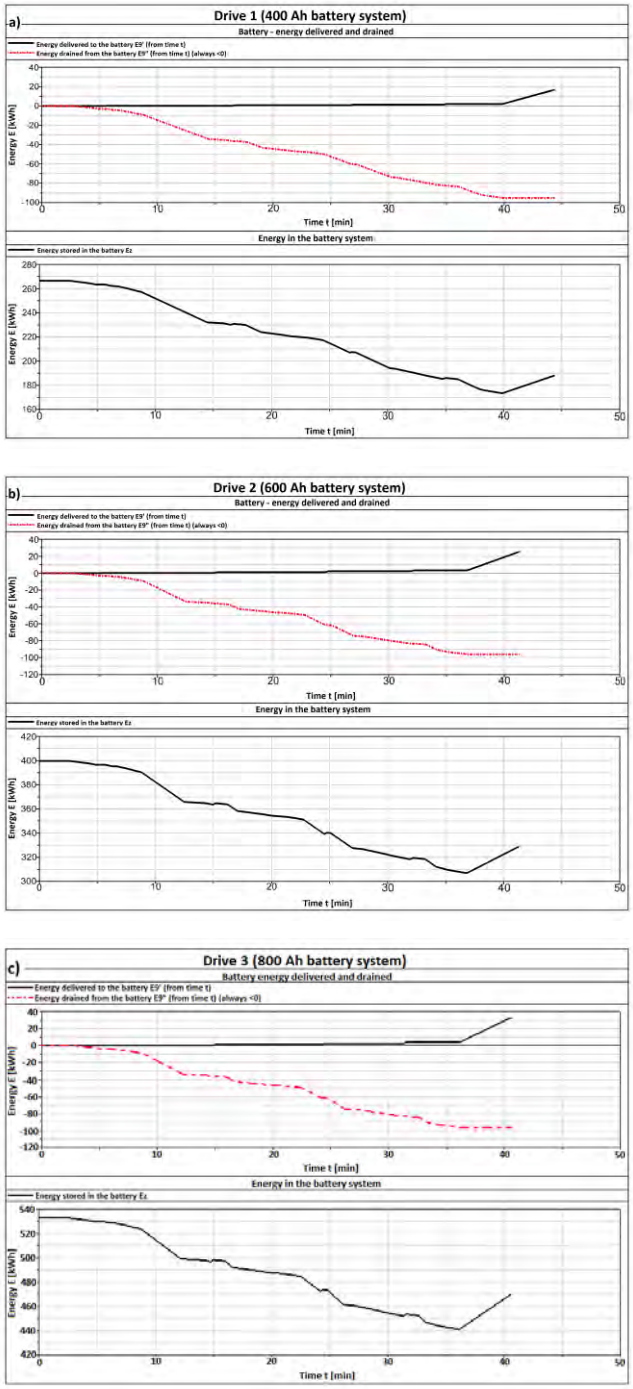

Fig. 4. Energy storage system state of charge and Energy depletion in the simulation drive for each vehicle variant: a) drive 1, b) drive 2, c) drive 3

It should be noted that in each test case the vehicle batteries started fully charged (with ~67 kWh of energy per battery), at approximately 465 kWh for 4 battery system, 400 kWh for the 6 battery system, and 530 kWh for the 8 battery system. This will not necessarily be the case in real operation, as keeping the batteries at full charge most of the time can accelerate their degradation. A proper BMS could be integrated with the rail network information to enable the vehicle to predictively charge up the batteries before their full charge is needed while still driving through an electrified rail section. The total energy used to travel the simulated distance was about 150 kWh. Each vehicle vari-

ant drew approx. 100 kWh of energy through the pantograph and returned over 10 kWh from regenerative braking. The mechanical power peaks when driving without an overhead power supply were flatter and smoother for variant 1 (400 Ah) while being higher and more rugged for variant 3 (800 Ah). Each vehicle managed to reach its peak driving speed of 160 km/h before slowing down to 60 km/h for the unpowered section of the track. Stops were added to simulate waiting time on crossings or switches (Fig. 5).

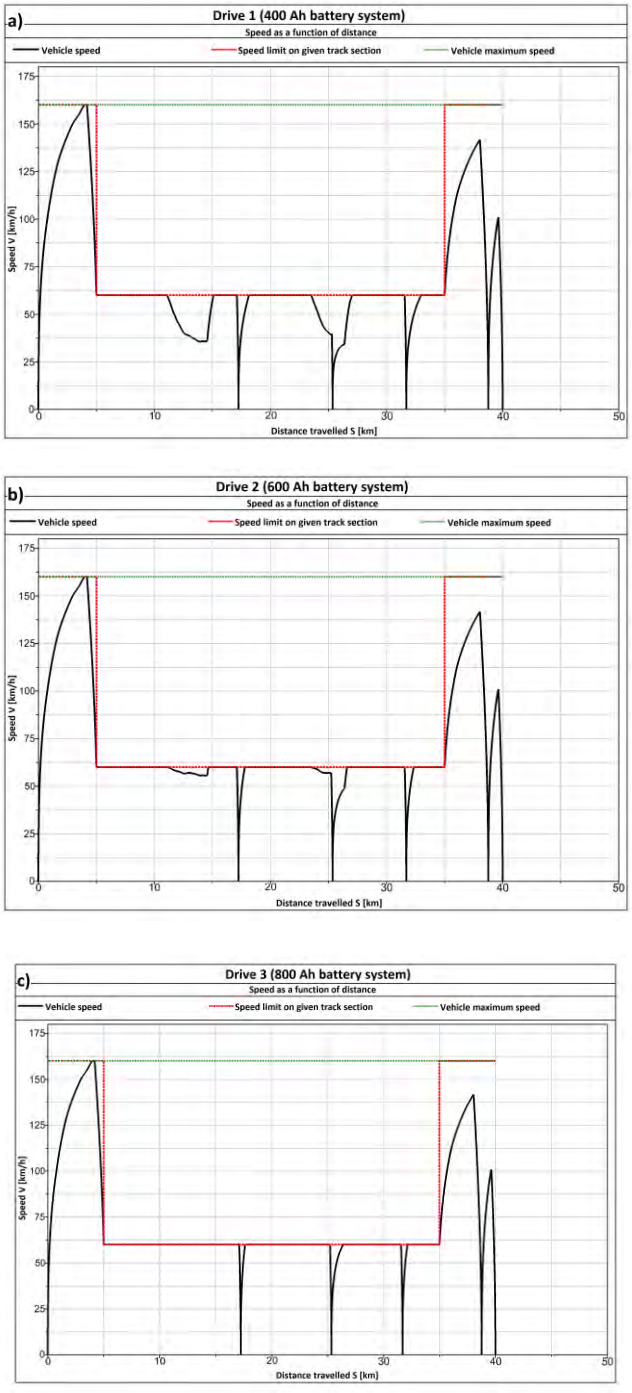

Fig. 5. Vehicle speed profile for the test route using each vehicle variant: a) drive 1, b) drive 2, c) drive 3

The obtained battery charge values at the end of the simulated drives show sufficient charge for continued driving and operation without the overhead power supply. Thus, the total remaining charge in the batteries was not the limiting factor on its own. However, due to the properties of battery systems the available power was affected by the battery SoC. It was therefore necessary to account for the drop in available traction force as the battery charge decreases due to basic battery current-voltage characteristics. This effect could be observed by the deeper drops or slower increase in vehicle speed for sections where the simulated track had an upwards slope. Especially for the section between the 10–15 km distance from the start point, where the train encountered an upwards climb, presenting an unintended drop in travel speed (Fig. 5a and 5b). This effect was not observed for the vehicle variant 3, equipped with the highest capacity battery system of 800 Ah (Fig. 5c). Thanks to the higher power reserve, and a batter response to the sudden power demand despite some energy depletion on the batteries, such drops in speed can be mitigated to a point where they are no longer noticeable. Although it is not always a significant enough issue to warrant the extra weight and cost of more batteries.

While a momentary drop in travel speed is unwanted, it is to some degree unavoidable. It was noted that vehicle variant 2 experienced a travel speed decrease of less than 5 km/h, which was deemed acceptable given the nature of the vehicle operation. Vehicle variant 1, on the other hand, was shown to significantly lose speed on the climb (decrease of over 20 km/h). Such a drop in speed can be noticeable and may cause unnecessary delays in how the vehicle performs its designated tasks. Ideally, the slowdown would not occur, such as in the case of variant 3, where the large reserve power still held by the 8 batteries was sufficient to ensure full tractive force.

Conclusions

The obtained power characteristics on the vehicle wheels indicated that the lower capacity battery system, while having sufficient energy to support the whole test drive, could not provide the power needed to safely travel the whole distance without a notable drop in speed. Such a situation was deemed dangerous, especially in the potential case of a track with a more significant slope. Vehicle speed curves show a drop in speed for variants 1 and 2 after 10 minutes of driving, where the track meets an incline of over 15‰. While variant 2 did not slow down more than 5 km/h, variant 1 slowed down by 25 km/h (down from 60 km/h), and variant 3 was unaffected. This was mostly caused by the drop in usable power due to the lower battery charge and the associated voltage drop as the on-board battery system charge level was drained when traveling. Variant 1 was deemed insufficient in order to ensure smooth travel on hilly terrain. Hence the lowest capacity battery system needed in such a vehicle was concluded to be 600 Ah, as tested for vehicle variant 2. The vehicle should be able to climb an incline of 15‰ without significant loss of speed even after its batteries were drained by driving for 30 minutes. This also ensures a sufficient battery capacity to support track operations after the vehicle arrives at its destination. Ideally the incline could be overcome with no loss of speed, but this was only possible for variant 3, with the highest reserve power thanks to its 8

batteries. Such slowdowns may be unacceptable for passenger rail vehicles, as they are jarring to the passengers on board, however, sue to the nature of the tested vehicle's operation, the result obtained for variant 2 was deemed acceptable. An MPV does not necessarily need to provide a completely smooth drive, and most of its work is expected to be performed while either stationary or moving at a low steady speed. Each of the tested variants used up 100 kWh of energy on the 30 km long non-electrified section of the track while also recovering about 10 kWh of energy back using regenerative braking. This means that the total effective vehicle range without power supply was approximately 10% greater than estimated, thanks to the energy recovery from braking.

Further research is planned using a real vehicle prototype, to validate the obtained results. Such validation should be performed in the form of a real drive on a selected rail section. It should be noted, however, that the chosen battery management system (BMS) is expected to have a significant effect on the obtained results, as well as any energy savings. The BMS defines how effectively the energy storage system is operated, while the EMS determines the overall energy use efficiency in the vehicle. Thus, the proper adjustment of these management systems will play a key role in increasing the efficiency of the vehicle drive system. Such solutions are especially important in order to ensure steady and stable operation of the entire energy storage system, as well as to monitor its operating parameters to prevent excessive heating or overloading. Another aspect would be predictive charging, which should prevent the vehicle from regularly moving on electrified railway lines with fully charged batteries. For longer term, modern lithium-ion batteries prefer to be kept at SoC at no greater than 80%. Hence the need to predict when a fully charged battery may be needed and charge it up while on the way to the non-electrified track section, or work location.

Acknowledgements

The article was written in connection with the project POIR.01.01.01-00-1601/20-00 entitled "An innovative special hybrid drive rail vehicle improved with independent power storage designed to transport equipment for building, diagnosing and measuring of rail infrastructure". The project is implemented under Sub-measure 1.1.1 Industrial research and development works carried out by enterprises, co-financed by the European Regional Development Fund.

Nomenclature

BMS	battery management system	EMU	electric multiple unit
DC	direct current	MPV	multi-purpose vehicle
EMS	energy management strategy	SoC	state of charge

Bibliography

[1] Ajanovic A, Haas R, Schrödl M. On the historical development and future prospects of various types of electric mobility. Energies. 2021;14(4):1070. https://doi.org/10.3390/en14041070

[2] Barros LAM, Tanta M, Martins AP, Afonso JL, Pinto JG. Opportunities and challenges of power electronics systems in future railway electrification. 2020 IEEE 14th International Conference on Compatibility, Power Electronics and Power Engineering (CPE-POWERENG). 2020:530-537. https://doi.org/10.1109/CPE-POWERENG48600.2020.9161695

[3] Bryk K, Urbański P, Gallas D, Tarnawski P. Michalak P, Stobnicki P. Simulation analysis of an electric multiple unit vehicle energy consumption. SAE Technical Paper 2022-01-1133. 2022. https://doi.org/10.4271/2022-01-1133

[4] Cipek M, Pavković D, Kljaić Z, Mlinarić TJ. Assessment of battery-hybrid diesel-electric locomotive fuel savings and emission reduction potentials based on a realistic mountainous rail route. Energy. 2019;173:1154-1171. https://doi.org/10.1016/j.energy.2019.02.144

[5] Daszkiewicz P, Andrzejewski M, Medwid M, Urbański P, Cierniewski M, Woch A et al. Analysis of the selection of chosen technical parameters of the powertrain system for a diesel-electric rail-road tractor. Combustion Engines. 2021; 186(3):64-71. https://doi.org/10.19206/CE-140723

[6] Daszkiewicz P, Andrzejewski M, Urbański P, Woch A, Stefańska N. Analysis of the exhaust emissions of toxic compounds from a special purpose rail machine PŁT-500 during profiling the ballast cess. Journal of Ecological Engineering. 2021;22(7):80-88. https://doi.org/10.12911/22998993/139214

[7] Fedele E, Iannuzzi D, Del Pizzo A. Onboard energy storage in rail transport: review of real applications and techno-economic assessments. IET Electr Syst Transp. 2021;11(4): 279-309. https://doi.org/10.1049/els2.12026

[8] Gallas D, Stobnicki P, Jakuszko W, Urbański P, Kikut J. Application of alternative drive systems in modern special-purpose rail vehicles. J Transp Eng, 2023;136:23-33. https://doi.org/10.5604/01.3001.0016.3417

[9] Gallo M, Botte M, Ruggiero A, D'Acierno L. A simulation approach for optimising energy-efficient driving speed profiles in metro lines. Energies. 2020;13(22):6038. https://doi.org/10.3390/en13226038

[10] Gee AM, Dunn RW. Analysis of trackside flywheel energy storage in light rail systems. IEEE T Veh Technol. 2015; 64(9):3858-3869. https://doi.org/10.1109/TVT.2014.2361865

[11] Herrera VI, Gaztañaga H, Milo A, Saez-de-Ibarra A, Etxeberria-Otadui I, Nieva T. Optimal energy management and sizing of a battery-supercapacitor-based light rail vehicle with a multiobjective approach. IEEE T Ind Appl. 2016; 52(4):3367-3377. https://doi.org/10.1109/TIA.2016.2555790

[12] Kamińska M, Rymaniak Ł, Lijewski P, Szymlet N, Daszkiewicz P, Grzeszczyk R. Investigations of exhaust

emissions from rail machinery during track maintenance operations. Energies. 2021;14(11):3141. https://doi.org/10.3390/en14113141
[13] Mayet C, Pouget J, Bouscayrol A, Lhomme W. Influence of an energy storage system on the energy consumption of a diesel-electric locomotive. IEEE T Veh Technol. 2014; 63(3):1032-1040. https://doi.org/10.1109/TVT.2013.2284634
[14] Merkisz J, Lijewski P, Pielecha J. PEMS-based investigations into exhaust emissions from non-road and rail vehicles. Combustion Engines. 2016;166(3):46-53. https://doi.org/10.19206/CE-2016-339
[15] Ogasa M. Energy saving and environmental measures in railway technologies: example with hybrid electric railway vehicles. IEEJ Trans Elec Electron Eng. 2008;3:15-20. https://doi.org/10.1002/tee.20227
[16] Pielecha I, Merkisz J, Andrzejewski M, Daszkiewicz P, Świechowicz R, Nowak M. Ultracapacitors and fuel cells in rail vehicle drive systems. Rail Vehicles/Pojazdy Szynowe. 2019;2:9-19. https://doi.org/10.53502/RAIL-138526
[17] Ratniyomchai T, Hillmansen S, Tricoli P. Recent developments and applications of energy storage devices in electrified railways. IET Electr Syst Transp. 2014;4:9-20. https://doi.org/10.1049/iet-est.2013.0031
[18] Rupp A, Baier H, Mertiny P, Secanell M. Analysis of a flywheel energy storage system for light rail transit. Energy. 2016;107:625-638. https://doi.org/10.1016/j.energy.2016.04.051
[19] Rybicka I, Stopka O, Ľupták V, Chovancová M, Droździel P. Application of the methodology related to the emission standard to specific railway line in comparison with parallel road transport: a case study. MATEC Web Conf. 2018;244: 03002. https://doi.org/10.1051/matecconf/201824403002
[20] Rymaniak Ł, Daszkiewicz P, Merkisz J, Bolzhelarskyi YV. Method of determining the locomotive engine specific fuel consumption based on its operating conditions. AIP Conf Proc. 2019;2078(1):020053. https://doi.org/10.1063/1.5092056
[21] Spiryagin M, Wolfs P, Szanto F, Sun Y, Cole C, Nielsen D. Application of flywheel energy storage for heavy haul locomotives. Appl Energ. 2015;157:607-618. https://doi.org/10.1016/j.apenergy.2015.02.082
[22] Spiryagin M, Wu Q, Wolfs P, Sun Y, Cole C. Comparison of locomotive energy storage systems for heavy-haul operation. International Journal of Rail Transportation. 2018;6(1): 1-15. https://doi.org/10.1080/23248378.2017.1325719
[23] Steiner M, Klohr M, Pagiela S. Energy storage system with ultracaps on board of railway vehicles. 2007 European Conference on Power Electronics and Applications. 2007:1-10. https://doi.org/10.1109/EPE.2007.4417400
[24] Tamor MA, Gearhart C, Soto C. A statistical approach to estimating acceptance of electric vehicles and electrification of personal transportation. Transport Res C-Emer. 2013;26: 125-134. https://doi.org/10.1016/j.trc.2012.07.007
[25] Urbański P, Gallas D, Stachowicz A, Jakuszko W, Stobnicki P. Analysis of the selection of the auxiliary drive system for a special purpose hybrid rail vehicle. Rail Vehicles/Pojazdy Szynowe. 2022;1-2:30-39. https://doi.org/10.53502/RAIL-149405
[26] Urząd Transportu Kolejowego – Sprawozdanie z funkcjonowania rynku kolejowego w 2022 r. (in Polish) https://utk.gov.pl/pl/dokumenty-i-formularze/opracowania-urzedu-tran/20286,Sprawozdanie-z-funkcjonowania-rynku-transportu-kolejowego-w-2022-r.html
[27] Teymourfar R, Asaei B, Iman-Eini H, Nejati R. Stationary super-capacitor energy storage system to save regenerative braking. Energ Convers Manage. 2012;56:206-214. https://doi.org/10.1016/j.enconman.2011.11.019
[28] Tian Z. Railway energy simulation considering traction power systems. In: Energy-efficient train operation. Lecture Notes in Mobility. Springer, Cham 2023. https://doi.org/10.1007/978-3-031-34656-9_7

Wojciech Jakuszko, MEng. – Division of Rail Vehicles Development, Łukasiewicz Research Network – Poznan Institute of Technology, Poland.
e-mail: *wojciech.jakuszko@pit.lukasiewicz.gov.pl*

Karol Bryk, MEng. – Division of Modeling and Simulation, Łukasiewicz Research Network – Poznan Institute of Technology, Poland.
e-mail: *karol.bryk@pit.lukasiewicz.gov.pl*

Dawid Gallas, DEng. – Division of Rail Vehicles Development, Łukasiewicz Research Network – Poznan Institute of Technology, Poland.
e-mail: *dawid.gallas@pit.lukasiewicz.gov.pl*

Paweł Stobnicki. DEng. – Division of Rail Vehicles Development, Łukasiewicz Research Network – Poznan Institute of Technology, Poland.
e-mail: *pawel.stobnicki@pit.lukasiewicz.gov.pl*

Piotr Tarnawski, DEng. – Director of Center of Modern Mobility, Łukasiewicz Research Network – Poznan Institute of Technology, Poland.
e-mail: *piotr.tarnawski@pit.lukasiewicz.gov.pl*

Article citation info:
Kosztyła T. Benefits of using titanium alloy as the construction material of the connecting rod and piston in the SI engine. Combustion Engines. 2024;199(4):37-42. https://doi.org/10.19206/CE-189830

Tomasz KOSZTYŁA

Combustion Engines
Polish Scientific Society of Combustion Engines

Benefits of using titanium alloy as the construction material of the connecting rod and piston in the SI engine

ARTICLE INFO

Received: 6 December 2023
Revised: 14 February 2024
Accepted: 9 June 2024
Available online: 9 July 2024

The overall efficiency of an internal combustion engine determines the ability to convert the energy generated during fuel combustion into useful mechanical work. One method to increase efficiency is to reduce internal losses. The component of the internal losses of an internal combustion engine is the inertia force of the parts in a reciprocating motion. In the work, the author presented the reduction of the inertia force in the reciprocating motion, obtained by reducing the masses of the connecting rod and piston. Reducing the masses of these elements was the result of the use of an innovative material: titanium alloy Grade 5. The paper presents the analytical determination of mechanical loads affecting the modified elements of the crank system. The process of designing a connecting rod and piston using finite element simulation tests is briefly described. Inertial force was determined analytically for two versions of crank systems: factory and modified. The obtained results were compared, and a significant reduction in inertial force is one of the advantages of using titanium alloy on selected elements of the crank system.

Key words: *inertial force, fuel saver, energy efficiency, connecting rod, piston*

1. Introduction

One of the methods of increasing the overall efficiency an Internal Combustion Engine (ICE) is based on reducing internal losses. The component of internal ICE losses is the friction force, related to the inertia force of the parts moving in a reciprocating motion. Therefore, reducing the value of inertia forces should reduce friction losses in the engine, with the value of the friction coefficient remaining unchanged. The magnitude of the inertial force depends on the acceleration on the ICE components moving on the cylinder axle and on the mass of these parts. The acceleration value depends on the geometry of the crank system and the instantaneous rotational speed of the crank. In the article, the author presented the benefits of using the Ti6Al4V titanium alloy as a construction material, as a reduction in the masses of the crank system (piston and connecting rod). By reducing the masses of these components, compared to the factory components of the modified engine, the designated inertial forces in reciprocating and rotary motion were reduced.

There are publications describing the use of titanium alloys for crank system elements, such as the connecting rod [1]. In the article, the authors presented the reduction in connecting rod mass achieved by optimizing its shape and dimensions. Ti6Al4V titanium alloy was used as the construction material. ANSYS software was used to calculate static and fatigue strength.

The manuscript [4] presents the methodology for using CAE software to design a connecting rod. The result of the analysis is a change in dimensions and shape in subsequent iterations of the connecting rod model subjected to simulations. As a result, a reduction in weight and the maximum value of reduced stresses were achieved.

In the paper [9], the authors presented the results of simulation calculations of a connecting rod using the finite element method. The computer analysis was carried out to determine the cause of failure (breakage) of the connecting rod in the existing design of a compression-ignition engine. Based on the results of the simulations, it was found that the main cause of failure of the connecting rod was a high level of stress near the bolt hole. in this zone, the stress pile-up is caused by high bolt preload. The use of the FEM method made it possible to determine the area of notch occurrence.

The manuscript [5] contains a description of the design process and numerical analyzes using ANSYS software to design the connecting rod of an ICE. The determination of the amount of static stresses was made using the Finite Element Method (FEM).

The paper [6] is concerned with the analysis of fatigue-damaged pistons. Also, static stress analysis is used to determine the stress distribution during the combustion on piston.

The manuscript [7] covers issues related to the design of an ICE piston with thermal load, for different materials. FEM were also used in simulation analyses for design the piston.

In their conclusions, the authors of the presented articles presented the possibility of using titanium alloy as a construction material for the connecting rod. Some of the works determined the weight reduction resulting from the use of titanium alloy in selected elements of the crank system. However, there is no determined reduced value of inertia forces resulting from the use of titanium alloy. This is the main goal of this article. Moreover, the author proposes the use of titanium alloy as a construction material for the piston of an ICE. the effect of simultaneous reduction in the mass of both the connecting rod and the piston (compared to the factory elements) will be presented in the form of a comparison of the course of inertia forces as a function of the crankshaft rotation angle, for the rotational speed corresponding to the maximum power of the modified ICE.

The object of modernization by the author of the paper is the ICE a single-cylinder, 4-stroke unit, powered by ethanol, with an eccentric crank system. The parts subject to modification are the connecting rod and the piston. The selected construction material is Ti6al4V titanium alloy, some of its physical parameters are presented in Table 1.

Table 1. Physical properties of the Ti6AL4V alloy (source https://asm.matweb.com)

Parameter	Unit	Value
Tensile strength Rm	MPa	896
Yield strength Rh	MPa	827
Young's module	GPa	114
Density	g/cm^3	4.43
Thermal conductivity	W/m·K	6.7
Specific heat capacity	J/kG·K	526

The modified engine is used to power the vehicle running in the Shell Eco-Marathon (SEM) competition. The idea of the international competition for student teams is to build vehicles whose goal is to cover the greatest possible distance on one liter of fuel. Therefore, all possibilities of increasing the efficiency of the combustion engine are desirable and justify the use of an unusual construction material, such as titanium alloy, for the connecting rod and piston. The desirability of minimizing inertial force by designing new parts results from the use of an ICE.

Selected parameters of the drive unit are included in Table 2.

Table 2. Technical data of ICE

Parameter		Unit	Value
Bore	D	mm	35
Crankshaft cranking	r	mm	21.9
Length of rod	l	mm	120
Cylinder axis shift	e	mm	1.5

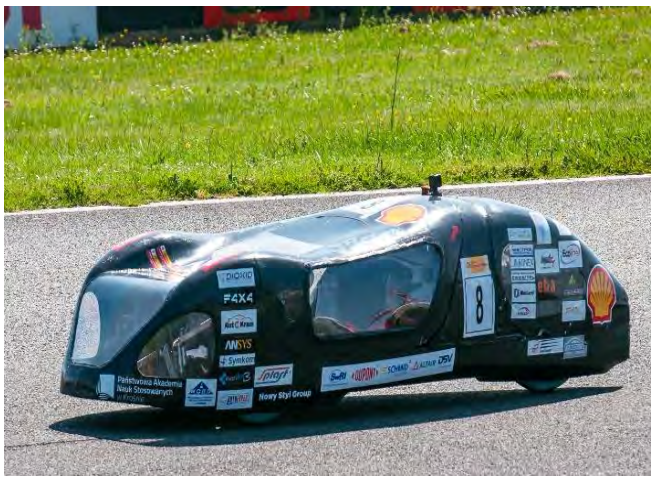

Fig. 1. The vehicle taking part in the Shell Eco-Marathon competition

2. Connecting rod

2.1. Determining the forces acting on the connecting rod

From the theory of the structure of the combustion engine, we know that the forces acting on the connecting rod come from the pressure in the cylinder and the inertia of the parts in translational motion [2]. The effect of the resultant force from the combustion pressure and inertia leads to the development of compressive and bending stresses on the connecting rod (buckling).

I-beam was chosen as the connecting rod cross-section. The cross-sectional markings used are shown in Fig. 2.

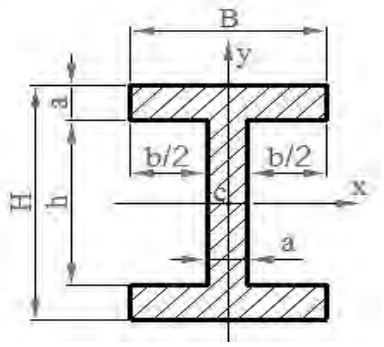

Fig. 2. Markings of the connecting rod head cross-section

The preliminary dimensions of the cross-section, selected to determine the masses and inertia loading the designed connecting rod, are as follows: B = 12 mm, b = 10 mm, H = = 18 mm, h = 14 mm, a = 2 mm. Total mass of the preliminary connecting rod model was 53.5 g, mass of the rotating part 31.3 g and mass of the translational part 22.1 g. Mass of the complete stock piston, i.e. with rings, piston pin and protection devices is 59 g. The values of these masses were then used to determine the value of the inertia force loading the connecting rod.

Figure 3 shows the kinematic diagram of the crank system of the ICE being upgraded.

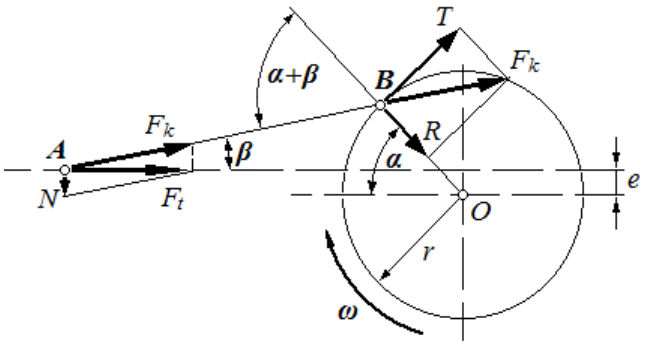

Fig. 3. Diagram of eccentric crank system

According to the simplification used in the study [2], we can present the acceleration in translational motion as equations (1)–(3). This simplification results from the development of an infinite trigonometric series, considering the first and second harmonics.

$$a = r\omega^2[(\cos\alpha + u\sin\alpha) + \lambda\cos 2\alpha] \quad (1)$$

$$u = \frac{e}{l} \quad (2)$$

$$\lambda = \frac{r}{l} \quad (3)$$

where: a – linear acceleration, α – crankshaft rotation angle, ω – angular rotational speed, u – eccentric shift coefficient of the rod length, λ – relative slenderness of the connecting rod.

The calculations of the acceleration were carried out for constant the rotational speed, corresponding to the maximum power of the ICE, i.e. 5000 rpm.

The results of the acceleration value as a function of the crankshaft rotation angle are shown in Fig. 4. The maximum value of positive acceleration is 5939 m/s^2 and the minimum value of negative acceleration is –8591 m/s^2.

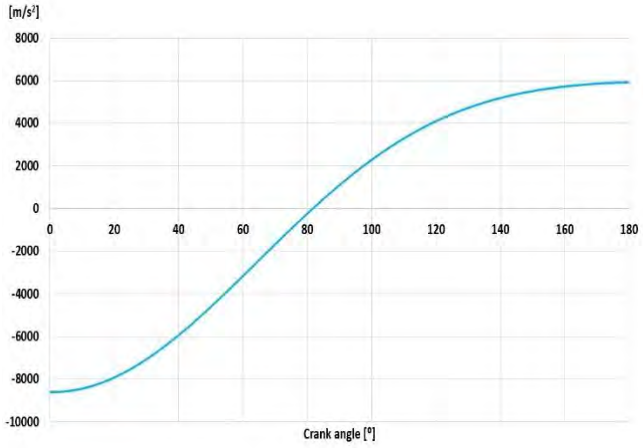

Fig. 4. Acceleration of translational moving parts as a function of the crankshaft angle

The inertia force for the reciprocating motion was determined from equation (4).

$$F_{mr} = \sum_{i=1}^{n} m_i \cdot a \tag{4}$$

where: F_{mr} – inertial force of all parts in sliding motion, m_i – mass of all crank system components in translational motion.

In ICE, the cylinder pressure as a function of the crankshaft rotation angle was determined by simulation using the AVL Boost program. The result in the form of a graph depending on the crankshaft rotation angle during the power stroke is shown in Fig. 5.

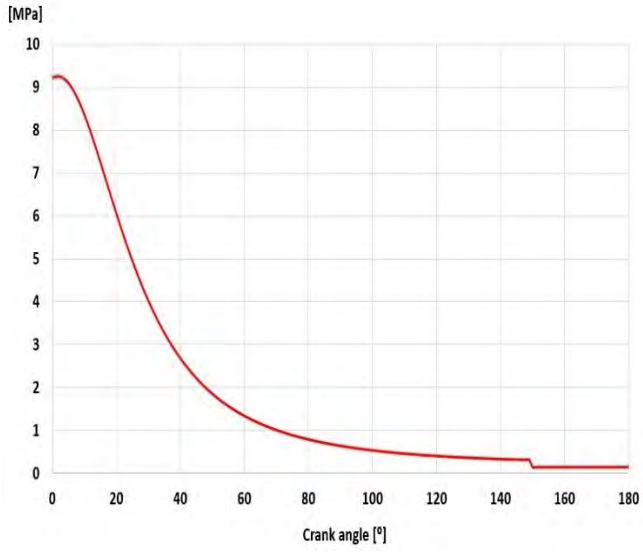

Fig. 5. Pressure in the cylinder during the combustion stroke

As we can observe in the graph above, the maximum pressure in the cylinder is 9.28 MPa and 8 degrees of crankshaft rotation are achieved after TDC.

The pressure force of the gases in the combustion chamber was determined from the equation (5).

$$F_g = p_g \cdot D^2 \cdot \frac{\pi}{4} \tag{5}$$

where: F_g – combustion force, p_g – combustion pressure.

The resultant force loading the connecting rod is determined from eq. (6) and (7), considering the sense of the determined forces.

$$F_t = F_g + F_{mr} \tag{6}$$

$$F_k = F_t \cos\beta \tag{7}$$

$$\cos\beta = \frac{r\cos\alpha - e}{l} \tag{8}$$

where: F_t – total force on the cylinder axis, F_k – total force on the rod axis, β – angle between cylinder and rod axis.

2.2. Numerical calculations of the connecting rod

The forces acting on the connecting rod determined in the previous subsection were used to perform the Finite Element Method (FEM) analysis. The software used to create the 3D model and static and fatigue simulation is SolidWorks

The boundary conditions of the analyzed connecting rod include support on the cylindrical wall of the connecting rod foot bearing, and receiving radial and axial displacement. Additionally, the piston pin axis is connected to a virtual wall, which corresponds to the physical contact of the piston leading part with the cylinder surface. The load was applied to the cylindrical wall of the piston pin sleeve, with a parabolic distribution corresponding to the unit pressures in the plain bearing.

The value of the safety factor was assumed to be 2.5. This means a maximum allowable static stress value of 350 MPa. If the stresses deviated significantly from the assumed level, the dimensions of the connecting rod head section were corrected and the simulation was repeated.

The final dimensions of the connecting rod head cross-section are as follows: B = 11.25 mm, b = 9.45 mm, H = = 13.05 mm, h = 9.45 mm. The cross-section of the connecting rod at its foot has the following dimensions: H = = 26.10 mm, h' = 22.50 mm. The distribution of reduced stresses according to Mises' theory for the performed static analysis is shown in Fig. 6.

Due to the variable loading conditions of the connecting rod, fatigue analysis was also used, in accordance with the guidelines for using FEM software for the calculation of crank system elements contained in [1]. The loading conditions are alternating (tension and compression), and uneven. The value of maximum compressive stresses was determined according to the static stress test. On the other hand, the value of tensile stresses was determined by knowing the maximum value of the inertia force, according to eq. (4).

The assumption of the fatigue tests used for FEM was to conduct a durability analysis for an assumed number of cycles of 100,000. The result is the number of cycles in which the tested item will not suffer damage. As you can see in Fig. 6, the entire connecting rod has a uniform red

color, corresponding to the assumed number of fatigue cycles.

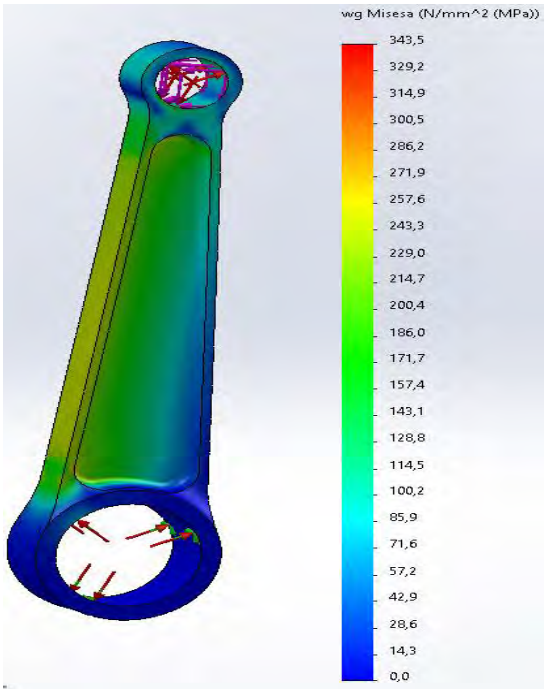

Fig. 6. Result of static analysis: reduced stresses according to Mises' theory

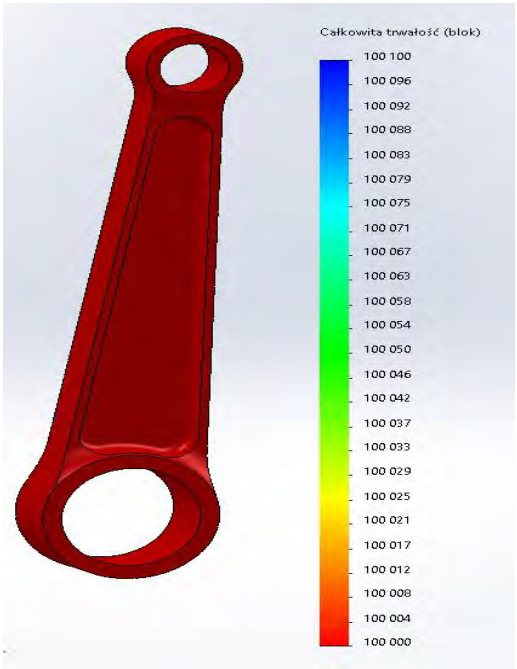

Fig. 7. Result of fatigue analysis

3. Piston

3.1. Determining the forces acting on the piston

The designed piston uses a single sealing ring and a loose pin fit, secured by two spring elements. The initial dimensions and shape of the piston were determined based on criteria given in [3].

The stresses in the piston result from the gas force load and the inertia of the piston itself. The gas force acting on the bottom of the piston is equal to the force given in eq. (5). The inertia force of the piston, similarly to the inertia force loading the connecting rod, is determined from eq. (1) and (4). The difference is the mass of the component parts in eq. (4): in the case of piston load, we only take into account its mass and the piston rings.

In addition to the gas force and inertia, the piston is additionally loaded with stresses resulting from the thermal effect and the force pressing the leading part against the cylinder surface. The force pressing the leading part of the piston against the cylinder surface is determined from the eq. (9).

$$F_n = (F_g + F_{mp})\sin\beta \tag{9}$$

where: F_n – force pressing the piston to cylinder, F_{mp} – inertia force of the piston with rings.

The value of the thermal load resulting from the impact of hot combustion products was determined according to the method included in [8]. From the known value of cylinder pressure (obtained in AVL Boost software), the average value was determined. The perfect gas equation was then used to determine the average duty cycle temperature (assuming no charge loss in the cylinder chamber). Assumptions for the calculations:

1) The medium is in thermodynamic equilibrium at all times. This is necessary so that equal values of the intensive parameters (pressure and temperature) for the entire combustion chamber can be assumed for calculations once the equations of classical thermodynamics are applied.

2) It is thermodynamically in a closed system (closed valves.

The temperature dependence as a function of the angle of rotation of the crankshaft was determined from eq. (10).

$$T_{(\alpha)} = \frac{P_{c(\alpha)}V_{(\alpha)}}{m_c R_C} \tag{10}$$

Due to the nature of the SEM competition, the operating time of the internal combustion engine is relatively short (up to 13 seconds), compared to the interruptions in its operation (more than 3 minutes) during track driving. Figure 8 is a graph of driving speed (green line) and engine speed (red line) during one vehicle start in the competition.

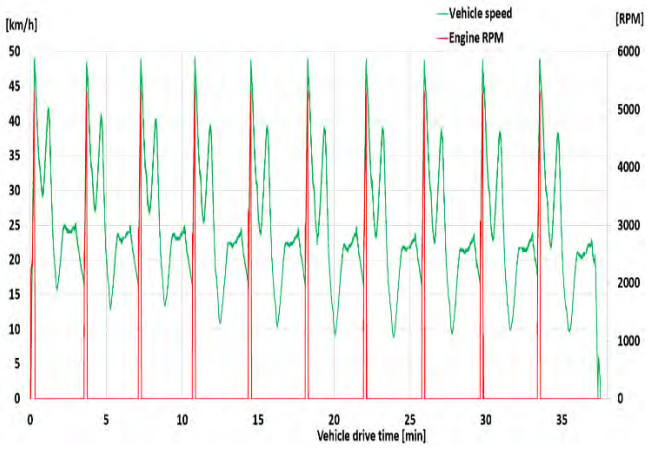

Fig. 8. Engine rotational speed and vehicle speed during one competition start

The effect of such a short engine run time is a low thermal load, due to the very short time for heat to affect the piston bottom. The effect of such a short engine operating time is a low thermal load, due to the very short time for heat to affect the piston bottom. The longest the internal combustion engine runs is during the start of the vehicle for the race. Other engine cycles do not last longer than 10 seconds. Figure 9 shows the engine speed over time, as recorded by the internal combustion engine controller.

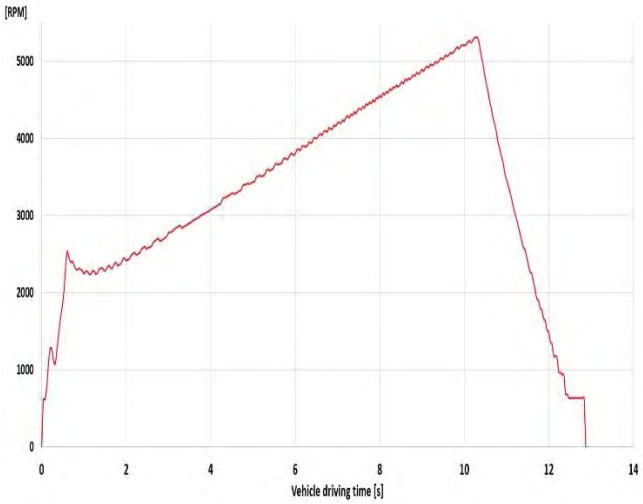

Fig. 9. Rotational speed of ICE as a function of time when starting the vehicle from a standstill

The heat transfer coefficient from the working medium to the piston bottom was determined from Woschni's experimental formula. The amount of heat transferred by radiation was ignored. The time of the transient thermal test was assumed to be the longest time of motor operation, i.e. 13 s. The initial temperature of the piston material was assumed to be 95°C. The engine is heated to this temperature with electric heaters before the start of the competition. The temperature distribution is shown in the following Fig. 10.

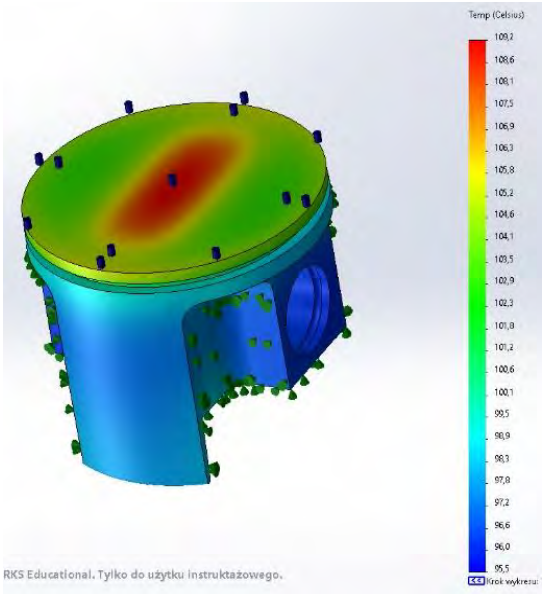

Fig. 10. Temperature distribution on the tested piston

The boundary conditions of the strength-analyzed piston include support on the cylindrical wall of the piston pin bore, accepting radial and axial displacement. In addition, the recesses under the piston pin protections received support from a movable support that receives displacement in the direction of the pin axis. The combustion pressure acts on the piston bottom and the lower surface of the sealing ring groove. The force of inertia of the piston is applied at the point of its center of mass.

The results of the FEM obtained in SolidWorks software are shown in Fig. 11.

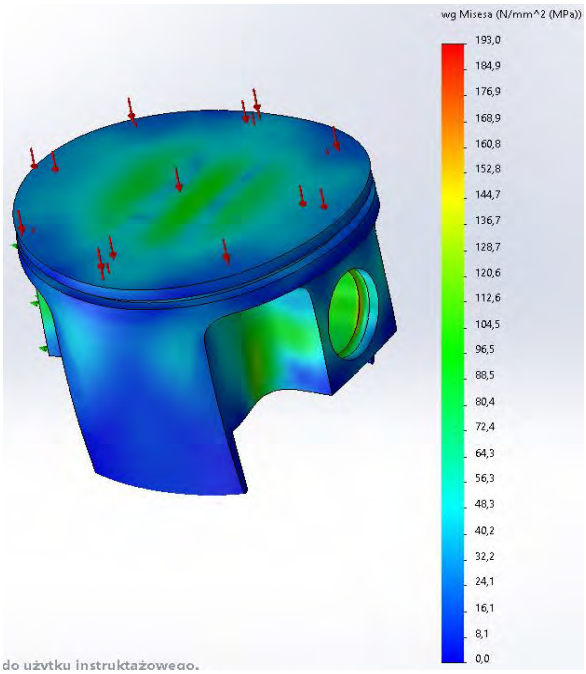

Fig. 11. Reduced stresses according to Mises theory

The criteria for evaluating the results of FEM simulations are the maximum values of reduced stresses and deformations of the piston face. The value of permissible reduced stresses was determined similarly to that for the connecting rod, with a safety factor of 2.5. In accordance with the recommendations of [3], a change of 0.006 mm in the diameter dimension was considered as a limit value, regardless of whether the diameter of the leading part increased or decreased. Such restrictive values of permissible displacements of the piston leading part force the use of thicker piston walls, which in turn leads to relatively small reduced stresses compared to the permissible ones.

4. Determination of inertia force

The value of the inertia forces depends on the magnitude of the accelerations acting on the engine components moving along the cylinder axis and on the mass of these parts. The eq. (1)–(3) determines the dependence of acceleration on the instantaneous angular position of the crankshaft. Table 3 is a summary of the masses values of individual elements of the crank system for the factory and modified versions.

Equation 4 was used to determine the value of the inertia force as a function of the crankshaft rotation angle, both for the standard and modified engines.

Table 3. Mass data of piston and rod

Parameter	Unit	Stock	Modified
Piston, rings, and pin rings	g	59	48
Rotating part of the connecting rod	g	93	36
Sliding part of the connecting rod	g	47	18

Figure 12 shows the dependence of the inertia forces of the original and modified crank system. These values were determined for a rotational speed of 5000 rpm.

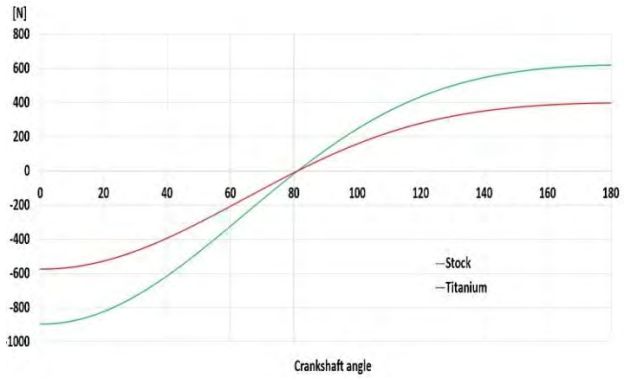

Fig. 12. Force of inertia of engine parts in reciprocating motion

5. Conclusions

The use of an innovative construction material in the form of titanium alloy Ti6Al4V allows to reduce the masses of the crank system components. A particularly noticeable difference concerns the connecting rod, for which the total mass reduction is around 53% from stock value. Such a large difference in mass is the result of twice the density of the titanium alloy compared to the construction material of the factory element. Greater strength allows for reduced dimensions required by permissible stresses. In addition, the technology of making the connecting rod outline (removal machining) allows the design of a cross-section that allows the transfer of greater bending stresses while minimizing the weight. Obtaining small wall thicknesses with a large moment of inertia of the cross-section is an example of considering the properties of available manufacturing methods at the design stage.

In the case of the piston, the mass reduction is not so significant because the factory component is made of an aluminum alloy, a material with a lower density than the titanium alloy used. Moreover, during the FEM analysis, the criterion of permissible displacements was used, which results in low structural effort and, as a result, weight reduction. Reducing the mass of the piston is 22% of the original piston weight.

The largest difference in the negative inertia force is 322 N, which is a 35.8% change from the factory engine's inertia force value. The largest difference in positive inertia force is 222 N. This is also a 35.8% change from the factory engine's inertia force value. This is a significant reduction in the value of the force of inertia in progressive-return motion. At the same time, it should be noted that reducing the mass of the rotating part of the connecting rod will also reduce the moment of inertia of the entire crank system. In addition, a reduction in the masses of parts in forward and rotary motion, required a reduction in the masses of the crankshaft counterweights. As a result, the total reduction in the inertia of the entire crankshaft system (including the crankshaft after the reduction of the counterweights) will be greater than would result from differences in the masses of the modified parts alone.

Nomenclature

FEM finited element method
ICE internal combusion engine
SEM Shell Eco-Marathon
TDC top dead center

Bibliography

[1] Ajayi OK, Malomo BO, Paul SD, Babalola SA, Adeleye AA. Failure modeling for titanium alloy used in special purpose connecting rods. Mater Today-Proc. 2021;45(6):4390-4397. https://doi.org/10.1016/j.matpr.2020.11.852
[2] Jędrzejowski J Mechanika układów korbowych silników samochodowych (in Polish). WKiŁ. Warszawa 1972.
[3] Kozaczewski W. Konstrukcja złożeń tłok-cylinder silników spalinowych (in Polish). WKiŁ. Warszawa 1987.
[4] Magryta P, Pietrykowski K, Majczak A. Optimizing the geometry of the connecting rod in opposite pistons engine. Combustion Engines. 2017;168(1):191-196. https://doi.org/10.19206/CE-2017-131
[5] Shanmugasundar G, Dharanidharan M, Vishwa D, Sanjeev Kumar A. Design, analysis and topology optimization of connecting rod. Mater Today-Proc. 2021;46(9):3430-3438. https://doi.org/10.1016/j.matpr.2020.11.778
[6] Silva FS. Fatigue on engine pistons – a compendium of case studies. Eng Fail Anal. 2006;13(3);480-492. https://doi.org/10.1016/j.engfailanal.2004.12.023
[7] Singh U, Lingwal J, Rathore A, Sharma S, Kaushik V. Comparative analysis of different materials for piston and justification by simulation. Mater Today-Proc. 2020;25(4):925-930. https://doi.org/10.1016/j.matpr.2020.03.078
[8] Wiśniewski S. Obciążenia cieplne silników tłokowych (in Polish). WKiŁ. Warszawa 1972.
[9] Witek L, Zelek P. Stress and failure analysis of the connecting rod of diesel engine. Eng Fail Anal. 2019;97:374-382. https://doi.org/10.1016/j.engfailanal.2019.01.004

Tomasz Kosztyła, DSc., DEng. – Faculty of State University of Applied Sciences in Krosno, Poland.
e-mail: *tomasz.kosztyla@pans.krosno.pl*

Article citation info:
Laskowski P, Zimakowska-Laskowska M, Matej J, Wiśniowski P. The problem of cold start emissions from vehicles. Combustion Engines. 2024;199(4):43-51. https://doi.org/10.19206/CE-186471

Piotr LASKOWSKI
Magdalena ZIMAKOWSKA-LASKOWSKA
Jan MATEJ
Piotr WIŚNIOWSKI

Combustion Engines
Polish Scientific Society of Combustion Engines

The problem of cold start emissions from vehicles

ARTICLE INFO

Received: 30 November 2023
Revised: 29 February 2024
Accepted: 25 March 2024
Available online: 7 June 2024

The progression of passenger vehicles is progressing, and regulations are continually being revised, resulting in a decrease in car exhaust emissions. The European Commission has revised the RDE test procedure to include exhaust emissions during a cold start as part of package 3. The article carried out simulations using COPERT software, which uses tests based on WLTP, assuming ambient temperatures from –10°C to +20°C, at intervals of 5°C. This paper aims to present the results of mathematically modelling the influence of ambient temperature on the cold start emissions of carbon dioxide (CO_2), nitrous oxide (N_2O), methane (CH_4), nitrogen oxides (NO_x), non–methane volatile organic compounds (NMVOC), hydrocarbons (treated as volatile organic compounds – VOC), total particulate matter (TSP) and particle number (PN) in passenger cars and light duty vehicles. The modelling results show that a change in ambient temperature significantly affects carbon dioxide (CO_2), nitrous oxide (N_2O), methane (CH_4), nitrogen oxides (NO_x), non-methane volatile organic compounds (NMVOC), hydrocarbons (treated as volatile organic compounds – VOC), total particulate matter (TSP) and particle number (PN) in cold start emissions.

Key words: *cold start emission, vehicle, COPERT, pollutant, GHG*

1. Introduction

Cold start emissions have received much attention due to their adverse impact on air quality and public health. Cold start emissions are the emissions a vehicle produces when it is started again after being left idle for a while [2]. When an engine is first started up, it typically runs inefficiently, leading to an increase in the emission of pollutants, including carbon monoxide, nitrogen oxides, and volatile organic compounds. This is known as the cold start problem [2]. The phrase "cold start emissions" refers to the pollution released when a vehicle is first started up after being inactive for an extended length of time, generally overnight or after a number of hours of not being used. Emissions from vehicles that have recently started up tend to be higher than those coming from cars that have been running for a while. The main cause of this is the engine and its parts not having reached the ideal working temperature yet. The fuel mixture, combustion efficiency, and emission control systems may not be operating at their best, causing more pollutants to be released into the atmosphere [2, 9]. The release of these substances into the air can lead to a high level of air contamination and can have a damaging impact on both the health of people and the environment [1]. The release of these substances can create smog and tiny particles, which can result in illnesses related to the lungs and heart, in addition to contributing to global warming [1, 15]. It is essential to take action to solve the issue of cold start emissions in order to reduce the amount of emissions from vehicles and enhance air quality.

The European Union Commission Regulation 2017/1154 [20] defines cold start as the initial start of the combustion engine until the engine has been running for a total of 5 minutes. Once the coolant temperature is determined, the cold start period will finish when the coolant reaches 343 K (70°C) for the first time or after the engine has been running for a total of five minutes from the time the engine was first started [9].

Research has indicated that the emissions from vehicles used on roads are a major contributor to air contamination and can have a detrimental effect on air quality and people's wellbeing, especially in metropolitan regions. The European Union is taking steps to lower air pollution and reach a state of climate neutrality, resulting in new, more stringent laws and regulations on vehicle exhaust. In order to comply with these regulations, more advanced exhaust gas aftertreatment systems are required. Research has been conducted in recent years about emissions from cold start operations, illustrating the global significance of this issue [12–14, 16, 22]. Additionally [7, 10, 11, 14], NO_x emissions from vehicles with gasoline engines should be considered in future updates to EU regulations [7].

In 2016 [8, 9], the European Union implemented the first two sets of actual driving emissions (RDE) tests – Regulations 2016/427 and 2016/646 – the world's first type-approved road tests for light duty vehicles. As of September 2017, the tests have binding emission limitations and use portable emission measurement systems (PEMS) to measure contaminants. The European Commission has begun creating two additional RDE programs, which focus on cold start emissions, testing for hybrid vehicles, the measurement of particulate emission numbers (PN) on the road, and the regular adjustment of aftertreatment systems. This is due to a cold start that has a significant impact on emissions, especially in urban areas with frequent short journeys and air quality problems [1, 9].

The latest analysis of [1] shows that the average daily distance travelled by passenger cars is not sufficient for the vehicle's pollution control system to warm up and become fully functional. The resulting high levels of NO_x emissions during cold-starts from both petrol and diesel engines may pose an additional challenge to urban air quality initiatives.

At normal temperatures, the amount of emissions released during a cold engine start-up is much greater than when the engine is already warm. In addition, exhaust aftertreatment devices are not effective in reducing emissions due to the catalyst failing to reach a temperature necessary for activation [9].

Diesel engines are commonly employed in the automotive and energy sectors. In order to meet the more demanding automotive exhaust emission regulations, newer and more advanced engine technologies have been created. Adhering to the current standards can be achieved by decreasing the emissions produced during combustion and/or improving the efficiency of exhaust aftertreatment systems [9].

The European Commission (EC) [8, 21] is aiming to lower nitrogen oxide (NO_x) emissions from diesel automobiles through the incorporation of cold start emissions into the Real Driving Emissions (RDE) testing process. The European Commission (EC) implemented particular regulations concerning cold-starts as part of the third Real Driving Emissions (RDE) legislative package due to the fact that selective catalytic reduction (SCR) and lean NO_x scavenger aftertreatment systems can cause heightened NO_x emissions during cold-start.

While conducting literature research, the authors paid attention to the ambient temperature and its impact on cold start emissions. Authors in articles [13, 22, 23] examined the effect that various ambient temperatures (–7°C and 23°C) had on the emission results of vehicles that were equipped with both compression and spark ignition engines. The purpose of the tests was to investigate whether the exhaust emissions during WLTC (Worldwide Harmonized Light Duty Vehicles Test Cycle) tests increase in colder temperatures in comparison to warmer temperatures [3–7, 13] and to check for compliance with Euro 6 emission standards.. Research shows that ambient temperature has a significant impact on cold start emissions.

The literature analysis shows that the problem of cold start emissions is important, and numerous studies confirm this. However, more information on cold start emissions in a wide temperature range is a significant issue. The novelty of this article lies in the detailed analysis of the impact of ambient temperature on cold start emissions for various pollutants emitted by vehicles. The study conducted by the authors using COPERT software to simulate different temperature scenarios and their effect on emissions is a novel approach to understanding the dynamics of cold start emissions. By highlighting the significant reduction in emissions as temperatures increase, the research provides valuable insights into potential strategies to reduce emissions and improve air quality in urban areas. This innovative use of simulation technology and data analysis adds to the knowledge of cold start emissions and provides a basis for further research.

2. Methodology

Vehicles that do not reach their optimal operating temperature tend to produce higher levels of air pollution [2].

For a given pollutant, engine speed, and initial engine temperature, the vehicle's emissions and development over time can be broken down into two stages: the first stage where emissions diminish due to a gradual rise in either the engine or catalyst temperature, and then a stability phase when the engine reaches a regular temperature (Fig. 1). The initial phase is aligned with time t_{cold} [2].

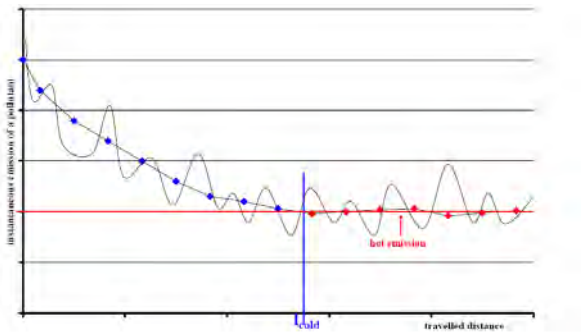

Fig. 1. The change in the amount of exhaust emitted by a vehicle as it travels distances in real-world settings [2]

The amount of pollution produced in excess when travelling a certain distance at a lower temperature than normal operating conditions is referred to as an excess cold emission. The same engine speed and average driving speed can be used to calculate how far a car has gone when driving in cold temperatures (as seen in Fig. 1) [2]. In a driving cycle involving various engines and vehicles in urban areas, the instantaneous emission output becomes much more intricate and irregular. The operating phases and the temperature rise can both affect the fluctuation in motor rotation frequency; this is illustrated in Fig. 1, where the fluctuation is much more rapid when the temperature goes up than it would be in reality. The difference in emissions from a vehicle when the engine is cold compared to when it is running hot is referred to as the total cold emissions of the vehicle and driving cycle. The amount of emission produced is dependent on the temperature surrounding it, which deviates from the standard temperature for operation. The understanding of this idea is dependent on the speed of the cycle of accelerations and decelerations being much quicker than the temperature increase of the vehicle. Once the driving cycle is continued for a sufficient period of time, a constant distance must be maintained so that all excess cold emissions are accounted for as heat emissions on the vehicle's interior. Excess emissions depend on the driving cycle and pollutants [2].

The authors used COPERT software for this article, as it is accepted for creating emissions inventories in European nations. This program makes use of the "Tier 3" methodology, which computes the complete exhaust emissions by separating between emissions released during the thermal engine operation ("cold start emissions") and those emitted when the engine reaches its regular operating temperature ("hot emissions"). The equation for the 'Tier 3' methodology is provided [15].

$$E_{Total} = E_{Hot} + E_{Cold} \quad (1)$$

where: E_{Total} – total emissions [g] of any pollutant for the spatial and temporal resolution of the application, E_{Hot} – emissions [g] during stabilized (hot) engine operation, E_{Cold} – emissions [g] during transient thermal engine operation (cold-start) [15].

When a vehicle is first turned on, its emissions are higher than when the engine is at its normal operating temperature. This is referred to as cold start emissions and is expressed as grams of pollutants per vehicle start. These emissions can be compared to the hot emissions released when the engine is running normally. The distance travelled before reaching stabilized emissions is known as l_{trip} [15].

To measure cold start emissions in a laboratory, a chassis dynamometer must be used together with a driving cycle that is lengthy enough to reach balance in the engine's operating conditions. This driving cycle should imitate the expected conditions of the vehicle's engine when it is being operated. Evaluating the correlation between the initial pollution and the chosen parameter (like the speed of the vehicle) through the driving cycle should maintain the same driving style during both the cold and hot times. It is commonly assumed that the majority of cold start emissions originate from urban driving, with rural driving as the second largest contributor. This is due to the fact that highway conditions are not usually the starting point for many trips [15].

$$E_{Total} = E_{Urban} + E_{Rural} + E_{Highway} \quad (2)$$

where E_{Ubran}, E_{Rural}, and $E_{Highway}$ are the total emissions [g] of any pollutant for the respective driving situations.

The ambient temperature can have a major effect on the amount of air pollutants released from both spark ignition and compression ignition engine vehicles. Research has suggested that there could be a link between the temperature of the environment and the amount of emissions given off during a cold-start. At present, the only emissions that are regulated during a vehicle's initial start-up are carbon monoxide, hydrocarbons, nitrogen oxides, and total particulate matter. For this reason, it is essential to review the current EU winter vehicle emissions regulations. Total emissions are calculated by combining the activity data and the emission factors for each vehicle [15]. The amount of emissions released can differ depending on the driving and weather conditions. Emissions produced during a cold start can be estimated by subtracting the amount of emissions that would be released if all vehicles ran with hot engines and active catalysts. This is done using a specific formula [17]:

$$E_{Cold,i,k} = \beta_{i,k} \cdot N_k \cdot M_k \cdot e_{hot,i,k} \cdot \left(\frac{e_{cold}}{e_{hot}}\right|_{i,k} - 1) \quad (3)$$

where $E_{Cold,i,k}$ – cold start emissions of pollutant i (for the reference year), produced by vehicles of the technology k, $\beta_{i,k}$ – fraction of the mileage driven with a cold engine (or the catalyst operated below the light-off temperature) for pollutant i and vehicles of the technology k, N_k – number of vehicles [veh] of the technology k in circulation; M_k – total mileage per vehicle [km/veh] in vehicles of the technology k, $e_{hot,i,k}$ – hot emission factor for pollutant i and vehicles of the technology k, $\left.\frac{e_{cold}}{e_{hot}}\right|_{i,k}$ – cold/hot emission quotient for pollutant i and vehicles of the technology k.

The β parameter is affected by the temperature of the environment, the way the vehicle is used, and the average distance travelled before emission levels stabilize (l_{trip}). The methodology followed the guidelines set out by the 2006 IPCC Guidelines for National Greenhouse Gas Inventories and EMEP/EEA air pollutant emission inventory guidebook 2019 [17] which serve as basic guidelines for inventories of greenhouse gases and air pollutants [15] indicate that l_{trip} is usually increased [15]. In accordance with the above guidelines, l_{trip} was adopted for passenger cars – 12 km and for light duty vehicles – 12 km.

The introduction of stricter emissions standards for catalyst petrol vehicles has shortened the amount of time needed for the catalyst to reach light-off temperature. As a result, the mileage driven under cold start conditions is lower. The β-parameter is also affected by the degree of emission control legislation for petrol catalyst vehicles [17].

The quantity of emissions released in cold or hot conditions is known as the e^{COLD}/e^{HOT} ratio and is impacted by the surrounding temperature and the type of pollutant being examined. While the model used in the original version of this methodology is still applied to the calculation of emissions during cold-starts, more current ratios were included in the last revision of this chapter for cars with catalytic converters [17].

Cold start emissions are usually only connected to urban driving, but a percentage can be ascribed to rural driving when the mileage driven with an engine that is not at the optimal temperature (β-parameter) is greater than the mileage driven in urban areas (S_{URBAN}). This means that equation (4) needs to be modified, which produces the following result [17]:

If $\beta_{i,k} > S_{URBAN}$

$$E_{COLD\ URBAN;i,k} = S_{URBAN;\,k} \cdot N_k \cdot M_k \cdot e_{HOT\ URBAN;\,i,k} \cdot \left(\frac{e_{cold}}{e_{hot}}\right|_{i,k} - 1) \quad (4)$$

It is thought that the mileage driven in urban areas is equivalent to warming up the engine, while any additional emissions are a result of driving in rural areas. Equation (4) is an extreme example for a national inventory, and only happens when a tiny amount is given as l_{trip}. It is also noteworthy that the urban hot emission factor is used for both variations of eq. (4). The overall emissions of N_2O and CH_4 should not be distinguished based on where they were released. The determination of these emissions is based on four types of driving conditions: 'cold urban', 'hot urban', 'rural', and 'highway'. This algorithm outlines the process for determining the emission of pollutants, particularly methane (CH_4). It is especially important to estimate CH_4 emissions because NMVOCs are calculated by taking the difference between VOCs and CH_4. To begin, it is necessary to determine if the portion of the mileage driven under non-stabilized engine temperature (represented by the β parameter) is greater than the portion of the mileage attributed to urban conditions (S_{URBAN}). For each vehicle type (j) and pollutant (i, either CH_4, N_2O), this calculation is expressed in the following way [17]:

if $\beta_{i,k} > S_{URBAN;k}$

$$E_{COLD\ URBAN;i,k} = \beta_{i,k} \cdot N_k \cdot M_k \cdot e_{HOT\ URBAN;i,k} \quad (5)$$

where: $S_{URBAN;k}$ – mileage share attributed to urban conditions for vehicle technology k, $S_{RURAL;k}$ – mileage share attributed to rural conditions for vehicle technology k, $S_{HIGHWAY;k}$ – mileage share attributed to highway conditions

for vehicle technology k, $e_{COLD\ URBAN;i,k}$ – urban cold start emission factor for pollutant i, by vehicle technology k, $e_{HOT\ URBAN;i,k}$ – urban hot emission factor for pollutant i, by vehicle technology k, $e_{HOT\ RURAL;i,k}$ – rural hot emission factor for pollutant *i*, by vehicle technology k, $e_{HOT\ HIGHWAY;i,k}$ – highway hot emission factor for pollutant *i*, by vehicle technology k.

It is important to note that all of the emissions values found in the COPERT model have been obtained through laboratory testing that follows the WLTP driving cycle [15]. In this paper, the authors investigated the impact of changes in ambient temperature on the cold start emissions carbon dioxide (CO_2), nitrous oxide (N_2O), methane (CH_4), nitrogen oxides (NO_x), non-methane volatile organic compounds (NMVOC), hydrocarbons (treated as volatile organic compounds – VOC), total particulate matter (TSP) and particle number (PN) in passenger cars and light duty vehicles.

The authors analyzed the average monthly temperatures in Poland in the years 2015–2021. The maximum and minimum average temperatures were adopted for the analysis and are presented in Table 1.

Table 1. Average monthly temperatures in Poland in 2015–2021

	2015	2016	2017	2018	2019	2020	2021
Average minimum temperature							
Jan.	–1.3	–5.9	–7.6	–2	–8.5	–2.3	–7.9
Feb.	–2.4	1.4	–2.2	–6.4	–6.4	–4.5	–5.2
Mar.	1.3	1.9	3.6	–2	–4.7	–4.5	–4.3
Apr.	5.1	6.7	4.6	9.5	–1.5	0.9	–3.8
May	9.9	10.8	11.1	13.4	1.9	1.6	1.3
Jun.	14	15.4	15.6	14.6	6.4	7.8	10.6
Jul.	16.9	16	12.7	16.2	8.3	9	10.4
Aug.	18.2	14.5	16.9	17.3	8.7	11.3	7.7
Sep.	12.3	12.9	10.8	12.3	5.2	7.8	7
Oct.	2.8	4.8	6.8	8	1.7	2.1	2.1
Nov.	3.7	1.3	1.2	2.4	–3	1	–1.3
Dec.	1.8	–2.5	–1.2	–1.8	–5	–3.2	–6
Average maximum temperature							
Jan.	2.9	–0.3	0.1	3.3	1	4.6	0.7
Feb.	2.1	4.9	1.9	–1.7	4	5.8	0.2
Mar.	6	5.2	7.6	1.9	6.3	5.8	4.8
Apr.	9.4	9.9	8.6	14.3	10.9	10.7	7
May	13.9	16	15	18.3	14.9	12.4	12.9
Jun.	18	19.5	19.3	19.7	22.8	19.3	20.7
Jul.	21.3	20.3	19.9	21.4	20.9	19.3	22.3
Aug.	23.2	19	20.3	22	20.9	21.1	18.1
Sep.	15.8	17.7	14.6	16.7	14.6	16.1	15.8
Oct.	9.2	9.1	11.5	11.5	11.2	11.7	10.6
Nov.	7.1	4.9	6.2	6.1	6	7.9	6.9
Dec.	6.7	3.9	3.6	3.9	3.6	3.3	1.2

Based on the temperature values in Table 1, the authors decided that simulations are performed assuming ambient temperatures from –10°C to +20°C with 5°C intervals.

Simulations were carried out by using the COPERT software, assuming that vehicles from each type of passenger cars travelled 10,000 km in each vehicle's category: passenger cars (PC) and light duty vehicles (LDV).

The authors checked how the external temperature affects cold start emissions from PC and LDV, but there was no division into Euro standards and fuel type. The result of the simulations is the sum of emissions caused by passenger cars of all classes (Mini, Small, Medium, Large) and for all types of fuels (petrol, diesel, LPG and CNG) and Euro categories (Pre-Euro-Euro 6) and by light duty vehicles also of all classes (N1-I, N1-II and N1-III) and for all types of fuels (petrol, diesel) and Euro categories (Conventional-Euro 6).

According to the above information, simulations were carried out for one vehicle that travelled 10,000 km.

In addition, a study was carried out to show the change in total emissions depending on the ambient temperature in urban areas where cold start emissions have the greatest impact.

3. Results

Figures 2–9 show the influence of ambient temperature on cold start emissions in all driving conditions (urban, rural, highway). Dependence is present for passenger cars and light duty vehicles. In Tables 2–9, pollutant emissions in urban areas in the cold and hot phases are shown.

The methane emission dependence for the cold start phase presented in Fig. 2 clearly shows that the emission decreases with increasing temperature. The difference between –10°C and +20°C is 74% for passenger cars and 64% for light duty vehicles. For methane, cold start emissions from passenger cars are approximately 30% higher than for light duty vehicles.

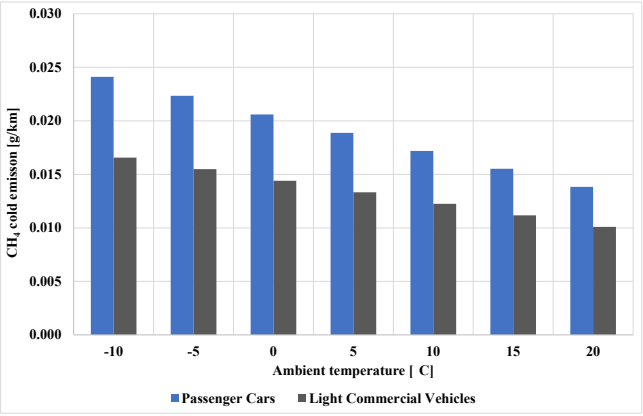

Fig. 2. The dependence of methane (CH_4) emissions from cold start on the ambient temperature

Table 2 shows the impact of temperature on emissions in the cold and hot phases in urban areas. It is clearly visible that in the city emissions in the cold start phase are much higher than in the hot phase. At temperatures –10°C and –5°C, the emission from the hot phase is equal to or close to 0. The differences in CH_4 emissions for other temperatures between the phases are up to 41 times.

The carbon dioxide emission dependence for the cold start phase presented in Fig. 3 clearly shows that the emission decreases with increasing temperature.

The difference between –10°C and +20°C is 226% for passenger cars and 238% for light duty vehicles. For carbon dioxide, cold start emissions from passenger cars are approximately 40% smaller than for light duty vehicles.

Table 2. Change of methane (CH_4) emissions in the cold start and hot phases depending on the ambient temperature

Temperature [°C]	PC CH_4 emission [g/km]		LDV CH_4 emission [g/km]	
	cold	hot	cold	hot
–10	0.024	0.000	0.017	0.000
–5	0.022	0.001	0.015	0.000
0	0.021	0.001	0.014	0.000
5	0.019	0.002	0.013	0.001
10	0.017	0.002	0.012	0.001
15	0.016	0.003	0.011	0.001
20	0.014	0.004	0.010	0.002
15	0.012	0.004	0.009	0.002
20	0.019	0.002	0.013	0.001

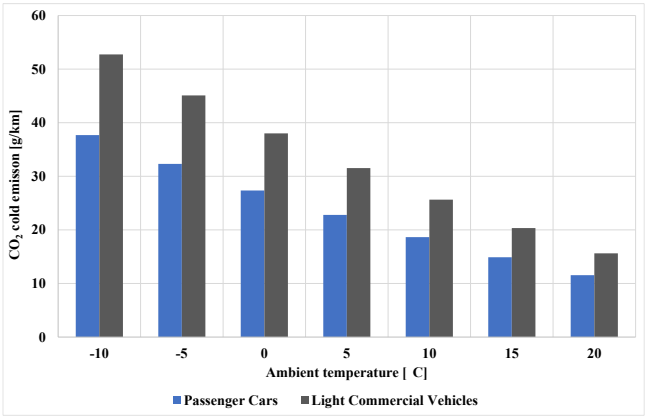

Fig. 3. The dependence of carbon dioxide (CO_2) emissions from cold start on the ambient temperature

Table 3 shows the impact of temperature on emissions in the cold and hot phases in urban areas. It is unmistakable that emanations within the cold start are much higher within the city than within the hot phase. At –10°C and 0°C, the emanation from the hot stage breaks even with or near light duty vehicles. The differences in carbon dioxide outflows for other temperatures between the stages are substantial.

Table 3. Change of carbon dioxide (CO_2) emissions in the cold start and hot phases depending on the ambient temperature

Temperature [°C]	PC CO_2 emission [g/km]		LDV CO_2 emission [g/km]	
	cold	hot	cold	hot
–10	37.380	0.000	49.625	0.000
–5	32.315	0.001	45.081	0.000
0	27.349	0.001	38.012	0.000
5	22.790	0.002	31.532	0.001
10	18.638	0.002	25.641	0.001
15	14.892	0.003	20.337	0.001
20	11.552	0.004	15.621	0.002
15	8.619	0.004	11.494	0.002
20	22.752	0.002	31.489	0.001

The nitrous oxide emission dependence for the cold start phase presented in Fig. 5 clearly shows that the emission decreases with increasing temperature.

The difference between –10°C and +20°C is 64% for passenger cars and light duty vehicles.

Table 4 shows the impact of temperature on emissions in urban areas' cold and hot phases. The emissions in the city are much higher in the cold start phase than in the hot phase. At –10°C and –5°C, hot phase emissions are at or near zero. The difference in nitrogen oxide emissions at other temperatures between phases can be up to 4 times, especially for passenger cars and 121 times for light duty vehicles at –5°C.

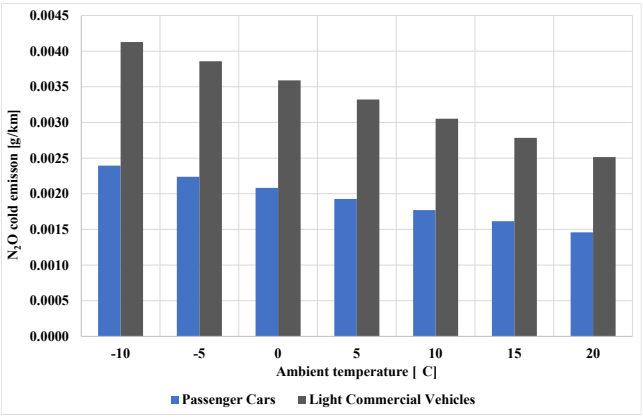

Fig. 4. The dependence of nitrous oxide (N_2O) emissions from cold start on the ambient temperature

Table 4. Change of nitrous oxide (N_2O) emissions in the cold start and hot phases depending on the ambient temperature

Temperature [°C]	PC N_2O emission [g/km]		LDV N_2O emission [g/km]	
	cold	hot	cold	hot
–10	0.002	0.000	0.004	0.000
–5	0.002	0.001	0.004	0.000
0	0.002	0.001	0.004	0.000
5	0.002	0.002	0.003	0.001
10	0.002	0.002	0.003	0.001
15	0.002	0.003	0.003	0.001
20	0.001	0.004	0.003	0.002
15	0.001	0.004	0.002	0.002
20	0.002	0.002	0.003	0.001

The non-methane volatile organic compounds emission dependence for the cold start phase presented in Fig. 5 clearly shows that the emission decreases with increasing temperature.

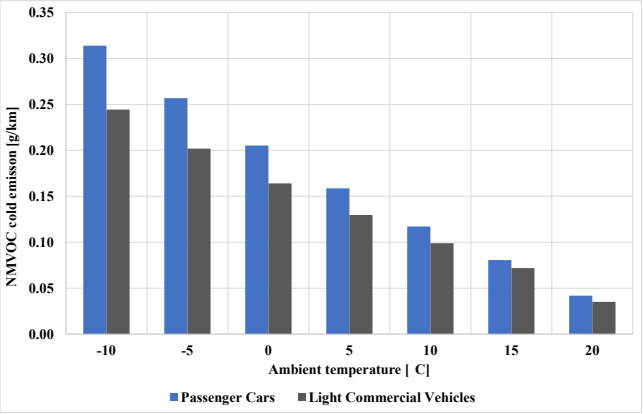

Fig. 5. The dependence of non-methane volatile organic compounds (NMVOC) emissions from cold start on the ambient temperature

The difference between –10°C and +20°C is 650% for passenger cars and 596% for light duty vehicles.

Table 5 shows the impact of temperature on emissions in the cold and hot phases in urban areas. Emissions in the city are significantly higher during the cold start than during the hot phase. The emission from the hot phase is equal to or nearly equal to zero for temperatures between –10°C

and 0°C. At –5°C, there are variations in non-methane volatile organic compound emissions for passenger cars up to 17 times and light duty vehicles up to 486 times between the phases.

Table 5. Change of non-methane volatile organic compounds (NMVOC) emissions in the cold start and hot phases depending on the ambient temperature

Temperature [°C]	PC NMVOC emission [g/km]		LDV NMVOC emission [g/km]	
	cold	hot	cold	hot
–10	0.312	0.000	0.233	0.000
–5	0.257	0.001	0.202	0.000
0	0.205	0.001	0.164	0.000
5	0.159	0.002	0.130	0.001
10	0.117	0.002	0.099	0.001
15	0.081	0.003	0.072	0.001
20	0.042	0.004	0.035	0.002
15	0.014	0.004	0.011	0.002
20	0.158	0.002	0.129	0.001

The nitrogen oxides emission dependence for the cold start phase presented in Fig. 6 clearly shows that the emission decreases with increasing temperature.

The difference between –10°C and +20°C is 195% for passenger cars and 319% for light duty vehicles.

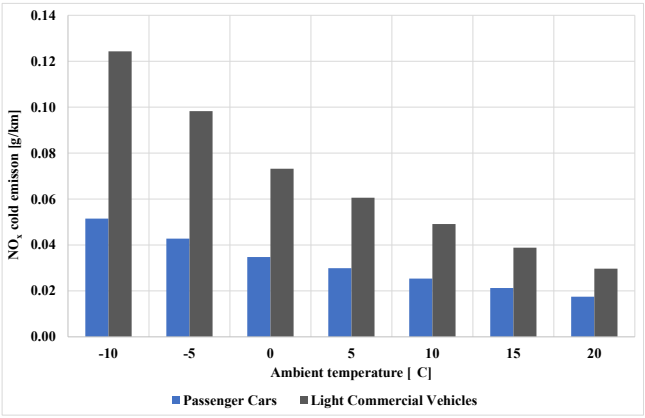

Fig. 6. The dependence of nitrogen oxides (NO_x) emissions from cold start on the ambient temperature

Table 6. Change of nitrogen oxides (NO_x) emissions in the cold start and hot phases depending on the ambient temperature

Temperature [°C]	PC NO_x emission [g/km]		LDV NO_x emission [g/km]	
	cold	hot	cold	hot
–10	0.051	0.000	0.120	0.000
–5	0.043	0.001	0.098	0.000
0	0.035	0.001	0.073	0.000
5	0.030	0.002	0.061	0.001
10	0.025	0.002	0.049	0.001
15	0.021	0.003	0.039	0.001
20	0.017	0.004	0.030	0.002
15	0.015	0.004	0.024	0.002
20	0.030	0.002	0.062	0.001

Table 6 shows the impact of temperature on emissions in the cold and hot phases in urban areas. The contrast between emissions during cold and warm phases in urban areas is evident. In temperatures of –10°C and –5°C, emissions during warm starts hover around zero or are negligible. The disparity in nitrogen oxide emissions between the two phases varies significantly across different temperatures, reaching up to 42 times for passenger cars and 480 times for light duty vehicles at –5°C.

The particulate matter emission dependence for the cold start phase presented in Fig. 7 clearly shows that the emission decreases with increasing temperature.

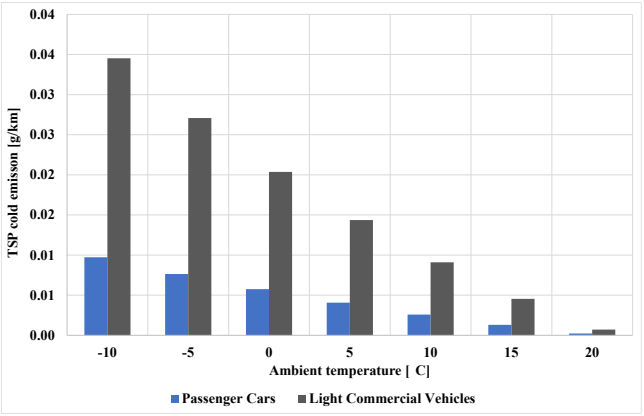

Fig. 7. The dependence of total particulate matter (TSP) emissions from cold start on the ambient temperature

Table 7 shows the impact of temperature on emissions in the cold and hot phases in urban areas. It is clearly visible that in the city emissions in the cold start phase are much higher than in the hot phase. At temperatures –10°C and –5°C, the emission from the hot phase is equal to or close to 0. The differences in particulate matter emissions for other temperatures between the phases are up to 42 times for passengers' cars and more than 480 times for light duty vehicles at –5°C.

Table 7. Change of total particulate matter (TSP) emissions in the cold start and hot phases depending on the ambient temperature

Temperature [°C]	PC TSP emission [g/km]		LDV TSP emission [g/km]	
	cold	hot	cold	hot
–10	0.010	0.000	0.032	0.000
–5	0.008	0.001	0.027	0.000
0	0.006	0.001	0.020	0.000
5	0.004	0.002	0.014	0.001
10	0.003	0.002	0.009	0.001
15	0.001	0.003	0.005	0.001
20	0.000	0.004	0.001	0.002
15	0.000	0.004	0.000	0.002
20	0.004	0.002	0.015	0.001

The particle number emission dependence for the cold start phase presented in Fig. 8 clearly shows that the emission decreases with increasing temperature.

The difference between –10°C and +20°C is 64% for passenger cars and light duty vehicles.

Table 8 shows the impact of temperature on emissions in the cold and hot phases in urban areas. The disparity is evident in urban environments, where emissions during cold start significantly surpass those during warm phases. At a temperature of –10°C, emissions during warm phases

are either zero or negligible. The contrast in particle number emissions between the two phases varies across different temperatures, with differences of up to 42 times for passenger cars and 480 times for light duty vehicles at –5°C.

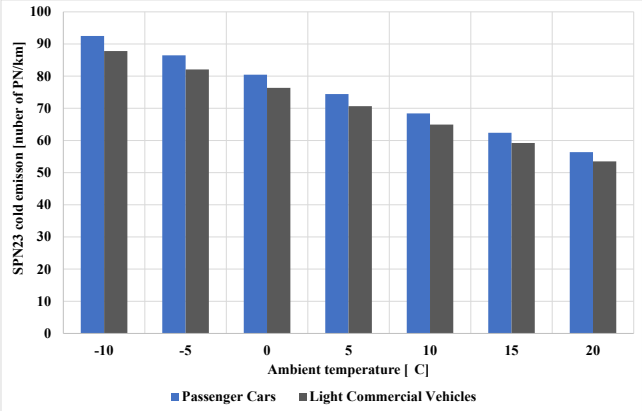

Fig. 8. The dependence of particle number (PN) emissions from cold start on the ambient temperature

Table 8. Change of particle number (PN) emissions in the cold start and hot phases depending on the ambient temperature

Temperature [°C]	PC PN emission [g/km]		LDV PN emission [g/km]	
	cold	hot	cold	hot
–10	91.736	0.000	82.627	0.000
–5	86.466	0.001	82.088	0.000
0	80.444	0.001	76.368	0.000
5	74.421	0.002	70.649	0.001
10	68.399	0.002	64.930	0.001
15	62.377	0.003	59.211	0.001
20	56.355	0.004	53.493	0.002
15	50.333	0.004	47.776	0.002
20	73.829	0.002	70.087	0.001

The hydrocarbons emission dependence for the cold start phase presented in Fig. 9 clearly shows that the emission decreases with increasing temperature.

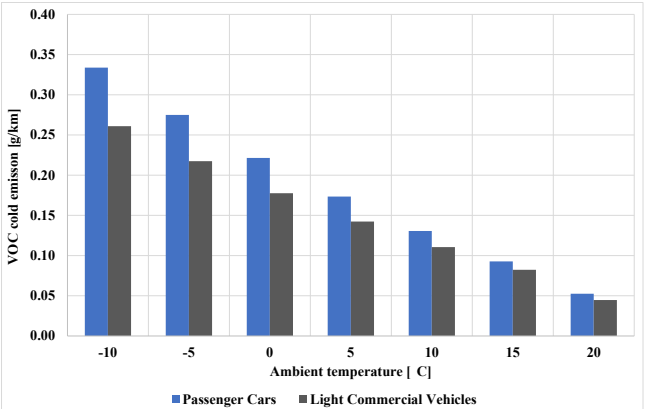

Fig. 9. The dependence of hydrocarbons (VOC) emissions from cold start on the ambient temperature

The difference between –10°C and +20°C is 536% for passenger cars and 485% for light duty vehicles.

Table 9 shows the impact of temperature on emissions in the cold and hot phases in urban areas. The difference is evident within urban settings, where emissions during cold start notably exceed those during warm phases. At temperatures of –10°C and –5°C, emissions during warm starts are virtually zero or negligible. Variations in hydrocarbon emissions between the two phases at other temperatures can reach up to 42 times for passenger cars and surpass 480 times for light duty vehicles at –5°C.

Table 9. Change of hydrocarbons (VOC) emissions in the cold start and hot phases depending on the ambient temperature

Temperature [°C]	PC VOC emission [g/km]		LDV VOC emission [g/km]	
	cold	hot	cold	hot
–10	0.332	0.000	0.250	0.000
–5	0.275	0.001	0.217	0.000
0	0.221	0.001	0.178	0.000
5	0.173	0.002	0.142	0.001
10	0.131	0.002	0.110	0.001
15	0.093	0.003	0.082	0.001
20	0.052	0.004	0.045	0.002
15	0.023	0.004	0.019	0.002
20	0.173	0.002	0.141	0.001

In Fig. 2–9 and are shown a comparison of a cold start emissions for CO_2, N_2O, CH_4, NO_x, NMVOC, VOC, TSP and SPN23, depending on the ambient temperature. The modelling showed that cold start emissions of all pollutants are highly influenced by variations in the ambient temperature. We can see that the levels of all modelled pollutants and cold start emissions have gone down. COPERT software was utilized to carry out the simulations, and the ambient temperatures ranged from –10°C to 20°C with 5°C intervals.

All of the simulations are conducted using COPERT software, assuming ambient temperatures from –10°C to +20°C, with 5°C intervals.

The results presented in Tables 2–9 show that for temperatures from –10°C to –5°C in city traffic, there are only emissions from the cold start phase for both passenger cars and light duty vehicles, which indicates that with the model used l_{trip} parameter, even after driving 12 km, the engine still does not heat up to the optimal temperature. Only at a temperature of 0°C do emissions from the heated engine begin to appear, but they are over 41 (for PCs) and 486 (for LDVs) times lower than in the cold start phase.

4. Conclusions

Similarly, to the research conducted by [3, 13, 15], it can be seen that as the temperature increases, cold start emissions decrease for all pollutants, which was also proven by simulation tests.

As shown in Fig. 2–9, changing the ambient temperature reduces emissions of CO_2, N_2O, CH_4, NO_x, NMVOC, VOC, TSP and PN during cold start for each vehicle category.

The simulations show how important it is to reduce emissions from the cold start phase. Emissions in this phase are much higher than in the case of emissions from the engine heated to the appropriate temperature. This is especially important in cities, where these emissions have the greatest impact on human health.

In summary, ambient temperature significantly impacts cold start emissions under various driving conditions for

passenger cars and light duty vehicles. Simulation results using COPERT software show that as temperature increases, emissions of carbon dioxide, nitrogen oxides, methane, nitrogen oxides, non-methane volatile organic compounds, hydrocarbons, total particle mass, and particle number decrease during cold start for both vehicle categories. The study highlights the importance of reducing emissions during the cold start phase, particularly in urban areas where these emissions significantly impact human health. Further testing on vehicles adjusted to appropriate temperatures is recommended to understand better and reduce cold start emissions.

It is therefore important to take effective action to reduce emissions during the cold start phase, especially in urban areas where these emissions significantly impact air quality and public health. It is essential to address cold start emissions to improve air quality and reduce negative impacts on health and the environment.

Further research and testing on vehicles is also recommended to confirm the simulation results and explore potential solutions to reduce cold start emissions. By addressing cold start emissions and implementing effective policies and regulations, we can work to minimise the impact of vehicle emissions on air quality and public health. Action is needed to reduce cold start emissions and improve air quality to benefit people and the environment. Additionally, continuous monitoring and regulation of vehicle emissions, particularly on cold start operations, is essential to achieving environmental goals and improving air quality in urban areas.

The authors also see the need to carry out tests on a real vehicle, which will be conditioned to an appropriate temperature and then tested on a chassis dynamometer and in real driving conditions.

Nomenclature

CH_4	methane
CO_2	carbon dioxide
COPERT	COmputer Programme to calculate Emissions from Road Transport
EC	European Commission
N_2O	nitrous oxide
NMVOC	non-methane volatile organic compounds
NO_x	nitrogen oxides
PN	particle number
RDE	real driving emissions
SCR	selective catalytic reduction
TSP	total particulate matter
VOC (HC)	hydrocarbons (treated as volatile organic compounds
WLTP	Worldwide Harmonised Light Vehicle Test Procedure

Bibliography

1. Air quality in Europe – 2021 report. EEA – European Environmental Agency. Copenhagen, Denmark.
2. André J-M, Joumard R. Modelling of cold start excess emissions for passenger cars. 2005. https://hal.archives-ouvertes.fr/hal-00917071
3. Bielaczyc P, Szczotka A, Woodburn J. The effect of a low ambient temperature on the cold-start emissions and fuel consumption of passenger cars. P I Mech Eng D-J Aut. 2011; 225(9):1253-1264. https://doi.org/10.1177/0954407011406613
4. Bielaczyc P, Szczotka A, Woodburn J. Cold start emissions of spark-ignition engines at low ambient temperatures as an air quality risk. Arch Environ Prot. 2014;40(3):86-100.
5. Chu Van T, Zare A, Jafari M, Bodisco TA, Surawski N, Verma P et al. Effect of cold start on engine performance and emissions from diesel engines using IMO-compliant distillate fuels. Environ Pollut. 2019;255(2):113260. https://doi.org/10.1016/j.envpol.2019.113260
6. Daham B, Li H, Andrews G. Comparison of real world emissions in urban driving for Euro 1-4 vehicles using a PEMS. SAE Technical Paper 2009-01-0941. 2009. https://doi.org/10.4271/2009-01-0941
7. Dimaratos A, Toumasatos Z, Doulgeris S, Triantafyllopoulos G, Konstses A, Samaras Z. Assessment of CO_2 and NO_x emissions of one diesel and one bi-fuel gasoline/CNG Euro 6 vehicles during realworld driving and laboratory testing. Frontiers in Mechanical Engineering. 2019;5:62. https://doi.org/10.3389/fmech.2019.00062
8. European Commission: Regulation 2016/427. EC – European Commission. Official Journal of the European Union L 82, 1-98. EC (2016b): Regulation 2016/646. EC – European Commission. Official Journal of the European Union L 109, 1-22.
9. European Commission, Joint Research Centre, Vlachos T, Bonnel P, Weiss M. et al., Including cold-start emissions in the Real-Driving Emissions (RDE) test procedure – an assessment of cold-start frequencies and emission effects. Publications Office. 2017. https://data.europa.eu/doi/10.2760/70237
10. Faria MV, Varella RA, Duarte GO, Farias TL, Baptista PC. Engine cold start analysis using naturalistic driving data: City level impacts on local pollutants emissions and energy consumption. Sci Total Environ. 2018;630:544-559. https://doi.org/10.1016/j.scitotenv.2018.02.232
11. Franco V, Zacharopoulou T, Hammer J, Schmidt H, Mock P, Weiss M et al. Evaluation of exhaust emissions from three diesel-hybrid cars and simulation of after-treatment systems for ultralow real-world NO_x emissions. Environ Sci Technol. 2016;50:13151-13159. https://doi.org/10.1021/acs.est.6b03585
12. Gis M. Assessment of exhaust emissions from vehicles in real traffic conditions. IOP Conf Ser: Earth Environ Sci. 2019; 214:012035. https://doi.org/10.1088/1755-1315/214/1/012035
13. Kurtyka K, Pielecha J. Cold start emissions from a gasoline engine in RDE tests at different ambient temperatures. Combustion Engines. 2020;181(2):24-30. https://doi.org/10.19206/CE-2020-204
14. Lairenlakpam R, Jain AK, Gupta P, Kamei W, Badola R, Singh Y. Effect of real world driving and different drive modes on vehicle emissions and fuel consumption. SAE Technical Paper 2018-01-5017. 2018. https://doi.org/10.4271/2018-01-5017
15. Laskowski P, Zimakowska-Laskowska M, Zasina D. Modelling of the air pollutants' cold-start emissions depending on

average vehicles' speed. Combustion Engines. 2022;188(1): 96-103. https://doi.org/10.19206/CE-142171
16. McCaffery C, Zhu H, Li C, Durbin TD, Johnson KC, Jung H et al. On-road gaseous and particulate emissions from GDI vehicles with and without gasoline particulate filters (GPFs) using portable emissions measurement systems (PEMS). Sci Total Environ. 2020;710:136366. https://doi.org/10.1016/j.scitotenv.2019.136366
17. Ntziachristos L, Boulter P. EMEP/EEA Air pollutant emissions inventory guidebook 2019. 1.A.3.b.i-iv Road transport 2019. European Environment Agency: Copenhagen, Denmark. 2023. https://www.eea.europa.eu/publications/emep-eea-guidebook-2019/part-b-sectoral-guidance-chapters/1-energy/1-a-combustion/1-a-3-b-i/view
18. Pielecha J, Merkisz J, Kurtyka K, Skobiej K. Cold start emissions of passenger cars with gasoline and diesel engines in Real Driving Emissions tests. Combustion Engines. 2019; 179(4):160-168. https://doi.org/10.19206/CE-2019-427
19. Prati M, Meccariello G, Della Ragione L, Costagliola MA. Real driving emissions of a light-duty vehicle in Naples. Influence of road grade. SAE Technical Paper 2015-24-2509. 2015. https://doi.org/10.4271/2015-24-2509
20. Ramadhas AS, Xu H, Liu D, Tian J. Reducing cold start emissions from automotive diesel engine at cold ambient temperatures. Aerosol Air Qual Res. 2016;16:3330-3337. https://doi.org/10.4209/aaqr.2015.11.0616
21. Regulation 2017/1154 – Amendment of Regulation (EU) 2017/1151 supplementing Regulation 715/2007 on type-approval of motor vehicles with respect to emissions from light passenger and commercial vehicles (Euro 5 and Euro 6) and on access to vehicle repair and maintenance information, amending Directive 2007/46/EC, Commission Regulation (EC) No 692/2008 and Commission Regulation (EU) No 1230/2012 and repealing Regulation (EC) No 692/2008 and Directive 2007/46/EC as regards real-driving emissions from light passenger and commercial vehicles (Euro 6).
22. Suarez-Bertoa R, Valverde V, Clairotte M, Pavlovic J, Giechaskiel B, Franco V et al. On-road emissions of passenger cars beyond the boundary conditions of the real-driving emissions test. Environ Res. 2019;176:108572. https://doi.org/10.1016/j.envres.2019.108572
23. Varella R., Duarte, G., Baptista, P. Mendoza Villafuerte P, Sousa L. Analysis of the influence of outdoor temperature in vehicle cold-start operation following EU real driving emission test procedure. SAE Int J Commer Veh. 2017;10(2): 596-697. https://doi.org/10.4271/2017-24-0140
24. Williams R, Andersson J, Hamje H, Ziman P, Kar K, Fittavolini C et al. Impact of demanding low temperature urban operation on the real driving emissions performance of three European diesel passenger cars. SAE Technical Paper 2018-01-1819. 2018. https://doi.org/10.4271/2018-01-1819

Piotr Laskowski, DEng. – Faculty of Automotive and Construction Machinery Engineering, Warsaw University of Technology, Poland.
e-mail: *piotr.laskowski@pw.edu.pl*

Jan Matej, DSc. DEng. – Faculty of Automotive and Construction Machinery Engineering, Warsaw University of Technology, Poland.
e-mail: *jan.matej@pw.edu.pl*

Magdalena Zimakowska-Laskowska, DEng. – Environment Protection Centre, Motor Transport Institute, Poland.
e-mail: *magdalena.zimakowska-laskowska@its.waw.pl*

Piotr Wisniowski, DEng. – Environment Protection Centre, Motor Transport Institute, Poland.
e-mail: *piotr.wisniowski@its.waw.pl*

Article citation info:
Czarnecki ML, Lech A. GTM-120 micro gas turbine engine noise identification. Combustion Engines. 2024;199(4):52-59. https://doi.org/10.19206/CE-189743

Michał Leszek CZARNECKI
Aleksandra LECH

Combustion Engines
Polish Scientific Society of Combustion Engines

GTM-120 micro gas turbine engine noise identification

ARTICLE INFO

Received: 29 November 2023
Revised:14 May 2024
Accepted: 6 June 2024
Available online: 27 June 2024

Micro gas turbine engines are a popular subject in research activities; most of them consider performance measurements and vibration analysis, which are related to operating running engines. Operating even small-size engines causes potential risk to operator health. The research problem was to identify the acoustic flow field from the front and back of an operating GTM-120 engine. Research was divided into three parts: identify noise at various rotational speeds, identify the acoustic field of the engine, and identify noise levels at additional points. Obtained results identifies noise, from such a small engine, is at a range of 67 to 109 dBC, which is harmful and unpleasant to people that are within a radius of 15 meters from the engine. The final conclusion is that installing a muffler for any size of turbomachinery should be mandatory.

Key words: *acoustics, noise, jet engine, micro, compressor, turbine, hearing, health*

1. Gas turbine and micro gas turbine engines noise

The noise spectrum in a gas turbine engine is unique, with characteristics that are a result of the engine design and its operation. All engine components (i.e. fan, compressor, combustor, turbine, and exhaust system) contribute to the overall broadband noise. In comparison to piston engines, gas turbine engines are continuous cycle engines that take place simultaneously in all stages of the Bryton cycle. The relative noise level for individual sources will vary not only due to different engine operating conditions. Turbine noise can be associated with two categories: internally generated noise, usually resulting from the operation of rotating engine parts, and externally generated jet noise. Noise sources are strictly related to engine design form. For example, in high-flow turbofan engines, the fan is responsible for the noise generation. It's size and airflow are up to five times greater than the airflow through the engine core. Noise generated by the fan and compressor propagates throughout the intake duct and the engine inlet that is going through the front of the engine. Noise from the combustor and turbines exits the engine through the jet pipe.

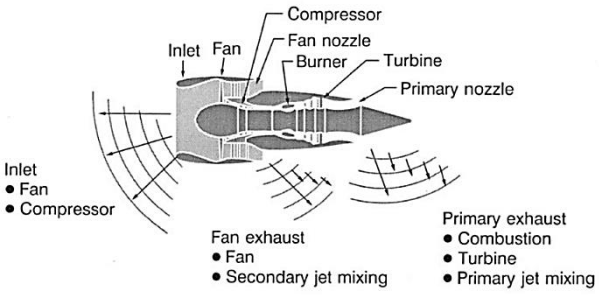

Fig. 1. Turbofan engine noise sources [1]

Figure 1 presents the main sources of noise in a turbofan engine, along with the direction of noise emissions.

1.1. Internal noise – turbomachinery noise

Internal noise generated by rotor components is similar and largely depends on the rotor tip blade speed. They vary based on the speed of sound criteria – Mach number M. For subsonic blade tip speeds regime, the main source of noise is pressure pulsations on the blade profiles that arise from the turbulent airflow. At static conditions, random changes in the pressure and velocity of the intake air can be observed resulting from natural atmospheric turbulence or turbulence caused by nearby structures. The compressor intake section composition – depending on engine layout (turbofan, turbojet, turboprop) – adds to the complexity of the obtained acoustic spectrum. Operating at flight conditions, airflow is more uniform – less turbulent. Rotating at supersonic speeds, the source of noise is shock waves generated at the edges of the blades. The distance between the turbomachinery stages also affects the generated noise. The combustor is a generator of engine noise. Noise, from the combustor, passes through the jet pipe. It is not an easily distinguishable component. The acoustic spectrum assigned to the combustor is very similar to that of the mixing streams, which makes it easy to confuse them. For angles corresponding to the angles of refraction propagating from inside the engine through to the jet mixing area, it is possible to determine both the level change and the distinct spectral shape associated with combustion and other internal sources. Generated noise is the result of very turbulent processes taking place in the combustion chamber. In other cases, it is the result of changes in the temperature of gases leaving the combustion chamber which affects other engine components – turbine, and jet pipe generated noise. No one has developed a definitive predictive procedure that considers all the observed features of gas turbine engines [17]. Micro gas turbine noise tests have shown that the noise level remains at 80 dB. It should be considered that the presented MGT (micro gas turbine) was based on a turbocharger. Radial turbines have lower rotational speeds that would significantly lower noise emissions [11].

1.2. External noise

Jet noise is related to the process of mixing exhaust gases with the atmosphere. Sound sources related to impact noise in an ineffectively expanded supercritical stream (Fig. 2). For engines operating at subcritical flow speeds, the

generated noise will only concern the processes of mixing the exhaust stream with the atmosphere. The vortices affecting the mixing process vary significantly as they move away from the outlet nozzle (growing along the stream and losing speed). For engines reaching supercritical flow speeds, shock noise is superimposed on stream mixing noise as a secondary source [17].

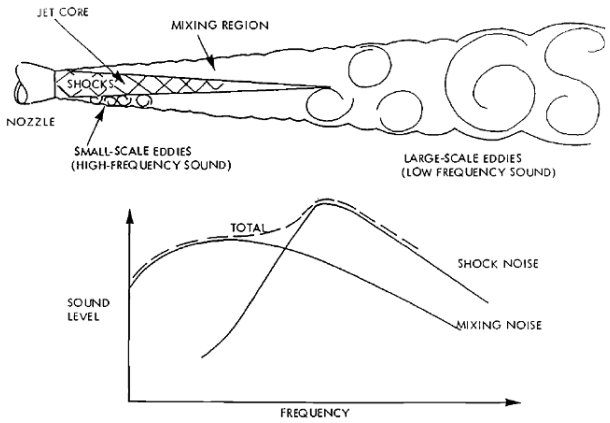

Fig. 2. Source of jet noise [1]

The most important factor influencing the noise, resulting from the mixing of exhaust gas streams with the atmosphere, is the velocity of the flowing exhaust gases. A second factor that also affects the overall noise is the exhaust gas temperature. The noise level will increase with the mass air flow (proportional to air density). The effect of speed can only be roughly estimated by taking the exhaust gas velocity value. For high exhaust gas velocities (approx. 400–500 m/s), the intensity of the emitted noise increases with the eighth power of the exhaust velocity; for low velocities (approx. 200 m/s), the intensity increases with the second power. Conventional turbojet engines are characterized by small cross-sections, relatively low air mass flow, and very high exhaust gas velocities. For them, the dominant sound source was the exhaust gases mixing with the surroundings.

1.3. Methodology and testing

Measurement methods for turbine engine acoustics are carried out for the purpose of creating engine acoustic models. The data collected in this manner can be used for engine certification or for further design modification. The most well-established method of collecting data for the purpose of creating an acoustic model of an engine is the empirical method. The noise spectrum obtained during engine testing contains the spectrum of all sources contributing to the overall engine noise. Therefore, the first step in creating an acoustic model is to subtract the jet noise (estimated by prediction or by extrapolation from model data) [14]. The acoustic tests are carried out at open spaces. Figure 3 presents the measurement site located in an open space. The measurement station consists of: an engine mounted on a tripod, a turbulence control system (TCS), and a measurement system – a microphone system. To avoid turbulence resulting from air turbulence reflected from the ground, the engine must be mounted at the appropriate height. The TCS is positioned upstream of the engine intake to reduce atmospheric turbulence. The stand itself must also be sufficiently far from acoustic obstacles.

Fig. 3. RR Trent on a test stand no.11 equipped with a TCS system [2]

As the measurements are carried out outdoors, it is important to monitor atmospheric conditions, for example, wind speed and direction, ambient temperature, atmospheric pressure, ground temperature, etc. Test stand no. 11 Rolls Royce is shown in the drawing (Fig. 3), the entire measurement platform has the ability to rotate 360° thanks to the hydraulic drive, which enables it to be adjusted according to the blowing wind. The entire measurement system is controlled from the control room and consists of three elements: a system control station – System Control Workstation – for initiating and controlling the noise measurement system and all processes; a weather monitoring computer – displaying current weather conditions, an analysis computer – allowing analysis (viewing or printing) of saved data [2].

The microphone arrangement depends on the type of research being conducted (Fig. 4). For example, the measurement system of the DGEN380 engine has 29 microphones placed on a 20 m long arc, the center of which coincides with the axis central engine. In addition, the right side of the engine was positioned in line with the engine axis foldable – a nine-bar system with a diameter of 2.5 m (6 microphones on each beam) [16].

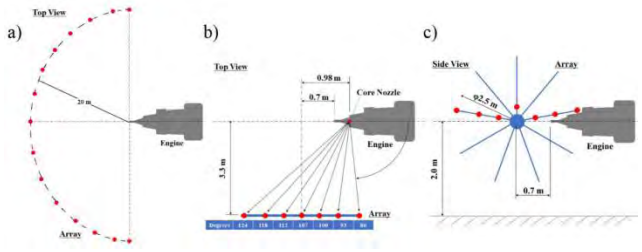

Fig. 4. DGEN 380 test stand. a) top view or microphone array form in arc, b) directional noise measurement, c) ray form measurement [8]

2. Micro gas turbine noise

2.1. Test engine

The research object was the GTM-120 micro-scale gas turbine engine. It is a single-spool gas turbine engine. The design is a 1R-1 – single-stage radial compressor, and single-stage axial turbine (Fig. 5). This layout is relevant to the early designs like Turbomecca Marbore (J-69) engines. This type of internal structure is still used by APUs (Auxil-

iary Power Units) or in simplified engines dedicated to drones.

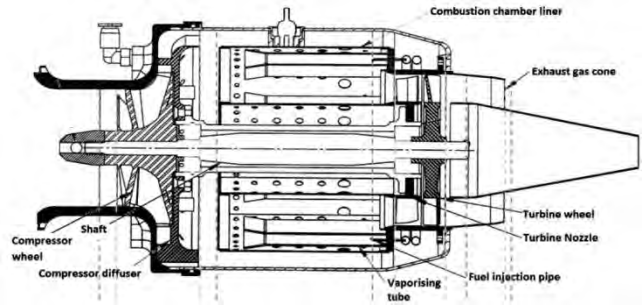

Fig. 5. GTM-120 turbojet engine [3]

Due to this design's affordable price, engines of this class are used in research university test facilities [4, 5, 13]. The total length of the engine is 265mm and the maximum diameter is 110 mm. This engine operates on Jet-A1 kerosene fuel and is controlled by a provided standard Project ECU control system. The engine rotor rotational speed in operating conditions reaches 32 to 120 thousand rpm from idle to the maximum thrust. Engine parameters at maximum conditions are thrust 12 daN, fuel flow – 440 ml/min. The engine's electric starter was disassembled due to the front of the compressor's interaction with the starter structure (air start configuration).

2.2. Test methodology

Experimental tests of the engine acoustic field were performed in an open space (Fig. 6). The reasons for conducting the research using this method were due to the following: lack of availability of the anechoic chamber, and to incorporate of safety measures aimed at protecting the health of the people conducting the research. A micro-class jet engine with an airflow of 0.2 kg/s is able to fill a room, with a volume of 25 m^2, with exhaust gases in less than 146 seconds, which is a serious health hazard. When performing acoustic tests in an open space, one should remember about certain limitations resulting from conducting this type of research. The measurement station itself should be at least 3.5 meters away from any reflective surfaces that could disturb the measurements by generating reflections of acoustic waves. Another factor worth considering is the level of the general acoustic background noise at the place of testing. If it's possible, the background sound pressure level should be measured with the sound source turned off. If the background noise is 10 dB more or less than the noise level produced by the source, the error from neglecting the background noise is less than 0.5 dB.

If the background noise is 20 dB more or less than the noise level of the measured source, the measurement error is less than 0.1 dB. In this case, the background noise level will have a negligible impact on the measurements. If the difference between the background noise level and the source noise level is less than 3 dB, accurate measurement of the noise level at the source is very difficult. A solution to perform more accurate measurements in the case of high background noise levels may be to move the microphone closer to the measured sound source [10]. Increasing the difference between the measured noise level and the background noise could be difficult due to high exhaust gas temperatures – in the case of measuring noise from the back of the engine.

Fig. 6. GTM-120 turbojet at an open space test area

The research was carried out during the holiday season in an empty car park. The measurement station prepared for the research is shown in the drawing (Fig. 8). The test site was a car park; there were no obstacles in the engine operating zone, the presence of which would significantly affect measurement disturbances. The day was sunny. Ambient conditions during the study were: air temperature of 22°C, pressure 1018 hPa, and calm conditions 0–1, according to the Beaufort scale.

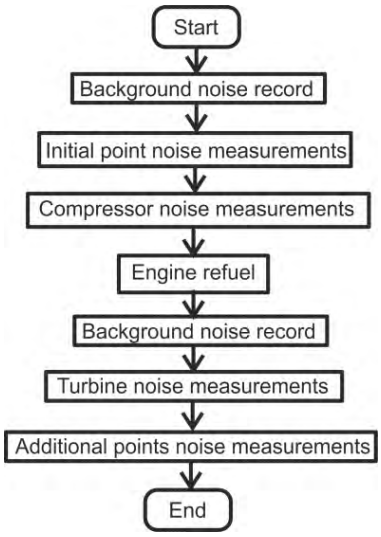

Fig. 7. Noise measurement procedure

The scope of the conducted research was divided into three parts. The first one was to measure the noise levels for specific engine speeds. The next part concerned measuring the acoustic field of the compressor and turbine. The final part provided the opportunity to measure the noise level of omitted points of particular interest that were not covered by previous measurements (Fig. 7).

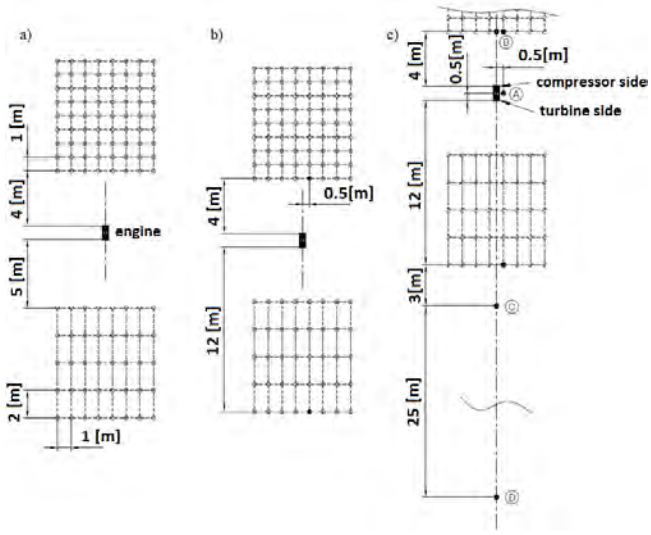

Fig. 8. Test stand configuration a) acoustic field compressor/turbine, b) various rpm configuration, c) far noise configuration

The measurement station for the tested acoustic field of the compressor and turbine is shown in (Fig. 8a). The array of measurement points is located 4 m from the front of the compressor and 5 m from the front of the turbine. To measure the acoustic field of the compressor, 64 points spaced 1m apart were used, and for the turbine, 40 measurement points were used.

Initial engine run "run zero" was used to identify the baseline noise level. Initial point (Fig. 8b) was chosen, they were placed at a point 0.5 m away from the engine axis to avoid interactions with the main part of airflow and for safety reasons. The initial distance was 4m from the front of the compressor, and 12 m from the turbine's front. The *First part of research*: the measurement of the noise level at various rotational speeds was carried out for two different configurations – the setting was different depending on whether the measurement concerned a compressor or a turbine (Fig. 8b) – black dot points. *Second part*: acoustic noise measurements for the compressor and turbine were carried out at a constant rotational speed that was set at 100,000 rpm. Measurements at each point lasted 30 seconds, then the meter was set to the next measurement point; the setting was different depending on whether the measurement concerned a compressor or a turbine. *The third part* was conducted to measure the noise level far away from the engine to identify safe/unsafe conditions. An additional consideration was to measure the noise near the combustor – point A (Fig. 8c).

3. Results

3.1. Noise measurement in characteristic points

For the analysis to be carried out, it is necessary to verify whether the measured results at selected points (Fig. 8c) are reliable; there is also a horizontal measurement of the acoustic background. This measurement was performed with the device's turned and non-operational engine. The average value measured was 51 dBC. This value is shown in a collective graph of the examined points, denoted by (T) with the marked average standard deviation (Fig. 9). The average measured value of the noise level for the combustion chamber (A) was 109 dBC. The average noise level measured at the engine axis for the compressor (B) was 98 dBC. For the turbine, the average measured noise level at point (C) was 77 dBC, while at point (D) 70 dBC. The collected data is presented in Fig. 9. The average standard deviation for the results of the tested measurement points was also considered. The noise level for the combustion chamber and compressor are significantly higher than the background noise level – greater than 20 dBC, hence the negligible measurement error (less than 0.1 dBC [5]). Turbine noise levels in the engine axis are closer to the background noise level, but they can still be considered reliable – a difference of 10 dBC introduces an error of approximately 0.5 dBC [5, 2].

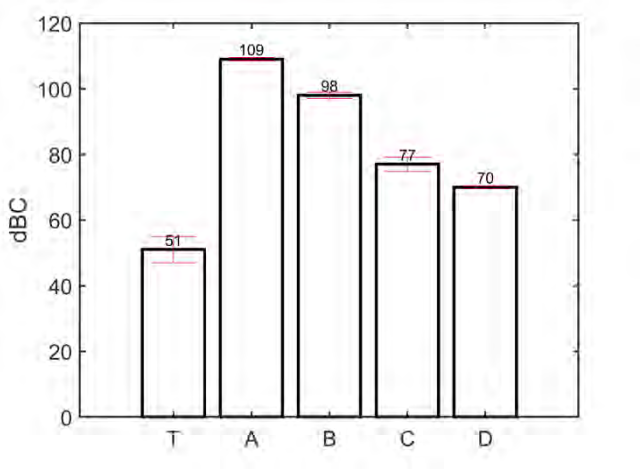

Fig. 9. GTM-120 engine noise levels at selected points.

3.2. Noise level measurement for variable rotational speeds

Figure 10 presents the compressor noise level in relation to the various rotational speeds along with the average standard deviation. It was observed that as the rotational speed increases, the sound pressure (noise) level increases. This phenomenon is noticed in both the compressor and the turbine. That is a qualitative indicator that research was conducted the proper way.

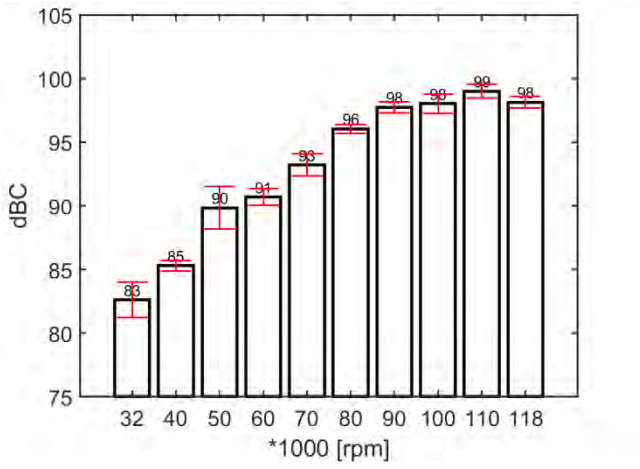

Fig. 10. GTM-120 engine compressor noise levels at various rotational speeds

Considering turbine measurements (Fig. 11), there is a noticeable difference in the noise level in comparison to the compressor side of the engine. The noise from the turbine is noticeably lower. This is largely due to the significant difference in the distance of the measurement point from the sound source (Fig. 8). During the test we followed the rule: safety first.

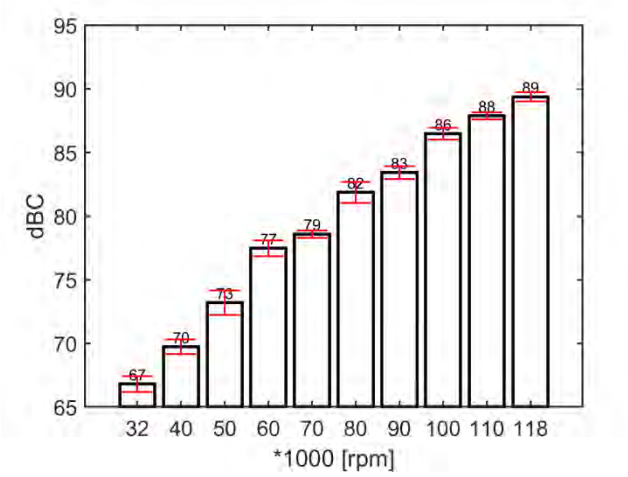

Fig. 11. GTM-120 engine turbine noise levels at various rotational speeds

3.3. Measurement of the noise level of the compressor and turbine acoustic field

To identify the acoustic array, we need to follow the numbering rule of selected points – Fig. 12. Measurement starts from the left-hand side and progresses by adding the next measurement (column direction) to the right-hand side. After completing the column, an addition matrix row is considered.

The difference in adding a row to the noise measurement matrix is the direction of measurement. For the compressor, measurements are taken while moving away from the noise source. For the turbine, measurements are taken while moving towards the noise source. If there is any risk, it is possible to stop the measurement procedure.

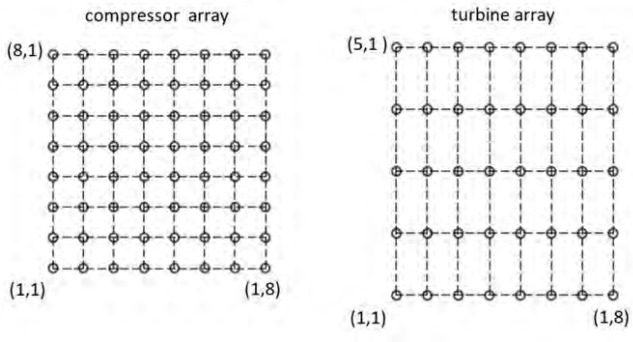

Fig. 12. Acoustics array for compressor & turbine noise measurements

Figure 13 presents the average measured noise level for compressor – specific points. According to the measurement procedure, it can be concluded that the conditions of the study were sufficiently stable, and the measurement errors obtained did not affect the results significantly. The highest value was measured at the axis closest to the front of the compressor, and its value was 97 dBC. The lowest value was recorded at the point furthest from the front of the compressor; its value was 87 dBC. The difference between the average highest measured value and the lowest is 10 dBC.

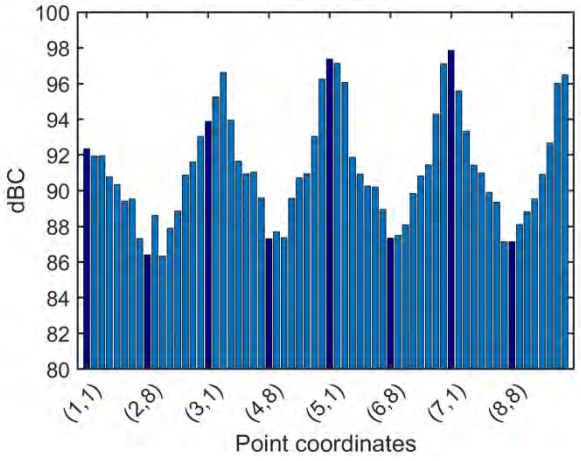

Fig. 13. Results for acoustics array for compressor noise measurements

The presented acoustic flow field (Fig. 14) informs us that the area with the highest values is not symmetrically distributed relative to the engine axis (on the graph between points 4 and 5). This phenomenon reveals the non-axial angle of air inflow into the rotor, which is the nature of the centrifugal compressor's design. GTM-120 engines were based on Garret T04B – series 409179 – compressor wheels. Additional disturbances in the measured acoustic field may be caused by changing environmental conditions resulting from the place where the test was carried out – the open space. The lowest measured value is greater than the acoustic background by 26 dBC, thus the measurement error can be considered negligible, and the results are reliable; in short, the acoustic background does not significantly affect the result values.

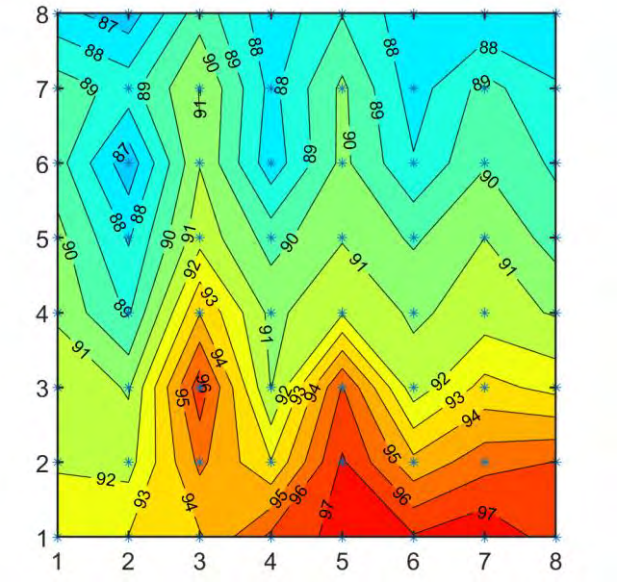

Fig. 14. Results of the acoustics flow field for compressor noise measurements (dBC)

The turbine noise measurements (Fig. 15), similar to the results of the compressor (Fig. 13), present average measured noise levels at the individual measurement points. The measured noise levels are noticeably lower than in the case of measurements of the compressor. It should be remembered that the measurement field was moved away from the noise source (turbine side) by one meter when compared to the measurements carried out for the compressor. The highest measured value for the turbine field was 92 dBC. The smallest measured value was 84 dBC. The acoustic background did not significantly affect the results.

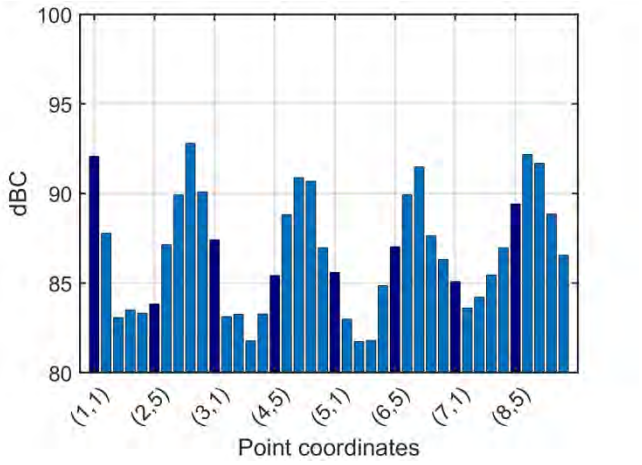

Fig. 15. Results for acoustics array for turbine noise measurements

It was identified that the character of the acoustic field for the turbine is not similar to the appearance of the compressor acoustic field. The main reason is the different characteristics of sound formation at the inlet and outlet of the engine.

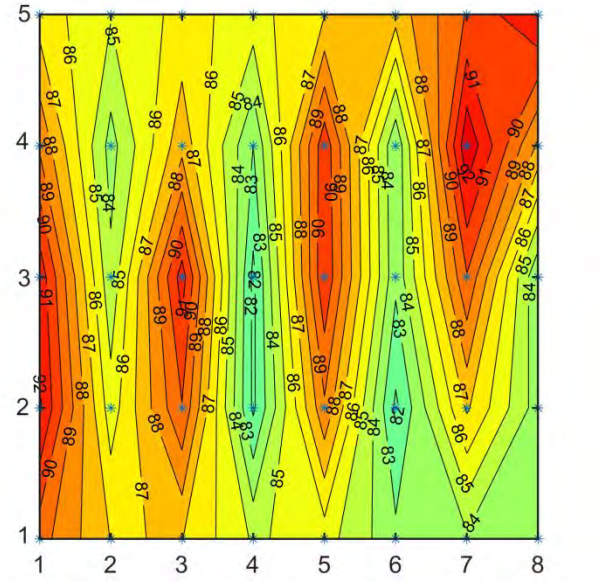

Fig. 16. Results of the acoustics flow field for turbine noise measurements (dBC)

The noise referred to the turbine side in comparison to the internal noise – machine noise, also includes the noise referred to as external that results from the turbulent flow and mixing of exhaust gases with the atmosphere. As in the case of a compressor, the appearance of the acoustic field is influenced by the non-axial turbine geometry and the strong effect of turbine stator-rotor interactions. The final effect is magnified by the elements (three) that hold the central body of the jet pipe cone. This results in the "silent bands" that can be observed in Fig. 16. The turbine flow field corresponds to the result obtained by Lee et al. [9], where the flow field is also asymmetric without rotor stator interaction due to test model configurations. The main difference between the acoustic field of the compressor and the turbine would be the result of a design configuration. The compressor is designed using the rotor-stator configuration and the turbine follows the stator-rotor scheme. The compressor acoustic field is dominated by reflections between the compressor wheel and compressor case. The turbine acoustic field is dominated by the stator-rotor interaction and jet pipe interaction. That phenomenon is consistent with the results published by Tanaka [15]. They correspond to the theory of turbomachinery according to the relative Mach number at the compressor inlet.

4. Summary

Knowing the basic processes of noise generation in a jet engine, we can expect that the main source of noise will be the engine exhaust. The noise level from the engine exhaust consists of all the turbomachine noises, including noise from the combustion chamber resulting from violent combustion processes, and the jet noise resulting from the turbulent mixing of exhaust gases with the atmosphere. The literature states that sound levels for jet engines are 150 dB [6]. Considering the size of the tested engine, we can expect lower sound levels, which are related to low-pressure ratios and a thermodynamically inefficient design.

Obtained results of the analysis that characterize noise generation in micro-class turbine engines allow one to move away from the hypotheses. Based on facts – experimental data – the noise level in the vicinity of the running engine was determined and visualized (Fig. 13, 15). As expected, the results obtained are significantly lower than those in the literature – representing sound levels for full-size engines. The obtained measurements can be considered reliable. The lowest difference between the obtained measurements and the acoustic background was around 10 dBC, the measurement error in this worst-case scenario remains at the level of approximately 0.5 dBC, which is considered negligible. Analysis of the acoustic field allows for determining the tendency of noise propagation for a jet engine, thus determining safety zones. After analyzing the results obtained by the acoustic field (Fig. 14, 16), there is the conclusion that working with micro gas turbines could be dangerous, or at least unpleasant [7]. The average noise level obtained for the compressor is from 87 dBC to 97 dbC; for the turbine, it is from 84 dBC to 92 dBC. In both cases, the measured noise level is harmful to humans. Noise above 70 dBC, over a prolonged period of time, may start to damage your hearing. Loud noises above 120 dBC can cause immediate harm to your ears according to the Centers for Disease and Control Prevention. The highest sound level was obtained near the combustion chamber, which was also the point closest to the engine. The impact of the

received noise level of 109 dBC is already very harmful and may cause severe disruption of the nervous system and permanent hearing damage. Other sources categorize "noise pollution" and noise above 105 dB as "traumatic", the range between 90 to 105 dB as "threatening", and noise below 80 dB as safe [12]. Therefore, any operator should use appropriate protective measures to avoid unpleasant effects resulting from a long-term stay in the risk zone. According to Fig. 8, the minimum safe distances to stay in the area of a micro class engine without protective measures should be no less than 12 m from the compressor side and at least 15 m from the turbine side. Staying within 5 meters of the engine will damage the hearing of an operator. Final recommendation for future research is to measure noise in order to determine its direction relative to the engine. Inside, near the combustor, install a muffler to suppress the sound level, and install additional protective mufflers when long-term engine operation is considered. It is also worth considering vibration measurement to allow the identification of machine noise and the diagnostic of the engine. As a warning for gas turbine operators, an author diagram of hearing loss is presented.

Working in a gas turbine environment as a maintenance engineer and scientist for twenty years has caused hearing loss of about 29 % in the left ear and 8% in the right ear (Fig. 17). Final recommendation is that, even for micro turbo machinery, a properly silenced test facility is essential. According to scientific reports, approximately 33% of working-age adults with a history of occupational noise exposure have audiometric evidence of noise-induced hearing damage, and 16% of noise-exposed workers have material hearing impairment [16]. Obtained results lead to the final conclusion that any type of micro gas turbine engine should be obligatorily tested at a prepared facility that allows one to separate operators from the noise source.

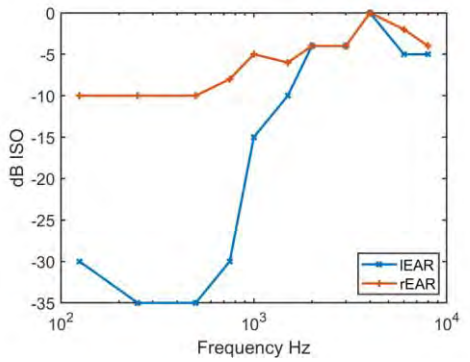

Fig. 17. Author audiometry results provided by Medyk medical center

Nomenclature

APU	auxiliary power units
dB	decibels
dBC	decibels in C scale
MGT	micro gas turbine
TCS	turbulence control system

Bibliography

[1] Barron RF. Industrial noise control and acoustics. Taylor & Francis. CRC Press 2003. https://doi.org/10.1201/9780203910085

[2] BRÜEL& KJÆR. Case study: new noise measurement system Rolls-Royce PLC. https://www.bksv.com/media/doc/bo0502.pdf

[3] Chmielewski M, Gieras M. Small gas turbine GTM-120 bench testing emission measurements. Journal of KONES Powertrain and Transport. 2015;22:47-54. https://yadda.icm.edu.pl/baztech/element/bwmeta1.element.baztech-2b2549ac-cace-484d-8955-b1ef2d94181d

[4] deOlloqui V, Margraves C. Developing a jet test system on a shoestring budget: an application of project based learning. ASEE Southeastern Section Conference. 2019. https://sites.asee.org/se/wp-content/uploads/sites/56/2021/04/2019ASEESE30.pdf

[5] Erario M, Grazia De Giorgi M, Przysowa R. Model-based dynamic performance simulation of a microturbine. IOP Conf Ser: Mater Sci Eng. 2022;1226:012032. https://doi.org/10.1088/1757-899X/1226/1/012032

[6] Fleming G. Aircraft noise measurement instrumentation and techniques. Volpe National Transportation Systems Center (U.S.). Acoustics Facility 1989. https://rosap.ntl.bts.gov/view/dot/8963

[7] Goelzer B, Hansen CH, Sehrndt G. Occupational exposure to noise: evaluation, prevention and control. WHO, Geneva 2001.

[8] Ishii T, Ishii Y, Hald J, Nagai K, Oinuma H. Application of sound source identification using CLEAN-SC to a turbofan engine. Berlin Beamforming Conference 2018. https://www.bksv.com/media/doc/bn2213.pdf

[9] Lee I, Zhang Y, Lin D. A model-scale test on noise from single-stream nozzle exhaust geometries in static conditions. Chinese J Aeronaut. 2018;31(12):2206-2220. https://doi.org/10.1016/j.cja.2018.08.001

[10] Lyon RH. Machinery noise and diagnostics. Butterworth-Heinemann 1987. https://doi.org/10.1016/C2009-0-24812-4

[11] Muiz A, Khalid A, Leman AM, Razzaly W, Sapit A, Razali A, Saleh, Analysis of Noise Reduction in Micro Gas Turbine. International Journal of Advanced Trends in Computer Science and Engineering. 2020;9(1.1):583-588. https://www.warse.org/IJATCSE/static/pdf/file/ijatcse94911sl2020.pdf

[12] Petric D. Noise pollution and health. Int J Audiol. 2022;3(1): 8-10. https://www.rehabilitationjournals.com/speech-and-audiology-journal/article/12/3-1-2-711.pdf

[13] Przysowa R, Majewski P, Ślęczek J, Grundas D, Wachłaczenko M. Health monitoring of the shaft bearings in a micro turbojet based on vibration analysis. J Phys: Conf Ser. 2023;2526:012070. https://doi.org/10.1088/1742-6596/2526/1/012070

[14] Smith MJT. Aircraft noise. Cambridge University Press 1989. https://doi.org/10.1017/CBO9780511584527

[15] Tanaka S. Acoustic and thermal packaging of small gas turbines for portable power. MIT 2009. Master of Science in Aeronautics and Astronautics. https://dspace.mit.edu/handle/1721.1/51648
[16] Themann CL, Masterson EA. Occupational noise exposure: a review of its effects, epidemiology, and impact with recommendations for reducing its burden. J Acoust Soc Am. 2019;146:3879-3905. https://doi.org/10.1121/1.5134465
[17] Viswanathan K. Does a model scale nozzle emit the same jet noise as a jet engine. 2008;46(2):336-355. AIAA Journal. https://doi.org/10.2514/1.18019

Michał Leszek Czarnecki, DSc., DEng. – Faculty of Mechanical Engineering and Aeronautics, Rzeszów University of Technology, Poland.
e-mail: *czarn@prz.edu.pl*

Aleksandra Lech, MEng.– Faculty of Mechanical Engineering and Aeronautics, Rzeszów University of Technology, Poland.
e-mail: *aleksandra.lech@g.pl*

Article citation info:
Zakrzewska D, Chłopek Z, Szczepański K. The criteria for qualifying fuels as a replacement fuels for internal combustion engines. Combustion Engines. 2024;199(4):60-66. https://doi.org/10.19206/CE-186848

Dagna ZAKRZEWSKA
Zdzisław CHŁOPEK
Krystian SZCZEPAŃSKI

Combustion Engines
Polish Scientific Society of Combustion Engines

The criteria for qualifying fuels as a replacement fuels for internal combustion engines

ARTICLE INFO

Received: 11 December 2023
Revised: 2 April 2024
Accepted: 2 April 2024
Available online: 25 May 2024

The article presents the classification of motor fuels into conventional and unconventional. The concept of replacement fuels is formalized as fuels that can replace conventional petroleum fuels for spark ignition and self-ignition engines without any structural or regulatory changes. The criteria for qualification of unconventional fuels as replacement fuels are presented. This article also introduces the results of empirical research conducted on a single-cylinder research engine powered by diesel fuel and rapeseed methyl esters (RME) in the summer version and winter versions. The engine was tested, and the combustion phenomenon in the cylinder was analyzed. Very similar engine properties were observed for diesel fuel and rapeseed methyl esters in the summer version, while greater differences were found for rapeseed methyl esters with winter additives. In light of the empirical research and the physicochemical properties of the fuels, it is concluded that RME warrants consideration as a replacement fuel for engines with self-ignition, especially in the case of biofuel in the summer version.

Key words: *replacement fuels, substitute fuels, emission of pollution, unconventional fuels, rapeseed methyl esters (RME)*

1. Introduction

In today's era, the use of fuels in internal combustion engines has emerged as a pressing global concern. The widespread utilization of energy sources poses a substantial environmental threat, impacting human health and accelerating the depletion of fossil resources essential for energy production. This situation markedly fuels socio-political tensions, driven by disparities in resource accessibility.

As a result, within the energy-related economy, there is currently a significant interest to explore broader avenues for obtaining accessible energy resources [2, 3, 9, 14, 15, 20–26, 28]. This is primarily driven by environmental protection issues [1, 13, 16–19, 29, 30] and the energy security of states and state structures, ultimately impacting the quality of human life. Therefore, this constitutes a global issue for sustainable civilizational development.

2. Classification of motor fuels and formalization of the concept of replacement fuels

Energy carriers encompass various substances, phenomena, objects, or devices utilized to meet civilization's energy demands [12]. Among these, fuels play a pivotal role by facilitating energy acquisition through combustion. This process involves an exothermic oxidation-reduction reaction, swiftly releasing heat that emits electromagnetic radiation within the visible frequency range – an intensity delineated as the threshold of luminescence. In this context, fuel operates as the reducing agent in the combustion reaction, interacting with an oxidizer, chiefly oxygen from the ambient air (though certain heat engines, like rocket engines, might utilize alternative oxidizing agents).

Due to the widespread use, engine fuels can be categorized in the following manner [12]:

– conventional
– unconventional.

Typically, conventional motor fuels refer to those specifically designed for standard adaptation by manufacturers of internal combustion engines. These fuels primarily stem from crude oil processing and predominantly include motor gasoline and diesel fuels. Unconventional fuels constitute an array of alternative options utilized to drive internal combustion engines, expanding beyond the traditional hydrocarbon-based choices (e.g., natural gas-based fuels [3, 26] and gas derived from petroleum [22]) and others derived from petroleum processing and other mineral resources encompass a spectrum of materials, including those derived from the refinement of biological raw materials (e.g., fuels based on biological oils – B20 and B100 – for self-ignition engines [10, 11, 15, 19, 20], ethanol-based fuels: E95 – for self-ignition engines [13, 14, 21] and E85 for flex-fuel spark-ignition engines [13, 30], and so-called biogas-based biomethane [26]), as well as synthetic fuels [24, 25].

Replacement fuels are unconventional fuels that can be used instead of conventional fuels: motor gasoline for engines with spark-ignition and diesel fuel for engines with self-ignition without structural or regulatory changes to the engines [12].

Several fundamental criteria evaluate unconventional fuels based on their compliance with substitute fuel conditions. These criteria can generally be classified as follows [12]:

– criteria derived from assessing the physicochemical properties guiding the selection of fuels for engine running
– criteria derived from assessing the processes within internal combustion engines fueled by the considered fuels
– criteria derived from assessing the performance characteristics of internal combustion engines fueled by the considered fuels.

3. Research methodology

The objective of the study was to evaluate the extent to which it is justified to consider bio-origin fuels – rapeseed

methyl esters (RME) as replacement fuels regarding diesel fuel.

The empirical research methodology encompassed studies conducted on the AVL 5402, a single-cylinder research engine with self-ignition capabilities. The study utilized the AVL Single Cylinder Test Bed [5–7] and relied on AVL PUMA [6] and AVL Concerto [4] software for data recording and analysis.

The empirical research was carried out at the Department of Vehicles and Automotive Engines of the Vehicle and Machine Exploitation Institute at the Faculty of Mechanical Engineering of the Kazimierz Pułaski University of Technology and Humanities in Radom. The research was conducted by Skrzek from the Department of Vehicles and Automotive Engines at the Vehicle and Machine Exploitation Institute of the Faculty of Mechanical Engineering at the Kazimierz Pułaski University of Technology and Humanities, along with engineers Jagiełło and Juwa – graduates supervised by Chłopek from the Faculty of Automotive and Construction Machinery Engineering at the Warsaw University of Technology [10]. The development of the empirical research program involved the researchers and Chłopek and Zakrzewska the Institute of Environmental Protection – National Research Institute [10, 11].

The apparatus used for the research complies with the requirements of the following regulations: Directive 1999/96/EC of the European Parliament and of the Council of 13 December 1999, Regulation (EC) No 715/2007 of the European Parliament and of the Council of 20 June 2007, and Commission Regulation (EC) No 692/2008 of 18 July 2008.

The fundamental data of the AVL 5402 engine are provided in Table 1.

Table 1. Basic information on the AVL 5402 engine

Number of cylinders	1
Cylinder diameter	85.01 mm
Piston stroke	90.00 mm
Displacement	511.00 cm^3
Combustion system	Self-ignition
Timing	Four-valve
Compression ratio	17.0–17.5
Engine power system	Direct injection, single injector, tray system (Common Rail)
Maximum net power, non-supercharged	6 kW
Maximum net power, supercharged	16 kW
Rated speed	4200 min^{-1}
Injection pressure	180 MPa

The AVL 5402 engine, thanks to the use of special head gaskets, allows for the adjustment of compression ratio. Special openings in the cylinder head enable the introduction of cameras into the combustion chamber and observing the combustion process of the mixture. The engine is equipped with an exhaust gas recirculation system and sensors allowing, among other things, the measurement of pressure in the combustion chamber and exhaust gas temperatures. Thanks to the installed injection equipment and accompanying software, it is possible to modify the engine's fuel supply algorithm. The research utilized a two-phase fuel injection.

The research program entailed the engine operating statically across a range of engine speeds (from 1200 rpm to 3600 rpm) at intervals of 400 rpm. Primary measurements encompassed diverse parameters:

- engine speed
- torque
- mass fuel consumption rate
- mass air consumption rate
- carbon monoxide (CO) volumetric concentration
- hydrocarbons (HC) volumetric concentration
- nitrogen oxides (NO_x) volumetric concentration
- particulate matter (PM) mass concentration
- indicated pressure recorded in the crankshaft rotation angle
- exhaust gas temperature.

The engine was fueled with:

- classic diesel fuel – ORLEN VERVA
- biofuel B100 with an additional summer blend, designated as RME-S
- biofuel B100 with an additional winter blend designated as RME-W.

Table 2 presents a comparison of the basic physicochemical properties of the tested fuels.

Table 2. Physical and chemical characteristics of fuels

Characteristics	Unit	Fuels		
		ORLEN VERVA	RME -S	RME -W
Density	kg/m^3	832.5	880.0	880.0
Calorific value	MJ/kg	43	38	39
Cetane number	LC	55.6	57.3	57.3
Kinematic viscosity at 40°C	mm^2/s	2.87	4.50	4.49
Elemental composition of the fuel:				
carbon content mass of the fuel, mass fraction	% m/m	0.837	0.772	0.772
hydrogen content of fuel, mass fraction	% m/m	0.149	0.120	0.120
oxygen content of fuel, mass fraction	% m/m	0.014	0.108	0.108
sulfur content of fuel, mass fraction	ppm	7.5	3.0	3.0
Cold filter plugging point (CFPP)	deg C	–28	–15	–20
Flash point	deg C	65	101	101

In Figure 1 to 6, a comparison of the basic properties of fuels is presented:

- elemental composition of fuels: mass content of carbon – u_C, hydrogen – u_H and oxygen – u_O
- calorific value – W_f
- density – ρ
- cetane number – LC
- kinematic viscosity at 40°C – ν
- temperature of cold fuel filter plugging – t_b.

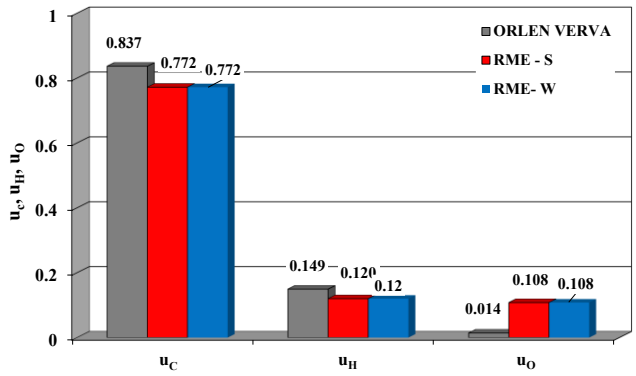

Fig. 1. Composition of the fuels in terms of elemental content: mass fraction of carbon – u_C, hydrogen – u_H and oxygen – u_O

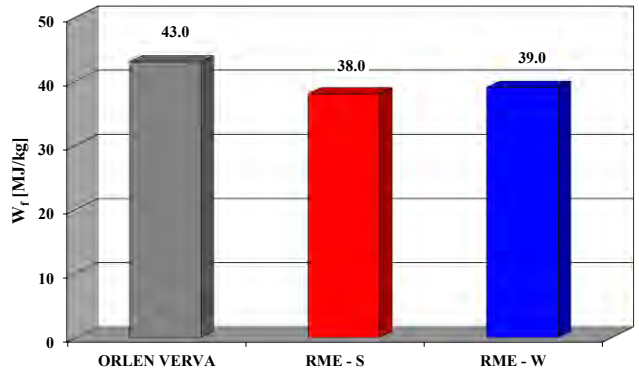

Fig. 2. Calorific values of the fuels tested – W_f

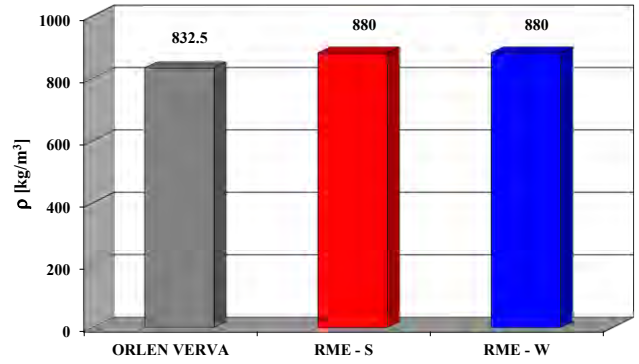

Fig. 3. Density of the fuels tested – ρ

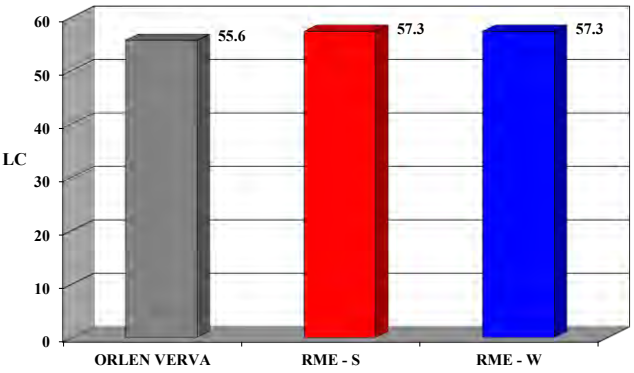

Fig. 4. Cetane number of the fuels tested – LC

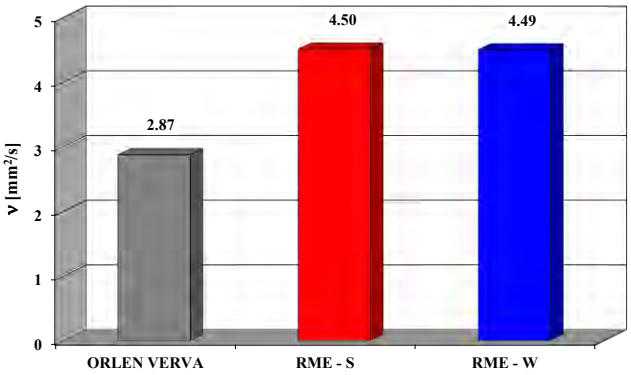

Fig. 5. Kinematic viscosity of the fuels tested at 40°C – ν

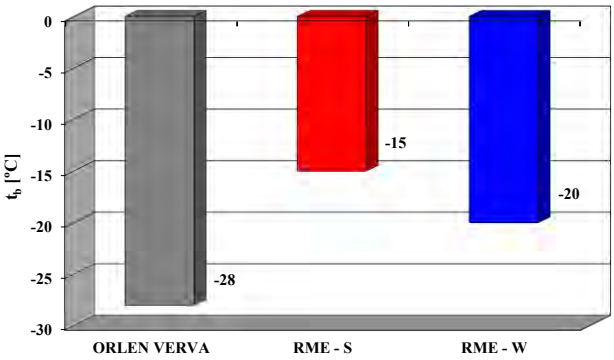

Fig. 6. Temperature of cold fuel filter plugging of the fuels tested – t_b

RME biofuels have a significantly higher mass fraction of oxygen – nearly ten times higher than the content found in diesel fuel, consequently, the calorific value of RME is over 10% less than that of diesel fuel. The density of RME surpasses that of diesel fuel by approximately 6%. However, RME has a higher tendency for auto-ignition – a cetane number greater by about 1.7. The kinematic viscosity of RME fuels at 40°C is much higher compared to diesel fuel – the relative difference is almost 60%. There are notable variations in the cold filter plugging point temperatures, particularly in the properties of RME biofuels, notably the summer variant – RME-S, which demonstrates considerably inferior characteristics.

4. The results of empirical research

Figures 7 to 13 present the results of empirical research and their analyses.

Figures 7 to 9 show external speed characteristics of fundamental parameters characterizing the engine's properties:

- energetic parameters: torque – M_e and effective power – N_e
- economic parameters related to fuel consumption: general efficiency – η_e.

Because of the lower calorific value in bio-based fuels, the engine's torque and effective power are lower when fueled by RME compared to diesel fuel. Yet, the variance in the summer fuel is minor, attributable to the engine's overall higher efficiency when running on RME-S compared to RME-W fuel.

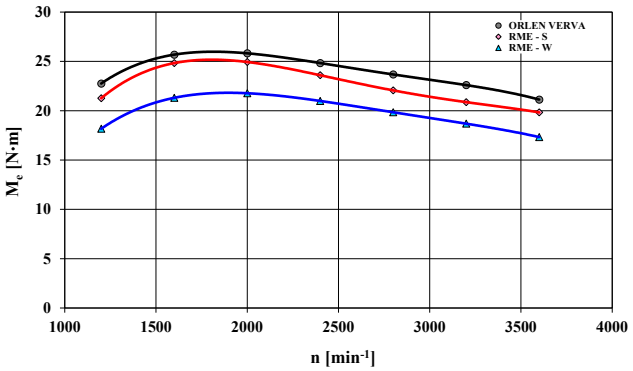

Fig. 7. External speed characteristic of the torque – M_e; n – engine speed

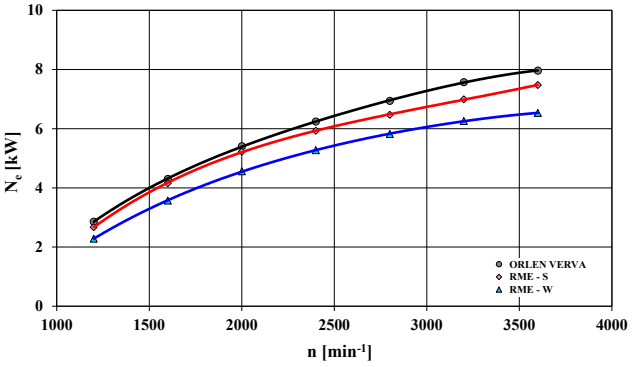

Fig. 8. External speed characteristic of the effective engine power – N_e; n – engine speed

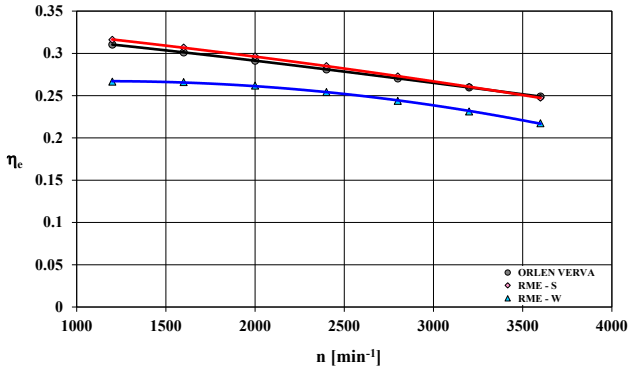

Fig. 9. External speed characteristic of the general efficiency – η_e; n – engine speed

Figures 10 and 11 depict the relative change δ in the average emissions value across the speed domain per unit.

The use of bio-origin fuels results in a relative decrease of approximately 30% in the mean value within the speed domain of the engine for CO and PM emissions. For HC and NO_x, the comparative variance is around 10%, wherein for RME-S fuel, there is a decrease in unit emissions, while for RME-W fuel, there is an increase.

Cylinder pressure indication data recording involved capturing 20 cycles of indicated pressure in each test point within the crankshaft rotation domain. A set of 20 recorded indicated pressure profiles at each measurement point is considered as a realization set of the stochastic process of indicated pressure at that point. The recordings were made with a resolution of 1 deg[1] of crankshaft rotation and within the range (–30–90) degrees for the top dead center position of the piston corresponding to combustion, with a resolution of 0.1 deg. To reduce the influence of high-frequency noise in the signals, a second-order Savitzky-Golay filter was applied for signal processing [8, 27].

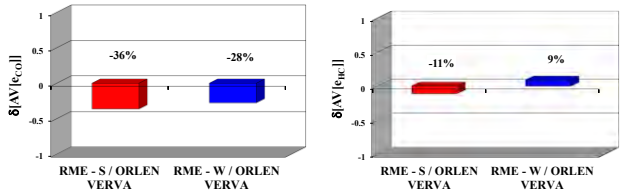

Fig. 10. The relative change – δ of the a mean value in the engine speed domain – AV of emissions: CO – e_{CO} and HC – e_{HC}

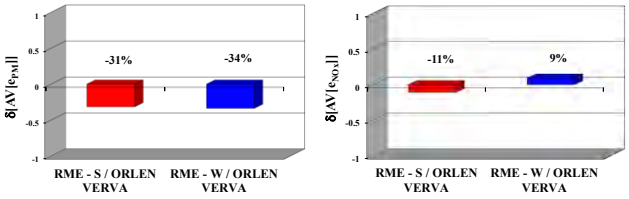

Fig. 11. The relative change – δ of the mean value in the engine speed domain – AV of emissions: NO_x – e_{NOx} and PM – e_{PM}

The engine was indicated. Each registered pressure trace was treated as a realization of a stochastic process. Figures 12 and 13 display a contrast between the indicated pressure and its derivative concerning the crankshaft rotation angle for the analyzed fuels at the point of maximum torque operation.

There is a clear resemblance between the indicator diagrams for diesel fuel and rapeseed methyl esters with summer additives, while the indicated pressure for rapeseed methyl esters with winter additives is lower. There's a distinct variance observed in the derivative of indicated pressure concerning the crankshaft rotation angle.

Drawing from the documented indicated pressure profiles and engine-specific details concerning fuel parameters, according to the AVL Concerto algorithm, the following profiles were determined: specific heat release, rate of heat release, and agent temperature – an exemplary graph for ORLEN VERVA fuel for maximum torque operation is shown in Figure 14. The crankshaft rotation angles corresponding to the start of fuel injection, auto-ignition, maximum indicated pressure, and maximum agent temperature are marked on the graphs.

Once more, there was a distinct likeness observed between diesel fuel and rapeseed methyl esters with summer blend, whereas there was a difference in the case of rapeseed methyl esters with winter blend.

[1] Since the work uses angle differentiation, "deg" rather than "°" is used to denote the degree to avoid the symbol "°" in the denominator of the unit of measurement of derivative with respect to an angle.

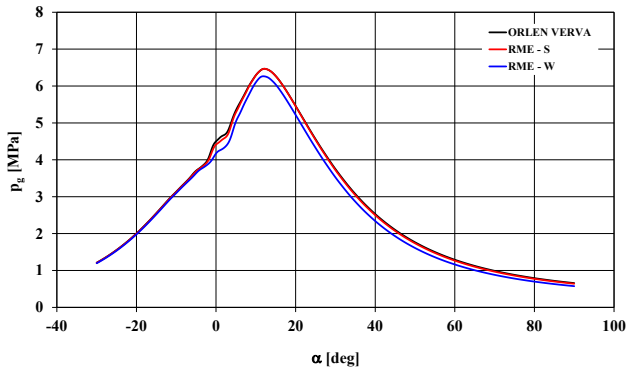

Fig. 12. Indicator diagram – indicated pressure – p_g for the maximum torque

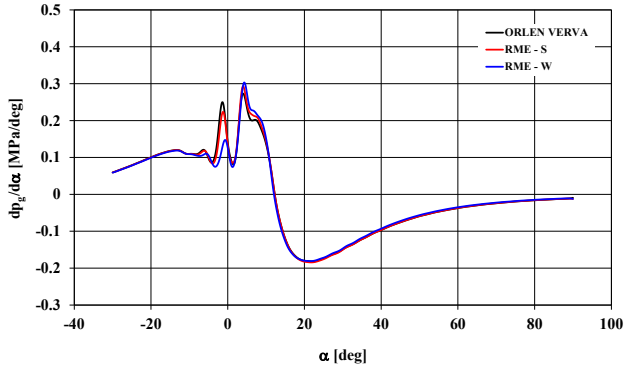

Fig. 13. The derivative of the pressure against the angle of rotation of the crankshaft – $p_g/d\alpha$ for the maximum torque

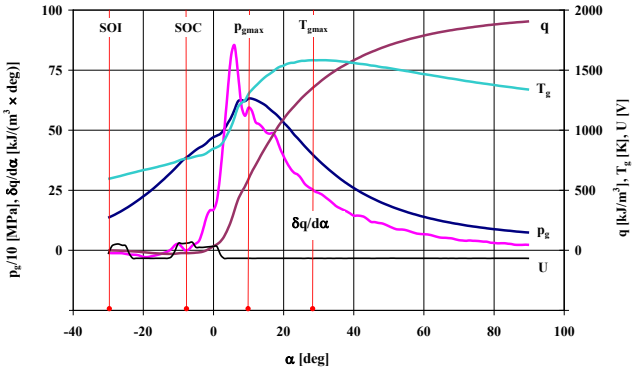

Fig. 14. Indicated pressure – p_g, temperature of the working medium – T_g, unit heat emission rate – δq/dα, unit heat emission – q, injector opening control voltage – U for the maximum torque for the ORLEN VERVA fuel; SOI – fuel injection start angle, SOC – combustion start angle, p_{gmax} – maximum indicated pressure, T_{gmax} – maximum temperature of the working medium

The empirical research yielded the following formulated conclusions:

1. Effective power and torque of the combustion engine are greater for diesel fuel, slightly lower for biofuel in the summer version, and significantly lower for biofuel in the winter version.
2. The utilization of rapeseed methyl esters (RME) led to a noticeable decrease in emissions of CO and PM emissions – by approximately 30%. For HC and NO_x, the relative change was around 10%, whereas for summer fuel, there was a decrease in unit emissions, and for winter fuel, an increase was observed.
3. Similar general efficiency was observed for the combustion engine running on diesel fuel and biofuel with summer blend. However, for biofuel with winter blend, the overall efficiency was noticeably lower.
4. Considering the similarity criteria applied in this study regarding the analyzed combustion processes, a significant resemblance was noted in the assessed characteristics between ORLEN VERVA and RME-fuels.
5. The characteristics determined for RME-W fuel, in most cases, deviate from the analogous characteristics of other fuels, despite the substantial resemblance in the physical and chemical properties of both types of biofuels. This situation primarily arises from the properties of the biofuel with summer blend and biofuel with winter blend used for rapeseed methyl esters.

5. Conclusions

Based on the conducted research and presented considerations, the following conclusions have been formulated:

1. Renewable energy sources are taking on a more significant role in society's development. Special attention is given to the development and practical implementation of unconventional fuels compared to conventional hydrocarbon fuels for internal combustion engines. Primarily, these fuels consist of bio-based fuels resulting from biomass processing.
2. The general principle is the effect of using bio-based fuels, leading to a reduction in carbon monoxide and organic compound emissions. Additionally, for engines with self-ignition, a decrease in particulate matter emissions is observed. Typically, using esters of plant oils in self-ignition engines may lead to increased nitrogen oxide emissions. This can be mitigated by using alcohols and their derivatives.
3. To comprehensively evaluate the effects of employing biofuels on emissions and engine properties, a detailed study of the combustion process via engine indication is required. This study conducted such research for esters of plant oils compared to traditional diesel fuel. The research results confirmed the effectiveness of such studies, particularly the positive ecological effects of using bio-based fuels in terms of emissions.
4. A practical implication drawn from the conducted research is the assertion that bio-based fuel – rapeseed methyl esters – might be regarded as a replacement fuel for diesel fuel [12], especially for rapeseed methyl esters with fuel additive packages for summer use.

Nomenclature

AV	average value
B100	fuel – vegetable oil methyl esters
B20	20% V/V vegetable oil methyl esters blended with diesel fuel

e	specific brake emission
LC	cetane number
M_e	(engine) torque
n	engine speed
N_e	effective (engine) power
p_g	indicated pressure
p_{gmax}	maximum indicated pressure
q	unit heat emission
RME	rapeseed methyl esters
RME-S	rapeseed methyl esters with summer additive
RME-W	rapeseed methyl esters with winter additive
SOC	combustion start angle
SOI	fuel injection start angle
t_b	cold filter plugging point (CFPP)
T_g	temperature of the working medium
T_{gmax}	maximum temperature of the working medium
U	injector opening control voltage
u_C	carbon content mass of the fuel, mass fraction
u_H	hydrogen content mass of the fuel, mass fraction
u_O	oxygen content mass of the fuel, mass fraction
V/V	volume fraction
W_f	calorific value
α	angle of crankshaft rotation
δ	relative change
$\delta q/\delta\alpha$	unit heat release rate
η_e	general efficiency
ν	kinematic viscosity of fuel
ρ	density of fuel

Bibliography

[1] Ambrozik A, Orliński P, Orliński S. Influence of diesel engine fuelling with different fuels on self-ignition delay in aspect of ecology. Eksploat Niezawodn. 2003;3:50-55.

[2] Andrych-Zalewska M, Sitnik L, Sroka Z, Mihaylov V. Fuel with a higher content of bio components in greenhouse effect aspects. Combustion Engines. 2023;192(1):36-42. https://doi.org/10.19206/CE-147741

[3] Arefin MA, Nabi MN, Akram MW, Islam MT, Chowdhury MW. A review on liquefied natural gas as fuels for dual fuel engines: opportunities, challenges and responses. Energies. 2020;13(22):6127. https://doi.org/10.3390/en13226127

[4] AVL. Concerto™ – Data Post-Processing. https://www.avl.com/-/avl-concerto-data-post-processing. (accessed on 2023.07.11).

[5] AVL. Product Description. Single cylinder research engine.

[6] AVL. PUMA Open Automation Platform. https://www.avl.com/-/avl-puma-open-automation-platform. (accessed on 2015.07.11).

[7] AVL. Testing Solutions. Measure and Control. Single cylinder research engines & compact test bed.

[8] Bendat JS, Piersol AG. Random Data: analysis and measurement procedures. John Wiley & Sons, Inc; 2010. https://doi.org/10.1002/9781118032428

[9] Bhan C, Verma L, Singh J. Alternative fuels for sustainable development. Environmental Concerns and Sustainable Development. Springer, Singapore 2020. https://doi.org/10.1007/978-981-13-5889-0_16

[10] Chłopek Z, Jagiełło S, Juwa S, Skrzek T. Comparative examination of performance characteristics of an IC engine fuelled with diesel oil and rape methyl esters. The Archives of Automotive Engineering – Archiwum Motoryzacji. 2016; 74(4):19-32. https://doi.org/10.14669/am.vol74.art2

[11] Chłopek Z, Jagiełło S, Juwa S, Zakrzewska D. Examination of the combustion process in a compression ignition engine fuelled with diesel oil and rape methyl esters. The Archives of Automotive Engineering – Archiwum Motoryzacji. 2017; 76(2):17-35. https://doi.org/10.14669.vol.76.art1

[12] Chłopek Z, Zakrzewska D. Kryteria oceny nośników energii jako paliw zastępczych do silników spalinowych (in Polish). TTS – Technika Transportu Szynowego. 2015;22(12):278-283.

[13] Chłopek Z. Ecological aspects of using bioethanol fuel to power combustion engines. Eksploat Niezawodn. 2007;35: 65-69.

[14] Chollacoop N, Saisirirat P, Fukuda T, Fukuda A. Scenario analyses of road transport energy demand: A case study of ethanol as a diesel substitute in Thailand. Energies. 2011;4: 108-125. https://doi.org/10.3390/en4010108

[15] Crookes RJ, Bob-Manuel KDH. RME or DME: a preferred alternative fuel option for future diesel engine operation. Energ Convers Manage. 2007;48(11):2971-2977. https://doi.org/10.1016/j.enconman.2007.07.002

[16] Labeckas G, Slavinskas S. The effect of rapeseed oil methyl ester on direct injection diesel engine performance and exhaust emissions. Energ Convers Manage. 2006;47:1954-1967.

[17] Merkisz J, Kozak M, Pielecha J, Andrzejewski M. The influence of application of different diesel fuel-RME blends on PM emissions from a diesel engine. Combustion Engines. 2012;148(1):35-39. https://doi.org/10.19206/CE-117049

[18] Mamat R, Abdullah NR, Xu H, Wyszynski ML, Tsolakis A. Effect of air intake pressure drop on performance and emissions of a diesel engine operating with biodiesel and ultra low sulphur diesel (ULSD). International Conference on Renewable Energies and Power Quality (ICREPQ'09). Valencia (Spain). 2009. https://doi.org/10.24084/repqj07.504

[19] Mayer ACR, Czerwiński J, Wyser M, Mattrel P, Heitzer A. Impact of RME/diesel blends on particle formation, particle filtration and PAH emissions. SAE Technical Paper 2005-01-1728. 2005. https://doi.org/10.4271/2005-01-1728

[20] Merkisz J, Fuć P, Lijewski P, Kozak M. Rapeseed oil methyl esters (RME) as fuel for urban transport. Alternative Fuels, Technical and Environmental Conditions. InTech; 2016. https://doi.org/10.5772/62218

[21] Odziemkowska M, Matuszewska A, Czarnocka J. Diesel oil with bioethanol as a fuel for compression-ignition engines. Appl Energ. 2016;184:1264-1272. https://doi.org/10.1016/j.apenergy.2016.07.069

[22] Paczuski M, Marchwiany M, Puławski R, Pankowski A, Kurpiel K, Przedlacki M. Liquefied petroleum gas (LPG) as a fuel for internal combustion engines. Alternative Fuels, Technical and Environmental Conditions. InTech; 2016. https://doi.org/10.5772/61736

[23] Prussi M, Panoutsou C, David Chiaramonti D. Assessment of the feedstock availability for covering EU alternative fuels demand. Appl Sci. 2022;12(2):740. https://doi.org/10.3390/app12020740

[24] Ram V, Salkuti SR. An overview of major synthetic fuels. Energies. 2023;16(6):2834. https://doi.org/10.3390/en16062834

[25] Ruth JC, Stephanopoulos G. Synthetic fuels: what are they and where do they come from? Curr Opin Biotech. 2023;81: 102919. https://doi.org/10.1016/j.copbio.2023.102919

[26] Savickis J, Zemite L, Zeltins N, Bode I, Jansons L, Dzelzitis E et al. The biomethane injection into the natural gas networks: The EU's gas synergy path. Latvian Journal of Physics and Technical Sciences. 2020;57(4):34-50. https://doi.org/10.2478/lpts-2020-0020

[27] Savitzky A, Golay MJE. Smoothing and differentiation of data by simplified least squares procedures. Anal Chem. 1964;36(8):1627-1639. https://doi.org/10.1021/ac60214a047

[28] Torres-Sebastián MJ. Methane, a renewable biofuel: from organic waste to bioenergy. Biofuels. 2021;13(25):1-11. https://doi.org/10.1080/17597269.2021.2016105

[29] Yanowitz J, McCormick RL. Effect of E85 on tailpipe emissions from light-duty vehicles. J Air Waste Manage. 2009; 59(2):172-182. https://doi.org/10.3155/1047-3289.59.2.172

[30] Zhai H, Frey HC, Rouphail NM, Gonçalves GA, Farias TL. Comparison of flexible fuel vehicle and life-cycle fuel consumption and emissions of selected pollutants and greenhouse gases for ethanol 85 versus gasoline. J Air Waste Manage. 1995;59(8):912-924. https://doi.org/10.3155/1047-3289.59.8.912

Dagna Zakrzewska, MSc. – Environmental Protection – National Research Institute, Warsaw, Poland.
e-mail: *dagna.zakrzewska@kobize.pl*

Prof. Zdzisław Chłopek, DSc., DEng. – Institute of Environmental Protection – National Research Institute, Poland.
e-mail: *zdzislaw.chlopek@kobize.pl*

Krystian Szczepański, DSc., DEng. – Professor of IOS-PIB – Institute of Environmental Protection – National Research Institute, Poland.
e-mail: *krystian.szczepanski@ios.edu.pl*

Article citation info:
Maciejewska M, Kurzawska-Pietrowicz P. Adopted LTO cycle to operational conditions at Polish airports. Combustion Engines. 2024;199(4):67-73. https://doi.org/10.19206/CE-187023

Marta MACIEJEWSKA
Paula KURZAWSKA-PIETROWICZ

Combustion Engines
Polish Scientific Society of Combustion Engines

Adopted LTO cycle to operational conditions at Polish airports

ARTICLE INFO

Received: 19 January 2024
Revised: 25 March 2024
Accepted: 10 April 2024
Available online: 6 August 2024

The aim of this article is to take into account specifications of the airport area in the LTO test when the impact of the air transport at the airport-proximate area is analysed. The LTO test doesn't consider the specifications of e.g. airport manoeuvring area and length of taxiways. The LTO test calculation methodology requires knowledge of aircraft engine parameters, such as thrust, specific fuel consumption and emission values indexes. Based on the data contained in the Engine Emissions Database (ICAO), the parameters of the LTO test can be determined. The main analysis element was to conduct a taxiing simulation using the CKAS MotionSim5 Flight Simulator to indicate the operational taxiing time at individual Polish airports. Statistically significant differences were found between the emissions of selected exhaust gas components in the regulation LTO test and the operational LTO test. Analyzes were carried out concerning three different propulsions that are most often used by carriers serving the largest number of passengers in Poland. The analysis covers current research topics, which are reflected in the presented discussion of the obtained results and their relation to conducted analysis by the scientific community in the area of aviation impact on the environment.

Key words: *LTO cycle, operational conditions, sustainability air transport, air transport impact*

1. Introduction

The dynamic development of transport systems is an important factor influencing the improvement of the economic world. For many years, one of the most important aspects of transport has been the assessment of its impact on the natural environment [13]. A significant issue in terms of the dynamics of air transport development is counteracting its harmful effects, achieving climate neutrality and reducing dependence on fossil fuels. The European Environment Agency puts the responsibility of air transport at around 4% of total greenhouse gas emissions in the European Union. On the other hand, they indicate an increase in the responsibility of air transport for greenhouse gas emissions by 146% over the years 1990-2019 [3]. According to European Union Aviation Safety Agency (EASA) reports, CO_2 emissions from all EU airports amount to 147 million tons (2019), of which emissions from long-haul flights (over 4000 km) are approximately 6% [5]. They account for half of the CO_2 and NO_x emissions in European air transport [1].

Carbon dioxide emissions, which directly contribute to the greenhouse effect, are relate to the combustion process in aircraft engines. The dominant units are the drives of passenger and transport aircraft, medium and long-range, which obtain mechanical energy from the combustion of aviation kerosene [19]. As indicated in one of the articles regarding Athens airport more than 6500 kt of CO_2, almost 28 kt of NO_x, about 18 kt of CO, almost 1.5 kt of HC and 0.3 kt of PM total have been released into the atmosphere during the total operating time of the airport [2]. Systems and projects gradually introduced into civil aviation, such as Single European Sky Air Traffic Management Research (SESAR) and Carbon Offsetting and Reduction Scheme for International Aviation (CORSIA), are aim at reducing CO_2 emissions in air transport. The above-mentioned projects, through activities such as more effective management of airspace, its capacity and the introduction of flexible route planning (an example is the Free Route Airspace project conducted by SEASAR), contribute to reducing emissions of harmful exhaust components from air transport. CORSIA is a global offsetting mechanism that aims to compensate for the increase in carbon dioxide emissions above 2020 levels, from international aviation. CO_2 offsetting involves calculating the emissions created during a flight and converting them into the purchase of project credits that aim to remove an equivalent amount of CO_2 from the atmosphere elsewhere. One of the articles showed, using the example of Antalya International Airport, that aircraft of the B737 family are found to have the highest global warming potential and environmental cost, with values of 630,633.3 GWP and 39,723.4 Euros, respectively [4]. The guidelines set by CORSIA and SESAR projects contribute to stabilizing carbon emissions from the aviation sector by implementing new technologies, improving operational efficiency and infrastructure, and gradually replacing fossil fuels with fuels from renewable sources. In the above-mentioned processes, it is also important to estimate the quantitative emissions of individual exhaust gas components, especially in areas surrounding the airport. Quantitative estimation of aviation emissions of combustion products is determined based on the landing and take-off cycle (LTO test). The test methodology is base on individual phases of the flight operation performed by the aircraft. The entire LTO test cycle lasts almost 33 minutes, of which the taxiing time is 26 minutes, which constitutes 78% of the entire cycle duration [18]. The LTO test does not take into account the specifications of the airport maneuvering area, the length of taxiways, and does not take into account the nature of a given airport.

The article focuses on a comparative analysis of the three propulsions most often used in the fleet of carriers that serve the highest number of passengers in domestic and international regular traffic at Polish airports. The analysis concerns the standard taxiing phase (following legal regula-

tions) of the LTO test and operational taxiing, where the time of the mentioned phase is adapted to the actual infrastructure of a given airport.

2. Materials and methods

In the LTO test, the parameters depend on the phase of the flight operation and are specified by the legislator [19]. The emission values of toxins in gases emitted by jet engines are determined depending on the maximum thrust for take-off, in the range of 85% for climb, in the range of 30% for approach and 7% of maximum thrust for taxiing (Table 1) [8, 9, 18].

Table 1. Characteristic of time and thrust for LTO cycle [9, 18]

LTO phase	Thrust [%]	Phase time [min]
Take-off	100	0.7
Climb	85	2.2
Approach	30	4.0
TAXI/Idle	7	26

The LTO test calculation methodology requires knowledge of aircraft engine parameters, such as thrust, specific fuel consumption and emission values and indexes. Based on the data contained in the Engine Emissions Database created by ICAO [10, 17], the parameters of the LTO test can be determined. The largest and most recognizable aircraft manufacturers in the world are Boeing and Airbus. These aircraft models constitute the largest percentage of the aircraft fleet used by airlines [16]. Low-cost carriers (LCC) offer air transportation services at lower prices than traditional airlines. One way to reduce costs is to standardize the aircraft fleet, which reduces the operating costs of a given fleet. An example of a traditional carrier is LOT Polish Airlines, which offers aircraft in its fleet of various models from Boeing and Embraer [16]. The most passengers served at Polish airports in 2022 were: Ryanair 37% market share, LOT Polish Airlines 23.5% market share, Wizzair 21.2% market share [16]. For each carrier, the type and model of the aircraft that most often operates on the Polish market and the corresponding drive were selected (Table 2).

Table 2. Type and model of aircraft for each airline

Airline	Type of aircraft	Propulsion
Ryanair	B737 8200	LEAP-1B CFM International (LEAP)
LOT Polish Airlines	Embraer 195	GE CF34-10E turbofans (GE)
Wizzair	Airbus A321neo	PW1133G-JM (PW)

For each of the indicated propulsion, using data from the ICAO Database [11], emission indicators and fuel consumption for the taxiing phase are present (Table 3).

Table 3. Emission indicators in taxi/idle phase for chosen propulsions

Compound	GE	LEAP	PW
HC [g/kg]	6.39	0.71	0.05
CO [g/kg]	49.98	16.19	17.89
NO_x [g/kg]	3.51	4.74	6.98
PM [mg/kg]	13.42	0.23	7.04
FF [kg/s]	0.084	0.089	0.099

The next step was to conduct a taxiing simulation using the CKAS MotionSim5 Flight Simulator at all airports in Poland in order to indicate the operational taxiing time at individual airports. This is an advanced flight simulation device that can simulate the work of light aircraft class: with one piston engine, two piston engine, turboprop engine and jet engines. The LTO regulation taxiing operation covers the route from landing to arrival at the passenger terminal (taxi/idle in phase) and the route from the passenger terminal to the runway (taxi/idle out phase). For each airport in Poland simulated taxi/idle in and out phase. Taxi/idle phase was mapped using infrastructure schemes (in according to Aeronautical Information Publication AIP Poland) of each airport and according to taxi ways leads to passenger terminal. A jet propulsion module was used to conduct the simulation, and the speed of taxiing operations was assumed to be 28 km/h (15 kt). This is the standard speed for taxiing operations at the airport. During the simulation of taxi/idle in phase time of operation was measured and multiplied by 2 for an estimated time of the whole LTO operational taxiing phase. Table 4 shows the times determined on the basis of simulations for each airport in Poland.

Table 4. Time in minutes for taxi operation for each airport. Airport were marked by ICAO code

Airport	Time [min]	Airport	Time [min]	Airport	Time [min]
EPWA A	17.4	EPWA K	15.8	EPGD	8.68
EPWA B	19.4	EPWA L	19.4	EPKT	9.32
EPWA C	13.2	EPWA M	17.4	EPKK	10.92
EPWA D	16.8	EPWA N	19.4	EPZG	4.5
EPWA E	10.4	EPWA O	13.2	EPSC	4.5
EPWA F	12.4	EPWA P	16.8	EPLB	8.4
EPWA G	6.2	EPMO	8.68	EPLL	11.88
EPWA H	9.8	EPSY	8.04	EPRA	5.78
EPWA I	20	EPPO	10.92	EPRZ	9
EPWA J	22	EPBY	9.66	EPWR	4.5

Since Warsaw Chopin Airport is the largest airport in Poland, is responsible for 35% of all traffic and is the only airport in Poland with two runways, several different taxiing scenarios have been prepared for it. For the analyses, the 16 scenarios were adopted – the longest taxiway takes 6.8 km, the shortest 1.9 km and the average occurs 4.8 km. It's caused that taxi time is from 3 to 11 minutes [9]. The analysis and preparation of scenarios for the EPWA airport were presented in detail in one of the authors' publications [15]. The last step was to calculate emissions in the operational LTO test (O_LTO) and the standard the LTO test (R_LTO). Emission in LTO cycle is calculated using the formula:

$$\mathrm{EPC} = \mathrm{TIM}/60 \times \mathrm{FFR} \times \mathrm{EF} \times \mathrm{NE} \quad (1)$$

where: EPCpol,mode – emissions per cycle for a particular, mode [g/phase], TIM – time in mode [h/phase], FFR – fuel, flow rate [kg/h], EF – emission factor [g/kg], NE – number, of engines on aircraft [–].

3. Results

Based on calculated results, the authors prepared Fig. 1–3, which present the mass of gaseous harmful compounds in exhaust gases obtained in the taxi cycle and estimated for each airport and each propulsion. Additionally, for each of the analyzed exhaust gas compounds, tests for normality of distributions (Shapiro-Wilk test) and tests for the significance of differences (Wilcoxon test) were performed, using a sample prepared for all airports and scenarios. None of the compounds had a normal distribution. However, it was important from the point of selecting significance tests. Significance tests between the results for taxi operation in R_LTO cycle and O_LTO cycle showed statistically significant differences at the p-value < 0.05 level for each of the analyzed compounds.

Figure 1 shows the emission of selected exhaust gases for the GE engine, which is used on aircraft most often operated by LOT Polish Airlines. As you can see, the differences in emission levels for R_LTO and O_LTO are large.

In the case of Chopin Airport, the best scenario is scenario G. In the case of CO emissions, the reduction ranges from 3000 to 12,000 g/phase for each airport. Hydrocarbon emissions using operational conditions will be reduced by 200–1400 g/phase. The reduction in nitrogen oxide emissions is from 100 to 750 g/phase. However, the mass amount of particulate matter emitted by the GE engine during the operational LTO test conditions is less than 0.5–3 g/phase. Figure 2 shows the emissions of selected exhaust gases for the LEAP engine, which is used on aircraft operated most often by the low-cost airline Ryanair.

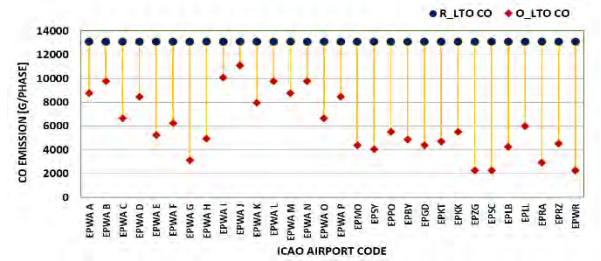

(a)

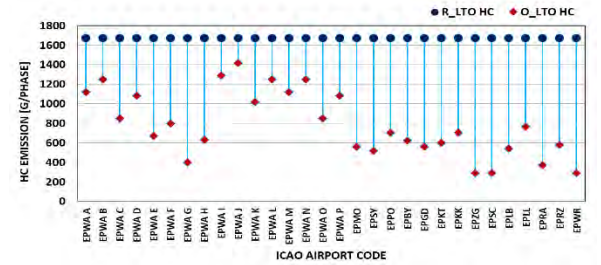

(b)

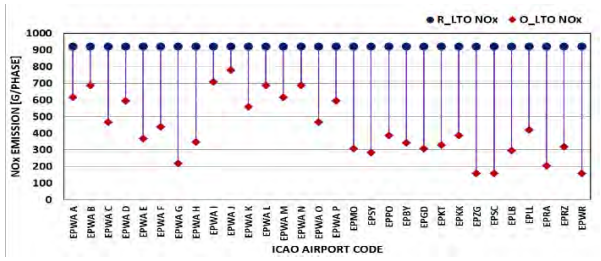

(c)

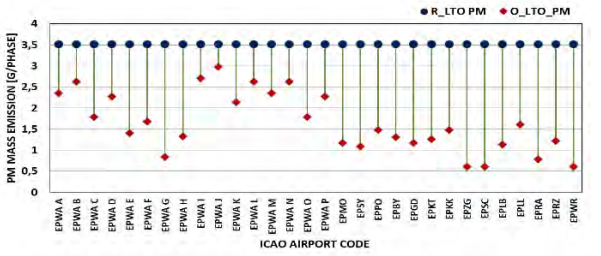

(d)

Fig. 1. Emission [g/phase] of harmful compounds from GE CF34-10E turbofans for each airport and scenario, (a) CO, (b) HC, (c) NO_x, (d) PM

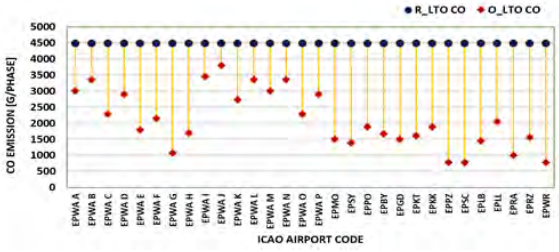

(a)

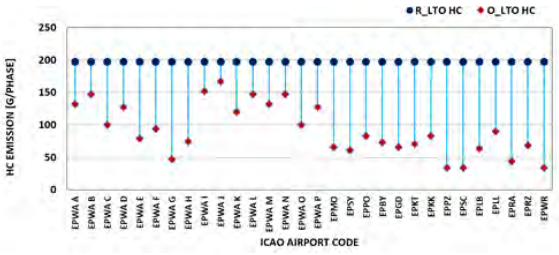

(b)

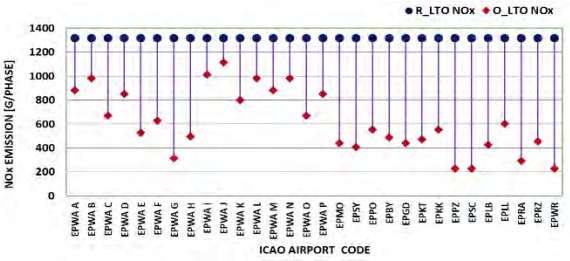

(c)

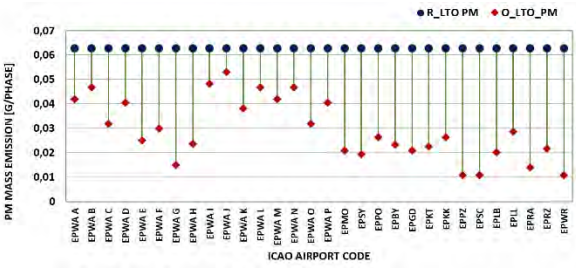

(d)

Fig. 2. Emission [g/phase] of harmful compounds from LEAP-1B from CFM International for each airport and scenario, (a) CO, (b) HC, (c) NO_x, (d) PM

As can be seen, the difference in emission levels for R_LTO and O_LTO is very large. In the case of CO emissions, the reduction ranges from 1000 to 3500 g/phase for each airport. Hydrocarbon emissions using operational conditions will be reduced by 50–160 g/phase. The reduction in nitrogen oxide emissions is from 300 to 1200 g/phase. However, the mass amount of particulate matter emitted by the LEAP engine during operational LTO test conditions is less than 0.03–0.05 g/phase. Figure 3 shows the emission of selected exhaust gases for the PW engine, which is installed on Wizzair's aircraft.

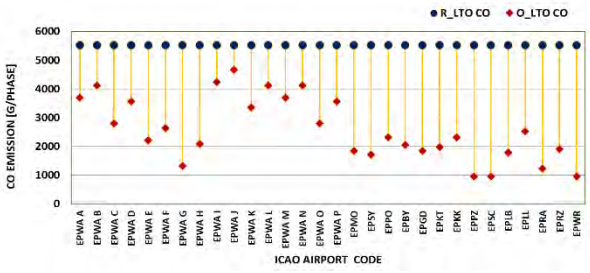

(a)

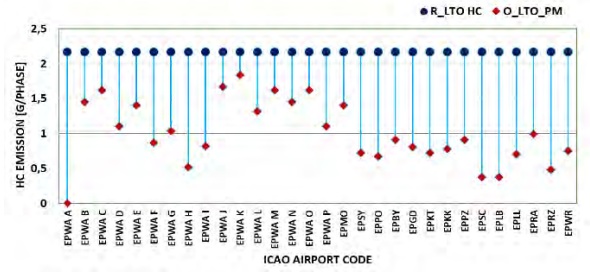

(b)

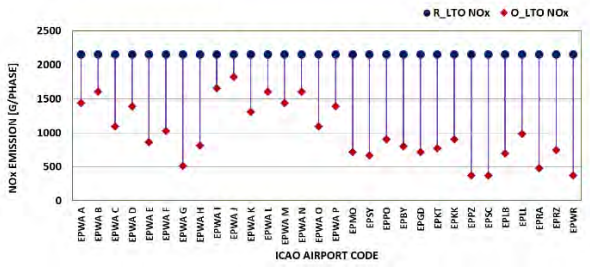

(c)

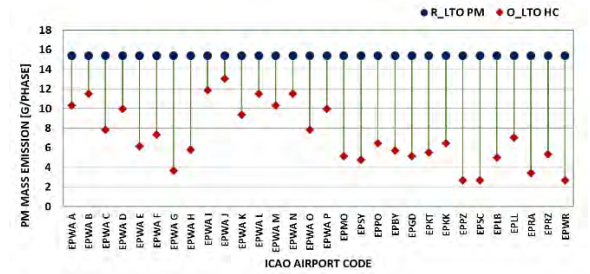

(d)

Fig. 3. Emission [g/phase] of harmful compounds from Pratt&Whitney PW1133G-JM for each airport and scenario, (a) CO, (b) HC, (c) NO_x, (d) PM

The difference in emission levels for R_LTO and O_LTO is very large. CO emissions are reduced by 1000–4500 g/phase, depending on the airport. Hydrocarbon emissions using LTO operating conditions will be reduced by 0.5–1.75 g/phase. The reduction in nitrogen oxide emissions is from 500 to 1750 g/phase. However, the mass amount of particulate matter emitted by the PW engine during the operational conditions of the LTO test is lower than 3 to 14 g/phase. Figure 4 shows the percentage reduction in emissions for each of the analyzed components. Due to the time variable used in formula (1), the reduction for each component will be the same percentage.

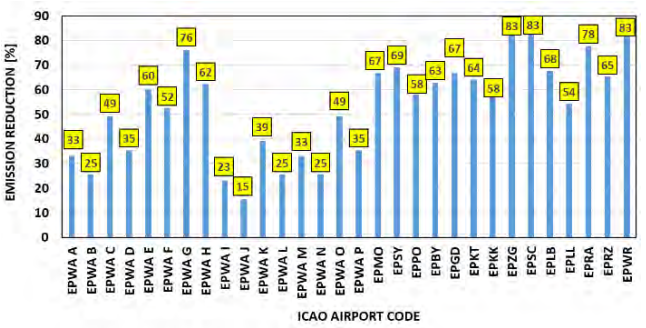

Fig. 4. Reduction of each analysed compound emission for each airport

As can be seen, the highest emission reduction occurs for the EPWR (Wroclaw), EPZG (Zielona-Gora) and EPSC (Szczecin) airports. For EPZG and EPSC airports, this is an expected result, due to the fact, that these are airports with one of the smallest numbers of passengers transported in Poland, so the infrastructure of these airports isn't highly developed. On the other hand, EPWR airport belongs to the group of airports that served at least 1 million passengers in 2022. A similar situation applies to the airport in Katowice (EPKT), Gdansk (EPGD) and scenario G at the Warsaw Chopin Airport (EPWA). The next step in the analysis was to compare and contrast the results obtained for each chosen propulsion. For this purpose, the analyzed variables were standardized (emissions for individual exhaust gas compounds).

Standardization enabled a numerical comparison of the analyzed propulsion units despite significant differences in the obtained emission values. Based on the calculated averages, charts were prepared showing the emission of each analyzed compound for each of the three compared drives (Fig. 5). Figure 5 shows the emission levels of selected exhaust gas components for each analyzed drive unit. As you can see, the GE unit, used mainly in the LOT Polish Airlines fleet, emits the largest amount of CO and HC and the lowest amount of NO_x. The LEAP engine used in the Ryanair fleet emits the lowest amount of PM, while the CO is emitted in larger amounts by GE and PW units. On the other hand LEAP unit emitted the highest values of PM. The PW engine, used mainly in the Wizzair fleet, is characterized by the highest emissions of NO_x. CO emissions reach a higher value for the PW unit than for the LEAP unit.

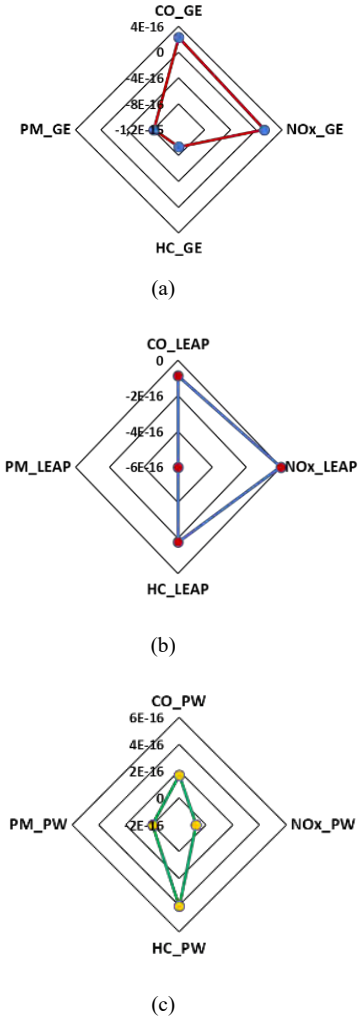

Fig. 5. Characteristic of compounds emission for each propulsion using standardization

The PW1133G-JM engine is the newest engine in terms of other units. It has the highest value of the double-flow rate and is designed with a fan reduction gear. This engine is most often found in the configuration of the Airbus A321neo aircraft. The value of the double-flow ratio is 12:1, i.e. for every 13 units of air sucked into the engine, 12 units bypass the core and do not participate in the combustion process [20, 21, 23]. The Pratt & Whitney engine produces the lowest emissions relative to the thrust produced, which means high engine operating efficiency. Continuous improvement of aircraft structures, construction and modification of combustion chambers and other elements used in aircraft engines has a significant impact on reducing emissions and improving the efficiency of engine units [15, 20, 23].

4. Discussion

To make accurate exhaust emission calculations from all modes of transport, the actual conditions should be considered. For example in road transport the emission measurements are performed in real driving conditions to receive the data in similar conditions in which the vehicle is operated by the user [18]. In aviation the regulation LTO cycle conditions present engine operation parameters during four phases, so this test procedure is proper in case of aircraft engines comparison. However, the same procedure is taken into account for calculations of the environmental impact of air transport to airport-proximate areas. For the taxiing phase, operational times at individual airports will be significantly different from those contained in the procedural regulations. The operational taxiing time of 26 minutes may apply to some of the largest airports in Europe, such as Istanbul, Amsterdam or Paris [17]. For Polish conditions and all smaller and medium-sized European airports, the time of 26 minutes used in assessing the impact of emissions from air transport on airport-proximate areas will be completely inadequate. In article indicated statistically significant differences between the emissions of selected exhaust gas components, which confirm legitimacy of operational conditions in the LTO aspect. EPWA airport served 14.5 million passengers in 2022, which is a larger number than airports in e.g. Barcelona or Copenhagen, and half of the passengers served at the largest airport in Europe – Istanbul [17].

Based on the research results, it was shown that LTO operating time is a very important aspect in analyzing the impact of air transport on airport-proximate areas. For EPWA airport, the best scenario is scenario G [9]. The location of the passenger terminal and arrival or departure procedures from the airport, as well as the location of taxiways, are key importance in this case. The above-mentioned factors mean that even an airport with relatively high passenger traffic (taking into account Polish conditions) can reduce the amount of exhaust gas components emitted through appropriate infrastructure and procedures. The issue of the impact of air transport on airport-proximate areas is actively discussed by the scientific community due to the dynamic development of aviation and emerging regulations aimed at limiting exhaust emissions [6, 7, 14, 22, 24, 25]. One of the articles discussed emissions at the Bejingdax International Airport. The article showed that among all aircraft types, the B738 emitted the most CO_2, as it accounted for almost half of all the flights. The air quality simulations showed that the air pollutant diffusion range was concentrated within 15 km of the airport and the surrounding areas. The contribution of airport emissions to NO_x concentrations was most apparent under the most unfavorable meteorological conditions [22]. One of the articles showed, using the example of Antalya International Airport, that aircraft of the B737 family are found to have the highest global warming potential and environmental cost, with values of 630,633.3 GWP and 39,723.4 Euros, respectively [4]. This is consistent with the research presented in the article. It was pointed out that the B737 emitted a larger amount of selected exhaust gas components compared to the Airbus A321neo. On the other hand, apart from the direct impact of air transport on airport-proximate areas, scientists also consider other sources of pollution occurring at the airport. One of the articles showed that motor vehicles including taxis and parking vehicles are a major source of air pollutants in the hub [7]. Another authors marked, that the impact of airport operations on a particular number concentration in the adjacent neighbor-

hood is comparable to the combined impact of busy roads in the area [24].

The presented considerations are intended to highlight the importance of operational conditions in analyzes related to the impact of air transport on emissions in airport-proximate areas and to demonstrate that the types and models of aircraft used by airlines are of great importance in local emissions of exhaust gas components. This is indicated by the emission of propulsions units made in this article.

5. Conclusions

The article presents considerations regarding the operational conditions of airports, that should be taken into account when assessing the impact of air transport on airport-proximate areas using the LTO test. Statistically significant differences were found between the emissions of selected exhaust gas components in the regulation LTO test and the operational LTO test. Analyzes were carried out concerning three different propulsions that are most often used by carriers serving the largest number of passengers in Poland.

Presented analyzes are important in the context of the dynamic development of aviation and developing projects aimed at neutralizing exhaust emissions into the atmosphere. The analysis covers current research topics, which are reflected in the presented discussion of the obtained results and their relation to conducted analysis by the scientific community in the area of aviation impact on the environment.

Nomenclature

AIP	compression ignition
CORSIA	Carbon Offsetting and Reduction Scheme for International Aviation
EASA	European Union Aviation Safety Agency
ICAO	International Civil Aviation Organisation
LCC	low-cost carriers
LTO	landing and take off
SESAR	Single European Sky ATM Research

Bibliography

[1] Boeing, Commercial Market Outlook 2022–2041. https://www.boeing.com/market/index.page (accessed on 11.2023).

[2] Christodoulakis J, Karinou F, Kelemen M, Kouremadas G, Fotaki EF, Varotsos CA. Assessment of air pollution from Athens International Airport and suggestions for adaptation to new aviation emissions restrictions, Atmos Pollut Res. 2022;13(6):101441. https://doi.org/10.1016/j.apr.2022.101441

[3] Civil Aviation Authority https://www.ulc.gov.pl/pl/statystyki-analizy/statystyki-i-analizy-rynku-transportu-lotniczego (accessed on 11.2023)

[4] Ekici S, Şöhret Y. A study on the environmental and economic aspects of aircraft emissions at the Antalya International Airport. Environ Sci Pollut R. 2021;28:10847-10859. https://doi.org/10.1007/s11356-020-11306-w

[5] Eurocontrol, Standard Inputs for Economic Analyses, December 2020. https://www.eurocontrol.int/publication/eurocontrol-standard-inputs-economic-analyses (accessed on 11.2023).

[6] Eurocontrol. Data Snapshot on CO_2 emissions by flight distance. https://www.eurocontrol.int/publication/eurocontrol-data-snapshot-co2-emissions-flight-distance (accessed on 11.2023).

[7] Fritz S, Grusdat F, Sharkey R, Schneider C. Impact of airport operations and road traffic on the particle number concen-tration in the vicinity of a suburban airport. Frontiers in Environmental Science. 2022;10:1-14. https://doi.org/10.3389/fenvs.2022.887493

[8] Galant M, Nowak M, Kardach M, Maciejewska M, Łęgowik A. Using the simulation technique to improve efficiency in general aviation. In: Computational Technologies in Engineering. Proceedings of the 15th Conference on Computational Technologies in Engineering. AIP Conf Proc. 2019: 2078:020097. https://doi.org/10.1063/1.5092100

[9] Galant-Gołębiewska M, Nowak M, Jasiński R, Ginter M, Kurzawska P, Maciejewska M. Methodical aspects of the LTO cycle use for environmental impact assessment of air operations based on the Warsaw Chopin Airport. Aviation. 2021;25(2):86-91. https://doi.org/10.3846/aviation.2021.14972

[10] ICAO, Aircraft Engine Emission Databank https://www.easa.europa.eu/en/domains/environment/icao-aircraft-engine-emissions-databank (accessed on 11.2023)

[11] ICAO, Annex 16: Environmental protection, vol. I: Aircraft noise, 4th ed. ICAO.

[12] Jasiński R, Galant-Gołębiewska M, Nowak M, Ginter M, Kurzawska P, Kurtyka K et al. Case study of pollution with particulate matter in selected locations of Polish cities. Energies. 2021;14(9):2529. https://doi.org/10.3390/en14092529

[13] Kozak M, Kryger T. Siejka P. Environmental analysis of the traffic closure on Piotrowo and Berdychowo streets in Poznań. Combustion Engines. 2022;190(3):18-22. https://doi.org/10.19206/CE-142593

[14] Kwasiborska A, Skorupski J. Assessment of the method of merging landing aircraft streams in the context of fuel consumption in the airspace. Sustainability. 2021;13(22):12859. https://doi.org/10.3390/su132212859

[15] Lasota MK, Zabielska A, Jacyna M, Żak J. Research and analysis of the operation of vehicles with various propulsion systems, including costs and CO_2 emissions. Combustion Engines. 2023;195(4):3-13. https://doi.org/10.19206/CE-169845

[16] LOT Polish Airlines. https://www.lot.com/us/en/explore/about-lot/fleet (accessed on 07.2023)

[17] National Geographic. The biggest airport in Europe. https://www.national-geographic.pl/traveler/artykul/najwieksze-lotnisko-w-europie (accessed on 11.2023)

[18] Nowak M, Jasiński R, Galant M. Implementation of the LTO cycle in flight conditions using FNPT II MCC simulator. IOP Conf Ser: Mater Sci Eng. 2018;421(4):042060. https://doi.org/10.1088/1757-899X/421/4/042060

[19] Palmer WJ. Will sustainability fly?: Aviation fuel options in a low-carbon world. Reciel. 2017;26(3):307-309 https://doi.org/10.1111/reel.12224

[20] Szczeciński S, Balicki W, Chachurski R, Głowacki P, Kawalec K, Kozakiewicz A et al. Aviation power units – part 3. Military Technical Academy. Warsaw 2016.
[21] Szuman B, Lipka P, Reklewski T. Exhaust emissions from aircraft engines (in Polish). Civil Aviation Office. Department of Aviation Technology. Department of Environmental Protection, Warsaw 2013.
[22] Wang Y, Zou C, Fang T, Sun N, Liang X, Wu L et al. Emissions from international airport and its impact on air quality: a case study of Beijing Daxing International Airport (PKX), China. Environ Pollut. 2023;336:122472. https://doi.org/10.1016/j.envpol.2023.122472
[23] Wisłocki K. Aircraft drives, basics, systematics, history, construction. Publishing House Poznan University of Technology, Poznan 2023.
[24] Xu H, Xiao K, Pan J, Fu O, Wei X, Zhou J et al. Evidence of aircraft activity impact on local air quality: A study in the context of uncommon airport operation. J Environ Sci. 2023; 125:603-615. https://doi.org/10.1016/j.jes.2022.02.039
[25] Zhu Y, Diao M, Li J. Examining indoor air pollution in a large-scale integrated transportation hub in Shanghai. Transport Res D-Tr E. 2021;97:102947. https://doi.org/10.1016/j.trd.2021.102947

Marta Maciejewska, DEng. – Faculty of Civil and Transport Engineering, Poznan University of Technology, Poland.
e-mail: *marta.maciejewska@put.poznan.pl*

Paula Kurzawska-Pietrowicz, MEng. – Faculty of Civil and Transport Engineering, Poznan University of Technology, Poland.
e-mail: *paula.kurzawska@put.poznan.pl*

Article citation info:
Kubica G, Lageweg S. Prospects for the development of drivetrain systems in trucks. Combustion Engines. 2024;199(4):74-80. https://doi.org/10.19206/CE-186564

Grzegorz KUBICA
Stefan LAGEWEG

Combustion Engines
Polish Scientific Society of Combustion Engines

Prospects for the development of drivetrain systems in trucks

ARTICLE INFO

Received: 30 November 2023
Revised: 31 January 2024
Accepted: 27 March 2024
Available online: 5 June 2024

The article presents the directions of development of drive systems in trucks. A database of vehicles and their technical data was developed. This data contains information about the drivetrain configuration. The external characteristics of the engines and the structure of the drivetrain were analyzed. It was found that the factors determining development are primarily economic and ecological aspects. It was noticed that, based on the configuration of the drive system, vehicles can be divided according to their purpose and type of transport. Vehicles intended for international transport are characterized by low gears and engines that achieve high torque at low engine speeds. Construction vehicles and vehicles intended for oversize transport are characterized by large gear ratios and torque amplification systems. The structure of electric vehicle drive systems is different from conventional vehicles. Gearboxes usually have two gears, and drive axles may have integrated engines located next to the main gear or in the final drive position. The study also made it possible to outline the problem of the short range of such cars and the need for further work on increasing it.

Key words: *drivetrain, truck, electrification, hybrid, e-axle*

1. Introduction

The key function of drivetrain systems is to transmit torque and rotational speed to the vehicle's drive wheels. Trucks perform specific tasks which causes these systems to be highly personalized. The purpose of customization of powertrain systems is to ensure the effectiveness, durability and efficiency of the vehicle at an appropriately high level required by the company. The essence of personalization is to adjust technical parameters and components to the specific requirements of the user. Depending on the intended use of the vehicle, deviations from standard configurations may affect elements such as: the engine, gearbox, drive axle or axles (depending on the required needs, the vehicle may be equipped with multiple drive axles), and drive support systems.

The configuration of the vehicle depends on the country, road quality and type of road surfaces, daily distance the vehicle covers, the type of cargo being transported, its weight, the topographical characteristics of the routes, and operating costs. Simultaneously work is being conducted on hydrogen technology and electric drive systems in heavy-duty trucks [20, 21]. The reduction of vehicle emissions is associated with certain challenges, including the increase in the vehicle's own weight due to the use of additional equipment [2, 13, 15, 25]. On the other hand, there is pressure from owners to reduce weight in order to increase payload capacity.

The article highlights the changes that have occurred in powertrain systems in recent years and shows the differences in the configuration of powertrain systems in trucks depending on their intended use.

1.1. Characteristics of the division of trucks

Trucks as previously mentioned are vehicles that have various applications. Therefore, these vehicles can be classified on the basis of their purpose [3]. Each group of vehicles will be characterized by specific differences in their configuration. There are many vehicles that, due to their specific features of the drivetrain, become specialized vehicles which normally are not used in different transport tasks that are intended. An example of such specialized configurations are trucks intended for long-distance transport on regular routes running through areas with gentle elevations of the ground. In this case, the drivetrain can be selected in such a way as to minimize fuel consumption, thereby reducing the company's operating costs associated with material and energy consumption as much as possible [8, 9, 14]. This is an example of a vehicle that in mountainous terrain will generate problems such as high fuel consumption, low average speed due to insufficient power, increase drivers' stress levels due to time pressure and the need for greater concentration on the road.

Another example of a specialized configuration is trucks designed for oversized loads - the priority is to efficiently transfer high torques to the ground via multiple drive axles. Another category of heavy-duty vehicles to mention is dump trucks used in the construction industry. These vehicles are characterized by a short, compact, multi-axle chassis, often with multiple drive axle systems for both steering and driving axles.

Ballast tractors, in contrast to distribution or long-haul transport vehicles, are equipped with a greater number of drive axles. Besides the increased number of wheels capable of transmitting high torque these vehicles are often featured in hub reduction gears.

Furthermore, there are cases in which vehicles also differ in the type of used clutch. Examples of this can be the aforementioned tractors used for transporting heavy, non-standard loads or construction vehicles. Examples would include the above-mentioned truck used to transport heavy, abnormal loads, or construction vehicles.

Depending on the needs, various types of gearboxes can be used in vehicles. Currently, the most popular type is the automated transmission. Among newly sold vehicles, only a small percentage feature a manual transmission. Despite the significant popularization of automated gear shifting,

there is not only one possible clutch variant in vehicles. Cars can now be equipped with a traditional single-disc or double-disc dry clutch or a turbo retarder clutch, enabling more smoother transmission of high torque during uphill starts and effective vehicle braking of the vehicle when going downhill.

Truck manufacturers mostly use components from other manufacturers that specialize in the production of specific drivetrain components. Gearboxes are mostly manufactured by companies such as ZF, Eaton or Voith. In the European market, the most commonly encountered gearboxes are ZF AS-Tronic and Traxon, which have gained significant popularity in vehicles manufactured by f. ex. MAN, DAF, IVECO. There is a group of manufacturers including VOLVO, MERCEDES-BENZ and SCANIA who have chosen to develop their own designs. The use of gearboxes made by external suppliers provides economic benefits, and these vehicles are often more cost-effective to operate due to the use of components produced on a larger scale [12].

1.2. Electric drive solutions in heavy-duty vehicles

1.2.1. Hybrid module

Reducing the pollution emitted by different cars is a crucial aspect in the European Union. One of the ways to lower the emissions is to reduce the fuel consumption. To do this, hybrid modules can be used. Below (Fig. 1), a kinematic scheme of an typical module that can be installed in commercial vehicles.

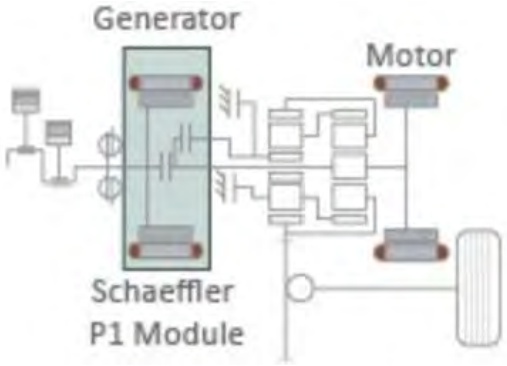

Fig. 1. Kinematic scheme of the P1 hybrid module [5]

The next photo (Fig. 2) shows the technical solution of the module mounted between the engine and the gearbox, developed by Schaeffler. The device can perform several functions. By installing an electric motor inside the flywheel, it is possible to support the operation of the drive system by generating additional torque. Depending on the version of the installed module, it also enables maneuvering at low speeds and provides propulsion in the initial phase of movement without involving a combustion engine [18].

1.2.2. Electric vehicle drive module

These modules are complete devices used in ICE vehicles. Their compact design allows for the installation of the system in the location where a traditional gearbox is usually mounted. This allows manufacturers to offer two drive versions of the vehicle on one platform. Both electric and internal combustion engine vehicles do not require any structural changes in the frame and other drivetrain components. An example of a powertrain module, such as the ZF CeTrax, incorporates an electric motor, a three-speed gearbox, gear shifting actuators, an inverter and an ECU.

Despite its small size, the engine can deliver up to 340 kW of continuous power [22, 23].

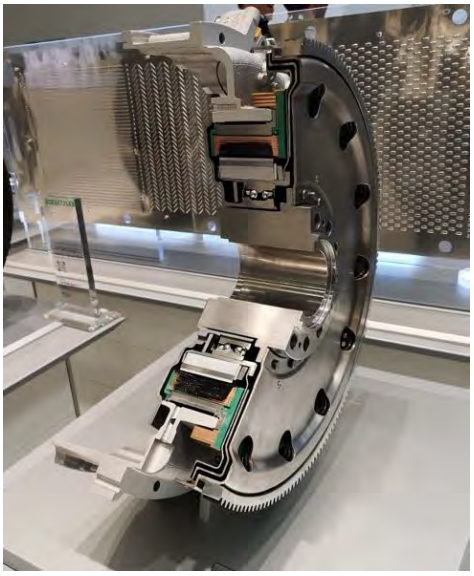

Fig. 2. A cross-sectional view of Schaeffler heavy duty hybrid module P1

Fig. 3. Combined drive module ZF CeTrax

1.2.3. Drive axles for electric vehicles

Electric vehicles come in various powertrain configurations. They can feature traditional setups similar to those in internal combustion engine vehicles designed for freight transport, using gearboxes, drive shafts and axles to transmit power. In this case, electrical modules such as the above-mentioned ZF CeTrax are used (Fig. 3). This system is primarily used in vehicles that share a common platform for different powertrain types, significantly reducing production costs.

A vehicle equipped with a drive axle with a built-in electric motor as example the Alison eGEN POWER 100s (Fig. 4) will be built in a different way. Electrified drive axles can be divided into two types depending on the place the electric motor or motors are installed:

1. With a centrally located engine – this is a solution in which an electric motor is placed at the input to the main transmission. There are designs in which two motors are mounted on both sides of the transmission and with integrated gearboxes. The advantage of this solution is that it frees up space in the vehicle between the frame rails where a gearbox is usually located In the case of emergency vehicles, this may be particularly important because the lack of a drive shaft and gearbox allows this space to be used to accommodate additional equipment (for example, in a fire truck) or by lowering the fire extinguishing water tank. This solution also enables the installation of larger traction battery packs.
2. With engines placed in the hubs of the drive axle – the axle is without a differential or final drive. The location of two independent motors in the hubs allows to differ the wheel speeds. This solution offers even greater space savings compared to a centrally located motor. Locating the engines in the hubs partially frees up space between the vehicle's wheels. This makes it possible to lower the floor level between the side members or, in the case of city buses, lower the floor level and create a low-floor vehicle with the floor at one level along the entire length of the vehicle.

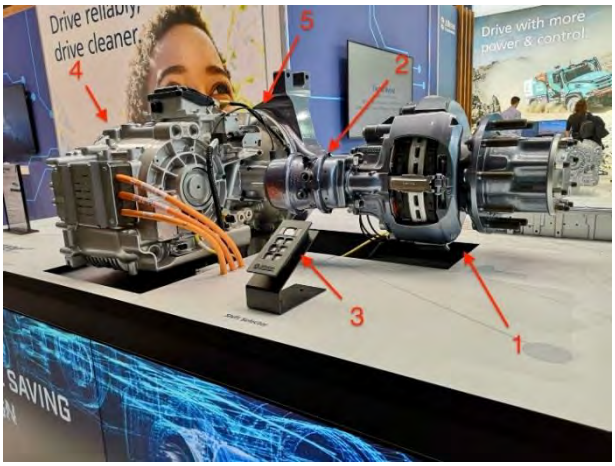

Fig. 4. Alison eGEN POWER 100s – electric drive axle with a centrally located motor; where: 1 – disc brake caliper; 2 – brake chamber; 3 – shift selector unit; 4 – electric motor; 5 – main gear with differential

1.2.4. Active trailer axles

Trailers for heavy-duty vehicles can be equipped with an energy recuperation system integrated into the axle. The low rolling resistance of the axles ensures that the vehicle rolls freely and does not affect fuel consumption. These axles can be fitted in various trailers as example reefers, walking floor trailers or curtain trailers. The trailers with these axles are equipped with battery packs which replace pallet boxes in traditional constructions. In reefer trailers the traditional refrigeration unit can be replaced by an electric one. It is already proven that these types of axles provide enough electricity for the refrigeration unit for the whole day when the trailer is used for typical local and city distribution [16].

In trailers with walking floor systems that use axles like the one shown on photo (Fig. 5), electric hydraulic pumps are installed in contrast to traditional walking floor trailers which need to be hooked up with tractors with additional hydraulic pumps. These types of axles can not only provide in electricity the mentioned above receivers but they can also assist in propelling the vehicles. SAF Holland offers an axle with an integrated motor generating 120 kW of power and 320 Nm of torque. Even though these axles are designed for trailers, they can be a good basis for developing a trailing axle for a hybrid truck. This will simplify the drivetrain's design while maintaining its conventional form, and the additional axle can function as an independent executive component controlled by a common controller. It is estimated that by implementing such an axle in a road vehicle it is possible to save up to 4,000 liters of diesel fuel per year [17].

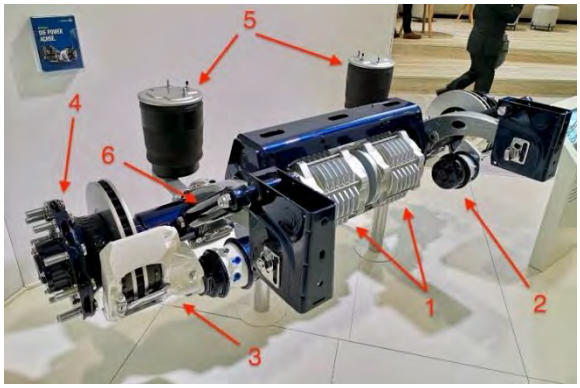

Fig. 5. Electric trailer axle with a build in electromotor for energy recuperation: 1 – electric motors; 2 – brake chamber; 3 – brake caliper and disc brake; 4 – wheel hub; 5– air suspension bellow; 6 –shock absorber

2. Methodology

In order to determine the prospects of the development of drive systems, it was necessary to create a vehicle database. Due to the variety of vehicle configurations, it was decided to assign each vehicle to a group corresponding to the type of transport performed. Each vehicle has been assigned at least one symbol graphically representing the type of transport performed (Table 1). The analysis examined the properties of elements such as engine displacement, maximum power and torque, gearbox type and its gears, drive axle ratios, the presence of differential and gearbox, and their gears.

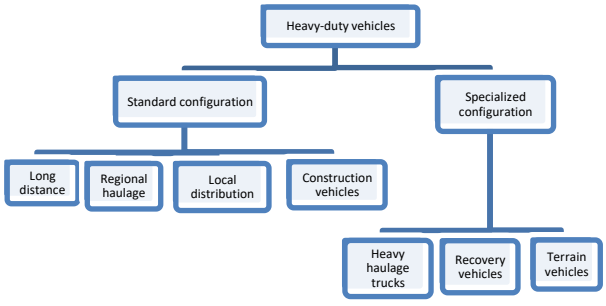

Fig. 6. Classification of HDV

In order to better illustrate the division into the specified vehicle categories, additional graphics have been developed showing the specialization of HDV (Fig. 6) and the use of electric drives (Fig. 7).

Table 1. List of trucks, their technical data and driveline parameters

	Made/ model	Purpose of use	Engine	Power [kW/RPM]	Torque [Nm/RPM]	Gearbox	Gear ratios	Type of gearbox	Drive axle ratio	Rub gear ratio
1	IVECO X-WAY 440X48 4X2 HI-TRACTION		FPT Cursor 11	353/1900	2300/970	ZF 12TX2210TD RAXON	16.69–1.00	Automated	2.85	–
2	DAF XF 480 4X2		Paccar MX13	355/1600	2350/ 900-1365	ZF 16S2300 ECO-SPLITTER	16.41–1.00	Manual	2.38	–
3	IVECO TRAKKER 4X4		FPT N67	206/1950-2500	1000/1250-1950	ZF 6S1005 ECO-LITE	6.75–0.78	Manual	6.95	0.525
4	DAF XF 480 4X2 LOW-DECK		Paccar MX13	355/1600	2350/ 900-1365	ZF 12TX2210 TD TRAXON	16.69–1.00	Automated	2.05	–
5	IVECO TRAKKER 450KM 8X8		FPT Cursor 10	331/1450-1900	2200/ 900-1450	ZF16S 2220 TO	13.8–0.84	Manual	4.67	N/A
6	SCANIA P280 6X2		Scania DC9	206/1400-1900	1400/ 1000-1400	G25CM1	20.8–0.78	Automated	3.8	–
7	SCANIA P450 4X2		Scania DC13	331/1340-1800	2350/ 900-1340	GRS905R	16,41-1,00	Automated	2.35	–
8	DAF CF 8X4		Paccar MX13	340/1450-1700	2300/N/A	ZF 16S2500	13.8–0.84	Manual	4.05	N/A
9	MERCEDES-BENZ ACTROS 3363 LS SLT 6X4		Mercedes-Benz OM473	460/1700	3000/1100	G280-16	11.7–0.69	Automated	4	1.333
10	VOLVO FE 6X2 ELEC-TRIC*			130/N/A		–	–	–	–	–
11	MERCEDES-BENZ UNIMOG U5023 4X4	Terrain vehicle	OM 934 LA	170/N/A	900/1400	UG 100/8	9.57–0.74	Automated	2.55	–
12	Pepper Actros MP3**		ZF CeTrax	175/0-8500	2170/–	ZF CeTrax	3.36	Automated	2.84	–
13	DAF LF		Paccar PX-5	157/2300	850/ 1200-1500	ZF 6S800	6.58–0.78	Manual	3.73	–

* Range: max. 275 km ** Range: max. 220 km

In addition to physically existing vehicles, the list also includes vehicles proposed by configurators available on manufacturers' websites. After entering basic data such as forecasted mileage, type of transport (distribution, international transport etc.), topography of the routes on which the truck will travel and the type of vehicle frame, the application selects the parameters of the drive system. All parameters are selected in such a way that the vehicle exhibits the highest possible efficiency.

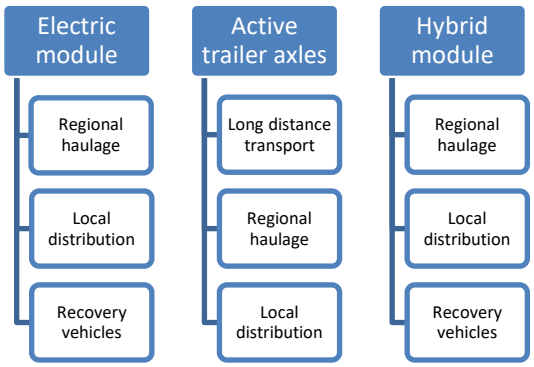

Fig. 7. Possible applications of electrical components depending on the tasks performed

The group of specialized vehicles includes cars such as a fire truck or the Mercedes-Benz Unimog, which is a heavy off-road vehicle, designed to work in difficult terrain. One vehicle that stands out significantly from the others is the Actros SLT, designed for transporting oversized cargo.

3. Results discussion

Table 1 presents a list consisting of various vehicles with different configurations. The analysis was conducted on base of technical parameters of drive systems.

3.1. Engines

Due to the key role of the drive unit in the drive system, the values of maximum torque, maximum power and displacement were analyzed. A clear observation emerges from the comparison of the parameters of the ICE used. Despite numerous solutions and different applications, the main parameters can be divided into four groups:

1. Small – power 160–170 kW; torque 0.9–1 kNm
2. Medium – power approx. 200 kW; torque 1.4–1.5 kNm
3. Large – power 330–350 kW; torque approx. 2.3 kNm
4. Extra large – power 460–500 kW; torque approx. 3 kNm.

Table 2 presents a list of engines used in the vehicles selected for analysis, taking into account the division according to engine. In the lower part of the table are shown engines used in electric vehicles included in Table 1.

Vehicles with a lower GVW are equipped with smaller engines. Reduction in performance resulting from the need to meet exhaust emission standards. Trucks equipped with

them have slightly different engine characteristics. The maximum torque is achieved at higher RPMs than in mid-size and large engines. This is closely related to the combustion process and corresponds to the range of the lowest specific fuel consumption.

Electric motors installed in heavy-duty trucks generate less power, but they achieve very high torque values compared to the engine power. It should also be mentioned that these engines can operate at very high rotational speeds, providing high torque values in almost the entire revolution range.

Table 2. Values of basic operating parameters of the analyzed engines

Vehicle	Max. power [kW]	Max. torque [Nm]	Max. rpm	Engine displacement
Small engines				
11	170	900	2600	5.1
13	157	850	2500	4.5
3	206	1000	3150	6.7
Mid-size engines				
6	206	1400	2200	9.3
Large engines				
1	353	2300	2250	11.1
2; 4	355	2350	1800	12.9
5	331	2200	2150	10.3
7	331	2350	2100	13.0
8	340	2300	1700	12.9
9	460	3000	1700	15.6
Electric motors				
10	130	N/A		N/A
12	175	2170	8500	N/A

3.2. Gearboxes

Among the vehicles included in the list, 62% are equipped with automatic or automated gearboxes. The use of automatic control primarily allows to elimination the so-called human factor and achieves maximum drive transmission efficiency in all traction conditions. The predominance of automatic gearboxes proves the declining popularity of manual gearboxes.

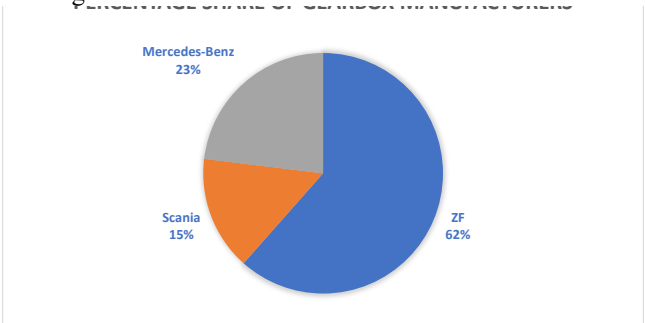

Fig. 8. Percentage share of gearbox manufacturers – based on Table 1

It can therefore be expected that in the upcoming years, the number of vehicles equipped with a manual gear shifting system will become even smaller, and the total number of vehicles with this technical solution will be only a small percentage. For many years, truck manufacturers have preferred to install proven and well-known units from well-known manufacturers (Fig. 8). Most truck brands outsource the development of mechanical transmissions to companies that supply this component. The most popular manufacturer on the European gearbox market is ZF. This company focuses on the production of ready-made technical solutions for drive systems. Their products are installed in as many as 62% of the vehicles included in the analysis.

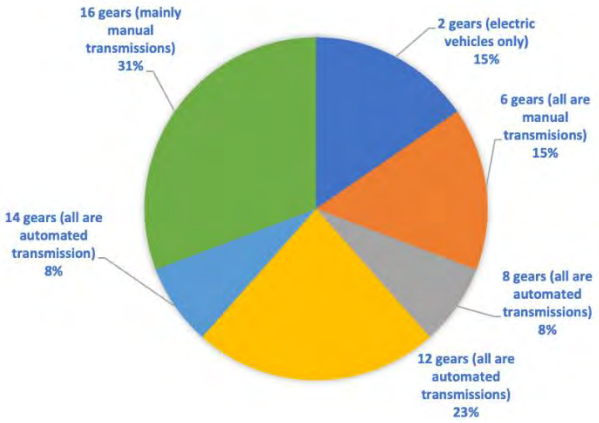

Fig. 9. Numbers of gears – based on Table 1

It can be concluded that trucks conventional use 12- and 16-speed gearboxes (Fig. 9). The number of gears is usually determined without taking into account the crawler or reverse gears. The least frequently used solutions in trucks are fourteen- and eight-speed gearboxes. The appearance of the 14-speed gearbox is due to the construction of the G25CM1 gearbox. This is a gearbox in which the first two gears take over the role of the crawler gears.

Among the gears with 16 gears, 75% are manually controlled. Considering the declining popularity of manual gearboxes, it can be concluded that transmissions with such a number of gears will become increasingly rare in the coming years. They will only be used in specialized vehicles for example in ballast tractors.

All 12-speed gearboxes are automated. Taking into account the increase in the number of vehicles equipped with twelve-speed gearboxes and the fact that 100% of them are automated, it can be expected that in the near future, mainly twelve-speed gearboxes will be installed in trucks.

Among the analyzed vehicles, 64% is equipped with an overdrive gear. Overdrive gear allows reducing engine RPM when driving at a constant speed, which combined with a wide range of maximum torque and obtaining high values at low rotational speeds, will lead to reduced fuel consumption.

3.3. Main gear

Reducing the main transmission's gear ratio results in a decrease in the engine speed at the same driving speed, which allows for reduced fuel consumption.

Each vehicle in the list has a different drive axle ratio value. In most vehicles without overdrive, gears around 2.3–2.8 are common. Trucks equipped with overdrive usually have higher final drive ratio values. If a low final drive ratio were also used in such a vehicle, a situation could arise in which the engine would not be able to generate a high enough torque to enable the vehicle to move in the highest gear.

Vehicles with very specific applications, such as ballast tractors moving with very heavy loads, are equipped with hub gears.

3.4. Devices supporting the operation of the drive system

Devices supporting drive systems, such as active axles in semi-trailers, do not currently constitute a very large population due to the fact that they are relatively new designs – they appeared in the offer of semi-trailer manufacturers a few years ago. During road tests conducted by the BMW concern, it was shown that Krone semi-trailers equipped with an active axle system reduce fuel consumption even up to 40% [1, 10]. In addition to supporting vehicle propulsion, these systems enable to power up receivers mounted in semi-trailers. For example, in a refrigerated vehicle, this allows the reefer to be powered, thus obtaining significant benefits in the form of no pollutant emissions and no unwanted sound, which is particularly desirable in urban distribution where deliveries often take place in the morning. Considering the benefits that their use can bring, they will become much more popular in the coming years [6, 19].

4. Conclusions

Climate protection will lead to more common adoptions of new solutions [7, 11]. Currently, road toll tariffs depending on the carbon dioxide emission class are being introduced in two EU countries [24]. This will undoubtedly motivate us to replace the fleet with a more fuel-efficient one, which will contribute to the increased use of micro-hybrid systems and active axles in semi-trailers.

In the context of road charges tied to CO_2 emissions, electric vehicles seem to be the best choice because they will benefit from very large discounts. may drive further efforts to extend the range of electric heavy-duty vehicles. Currently, the technology of storing electrical energy in battery packs allows a driving distance of approximately 300 km in optimal conditions. In winter, this range is reduced due to low temperatures.

A way to increase the range of electric vehicles may be to use a hydrogen cell and "Hydrozine" fuel, commonly known as formic acid. Intensive work is conducted to use hydrogen as a fuel, which also allows for increasing the range of electric vehicles [4].

Observing contemporary trends in the design of powertrains in trucks, the following conclusions can be drawn:

1. The gearbox offer is dominated by automated transmissions. 12- and 16-speed gearboxes are most often used in trucks. The aim is to lower the top gear in order to reduce fuel/energy consumption. Manual transmissions are systematically being pushed out of the market.
2. The increasing flexibility of drive units, the popularization of automated control and the use of electric motors make it possible to reduce the number of gears in gearboxes. New forms of energy storage are being developed to extend the range of electric vehicles.
3. Further development of hybrid modules makes it possible to simplify the design of drive systems. This module can be used as an electronic clutch, torsional vibration damper or starter for an internal combustion engine.
4. Additional powertrain support systems gain popularity due to increasing torque in phases of increased load and reducing overall exhaust emissions. Systems of this type use primarily electricity for propulsion. They can be seen as transitional solutions before the full implementation of electric drivetrains in this vehicle category.

Nomenclature

CNG compressed natural gas
ECU electronic control unit
GVW gross vehicle weight
HDV heavy-duty vehicles
ICE internal combustion engine

Bibliography

[1] A semi-trailer with a drive as powerful as the tractor (Naczepa z napędem równie mocnym co ciągnik – in Polish). https://40ton.net/naczepa-z-napedem-rownie-mocnym-co-ciagnik-500-km-na-osi-w-krone-mega-liner/

[2] Andrych-Zalewska M, Chłopek J, Merkisz J, Pielecha J. Investigations of exhaust emissions from a combustion engine under simulated actual operating conditions in real driving emissions test. Energies. 2021;14:1-20. https://doi.org/10.3390/en14040935

[3] Chojnowski J, Karczewski M. Analysis of the market structure of long-distance transport vehicles in the context of retrofitting diesel engines with modern dual-fuel systems. Combustion Engines. 2022;188(1):13-17. https://doi.org/10.19206/CE-142167

[4] DENS pilot demos for hydrozine generator. Fuel Cells Bulletin. 2021;2021(5). https://doi.org/10.1016/S1464-2859(21)00264-9

[5] Eckenfels T, Fischer N, Lehmann S, Neuberth U, Reitz D. Innovative hybrid transmissions with electric DNA. Schaeffler Kolloquium. Digital conference book 2022. https://www.schaeffler.com/remotemedien/media/_shared_media_rwd/06_press/press_kits_events/kolloquium_2022/digital_conference_book/hybrid_powertrain/16_9-schaeffler-kolloquium-2022-hybrid-powertrain_03_rwd_1200.jpg

[6] Electric refrigerator with an electric generator (Elektryczna chłodnia z elektrycznym agregatem – in Polish). Transport Technika Motoryzacyjna 2018;7.

[7] Karczewski M, Szamrej G, Chojnowski J. Experimental assessment of the impact of replacing diesel fuel with CNG on the concentration of harmful substances in exhaust gases in a dual fuel diesel engine. Energies. 2022;15:4563. https://doi.org/10.3390/en15134563

[8] Kozak M, Lijewski P, Fuc P. Exhaust emissions from a city bus fuelled by oxygenated diesel fuel. SAE Technical Paper 2020-01-2095. 2020. https://doi.org/10.4271/2020-01-2095

[9] Kozak M, Lijewski P, Waligórski M. Exhaust emissions from a hybrid city bus fuelled by conventional and oxygenated fuel. Energies. 2022;15(3):1123. https://doi.org/10.3390/en15031123

[10] Krone semi-trailer equipped with e-axle – up to 40% savings (Naczepa Krone wyposażona w e-oś – do 40% oszczędności – in Polish). https://trailertotaal.nl/nieuws/item/krone-tot-40-besparing-met-e-as

[11] Longwic R, Tatarynow D, Kuszneruk M, Wozniak-Borawska G. Preliminary tests of a Diesel engine powered by diesel and hydrogen. Combustion Engines. 2023;195(4): 35-39. https://doi.org/10.19206/CE-169485
[12] MAN Truck&Bus Polska has a successful anniversary year (MAN Truck&Bus Polska udany rok jubileuszu – in Polish). Transport Technika Motoryzacyjna. 2018;8.
[13] Merkisz J, Bajerlein M, Zieliński B. The impact of parameter modifications in the Diesel engine power system on the emissions of harmful compounds. Combustion Engines. 2020;180(1):36-40. https://doi:10.19206/CE-2020-106
[14] Merkisz J, Kozak M, Molik P, Nijak D, Andrzejewski M, Nowak M et al. The analysis of the emission level from a heavy-duty truck in city traffic. Combustion Engines. 2012; 150(3):80-88. https://doi.org/10.19206/CE-117033
[15] Quiros DC, Thiruvengadam A, Pradhan S, Besch M, Thiruvengadam P, Demirgok B et al. Real-world emissions from modern heavy-duty diesel, natural gas, and hybrid diesel trucks operating along major California Freight Corridors. Emiss Control Sci Technol. 2016;2:156-172. https://doi.org/10.1007/s40825-016-0044-0
[16] Refrigerator tests with a power-generating axle – up to 9 hours of pause without turning on the diesel (Testy chłodni z osią generującą prąd – nawet 9 godzin pauzy bez włączania diesla – in Polish). https://40ton.net/testy-chlodni-z-osia-generujaca-prad-nawet-9-godzin-pauzy-bez-wlaczania-diesla/
[17] SAF-Holland E-axle Family from SAF. https://safholland.com/pl/en/download-center/document/resource/environment/project1_p/documents/documentationP/2022/2022_09/SAF-HOLLAND_E-Axles_en-DE.pdf
[18] Schaefler Technologies for hybrid and all-electric drive systems. https://www.schaeffler.pl/en/products-and-solutions/automotive-oem/hybrid_electrical_drive_systems/
[19] Schmitz Cargobull S.KOe koelt elektrisch. https://trailertotaal.nl/nieuws/item/schmitz-cargobull-s-koe-koelt-elektrisch
[20] Volvo FL electric truck. https://www.volvotrucks.pl/pl-pl/trucks/electric/volvo-fl-electric.html
[21] XCIENT Fuel Cell Truck. https://ecv.hyundai.com/global/en/products/xcient-fuel-cell-truck-fcev
[22] ZF's CeTrax lite electric drive for LCVs begins series production. https://www.greencarcongress.com/2023/04/20230413-zf.html
[23] ZF Tansmision & E-Mobility Driveline Systems for Trucks & Vans. https://www.zf.com/public/org/TruckVanDrivelineTechnoloTruck-undVan-Antriebstechnik_72596.pdf
[24] Ziółkowski A, Fuć, P, Jagielski A, Bednarek M. Analysis of emissions and fuel consumption in freight transport. Energies. 2022;15:4706. https://doi.org/10.3390/en15134706
[25] Ziółkowski A, Fuć P, Lijewski P, Rymaniak Ł, Daszkiewicz P, Kamińska M et al. Analysis of exhaust emission measurements in rural conditions from heavy-duty vehicle. Combustion Engines. 2020;182(3):54-58. https://doi.org/10.19206/CE-2020-309

Stefan Lageweg, MEng. – Faculty of Transport and Aviation Engineering, Silesian University of Technology, Katowice, Poland.
e-mail: *lagewegstefan@gmail.com*

Grzegorz Kubica, DSc., DEng. – Faculty of Transport and Aviation Engineering, Silesian University of Technology, Katowice, Poland.
e-mail: *grzegorz.kubica@polsl.pl*

Article citation info:
Birut A, Wójcik P, Niedworok A, Dziki R, Orzech Ł, Janicka A et al. Performance analysis of electric motor for Formula Student race car. Combustion Engines. 2024;199(4):81-87. https://doi.org/10.19206/CE-189938

Aleksandra BIRUT
Paweł WÓJCIK
Andrzej NIEDWOROK
Rafał DZIKI
Łukasz ORZECH
Anna JANICKA
Monika MAGDZIAK-TOKŁOWICZ

Combustion Engines
Polish Scientific Society of Combustion Engines

Performance analysis of electric motor for Formula Student race car

ARTICLE INFO

Received: 16 January 2024
Revised: 10 June 2024
Accepted: 11 June 2024
Available online: 28 August 2024

Formula Student presents a unique engineering challenge for students offering them a platform to introduce innovative ideas related to control algorithms and electric drives. This article presents design of the electric motor made by PWR Racing Team and its expected performance characteristics derived from the simulation. Developed control algorithm of tractive system implemented in SpeedGoat – a control computer based on Simulink – is introduced as well as adaptation of this algorithm for research on a torque transducer. Results from measurements gathered through this system are presented and compared to theoretical expectations offering insights into the real-world performance of the electric motor made by Formula Student team.

Key words: *electric vehicle, permanent magnet synchronous motor (PMSM), torque characteristics, real-time control system*

1. Introduction: the influence of Formula 1 on automotive development

Formula 1 (F1) is not merely a spectacle of speed and precision; it is a crucible of innovation that has significantly influenced automotive technology. This high-stakes motorsport, with its relentless pursuit of performance and efficiency, has driven advancements that permeate the broader automotive industry. This essay delves into the scientific and technical aspects of how F1 has shaped automotive development, focusing on engine technology, materials science, aerodynamics, electronics, and safety systems.

One of the most significant contributions of F1 to automotive engineering is the development of hybrid power units. Introduced in 2014, F1's hybrid engines combine a traditional internal combustion engine (ICE) with an Energy Recovery System (ERS) that captures and reuses energy. This technology has directly influenced the hybrid systems used in modern road cars. The ERS in F1 recovers energy from both braking (via the MGU-K or Motor Generator Unit-Kinetic) and heat from the turbocharger (via the MGU-H or Motor Generator Unit-Heat). This recovered energy is stored in batteries and can be deployed to boost performance. In consumer vehicles, similar hybrid systems improve fuel efficiency and reduce emissions. The principles of energy recovery and hybridization seen in F1 are evident in the regenerative braking systems and electric motors of hybrid and electric cars. For example, Toyota's Prius, a leading hybrid vehicle, employs regenerative braking to enhance fuel efficiency, a concept that owes much to the advancements pioneered in F1.

F1's adoption of turbocharging to boost engine power without increasing engine size has had a profound impact on road car engines. Turbochargers compress the intake air, allowing more oxygen to enter the engine, thereby increasing power output from a smaller engine displacement. This principle of downsizing, where smaller engines deliver the power of larger ones, is now common in the automotive industry.

Modern cars, such as the Ford EcoBoost series, use turbocharged engines to achieve a balance between performance and fuel efficiency. The lessons learned in managing heat, pressure, and durability in F1 turbo engines have been directly applied to improve the reliability and efficiency of road-going turbocharged engines.

The use of carbon fiber reinforced polymer (CFRP) in F1 car construction has revolutionized automotive materials science. CFRP offers a remarkable strength-to-weight ratio, which is crucial for both performance and safety. F1 cars use carbon fiber extensively in their chassis and bodywork to reduce weight while maintaining structural integrity.

This technology has transitioned into high-performance road cars and even some mainstream vehicles. The BMW i3 and i8, for instance, utilize carbon fiber in their construction to improve efficiency and performance. The lightweight nature of carbon fiber reduces overall vehicle weight, enhancing fuel efficiency and handling characteristics.

F1 teams have also pioneered the use of advanced metal alloys to withstand extreme conditions. Titanium, for example, is used in F1 for its excellent strength-to-weight ratio and resistance to high temperatures. These materials are now used in critical components of road cars, such as engine valves, connecting rods, and exhaust systems. The aerospace-grade alloys used in F1 enhance durability and performance in consumer vehicles.

Aerodynamics is a critical factor in F1 performance, influencing speed, stability, and fuel efficiency. F1 teams utilize Computational Fluid Dynamics (CFD) to design and optimize aerodynamic components. CFD simulations allow engineers to predict how air flows over the car and identify areas for improvement.

These techniques have been adopted by automotive manufacturers to design more aerodynamically efficient road cars. Enhanced aerodynamics reduce drag, improving

fuel efficiency and high-speed stability. The streamlined shapes and underbody designs of modern cars owe much to the aerodynamic research conducted in F1. For instance, the drag coefficient of production cars has significantly decreased over the years due to these advancements.

F1 has also been a testing ground for active aerodynamic systems, which adjust aerodynamic elements in real-time to optimize performance. The Drag Reduction System (DRS) in F1 is a notable example, reducing drag to increase straight-line speed.

Similar concepts are now seen in high-performance road cars, such as active rear spoilers and adjustable front splitters. These systems enhance performance by dynamically adjusting the car's aerodynamic profile based on driving conditions. The Porsche 911 Turbo S, for example, features an active rear spoiler that adjusts to improve downforce or reduce drag as needed.

The sophisticated electronic control systems developed for F1 cars have had a significant impact on road car technologies. F1 cars are equipped with telemetry systems that monitor and transmit vast amounts of data in real-time. These systems optimize engine performance, monitor tire conditions, and adjust suspension settings dynamically.

This technology has paved the way for Advanced Driver Assistance Systems (ADAS) in consumer vehicles. Features such as adaptive cruise control, lane-keeping assist, and automated emergency braking rely on advanced sensors and control systems. The real-time data processing and control algorithms developed in F1 have directly contributed to the development of these systems, enhancing safety and driving convenience.

F1's development of traction control and electronic stability systems has been instrumental in improving road car safety and performance. Traction control systems prevent wheel spin during acceleration, while stability control helps maintain vehicle stability during cornering.

These technologies have become standard in modern vehicles, enhancing safety by helping drivers maintain control in various driving conditions. The principles of electronic stability control (ESC) and anti-lock braking systems (ABS) in road cars are rooted in the control technologies refined in F1.

Safety is paramount in F1, and the sport has led to significant advancements in crash safety technologies. The carbon fiber monocoque chassis used in F1 provides a strong and lightweight survival cell that protects the driver. These monocoques are designed to withstand severe impacts and provide a safe environment for the driver.

The concept of a strong passenger cell has been adopted in road car design, leading to the development of rigid passenger compartments that protect occupants during a crash. Crumple zones, which absorb and dissipate impact energy, are another innovation inspired by F1. These zones deform in a controlled manner to reduce the forces transmitted to occupants, enhancing crash safety.

F1 has also pioneered advances in fire safety, crucial given the high-speed, high-risk nature of the sport. F1 cars use fire-resistant materials and advanced fire suppression systems to protect drivers in the event of a crash.

These innovations have influenced the design of road cars, particularly in the use of fire-resistant materials and improved fuel system safety. Modern vehicles incorporate advanced materials and safety systems to reduce the risk of fire and enhance occupant protection during a crash.

F1's focus on sustainability has led to innovations that benefit the broader automotive industry. The shift towards hybrid power units in F1 reflects a commitment to reducing environmental impact. The development of efficient hybrid systems and energy recovery technologies in F1 has accelerated the adoption of similar technologies in road cars.

Moreover, F1 is exploring the use of sustainable materials and biofuels, which could further influence automotive manufacturing. The emphasis on reducing carbon emissions and improving energy efficiency in F1 aligns with global efforts to combat climate change and promote sustainable transportation.

The intense competition and strict regulations in F1 drive teams to maximize efficiency in all aspects of car performance. This focus on efficiency has led to advancements in engine design, aerodynamics, and materials that contribute to more fuel-efficient road cars. The principles of reducing energy loss and optimizing performance are fundamental to both F1 and consumer vehicle design, driving continuous improvements in fuel economy and emissions reduction.

The suspension systems in F1 cars are designed for optimal performance and handling under extreme conditions. Innovations such as active suspension and advanced damper technology have been developed to enhance stability and control. These technologies have been adapted for road cars, leading to advanced suspension systems that improve ride comfort, handling, and safety. Active suspension systems, for example, adjust damping rates in real-time to provide the best possible handling and comfort based on driving conditions. High-performance vehicles, such as the Mercedes-Benz S-Class, use similar technology to offer a balanced blend of comfort and performance. F1 has also driven advancements in braking technology, with a focus on improving stopping power and reducing brake fade. The use of carbon-ceramic brake discs in F1 offers superior performance compared to traditional steel brakes. These high-performance braking systems provide consistent braking force and are resistant to high temperatures.

Carbon-ceramic brakes are now used in high-performance road cars, providing drivers with enhanced braking performance and durability. The principles of brake cooling and energy management developed in F1 have also influenced the design of modern braking systems, ensuring reliable and efficient braking under various conditions.

The influence of F1 extends beyond technology and safety to shape automotive culture and consumer expectations. The sleek, aerodynamic designs of F1 cars inspire the aesthetics of many road cars. Manufacturers incorporate motorsport-inspired elements, such as aggressive styling, aerodynamic features, and sporty interiors, to appeal to enthusiasts and convey a sense of performance and speed.

F1’s emphasis on performance and competition has shaped consumer expectations and marketing strategies in the automotive industry. Manufacturers leverage their in-

volvement in F1 to promote their brand and showcase their technological prowess. Success in F1 is seen as a testament to a manufacturer's engineering excellence, and this success is often used in marketing campaigns to highlight the performance and reliability of their vehicles.

2. Formula Student

Formula Student is an engineering project that involves a team of students constructing a high-performance race car within a single year. Meeting the requirements of the competition rules adds an extra layer of complexity, demanding teams to navigate a delicate balance between innovation, adherence to safety standards, and the race against time to attain success in this highly competitive arena. Originating in an era dominated by internal combustion engine vehicles, Formula Student has undergone a significant transformation in response to prevailing trends in the automotive industry, characterized by a discernible shift towards the prominence of electric vehicles. This transformation is motivated by a heightened awareness of environmental issues [5], legal motivations [13], and the continuous advancements in electric vehicle effectiveness, for example, for urban operating conditions [10, 11].

For well-established teams like the PWR Racing Team, a scientific club associated with the Wroclaw University of Science and Technology, initially excelling in the era of combustion engines, the evolving requirements and escalating electrification within Formula Student present a significant challenge. In response to that shift, the team has constructed its own electric motor prototype due to their specific application requirements, choosing Interior Permanent Magnet Synchronous Motor (IPMSM) [1, 8, 17]. Additionally, an appropriate control algorithm had to be developed – given the restricted maximum power derived from the accumulator [2], the optimization of electric motor control emerges as a crucial area for competitive engagement.

The Maximum Torque Per Ampere (MTPA) control algorithm is frequently employed in the automotive industry, particularly within the context of electric vehicle powertrains, enhancing the overall efficiency and effectiveness of Interior Permanent Magnet (IMP) machines [9]. This algorithm prioritizes the optimization of the drive system's efficiency by aiming to achieve the maximum torque output while minimizing the electrical current (ampere) consumption [3]. By reducing the amount of current used, MTPA limits copper losses, mitigating the negative effects of temperature variation [12]. The Maximum Torque Per Ampere control method can be used in constant torque region [14, 16].

In order to effectively use the Maximum Torque Per Ampere method, employing a rotational rotor reference frame is highly advantageous. Using Clarke transform, three phase currents (U, V, W) are firstly converted into a two-axis stationary stator frame (α, β). Subsequently, Park transforms, considering the actual position of the rotor, changes it to a two-axis reference frame (d, q) that rotates synchronously with it. Here, the d-axis (direct) indicates the direction of the permanent magnet flux, while the q-axis (quadrature) is orthogonal to it [4, 7].

Using a d-q frame is extremely helpful in control because it provides an easy way to control the motor torque in terms of two separate components. The first one results from the interaction between magnetic flux and the stator current along the q-axis. Meanwhile, the second component is the reluctance torque, which is directly related to the difference between the q-axis and d-axis inductance of the stator [3, 15].

The Maximum Torque Per Ampere aims to maximize electro-magnetic torque given by eq. (1) choosing optimal values of I_d and I_q subject to (2) and (3) [6].

$$T_e = \frac{m}{2} \cdot \frac{p}{2}\left(\psi_d I_q - \psi_q I_d\right) \tag{1}$$

$$\omega_s \sqrt{(\psi_d^2 + \psi_q^2)} \leq V_s \tag{2}$$

$$\sqrt{I_d^2 + I_q^2} \leq I_{smax} \tag{3}$$

where m is a number of phases, p is a number of poles, $\psi_d\psi_q$ are d-q axis flux linkages, I_dI_q are d-q axis peak current components, V_s and I_s are stator voltage and current.

In this article electric motor control algorithm for Formula Student race car is proposed. Then after introducing necessary modifications for controlling a motor on torque transducer its performance was measured and analyzed.

3. Tractive system and control algorithm

The Tractive System consists of two IPMSM positioned in the rear wheels, coupled with a planetary gearbox, two inverters, and the battery located in the vehicle behind the driver, similar to the main control computer.

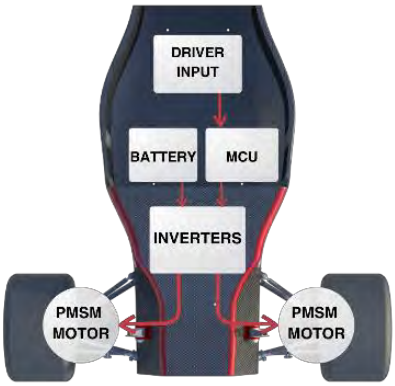

Fig. 1. Scheme of the Formula Student car's tractive system with rear wheel drive

The motor was designed by the team according to specific requirements and conditions to capitalize on its uniqueness. Initially, rule specifications and accumulator design were considered as constraints for voltage and power. Subsequently, utilizing vehicle dynamics simulation, the maximum torque of the motor was defined to optimize performance on Formula Student tracks. Once the maximum motor torque was established, the power base speed could be determined. Considering additional factors such as limited space in the rear wheels, available materials, and technical feasibility, the motor design underwent iterative refinement to meet the set design goals. The final motor performance simulated in MotorCAD software is illustrated in Fig. 2, and simulation results are gathered in Table 1.

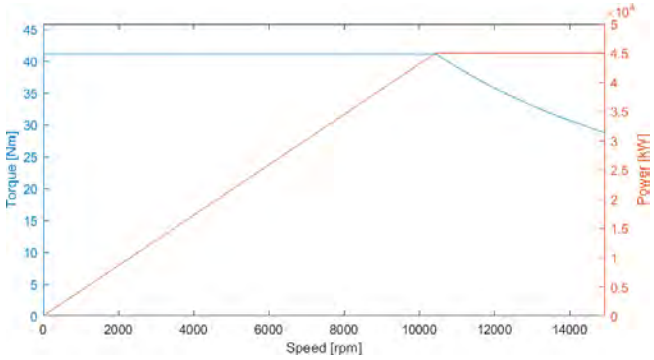

Fig. 2. Motor simulated torque-speed curve

The control system utilizes the Speedgoat computer, based on the Simulink platform, which serves as the main control unit mounted in the car. This system reads data from sensors, implements algorithms specified in the competition regulations, and manages the operation of the drivetrain.

Driver requests, transmitted through the Accelerator Pedal Position Sensor, are transformed into percent of maximum torque. Then, input value is processed by Torque Vectoring (TV) and Traction Control (TC) algorithms, considering the regulatory power limitations. Based on the motor speed read from the resolver and the desired torque, appropriate values of d-q axis current are selected from lookup tables. These values serve as a reference for the current regulator in the inverter, enabling precise control over the operation of the vehicle's motors. The control algorithm diagram for the vehicle's motors, executed by the Main Control Unit and inverter, is presented in Fig. 3.

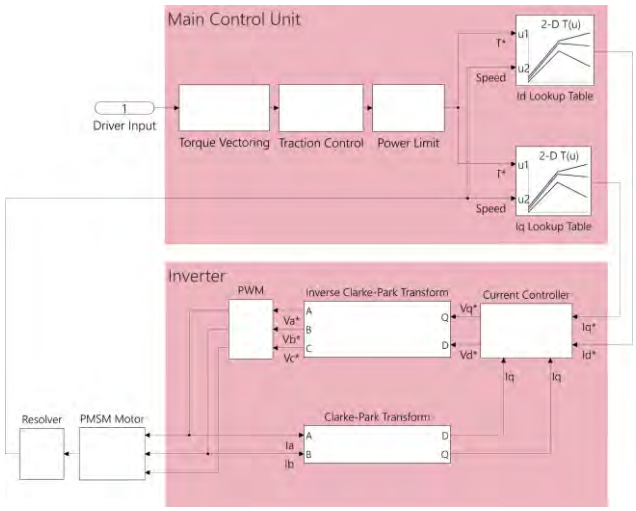

Fig. 3. Motor Control System executed by Main Control Unit and inverters, second pair of inverter and motor is controlled similarly

Reference values of currents were computed using MotorCAD software. Through electromagnetic simulation of the motor, current values for maximum torque were determined for 1650 operating points using eq. (1)–(3). Values for the whole range of motor speed are presented in Fig. 4 and 5, as well as the simulated output of torque given in Fig. 6.

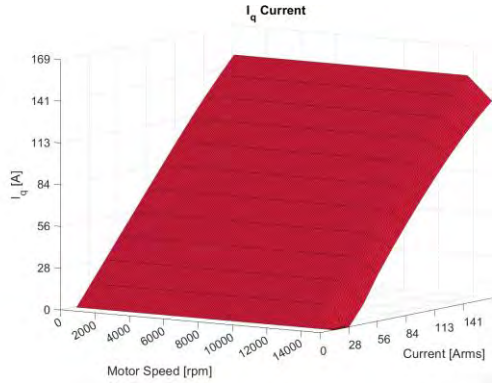

Fig. 4. Simulated values of q axis peak current

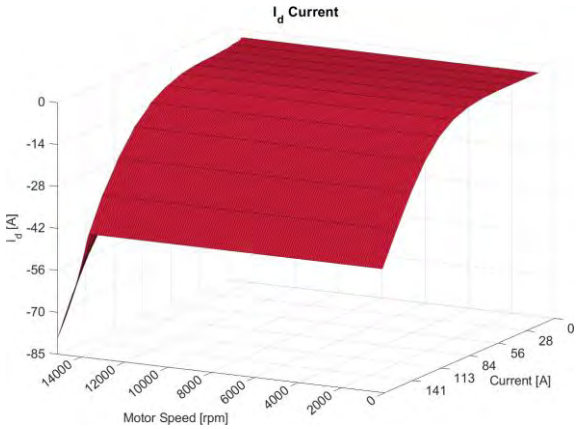

Fig. 5. Simulated values of d axis peak current

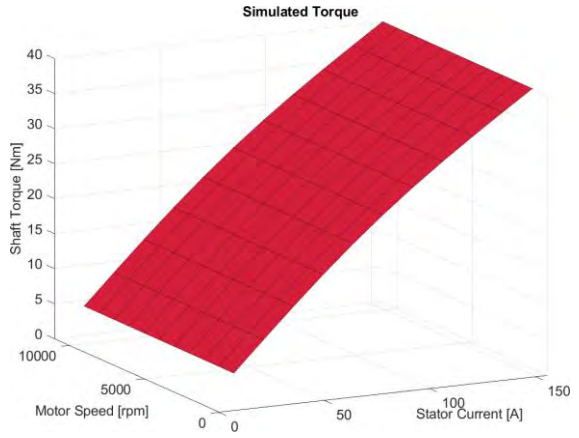

Fig. 6. Simulated output of torque for computed values of peak currents

4. Experimental setup

The parameters of tested motor are presented in Table 1.

Table 1. Theoretical parameters of measured motor

Motor type	IPMSM
DC Bus voltage	538 V
Maximum possible torque	41.4 Nm
Speed limit for constant torque	11467 rpm
Torque constant (k_T)	0.253596 Nm/A
Back EMF constant (k_e)	0.352145 V/rpm
Number of phases	3
Number of poles	8
Inductance of phase L_d/L_q [µL]	161/218
Flux linkage ψ_d/ψ_q [mWb]	43/32
Motor controller	Cascadia Motion PM100DZ
Gear ratio	9.8

The motor control algorithm was adjusted to conduct an experiment, separating the part responsible for Maximum Torque Per Ampere control from other algorithms such as Torque Vectoring and Traction Control. Additionally, power limitation was excluded from the research. The experiment involved iterating the stator current values. Using lookup tables implemented in MCU, appropriate peak currents in the d-q axis were sent to the inverter. This process was repeated for different speeds specified in the table, allowing for the measurement of real torque values correlated with the given currents.

The torque and speed measured by the torque transducer were recorded as analog signals using a power analyzer. Additionally, current and voltage probes were connected to the three phases and power supply cables, enabling the measurement of currents, voltages and power. The temperature of the motor was monitored at various points on its surface and through a sensor placed in the winding. Furthermore, the temperature of the planetary gearbox was read using an analog input in Speedgoat computer. During the tests, a thermal camera was also used to capture images, and the motor's operation was recorded. Setpoints were logged in Speedgoat and all signals from the inverter and motor were recorded in the datalogger. The measurement setup is presented in Fig. 7.

5. Results

Torque values produced for given d-q axis currents were measured in the constant torque region for this motor, and the outcomes are illustrated in Fig. 9. It is evident that the measured torque consistently falls below the simulated values, with the maximum achieved torque reaching 31.8 Nm. This represents a notable 23.2% discrepancy compared to the predicted values. Notably, the torque recorded at various speeds within the constant torque region remains nearly constant for identical currents.

A visual comparison with the simulated values is depicted in Fig. 10. Beyond the observed lower torque constant in the measured data, the relationship is not strictly linear. The proportionality factor decreases with higher currents. It could be caused by increasing temperature during measurements as well as saturation. In Figure 11 the difference between measured and expected torque is presented according to the formula:

$$\Delta = \frac{T_{measured}}{T_{simulated}}$$

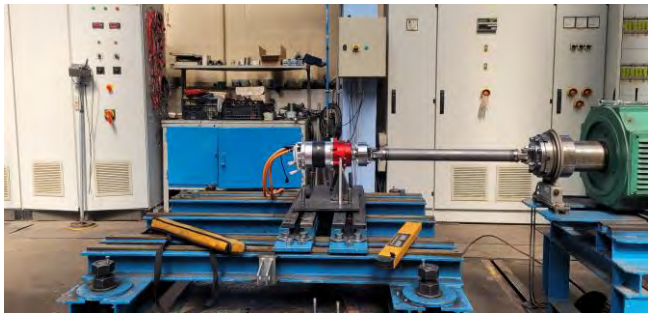

Fig. 8. The tested motor coupled with a planetary gearbox mounted on the torque transducer

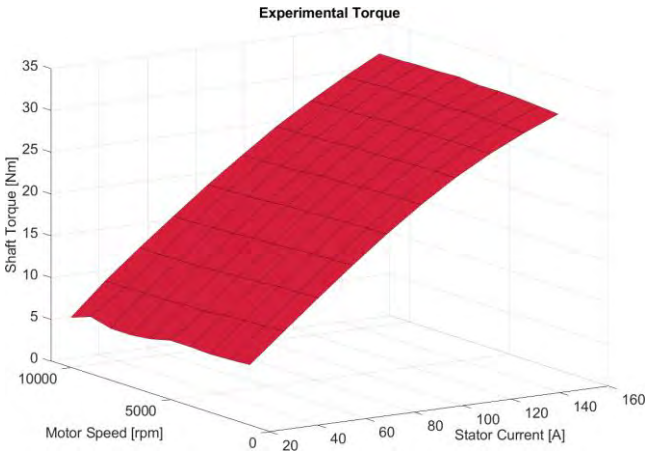

Fig. 9. Measured torque for computed values of peak currents

As shown, results are the most consistent for the middle range of measured currents with the maximum value of 81.3% for stator current I_s = 126.9 A and motor speed ω = = 3000 rpm. For low current values, the difference is significant, primarily due to lower efficiency in this operational range. Similarly, at high current values, the measured torque becomes more divergent, owning to the aforementioned impact of temperature and saturation.

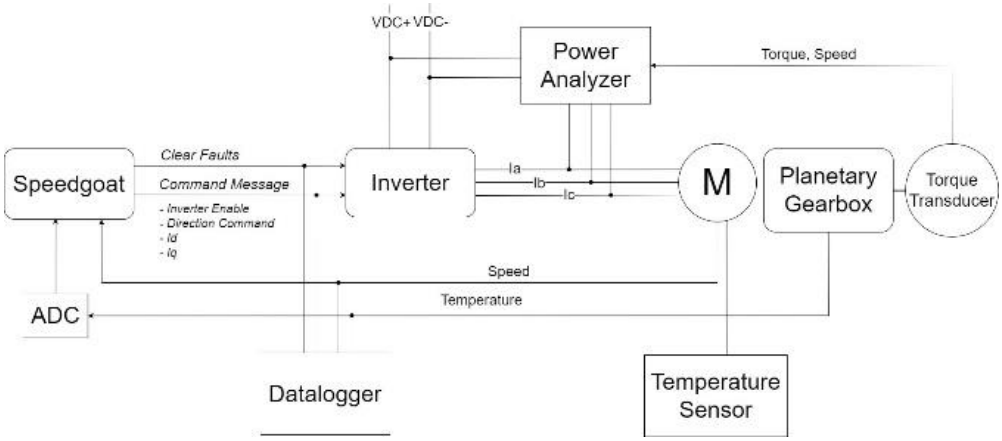

Fig. 7. The measurement setup

For obtained results from torque transducer, expanded uncertainty estimated with a level of confidence of 95% (k = 2) is respectively U(T) = 4.3 Nm and U(ω) = 3.7 rpm.

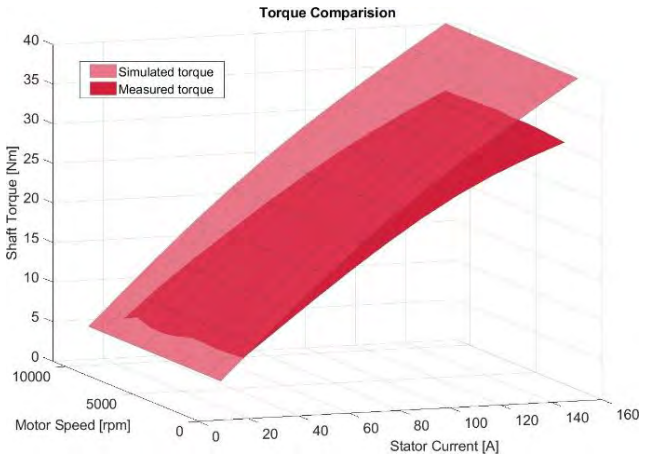

Fig. 10. Comparison between simulated and measured values of torque

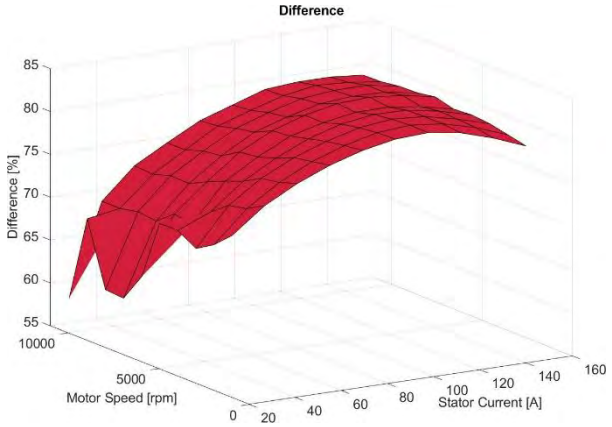

Fig. 11. Difference between simulated and measured values of torque

Conclusions

The motor prototypes were thoroughly examined, and a comparison was made between the simulated and actual performance characteristics. The research revealed significant discrepancies between the simulated and measured torque due to prototype execution errors. The torque was proportionally lower due to reduced turn number. However, control using MTPA yielded higher values compared to control without it.

The proposed control algorithm is suitable for use in the race car because it employs lookup table values instead of recomputation for each change in torque, which is advantageous in this application given the rapid changes in desired torque. Use of SpeedGoat as the Main Control Unit is beneficial as it allows for easy integration with other algorithms on the vehicle, such as Torque Vectoring and Traction Control and facilitates frequent modifications during the testing phase.

Acknowledgements

Our deep gratitude goes to Institute of Mining Technology KOMAG for the invaluable opportunity to conduct this research. We're grateful for the resources and support provided, enabling us to achieve our research objectives.

The article was written in cooperation with Autocomp Management sp. z o.o. from Szczecin, Research and Development Center Producer of simulators on the military and civilian market from Poland.

Bibliography

[1] Bose BK. A high-performance inverter-fed drive system of an interior permanent magnet synchronous machine. IEEE T Ind Appl. 1988;24(6):987-997. https://doi.org/10.1109/28.17470

[2] Formula Student Rules. Version: 1.0, Rev-ba690a0, p. 81 of 135 (2024).

[3] Halder S, Srivastava SP, Agarwal P. Flux weakening control algorithm with MTPA control of PMSM drive. IEEE 6th India International Conference on Power Electronics (IICPE). 2014;1-5. https://doi.org/10.1109/IICPE.2014.7115810

[4] Helsing R, Sanchez T. Modeling and control of a PMSM operating in low speeds. Master of Science Thesis. 2022. https://tiny.pl/d9qks (accessed on 16.04.2024).

[5] Hickman R, Hannigan C. Transport and climate change. International Encyclopedia of Transportation. 2021;94-100. https://doi.org/10.1016/B978-0-08-102671-7.10620-7

[6] Hoang KD, Wang J, Cyriacks M, Melkonyan A, Kriegel K. Feed-forward torque control of interior permanent magnet brushless AC drive for traction applications. 2013 International Electric Machines & Drives Conference. 2013. https://doi.org/10.1109/IEMDC.2013.6556247

[7] Jaber FF, Abdulhasan AF. Mathematical model of permanent magnet synchronous motor. University of Thi-Qar Journal for Engineering Sciences. 2022;12.2:10-14. https://jeng.utq.edu.iq/index.php/main/article/view/483/417

[8] Jahns TM. Flux-weakening regime operation of an interior permanent-magnet synchronous motor drive. IEEE T Ind Appl. 1987;23:681-689. https://doi.org/10.1109/TIA.1987.4504966

[9] Jahns TM, Kliman GB, Neumann TW. Interior permanent magnet synchronous motors for adjustable-speed drives. IEEE T Ind Appl. 1986;4:738-747. https://doi.org/10.1109/TIA.1986.4504786

[10] Kropiwnicki J, Furmanek M. Analysis of the regenerative braking process for the urban traffic conditions. Combustion Engines. 2019;178(3):203-207. https://doi.org/10.19206/CE-2019-335

[11] Kropiwnicki J, Gawłas T. Evaluation of the energy efficiency of electric vehicle drivetrains under urban operating conditions. Combustion Engines. 2023;195(4):28-34. https://doi.org/10.19206/CE-169492

[12] Li S, Sarlioglu B, Jurkovic S, Patel NR, Savagian P. Comparative analysis of torque compensation control algorithms of interior permanent magnet machines for automotive applications considering the effects of temperature variation. IEEE Transactions on Transportation Electrification. 2017; 3(3):668-681. https://doi.org/10.1109/TTE.2017.2684080

[13] Martins H, Henriques CO, Figueira JR, Silva CS, Costa AS. Assessing policy interventions to stimulate the transition of

electric vehicle technology in the European Union. Socio Econ Plan Sci. 2023;87B:101505. https://doi.org/10.1016/j.seps.2022.101505

[14] Morimoto S, Sanada M, Takeda Y. Wide-speed operation of interior permanent magnet synchronous motors with high performance current regulator. IEEE T Ind Appl. 1994; 30(4):920-926. https://doi.org/10.1109/28.297908

[15] Song L, Jiang D, Cui S, Sheng S. Reluctance torque analysis and reactance calculation of IPM for HEVs based on FEM. IEEE Vehicle Power and Propulsion Conference. 2010;1-4. https://doi.org/10.1109/VPPC.2010.5729146

[16] Uddin MN, Radwan TS, Rahman MA. Performance of interior permanent magnet motor drive over wide speed range. IEEE T Energy Conver. 2002;17(1):79-84. https://doi.org/10.1109/60.986441

[17] Yang Y, Castano SM, Yang R, Kasprzak M, Bilgin B, Sathyan A et al. Design and comparison of interior permanent magnet motor topologies for traction applications. IEEE Transactions on Transportation Electrification. 2017;3(1): 86-97. https://doi.org/10.1109/TTE.2016.2614972

Aleksandra Birut – PWR Racing Team, Faculty of Mechanical Engineering, Wroclaw University of Science and Technology, Poland.
e-mail: *aleksandrabirut@gmail.com*

Rafał Dziki – PWR Racing Team, Faculty of Mechanical Engineering, Wroclaw University of Science and Technology, Poland.
e-mail: *rafal.dziki.pwrrt@gmail.com*

Paweł Wójcik, Eng. – PWR Racing Team, Faculty of Mechanical Engineering, Wroclaw University of Science and Technology, Poland.
e-mail: *pawel.wojcik.pwrrt@gmail.com*

Łukasz Orzech, DEng. – Institute of Mining Technology KOMAG, Laboratory of Applied Tests, Poland.
e-mail: *lorzech@komag.eu*

Andrzej Niedworok, DEng. – Institute of Mining Technology KOMAG, Laboratory of Applied Tests, Poland.
e-mail: *aniedworok@komag.eu*

Prof. Anna Janicka, DSc., DEng. – Faculty of Mechanical Engineering, Wroclaw University of Science and Technology, Poland.
e-mail: *anna.janicka@pwr.edu.pl*

Monika Magdziak-Tokłowicz, DEng. – Faculty of Mechanical Engineering, Wroclaw University of Science and Technology, Poland.
e-mail: *monika.magdziak-toklowicz@pwr.edu.pl*

Article citation info:
Mindur L, Zamiar Z, Mindur M. High-speed trains in Japan in the years 2002–2020. Combustion Engines. 2024;199(4):88-96. https://doi.org/10.19206/CE-190604

Leszek MINDUR
Zenon ZAMIAR
Maciej MINDUR

Combustion Engines
Polish Scientific Society of Combustion Engines

High-speed trains in Japan in the years 2002–2020

ARTICLE INFO

Received: 4 March 2024
Revised: 28 March 2024
Accepted: 28 June 2024
Available online: 5 August 2024

The article presents the development of high-speed rail in Japan, an island country located within the Ring of Fire of the Pacific. The analysis of the technical condition and the stages of the historical development of high-speed railways were preceded by an assessment of the economy and transport as well as a study of transport intensity. The summary of the article includes the effects and benefits of using high-speed rail, as well as methods of financing and plans for further development.

Key words: *Japanese economy, transport intensity, passenger transport, high-speed railways*

1. Introduction

High-speed trains are the most modern and advanced technology for moving passengers in land transport. Their main advantage is that they achieve high speeds, usually from over 200 to 300 km/h, which significantly shortens the travel time in relation to the time needed to cover the same distance by conventional trains. On the other hand, they are serious competition for high-speed air transport.

High-speed railways require special wagons and locomotives as well as appropriate infrastructure with much larger turning arcs, which are very durable and have a strong subgrade. Thus, as a rule, this type of infrastructure is built from scratch, and only in a few cases is the existing infrastructure adapted to the needs of high-speed rail. For the operation of high-speed rail, not only special trains and railway lines are needed, but stations and separate ticketing systems are also needed.

It should be emphasized that the implementation of investments to perform transport in this technology is very capital-intensive. Nevertheless, the required large expenditures for development are compensated by:

– high comfort and short travel time
– a huge impact on the economic development of regions and the country
– high level of safety and relatively low level of negative impact on the natural environment in relation to other transport branches
– high energy efficiency
– low external costs.

The above-mentioned basic premises resulted in the fact that in the rich countries of Western Europe and Asia, transport using this technology is developing dynamically.

The research period ended in 2020 in order to eliminate the negative impact on the economy of the effects of the global COVID-19 pandemic. The idea was for the research to be based on the main development trend and not be obscured by side causes.

2. General characteristics of the country

Japan is an island country located in the eastern part of Asia. The archipelago consists of four main islands: Hokkaido, Honshu, Shikoku and Kyushu, as well as about four thousand smaller ones. The country is located between the western Pacific Rim and the Sea of Japan, through which it borders with:

– China – from the south-west and west (Ryukyu Islands area) through the East China Sea
– the Republic of Korea – through the Korean Strait
– Russia – from the north through the Strait of La Pérouse (Hokkaido–Sakhalin region) connecting the Sea of Japan with the Sea of Okhotsk.

Fig. 1. Location of Japan [7]

The Japanese islands lie both within the seismically active orogenic zone and at the junction of three tectonic plates, within the so-called the Ring of Fire of the Pacific. Most of Japan is covered by mountains. According to the Japan Meteorological Agency, there were more than 110 active volcanoes in the country in 2018, including 10 submarines [14].

About 50 volcanoes erupted in the period 1900–2016 [37]. The largest population centres are therefore in the lowlands – between the cities of Nagoya and Osaka and Tokyo.

Japan's total population was 125.50 million inhabitants (16% of the world's population) in 2021 [34]. Japan is characterized by a high population density, in 2020 it reached the value of 338.2 people/km². Of the 47 prefectures of Japan, the largest population was in Tokyo Metropolis (14.05 million), followed by Kanagawa, Osaka, Aichi, Saitama, Chiba, Hyogo and Hokkaido prefectures – a total of 63.98 million inhabitants, which accounted for over 50% the entire population. The population density in the Tokyo metropolis was the highest among the prefectures of Japan and amounted to 6,402.6 people/km², i.e. almost 18.9 times more than the national average.

Japan is recognized around the world as one of the leaders of modern technologies. An excellent example of their use in practice is the development of high-speed rail since 1964, when the world's first Tōkaidō Shinkansen line was launched.

3. The level and assessment of the economic situation based on basic economic variables for the years 2002–2020

Japan's economy is one of the largest economies in the world, currently in third place behind the economies of the United States and China [6]. At the same time, Japan is the most indebted country in the world after the United States [41].

Among the most developed industries in Japan are the automotive, electronics, machinery, pharmaceutical, steel and chemical industries. Industries crucial to the country's security also include petrochemicals, bio-industries, shipbuilding and aerospace. The products in which Japan is a technological leader include, among others, semiconductors, optical fibres and biochemistry [25]. At the same time, the domestic manufacturing industry increased its involvement in global production chains, moving production bases abroad in order to reduce manufacturing costs and avoid currency fluctuations [36].

The economic situation of Japan in 2002–2020 is presented in Table 1.

Analysing the data contained in Table 1, it should be stated that, similarly to other world economies, a clear deterioration of the economic situation occurred in 2008–2009 during the global economic crisis and in 2020 due to the outbreak of the COVID-19 pandemic, when economic activity fell as a result of sanitary restrictions, slowing down consumption and investment.

In the years 2002–2020, the inflation rate remained at a similar level, while unemployment after 2010 never exceeded 5%, reaching less than 3% in 2020.

In terms of international trade, Japan ranks fifth in the world. The most important trade and investment partner is the United States.

In 2019, the largest export partners were the United States (19%), China (18%), South Korea (6%), and Taiwan (6%), while in imports, China (23%), the United States (11%) and Australia (6%). The weak domestic demand of the Chinese economy and the stagnation of global demand (including in the United States and Europe), as well as the unprecedented economic slowdown caused by the global COVID-19 pandemic, resulted in, in the last two years, a weakening in some areas of exports and production. However, the upward trend in domestic demand was maintained, supported by factors such as improved employment and income situation and strong corporate profits.

In 2021, business activity in Japan was restricted periodically to prevent the spread of infection. Although the economy was recovering, the rate of growth was slow [36].

Figure 2 presents a study based on a sixth-degree polynomial showing the effects of socio-economic activity expressed in the value of Japan's gross domestic product in the years 2002–2020.

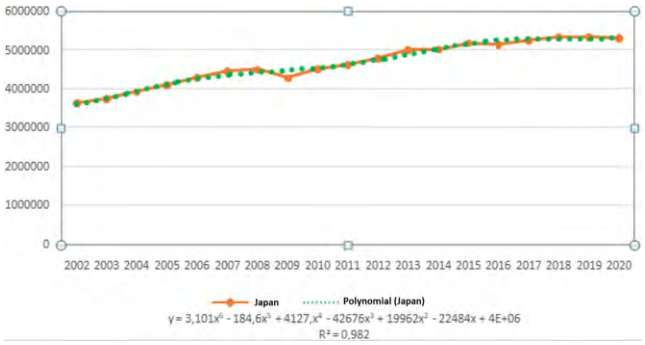

Fig. 2. Development of Japan's GDP in 2002–2020, in USD million [28]

Table 1. Basic macroeconomic indicators of the Japanese economy in 2002–2020 (annual changes in %) [37]

Details	2002	2003	2004	2005	2006	2007	2008	2009	2010	2011
GDP	0.3	1.7	2.4	1.3	1.7	2.2	–1.0	–5.5	4.7	–0.5
Private consumption	1.3	0.6	1.3	1.5	0.9	0.8	–1.1	–0.9	2.3	–0.5
Unemployment (rate in %)	5.4	5.3	4.7	4.4	4.1	3.9	4.0	5.0	5.0	4.6
Inflation (in %)	2.8	2.5	2.4	2.6	2.7	2.5	3.7	0.6	1.8	2.9
Current account balance (% of GDP)	2.6	3.1	3.7	3.5	3.8	4.7	2.8	2.7	3.8	2.1
Exports of goods and services (% of GDP)	7.9	9.6	14.4	7.1	10.3	8.7	1.6	–23.4	24.9	–0.1
Imports of goods and services (% of GDP)	0.8	3.4	8.5	5.9	4.7	2.3	0.7	–15.6	11.3	5.7

Details	2012	2013	2014	2015	2016	2017	2018	2019	2020
GDP	1.7	1.4	0.0	1.6	0.8	1.7	0.6	0.0	–4.5
Private consumption	2.0	2.6	–0.9	–0.2	–0.4	1.1	0.2	–0.5	–5.3
Unemployment (rate in %)	4.3	4.0	3.6	3.4	3.1	2.8	2.4	2.4	2.8
Inflation (in %)	2.2	1.6	1.7	0.7	1.2	2.3	2.6	2.1	1.4
Current account balance (% of GDP)	1.0	0.9	0.8	3.1	3.8	4.2	3.2	3.4	2.9
Exports of goods and services (% of GDP)	0.1	0.8	9.3	3.2	1.6	6.6	3.8	–1.5	–11.8
Imports of goods and services (% of GDP)	5.5	3.2	8.1	0.4	–1.2	3.3	3.8	1.0	–7.2

The values of the gross domestic product of Japan in the analyzed years were characterized by an upward trend with a noticeable decrease during the global financial crisis, which peaked in 2007–2009. Emerging from the crisis, the Japanese economy continued the development from before 2007, which was characterized by a continuous increase in GDP in the following years.

The credibility of the above study was checked with the R^2 agreement coefficient, which reached the value of 0.982.

4. Transport in Japan

In Japan's general transport infrastructure, the road network is the best developed, with a length of 1 227 000 km. km. The second place is occupied by rail transport, with a total length of the network of 27.3 thousand km. km, with the vast majority of electrified railway lines (15.7 thousand km). The length of the pipelines is 4.7 thousand km. km, and inland waterways 1.8 thousand. km (Table 2).

Table 2. Transport infrastructure in Japan in 2020 (in km) [36]

Type of transport infrastructure	Length
Railway lines	27 311
Roads	1 227 000
Highways	9 100
National roads	56 000
Regional roads	130 000
Municipal roads	1 033 000
Inland waterways	1 770
Pipelines	4 734

Almost all freight transport is carried out by cars and cargo ships, while rail transport is the most important in passenger transport.

The road infrastructure includes 9.1 thousand km of motorways, 56 thousand km of national roads, 130 thousand km of regional roads, and 1 033 000 km of municipal roads. Roads are managed by the Ministry of Land, Infrastructure, Transport and Tourism (MLIT).

The operator of Japanese railway lines with a total length of 27.3 thousand km. km is in the vast majority of Japan Railways Group [41]. Shinkansen high-speed rail lines run through the most important industrial, political, cultural and financial centers [11], with rail connections to the four largest islands of the archipelago (Fig. 3).

Inland waterway transport plays a marginal role in the movement of goods [41]. The main problem limiting the possibility of using inland waterways is their swift current and large seasonal fluctuations in the water level, which is mainly caused by the mountainous topography of Japan. Due to topographic features, inland waterway transport developed near coastal regions where wider channels and calmer river currents allowed it [35].

Fig. 3. The network of railway connections in Japan [30]

There is a total of 4,734 km of pipelines in Japan, mainly used to transport LNG [41]. Japan, like China, is almost entirely dependent on gas imports due to its small domestic production [15]. The existing and planned pipeline networks in Japan are shown in Fig. 4.

Fig. 4. Existing and planned pipeline networks in Japan [21]

Table 3 shows the transport performance performed in the years 2002–2020 by land transport.

The analysis of both the transport infrastructure and the volume of transport performance shows that in the years 2002–2020, road transport was of dominant importance in the transport of goods by land. A much lower level in relation to road transport was reached in the period under examination, measured by the volume of transport performance carried out by pipelines and rail transport. It should be noted, however, that road transport, measured by the volume of transport performance, decreased in 2010 and, for the following years, remained at a similar level. Issues in the field of cargo transport have been discussed in more detail in the book "Transport Technologies" [24].

Table 3. Transport performance in Japan in 2020 (in billion tkm) [36]

Mode of transport	2002	2003	2004	2005	2006	2007	2008	2009	2010	2011
Road	312	322	328	334	346	355	345	333	243	233
Rail	22	23	23	23	23	23	22	21	20	20
Pipeline	60	62	63	63	62	61	58	58	59	58

Mode of transport	2012	2013	2014	2015	2016	2017	2018	2019	2020
Road	209	214	210	204	210	211	210	214	212
Rail	20	21	21	21	21	22	19	20	20
Pipeline	56	55	52	53	53	51	49	47	48

The transport intensity of Japan in the years 2002–2020 using the sixth-degree polynomial and the exponential function curve is shown in Fig. 5 and 6.

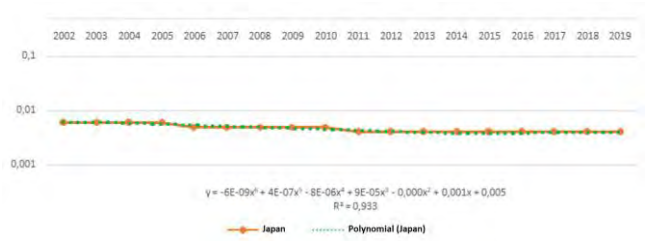

Fig. 5. Japan's transport intensity calculated using a sixth-degree polynomial

The analysis of the curve calculated on the basis of a sixth-degree polynomial allows us to conclude that the transport intensity of Japan in the analyzed period remained at a low, stable level. The coefficient of conformity R^2 was 0.933.

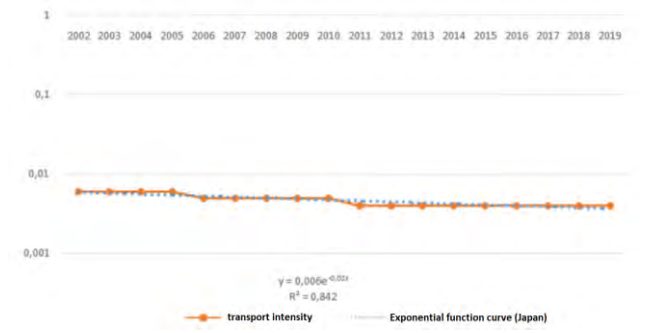

Fig. 6. Japan's transport intensity calculated using the exponential function curve

Figure 6 shows the curve of the exponential function illustrating the development of the transport intensity of the Japanese economy in the analyzed period. The R^2 coefficient is 0.842 [35].

Comparing the studies, it can be concluded that the study based on the sixth-degree polynomial, in this case, is characterized by more reliable results, as indicated by the higher result of the R^2 coefficient of agreement.

Transport intensity in the analyzed period remains at a low level with a downward trend. This means a stable cost of producing and moving individual goods, which in turn results in stable prices. On this basis, it can be concluded that Japan takes appropriate rationalizing and limiting measures to increase transport intensity and maintains it at a constant level [26].

5. Characteristics of the high-speed railway

Japan is considered the home of high-speed rail, as well as the first country to face the challenges of such an innovative technical and structural design. The implementation of the project began in 1958 with the approval by a special government commission of the plan to build the Tokyo–Osaka line [11]. The world's first high-speed line, the Tōkaidō Shinkansen, opened in October 1964 for the Tokyo Olympic Games. This line, 515 km long, runs from Tokyo to Osaka via Nagoya and Kyoto. Its initial maximum speed was 210 km/h [8]. Currently, in Japan there is a whole system of high-speed rail called Shinkansen, reaching speeds of up to 320 km/h.

The high debt of the Japanese State Railways related to the construction of high-speed lines, which – despite the growing number of passengers – was not compensated by the proceeds from ticket sales, forced the Japanese government to decide in 1987 to privatize the railway and introduce its shares to the stock exchange. Such a move made it possible to repay the loans taken out for the implementation of this investment [11]. At the same time, Japanese railways were privatized by dividing them into six passenger operators, forming the Japan Railways Group, and one freight operator:

– East Japan Railway Company
– Central Japan Railway Company
– West Japan Railway Company
– Hokkaido Japan Railway Company
– Shikoku Japan Railway Company
– Kyushu Japan Railway Company
– Japan Freight Railway Company.

Each of the above-mentioned passenger transport companies operates in a specific area of the country (Fig. 7), while the Japan Freight Railway Company provides freight services on the entire national network. The restructuring of the railroad has already yielded profits in the first year of operation under the new rules.

Fig. 7. Territorial range of passenger railway operators in Japan [19]

Initially, the state retained its shares in each of these companies, but in 2000, the process of complete privatization of JR Central, JR East, and JR West began, which was completed in 2003, 2002, and 2004, respectively [11].

6. Technical solutions in trains and locomotives – power supply methods

The decision to build a high-speed railway was a big challenge for its creators. In addition to designing the route itself, an important element was the appropriate rolling

stock. It was necessary to develop a completely new type of trains, for which the following assumptions were made:
– number of wagons – from 12 to 16
– axle load – approx. 16 tons
– train weight – approx. 800 tons [11].

Due to the weight of the train, it was impossible to use a traditional locomotive, and the decision was taken to use the so-called traction unit. It consisted in installing electric motors along the entire length of the train. Each motor was a DC motor with relatively low power (185 kW).

Series 0 Shinkansen

The first generation of trains designed to transport passengers on high-speed lines were Shinkansen series 0 trains. The weight of each car was 64 t, and the axle load, as assumed, was 16 t. A pantograph, transformer, rectifier and other electrical equipment were mounted on every second car. The trains were powered by 25 kV at 50 Hz, with all wagon axles powered by 185 kW (248 hp) traction motors, giving a maximum operating speed of 220 km/h (137 mph). Originally, the trains consisted of 12 sets. However, some were extended to 16 sets. To ensure sufficient sound insulation, the windows of the carriages were equipped with triple glazing.

The train could take 1,208 passengers in second class, and 132 passengers in the first class, while the seating arrangement was as follows:
– 2+3 in class 2
– 2+2 in class 1.

At the head of the train, under a cover in the shape of a hemisphere, there was a coupler, after disassembly of which the train could be towed (Fig. 8).

Fig. 8. A series 0 Shinkansen train at the Kyoto Railway Museum [3]

The 0-series trains were in operation between 1964 and 2008, with a total of approximately 3,216 sets produced, which ran on the Tokaido and Sanyo routes. The last 6-car sets were used by JR West on the service between Shin-Osaka and Hakata and on the Hakata-Minami line.

Series 100 Shinkansen

The series 0 had many successors, one of them was the series 100 Shinkansen, operated from 1986 to 2012. The nose profile of the train in series 100 was more pointed than in series 0. Light alloy body sheathing was replaced with steel. In the 16-set trains, not all members were powered; the sections at each end were unpowered, as were the two two-level middle sections.

Fig. 9. Shinkansen 100 series train [20]

The power of the traction motors was 230 kW (in series 0–180 kW), while the power of the entire train was 11,040 kW (in series 0–11,840 kW). A new solution has been introduced where the brakes use eddy currents. The train reached a maximum speed of 220 km/h.

Double-deck cars were used in the train for the first time – on the upper deck, there was a restaurant section with kitchen facilities, and on the lower deck, there was a small buffet. The number of seats in the second class (standard) was 1,153, while the first class (green) was 168. Series 100 trains ran on the Tokaido and Sanyo route [11].

Series 300 Shinkansen

Another high-speed train in Japan was the Shinkansen series 300. It was introduced into production and operation in the 1990s, and was withdrawn in 2012. Compared to the older type of trains, a number of changes and improvements have been made to the structure. A more aerodynamic shape was introduced, which allowed for a significant (by about 20%) reduction in air resistance. Light steel alloys were used for the production of the train, thanks to which the weight of the 16-car set was reduced to about 710 tons (in the 0 series, the weight was 925 tons). The modernization of the structure also resulted in a reduction of the axle load to approx. 11.3 t.

Fig. 10. Series 300 Shinkansen train [38]

The maximum speed of the train was 270 km/h. The train could take 1,323 passengers (200 in the green class and 1,123 in the standard class). The train ran on the Tokaido and Sanyo routes.

The biggest change for the 300 series was the replacement of DC motors with AC motors (three-phase asynchro-

nous motors) and the use of kick starting. These motors were much lighter than DC motors, more powerful, and took up much less space. This made it possible to reduce the number of powered cars to 10. The introduction of a new type of engine also required the development of new electronic equipment and a computer controlling the entire system.

In the 300 series, bogies of a different design were also used, omitting the bolster beam, which was present in older generations. The box rested on air cushions.

Thanks to weight reduction, new engines, and a number of other improvements and innovations, it was possible to shorten the travel time between individual stations. For example, the average travel time from Tokyo Central Station to Shin-Osaka Station in 1992-1993 was 2 hours 54 minutes, the maximum speed was 220 km/h, while the average was 177 km/h. This increased the attractiveness of this type of transport for passengers [11].

Series E5 Shinkansen

The research program for the E5 series was initiated in 2002 to design a train that could reach speeds of 360 km/h. The rolling stock is produced by a consortium of Hitachi and Kawasaki companies [5]. The train consists of two units, each consisting of four driving cars and a steering car without a drive. In the case of this model, the hull sheathing was made of reinforced aluminium sections. As a result of air flow tests, the characteristic shape of the head car was extended to 15 m.

Fig. 11. Series E5 Shinkansen train [22]

The construction uses three TM212 transformers with a unit power of 3130 kVA, the voltage of which is converted into 32 three-phase MT207 traction motors with a unit power of 300 kW. Two pantographs type PS208, located on the roofs of carriages No. 3 and 7, are used to collect electricity. The trains are powered with a voltage of 25 kV 50 Hz. The weight of each of the 10 powered cars is 47 t (42.7 t without the drive), and the total weight is 453.5 t. The trains are equipped with the DS-ATC traffic safety system. The maximum speed they reach is 320 km/h [13].

The trains can carry 731 passengers at a time, including 658 in the standard class, 55 in the green class and 18 in the luxury gran class, which was introduced for the first time in the trains of this series.

The E5 series is operated by the East Japan Railway Company. The trains were introduced to Tohoku routes in March 2011 and Hokkaido routes in March 2016.

Series E7/W7 Shinkansen

One of the newer high-speed trains running on Japanese railway lines is the Shinkansen of the E7/W7 series, built in 2013. The production of the kits was jointly developed by Kawasaki Heavy Industries, Hitachi Kasado and other Japanese companies.

The external appearance of both the E7 and W7 series (in terms of painting and overall shape) is virtually identical. The difference is that the E7 sets are operated by the East Japan Railway Company and have a number starting with the letter F, while the E7 sets are operated by the West Japan Railway Company and have a number starting with the letter W.

Fig. 12. Series E7 Shinkansen train [22]

The sets consist of 12 cars, of which 10 are powered cars. The hull sheathing of the train is made of aluminium, the front of the train is designed in an aerodynamic shape. Thanks to the use of four airbags, the car body could be placed on the bogie. A distributed drive was used to move the train; each driving car had 4 three-phase motors, each with a power of 300 kW. Two PS208A pantographs located on the roofs of the cars No. 3 and 7 were used to collect the current.

The trains are powered by 25 kV 50/60 Hz. The total weight of the train is 543 t. The trains are equipped with the DS-ATC and RS-ATC traffic safety systems. The maximum speed they achieve is 260 km/h [27].

Each train has 934 seats, including 853 in standard class, 63 in green class and 18 in gran class (apart from the Tsurugi configuration, which does not have gran class [20]). Economical LEDs were used to illuminate the compartments. The seats can be adjusted individually using an electric adjustment system. The train also has a compartment for a mother with a child and a compartment for a person requiring special care.

Trains operate on the following routes: Tokyo–Nagano (E7 from 2014 and W7 from 2015), Tokyo–Kanazawa and Toyama–Kanazawa (from 2015), as well as Tokyo–Niigata and Tokyo–Echigo–Yuzawa (from 2019). The route to Kanazawa with a length of 454 km is covered in 2 hours and 30 minutes. The maximum speed of the train is reached in the Takasaki–Kanazawa section.

7. Line infrastructure for high-speed trains

Currently, Shinkansen trains can run at a maximum speed of 320 km/h. Due to the high speed they reach and the aerodynamic shape of their beaks, they are called "bullet trains".

Each Shinkansen line includes fast, semi-fast and local trains. Train traffic is mainly on conventional steel rails mounted on concrete sleepers, with the fastest ones using dedicated tracks to avoid collisions with slower trains and only stopping at major stations [34]. In order for the trains to run at their maximum speed (up to 320 km/h), the Shinkansen tracks do not have sharp curves and, moreover, do not cross other railway lines at the same level.

Existing high-speed rail lines allow trains to move at speeds above 200 km/h, and the most modern solutions even allow for speeds exceeding 300 km/h. Such performance would be impossible if not for the appropriate linear infrastructure. Among the basic design parameters for the Shinkansen line, the following are distinguished:

- track gauge 1067 mm and 1435 mm
- cant 290/330 mm
- radius of the horizontal curve (2500 m for the speed of 270 km/h, 4000 m for the speed of 320 km/h)
- longitudinal inclination 25/35‰
- vertical curve radius 10,000 m (5,000 m on sections where the maximum speed is 250 km/h)
- width of the intertrack 1.435 m.

Turnouts are an important structure of high-speed lines. On the Shinkansen lines, the solution is to locate the turnouts very close to the ends of the platforms. High-speed turnouts are not used, and trains move at a relatively low speed on the existing turnouts. The inner radius of the largest turnouts used on the Shinkansen is 1,106 m [39].

The above-mentioned parameters, combined with appropriate service, as well as care for travel comfort and safety, have a real impact on the number of passengers who decide to use train services in Japan. The Shinkansen lines are in a phase of continuous development. Currently, several investments are planned to provide for the creation of new connections, which will be discussed later in the article. Despite the great benefits resulting from traveling by high-speed rail, Shinkansen lines account for only a few percent of all trips made by rail.

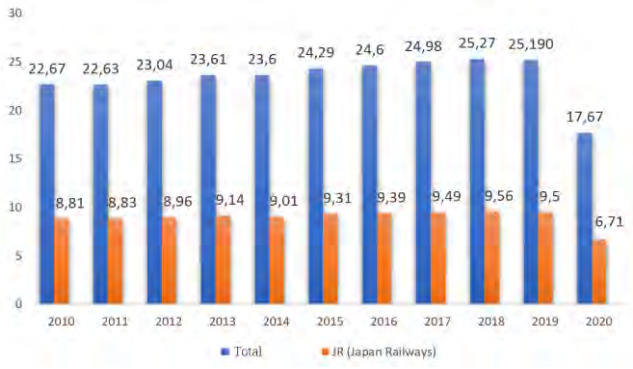

Fig. 13. Total rail passenger transport, including the Japan Railways Group, in 2010–2020, in billions [35]

Figure 13 presents the number of passengers using railway services in general and Japan Railways Group in 2010–2020. In the analyzed period, the number of passengers using the services of the Japan Railways Group accounted for almost 40% of all rail transport passengers and was systematically increasing every year, with the exception of slight decreases in 2014 and 2019. A clear slowdown occurred in 2020, i.e. in the first year of the COVID-19 pandemic.

8. Ways of financing

The current structure of Japanese railways is the result of the privatization of the national railway, which was completed in 2004, forced by a financial deficit, which was caused by high expenses incurred for the construction and launch of the Shinkansen. Three out of seven privatized companies (Central JR, East JR, West JR) are profitable and do not receive state subsidies. They are listed on the Tokyo Stock Exchange. In addition, rail operators are profitable in real estate around their rail stations, and they also make profits from servicing shopping centers, restaurants and hotels. At the same time, profitable Shinkansen lines and express trains subsidize the smaller, non-profit lines they operate [3]. Other companies (especially JR Hokkaido operating in the north of the country), unprofitable due to the small number of transports on smaller islands, receive subsidies from public funds and all remain state property. Most of the funding for the development of new Shinkansen lines is contributed by central and local governments.

In accordance with the existing cost-sharing rules, members of the former state-owned Japan Railways group lease high-speed train infrastructure from the Japan Railway Construction, Transport and Technology Agency (JRTT) – an independent government agency established in 2003 under a parliamentary act that deals with the construction of new Shinkansen lines and providing state-of-the-art technology for railway expansion projects (including tunnels and bridges) and other transportation projects throughout Japan [2].

In 2019, lease payments were calculated on the basis of estimated revenues from railway operations over 30 years. On the other hand, costs other than lease payments were shared between the central government and local governments 2:1 [29].

Since 2014, Japanese railways have been promoting their own technology of high-speed rail lines on the international arena (e.g. in the United States or India), which in the future may undoubtedly help find new customers willing to purchase their systems [19].

9. Plans and directions of further development

Huge sums, counted in billions of dollars, invested in the expansion and development of Shinkansen did not stop Japan from working on new technology – a super-fast maglev train moving without contact between the vehicle and the track, thanks to electromagnetic lift obtained by repulsion or attraction of permanent magnets or a system of electromagnets laid in the track and placed in the vehicle. The maglev, starting its journey, initially moves on rubber wheels, thanks to which the magnets under the train interact with the magnets of the runner. When the train reaches 150 km/h, the magnetic force lifts it to a height of 100 mm. At the same time, friction is

eliminated so that ever higher speeds can be achieved. The same magnetic forces that lift the train also move it forward and keep it centered in the track.

During the experimental tests of the L0 using Superconducting Maglev (SCMAGLEV) technology, a maximum speed of 603 km/h was recorded, which was a world record in this range [16].

Fig. 14. Test run of the Maglev L0-950 train [31]

Japan's first magnetic rail line (SCMAGLEV) will be the Chuo Shinkansen connecting Tokyo to Osaka. It is performed by JR Central, the operator of the Tokaido Shinkansen. The planned speed of trains on this route would be up to 505 km/h, which would reduce the travel time from 2 hours and 22 minutes to only 67 minutes. Construction of the Chuo Shinkansen began in 2014 with an estimated cost of at least $90 billion. The planned date for launching the connection to Nagoya is 2027 and to Osaka, 2045. Chuo Shinkansen will be an alternative to the 57-year-old Tokaido Shinkansen – the oldest, most crowded and operated high-speed line in Japan [13].

The nationwide Shinkansen high-speed railway is in a phase of continuous development.

In the fall of 2022, a new section of the Nishi Kyushu Shinkansen line connecting Nagasaki with Takeo–Onsen was commissioned. Of the five stations on this route, two were built from scratch, especially for the needs of this line. It is the shortest Shinkansen high-speed rail line in Japan in terms of length (its total length is 66 km). Ultimately, the entire line is to connect Hakata with Nagasaki [40].

Fig. 15. Map of the existing Shinkansen network and new lines [33]

Currently, the Hokuriku Shinkansen line is being extended with another connection between the cities of Kanazawa and Tsuruga. It is estimated that the opening will take place in 2024, and the connection will be about 125 km long. Of the six stations, five will be added to the existing stations, and Echizen–Takefu Station will be built from scratch. Construction of the last section of this Osaka–Kyoto line is scheduled to start in 2030, with its exploitation scheduled for 2045 [17]. The Hokkaido Shinkansen line will be extended by 2031 with a section connecting Shin–Hakodate–Hokuto and Sapporo. The total length of the newly constructed section will be 212 km. The route will include 17 tunnels (80% of the new route) with a total length of 168.9 km, viaducts (30.3 km), and bridges (5.3 km) [17].

The existing Shinkansen lines and the location of the planned new connections are shown in Fig. 15.

10. Summary – benefits and effects of high-speed rail transport

Investing in high-speed railways brings a number of benefits, such as shortening the travel time between the largest agglomerations or greater convenience for passengers. In addition, it is a beneficial solution for the natural environment, which can be confirmed by the success of such lines in, among others, Japan or Western European countries, e.g. in the Federal Republic of Germany [23].

Although high-speed rail travel times may seem longer than air transport, there are a number of factors that make it more attractive, including:

– faster and easier access to the station, which in the case of high-speed rail is usually located in the city center
– connections from the center to the center of large agglomerations
– price
– frequency of connections
– more freedom to work with a computer
– no requirements as to the weight and dimensions of hand luggage [9].

High-speed railways also have many significant advantages in terms of environmental impact. These include:

– relatively low level of land occupation, especially in comparison with road transport (on average 3.2 ha/km of line, with 9.3 ha/km of motorway)
– high energy efficiency both compared to car transport (about 3.4 times higher) and air transport (about 8.5 times higher)
– low level of CO_2 emissions
– low external costs (about 9 times lower than those generated by passenger cars and 5 times lower than in air transport) [4].

A fundamental element of a developed high-speed railway system is a high level of safety, which is guaranteed by advanced technical systems. Very often, a high-speed railway line is an attraction in itself, which attracts tourists to the places where it is located and additionally causes economic growth in such regions. In addition to the advantages in terms of time, convenience and environment, high-speed rail also has a huge impact on the development of the regions and countries in which it operates, as it is an important element of an efficient transport system [4].

Bibliography

[1] Andrzejewski M, Pielecha I, Merkisz J, Świechowicz R, Nowak M. Modern drive systems of rail vehicles. Combustion engines. 2019;178(3):76-81. https://doi.org/10.19206/CE-2019-314

[2] Bloomberg. https://www.bloomberg.com/news/features/2020-10-07/can-japan-s-bullet-trains-get-back-up-to-speed

[3] Cheng-en C. (photo). https://creativecommons.org/licenses/by-sa/2.0/deed.en

[4] Dyr T. High-speed railways as a factor in improving the competitiveness of railways on the transport market (in Polish). Technika Transportu Szynowego. 2010;11-12:33-43.

[5] E5 Series Shinkansen Bullet Train, Railway Technology 2012. https://www.railway-technology.com/projects/shinkansen-bullet-train-high-speed-japan/

[6] Economic observer (in Polish). https://obserwatorgospodarczy.pl/2022/03/29/najwieksze-gospodarki-swiata-w-2022-roku-na-szczycie-pozostaja-usa-chiny-i-japonia/

[7] FreeImages. https://clipart.me/free-vector/map-of-japan

[8] Gancleya J. Japan's Shinkansen: Revolutionary design at 50. https://www.bbc.com/culture/article/20140714-built-for-speed-the-bullet-train

[9] Gorlewski B. High-speed rail. Economic conditions (in Polish). Publishing House of the Warsaw School of Economics. Warsaw 2012.

[10] Graff M. E5 series Shinkansen train (in Polish). Technika Transportu Szynowego.2012;10:34-36.

[11] Graff M. Shinkansen – high-speed lines and trains in Japan (in Polish). Technika Transportu Szynowego. 2011;7-8:21-52.

[12] Heimburger J.-F. Japan and natural disasters: prevention and risk management. John Wiley & Sons 2018.

[13] Hornyak T. Shinkansen high-speed train network in Japan, Japan Station. https://www.japanstation.com/shinkansen-high-speed-train-network-in-japan/

[14] Japan Meteorological Agency. List of active volcanoes in Japan. data.jma.go.jp

[15] Japan Pipeline Development & Operation, Inc (JPDO). https://www.jpdo.co.jp/eindex.html

[16] Japan RailPass. https://www.jrailpass.com/blog/maglev-bullet-train

[17] JRTT. https://www.jrtt.go.jp/english/

[18] Kagayaki (E7/W7-Series), Japan Rail&Travel. https://japanrailandtravel.com/trains/jr-west/kagayaki-e7-w7-series/

[19] Koleo.travel. https://koleo.travel/japonia/koleje-japonskie-jr/

[20] Kuboki T. (photo). https://creativecommons.org/licenses/by-sa/2.0/deed.en

[21] MAE. https://creativecommons.org/licenses/by/4.0/

[22] Maeda A. (photo). https://creativecommons.org/licenses/by-sa/2.0/deed.en

[23] Mindur L, Mindur M. The development of high-speed rail in the Federal Republic of Germany between 2002-202. Scientific Journal of Silesian University of Technology. Series Transport. 2022;117:151-174.

[24] Mindur L. (ed.). Technologie transportowe (in Polish). Publishing House ITEe–PIB, Warsaw–Radom 2014.

[25] Mindur M. (ed.). Logistyka. Nauka–Badania–Rozwój (in Polish). Publishing House ITEe–PIB, Warsaw–Radom 2017.

[26] Mindur M. Transportochłonność gospodarki światowej w latach 1998-2015 (in Polish). Gospodarka Materiałowa i Logistyka. 2016;10.

[27] Nakamura A, Graff M. Shinkansen E7/W7 (in Polish). Technika Transportu Szynowego. 2015;11:43-45.

[28] OECD Data. https://data.oecd.org

[29] Ogawa K. Japan wants more 'private' in public-private bullet train funding. NikkeiAsia 2019. https://asia.nikkei.com/Business/Transportation/Japan-wants-more-private-in-public-private-bullet-train-funding

[30] Pinterest. https://nl.pinterest.com/pin/834503005930752907/

[31] Saruno H. (photo). https://creativecommons.org/licenses/by-sa/2.0/deed.en

[32] Sawczuk W, Kołodziejski S, Rilo Cañás AM. Determination of the resistance to motion of a cargo train when driving without a drive. Combustion Engines. 2024;197(2):64-70. https://doi.org/10.19206/CE-184051

[33] Shinkansen Route Map. https://www.nippon.com/en/features/h00077

[34] Shinkansen, Japan, Railway Technology 2020. https://www.railway-technology.com/projects/shinkansen-bullet-train/

[35] Statistical Handbook of Japan 2013-2022, Ministry of Internal Affairs and Communications. https://www.stat.go.jp/english/data/handbook/pdf/

[36] Statistics Bureau of Japan. https://www.stat.go.jp/english/data/

[37] Statistics Dashboard. https://dashboard.e-stat.go.jp

[38] Sui-setz (photo). https://creativecommons.org/licenses/by-sa/2.0/deed.en

[39] Technical Regulatory Standards on Japanese Railways. Railway Bureau Ministry of Land, Infrastructure, Transport and Tourism. https://www.mlit.go.jp/english/2006/h_railway_bureau/Laws_concerning/14.pdf

[40] The Japantimes. https://japantimes.co.jp/news/2022/09/12/business/corporate-business/nishi-kyushu-shinkansen/

[41] The World Factbook. https://www.cia.gov/the-world-factbook/countries/japan/

Prof. Leszek Mindur, DSc., DEng. – The International University of Logistics and Transport in Wrocław, Poland.
e-mail: *lmindur@vp.pl*

Prof. Zenon Zamiar, DSc., DEng. – The International University of Logistics and Transport in Wrocław, Poland.
e-mail: *zzamiar@msl.com.pl*

Prof. Maciej Mindur, DSc., DEng. – Lublin University Technology, Poland.
e-mail: *m.mindur@pollub.pl*

Article citation info:
Stecuła B, Sitko J, Stecuła K, Witkowski M, Orzeł B. Comparison of the strength of popular thermoplastic materials used in 3D printing – PLA, ABS and PET-G. Combustion Engines. 2024;199(4):97-103. https://doi.org/10.19206/CE-189386

Beniamin STECUŁA
Jacek SITKO
Kinga STECUŁA
Mirosław WITKOWSKI
Bartosz ORZEŁ

Combustion Engines
Polish Scientific Society of Combustion Engines

Comparison of the strength of popular thermoplastic materials used in 3D printing – PLA, ABS and PET-G

ARTICLE INFO

Received: 30 November 2023
Revised: 17 April 2024
Accepted: 27 May 2024
Available online: 19 July 2024

This paper presents the results of a comparative analysis of three prevalent materials used in 3D printing. PLA (Polylactic Acid), ABS (Acrylonitrile Butadiene Styrene), and PET-G (Polyethylene Terephthalate Glycol). The study includes strength testing using a tensile testing machine. Beginning with the selection of the input material used in the 3D printing process, the research aimed to provide insights into the strength properties of these materials. Autodesk Fusion 360 software was used for the precise design of the 3D model, ensuring suitability for subsequent tensile testing. The physical samples were then printed using 3D printing technology. The samples were subjected to a strength examination using a tensile testing machine. The data collection phase recorded and compiled the results of each strength test, forming the foundation for a comprehensive analysis. Using statistical methods and comparative analyzes, the data were thoroughly examined, allowing the derivation of conclusive observations and insights into the comparative strengths of PLA, ABS, and PET-G. The findings not only contribute to a deeper understanding of material performance but also provide a guide for material selection in 3D printing applications, guiding future research endeavors and industry applications in the ever-evolving landscape of additive manufacturing.

Key words: *strength, materials, 3D printing, tensile testing machines, engines, PLA, ABS, PET-G*

1. Introduction

With the continuous progress of technology, the industry connected with its production has undergone a great change. The emergence of Industry 4.0 has started a new era, where the fusion of cutting-edge technologies meets traditional manufacturing, reshaping the essence of production methods. One of the trends of this transformative wave is connected to additive technologies and advances in materials; this is a change in the way people think, design, and produce. It is related to Industry 4.0, which assumes the synergy between digital advances and physical systems [1]. This fourth industrial revolution represents a holistic evolution, including interconnected cyber-physical systems, the Internet of Things (IoT) [2], cloud computing [27], and cognitive computing [8]. These elements are converged to optimize processes, improve efficiency, and introduce more innovation in manufacturing and everyday life. Industry 4.0 also includes the development of additive technologies, covering a spectrum of techniques such as 3D printing [19], bioprinting [11], and advanced manufacturing methodologies [18, 23, 28, 36]. These technologies transcend the limitations of conventional manufacturing by enabling layer-by-layer construction, empowering designers and engineers to materialize designs with precision and customization. This change not only expedites production but also leads to material innovation that was previously unimaginable. Material innovation, as another element of the revolution, opens new possibilities. The ability to craft and manipulate materials at the microscopic level has redefined material properties, durability, strength, and functionality. Additive manufacturing, when paired with novel materials, including bioderived substances, is driving industries towards innovation and sustainability.

2. Engines and 3D printing

Industry 4.0 opens new possibilities for new research on engine topics, and the range of topics is broad, starting from studies on materials [33], through types of fuel [31], to emissions issues [32]. 3D printing is also a highly developing direction for research and practical application. 3D printing opens new possibilities in the field of vehicles and their engines. In the literature and practice, there are more and more examples of replacement of vehicle elements, and even engines parts, with elements and parts printed from popular filaments on a 3D printer. Products that come from additive manufacturing processes have broad industrial applications, including the automotive sector. The adaptability and mechanical properties of materials used as inputs in 3D printing make them pertinent for manufacturing components within engines and vehicles. Examples of 3D printing applications in the mentioned areas:

- components for the gas-discharge chamber of electric engines [24]
- solid fuel block mold geometries for hybrid engines [6]
- different gaskets in engines [29]
- air intake manifolds [30]
- pistons for engines [5]
- engine o-rings [12].

The adaptability and mechanical properties of materials used in 3D printing make them highly relevant for manufacturing components within engines and vehicles. This diversity is exemplified by various applications in the engine sector. For instance, 3D printing is utilized to fabricate components for gas-discharge chambers in electric engines, enabling precise customization. Additionally, it enables the creation of intricate mold geometries for solid fuel blocks in

hybrid engines, enhancing efficiency. Also, 3D printing is employed in producing customized gaskets tailored to specific engine requirements. Moreover, it facilitates the manufacturing of air intake manifolds with optimized designs, leading to better engine efficiency. Furthermore, 3D printing allows for the crafting of high-strength, lightweight pistons, consequently enhancing engine performance and fuel efficiency. It also enables the production of customized engine o-rings for reliable sealing and functionality. These diverse applications underscore the adaptability and potential of 3D printing in producing a wide array of components and parts within the engine sector, offering increased customization, efficiency, and functionality in the manufacturing process.

These diverse applications illustrate the adaptability and potential of 3D printing in producing a wide array of components and parts within the engine sectors. The ability to tailor design, material selection, and manufacturing processes via 3D printing continues to revolutionize the production of various elements in vehicles and their engines, offering increased customization, efficiency, and functionality.

On the one hand, there are wide possibilities for using 3D printing in engines, and on the other hand, there is progress in input materials used in 3D printing. These two areas should be combined in research. Namely, the first stage in the above-mentioned areas should be research on the properties and capabilities of 3D printing materials that will be used in engines. For this reason, the authors undertook research on the strength of various materials used in 3D printing in order to focus on the production of selected engine components in the next stages. The strength testing stage is extremely important. This article presents only preliminary research on the strength of materials, which is only a fragment of larger research.

Based, on the above, the authors decided to conduct research in the field of comparing the strength of materials used for 3D printing. The authors selected the three most popular materials, PLA, ABS and PET-G, and conducted tests on their strength. Research included the preparation of a 3D model for the samples, the printing of the samples in each material, and carrying out strength tests on a tensile testing machine. After completing this stage of research, the authors analysed the results and drew conclusions.

3. Materials and methods

3.1. Research methodology

The methodology of the research included several steps:

- Step 1: Material selection: the initial phase involved a meticulous selection process to identify and choose the most prevalent materials in the 3D printing area. PLA (Polylactic Acid), ABS (Acrylonitrile Butadiene Styrene), and PET-G (Polyethylene Terephthalate Glycol) were chosen due to their widespread use, distinct properties, and relevance in various industries.
- Step 2: Design of the 3D model: to ensure consistency and accuracy in testing, the 3D model for the samples were designed using Autodesk Fusion 360 software. The model was the step before printing the samples, so the design had to be suitable for a tensile testing machine.
- Step 3: printing process: using 3D printing technology, the designed models were fabricated into physical samples using each of the selected materials – PLA, ABS, and PET-G. This step also included setting the printing parameters.
- Step 4: sample preparation: after printing the samples underwent meticulous post-processing to eliminate any inconsistencies or imperfections that could potentially impact the strength testing phase.
- Step 5: strength testing: the strength examination was conducted using a tensile testing machine capable of performing various mechanical tests. This step also included setting the machine's input parameters for strength tests – before examination began.
- Step 6: data collection: after each strength test, the computer generated the test results. Therefore, this stage of the research included the generation and collection of data from each strength test.
- Step 7: data analysis: the data collected from the strength tests were comprehensively analyzed, employing statistical methods and comparative analyzes. Based on the analysis of the test results, conclusive observations and insights were drawn regarding the comparative strengths of PLA, ABS, and PET-G.

3.2. Model designing

Autodesk's Fusion 360 software was used to prepare the model of the sample used in the experiment. Figure 1 presents a design in accordance with the E8/E8M-16a standard, with dimensions of L = 200 mm, C = 16 mm, and W = = 16 mm.

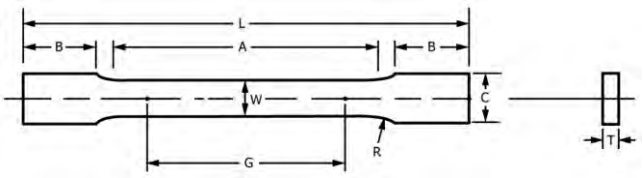

Fig. 1. A design of a round tensile specimen

Figure 2 shows a visualization of the sample in the form of a three-dimensional render.

Fig. 2. A three-dimensional render that is a visualization of a sample prepared in Autodesk's Fusion 360 software

3.3. Materials

A 3D printer allows you to produce different objects from specific materials. Popular polymer materials used for 3D printing are PLA, PET-G and ABS [35]. The study tested the strength of these materials.

3.3.1. PLA

It is a polymer produced from lactic acid [25]. It is a biodegradable material produced from renewable sources [20]. PLA is considered a non-toxic material, [13] but the authors of the article "Photolytic degradation elevated the toxicity of polylactic acid microplastics to developing zebrafish by triggering mitochondrial dysfunction and apoptosis." point out that PLA microplastics have a higher toxicity after degradation, in the context of a threat to aquatic ecosystems [21]. PLA prints are hard and brittle. The melting point of PLA filaments is low, about 175°C [37]. It is one of the most popular materials for 3D printing. It is often used in home or school 3D printers.

3.3.2. PET-G

It is a polyethylene terephthalate with the addition of glycol [10]. It is also a frequently used material in 3D printing. It has high resistance to damage and is malleable [26]. It is a material that biodegrades quickly, is harmless to humans and does not exhibit significant toxicity [7]. Prints made of PET-G material are stiff and have a glossy surface. It is worth noting the low hygroscopicity of this material, as well as its elasticity and lower shrinkage [3]. It is also often used in home and school 3D printers.

3.3.3. ABS

It is an acrylonitrile-butadiene styrene [34]. Also often used in 3D printing. It is a durable material, but at the same time, it has an easy ability to process [17], e.g., by drilling or grinding it. ABS printing produces harmful fumes, which is why ABS 3D printing should be done with adequate ventilation [22]. ABS also has a high degree of thermal shrinkage, compared to a low degree of thermal shrinkage in the case of PLA and PETG materials. This can lead to the so-called warping of ABS prints [9]. The coating of objects printed with ABS material can be smoothed with acetone, but this changes the structure and mechanical properties of the prints [13].

3.4. 3D printing process

Samples were printed from three types of materials: PLA, PET-G and ABS. The printing process was carried out according to the specifics of the manufacturer of a given 3D printer. For each 3D printer, the same sample output 3D model was used.

Samples made of PET-G material were printed on a Prusa i3 MK3S+ printer, and materials PLA and ABS were used in an Anycubic 4MAX pro printer. These are models of 3D printers that allow you to print from such materials. The 3D model was prepared for printing using Slicer and Ultimaker Cura software, which saved the model in a format known to a 3D printer. The Slicer program used was Prusa Slicer. In this program, printing parameters such as layer height and infill pattern have been assigned. Then, the file prepared for the 3D printer was saved on a memory card, which was placed in the 3D printer. The appropriate project was selected from the 3D printer menu to start the 3D printing process. After its completion, the model was properly described (Fig. 3).

Fig. 3. Printed and labeled samples

3.4.1. 3D printing settings

The 3D models were printed from each material in three different versions. Models with a layer height of 0.1 mm, 0.2 mm and 0.3 mm. A grid infill pattern and an infill density of 20% were used in all 3D prints. The models were printed vertically, and there was no need for supports. An extruder nozzle with a diameter of 0.4 mm was used. Speed of printing was adjusted by slicer software depending on used material and the print move types. The speed of printing the PETG model with 0.1 mm layer height is presented in Fig. 4. The nozzle and print bed temperatures have been adjusted to the characteristics of the material being used. For PLA material, the nozzle temperature was in the range of 210–215°C, and the printbed temperature was 60°C. For PET-G material, the nozzle temperature was 230°C, and the printbed temperature was in the range of 85–90°C. For ABS material, the nozzle temperature was 235°C, and the printbed temperature was 95°C.

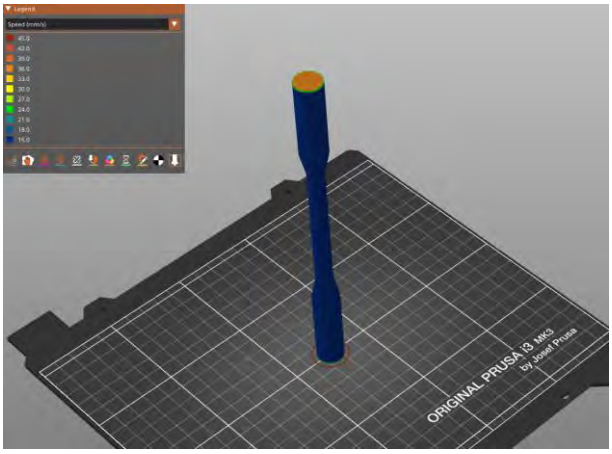

Fig. 4. Speed of printing PETG model with 0.1mm layer height

3.4.2. Filaments used during the 3d printing process

3D models were printed with PLA, PET-G and ABS materials.

For PET-G models, filament Devil Design PET-G Yellow was used. This filament has a diameter of 1.75 mm. Referring to the manufacturer's product card [38], this filament has a diameter tolerance of ±0.05 mm and an oval tolerance of + 0.02 mm. The recommended nozzle temperature during printing is in the range of 220–250°C, and the

recommended printbed temperature is in the range of 70–80°C. However, the manufacturer of the Prusa 3D printer, in its profile for the Devil Design PET-G filament, specified a nozzle temperature of 230°C and a printbed temperature in the range of 85–90°C.

For PLA models, filament Devil Design PLA Bright Yellow was used. This filament has a diameter of 1.75 mm. Referring to the manufacturer's product card [39], this filament has a diameter tolerance of ±0.05 mm and an oval tolerance of + 0.02 mm. The recommended nozzle temperature during printing is in the range of 200–235°C, and the recommended printbed temperature is in the range of 50–60°C.

For ABS models, filament Devil Design ABS+ White was used. This filament has a diameter of 1.75 mm. Referring to the manufacturer's product card [40], this filament has a diameter tolerance of ±0.05 mm and an oval tolerance of + 0.02 mm. The recommended nozzle temperature during printing is in the range of 230–240°C, and the recommended printbed temperature is in the range of 90–100°C.

3.5. Characteristics of the machine

For the research, we used the Universal Material Testing Machine (Fig. 5) named model QC-503M2F (100kN). The manufacturer of the machine used for testing declares that it meets the following features [11]:

- compliance with standards: ISO 7500-1, ASTM E4, ASTM D-76, DIN5122, JIS B7721/B7733, EN 1002-2, BS1610, GB T228
- this series model is able to withstand a load of more than 100 kN
- qualified for ASTM, ISO, JIS, GB standard
- application to plastics, textiles and metals
- max capacity: 100 kN
- force units: gF, kgF, N, kN, tons
- pressure: kPa, MPa, bar, mm-Aq, mm-Hg

Measurement parameters:

- specimen diameter: 10 mm
- preload: 15 N
- minimum force from which we check the condition 50 N
- test speed: 15 mm/min.

Fig. 5. Jaws of the QC-503M2F Universal Testing Machine, general view

Other features described by the manufacturer [4]:

- automatic reading of load cell property information
- automatic reading of information from the displacement sensor
- force display, displacement display, time display, stress display, and strain display
- external analog input (2-channel simultaneous voltage or current readout)
- test force automatically reset
- self-definable test force calibration
- breakage detection
- automatic return
- force overload protection.

4. Results

4.1. Results of strength examination

The subject of the study were samples made of PETG, ABS and PLA, made in the 3D printing technique.

Samples with a diameter of 10 mm and a filling of 20% (characterized by lower material consumption, which translates into lower cost and shorter time of printing the sample) were tested. The technique of layered printing with layer thicknesses was used:

- 0.1 mm
- 0.2 mm
- 0.3 mm.

A static tensile test of the material was used for the tests.

Tests at room ambient temperature, about 20ºC, allowed us to draw many conclusions. The tested samples were characterized by similar strength compared to the steel sample, which is the comparative material:

- PETG 6 MPa
- PLA 5.8 MPa
- ABS 5.4 MPa
- steel reference sample 480 MPa.

According to a scientific website Matweb, the tensile strength of beforementioned materials is approximately:

- PETG 45 MPa [14]
- ABS 38 MPa [15]
- PLA 60 MPa [16].

4.2. Analysis of results

It can be noted that the obtained in the study tensile strength of PETG, PLA, and ABS materials are several times lower than values from the scientific website Matweb. This could be due to 20% filling of 3D models and as a consequence of the layering nature of 3D printing. It should be noted that the break has always occurred between the layers. The obtained results are different because this research was meant to be unique in terms of testing not the material itself but the use of this material in the context of 3D printing.

The ABS material in our measurements had the least tensile strength, which agrees with the data presented, while PLA and PETG had similar values, so further testing on a larger number of samples is indicated. The lowest tensile strength was found in the printed plastic with a layer of 0.3 mm. A selected graph of a material PETG is presented in the Fig. 6.

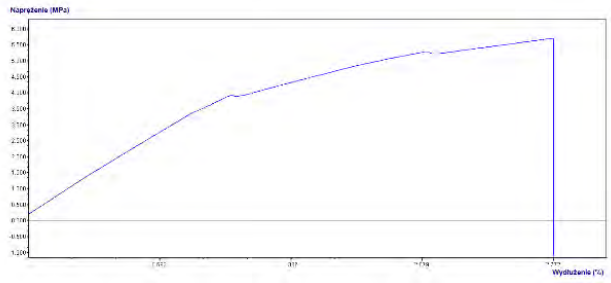

Fig. 6. Diagram showing the result of the tensile test of a PETG sample with a density of 20 % and a printing layer of 0.3 mm

ABS plastic (Fig. 7) is characterized by the highest elongation, up to 5%, with an average tensile force of approx. 5.4 MPa. This proves that the material is highly plastic, maintaining optimal tensile strength. The highest strength up to 6 MPa, ABS achieves for a layer with a thickness of 0.1 mm.

The elongation before tearing tested by us was:

– PETG 2.5%
– PLA 1.1%
– ABS 3.4%.

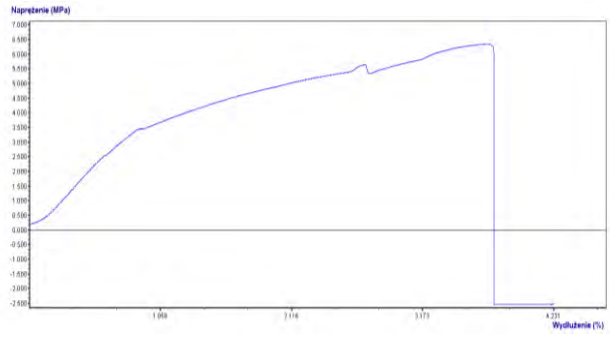

Fig. 7. Diagram showing the result of the tensile test of an ABS sample with a density of 20 % and a printing layer of 0.1 mm

PLA material (Fig. 8), printed with a layer of 0.1 mm, has the highest tensile strength of approx. 7.5 MPa and the highest plasticity of approx. 1.5% compared to prints with a different layer thickness. PLA is characterized by the highest rigidity, hardness, and abrasion resistance among the tested materials.

The non-uniform course of diagrams, especially for ABS and PET-G plastics with a characteristic step, visible around 2/3 of the elongation (Fig. 7 and 8), may result from the influence of internal forces on or between polymer chains. It is advisable to perform additional tests for the above-mentioned materials with a filling of up to 80%. This will make it possible to compare the results of strength and plasticity as well as the reaction of plastics to statically increasing mechanical load.

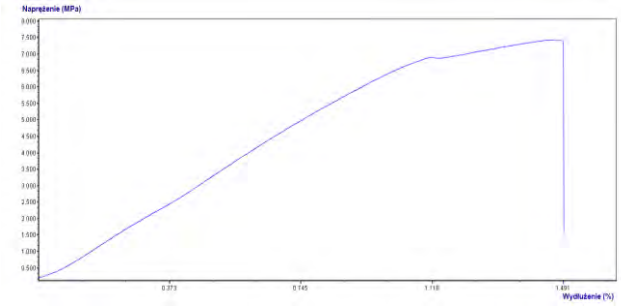

Fig. 8. Diagram showing the result of tensile testing of a PLA sample with a density of 20 % and a printing layer of 0.1 mm

5. Conclusions

Summarizing the results of the research, it can be concluded that the used testing machine is also suitable for testing polymers intended for 3D printing, and its selection turned out to be right. The results of the tests allow to compare the strength of 3D models printed from PLA, PET-G, and ABS. An important conclusion is that the selection of 3D printing parameters, as well as the selection of the polymer material used, affects the durability of the printed models. Changing the height of the 3D printing layer causes a change in the strength of a given model. It is advisable to explore the research, e.g. by comparing 3D prints with a different degree of filling.

To improve the quality of the designed materials, their properties can be tested when the 3D printing model will be made with thicker layers or using two different materials.

The research presented in the article is only the initial stage of larger research on the strength of materials used in 3D printing. Expanding from the foundational strength testing of PLA, ABS, and PET-G materials, future research will focus on optimizing these materials for engine-specific conditions, possibly through composite formulations or altered manufacturing processes. Subsequent stages will involve fabricating actual engine components via 3D printing and subjecting them to rigorous performance tests simulating real-world engine stresses. Additionally, analyzing the lifecycle and environmental impact of these materials and fostering collaborations with engine manufacturers would ensure alignment with industry needs and sustainable advancements in additive manufacturing for engine components.

Bibliography

[1] Asadollahi-Yazdi E, Couzon P, Nguyen NQ, Ouazene Y, Yalaoui F. Industry 4.0: Revolution or evolution? Am J Oper Res. 2020;10(6):241. https://doi.org/10.4236/ajor.2020.106014

[2] Banaeian Far S, Imani Rad A, Hosseini Bamakan SM, Rajabzadeh Asaar M. Toward metaverse of everything: opportunities, challenges, and future directions of the next generation of visual/virtual communications. J Netw Comput Appl. 2023;217:103675. https://doi.org/10.1016/j.jnca.2023.103675

[3] Belloncle B, Bunel C, Menu-Bouaouiche L, Lesouhaitier O, Burel F. Study of the degradation of poly(ethyl glyoxylate): biodegradation, toxicity and ecotoxicity assays. J Polym Environ. 2012;20:726-731. https://doi.org/10.1007/s10924-012-0429-2

[4] Cometech Testing Machines Co., Ltd. https://www.cometech.com.tw/tensile-testing-machine/QC-501M2F-502M2F-503M2F.html (accessed on 2023-11-20).

[5] Dolan R, Budde R, Schramm C, Rezaei R. 3D printed piston for heavy-duty diesel engines. Proc. of the 2018 Ground

Vehicle Systems Engineering and Technology Symposium. 2018. https://events.esd.org/wp-content/uploads/2018/07/3D-Printed-Piston-for-Heavy-Duty-Diesel-Engines.pdf
[6] Grefen B, Becker J, Linke S, Stoll E. Design, production and evaluation of 3d-printed mold geometries for a hybrid rocket engine. Aerospace, 2021;8(8):220. https://doi.org/10.3390/aerospace8080220
[7] Guessasma S, Belhabib S, Nouri H. Printability and tensile performance of 3D printed polyethylene terephthalate glycol using fused deposition modelling. Polymers. 2019;11(7): 1220. https://doi.org/10.3390/polym11071220
[8] Gupta S, Kar AK, Baabdullah A, Al-Khowaiter WAA. Big data with cognitive computing: a review for the future. Int J Inf Manage. 2018;42:78-89. https://doi.org/10.1016/j.ijinfomgt.2018.06.005
[9] Gwiazda P. Praca z filamentem – najczęściej zadawane pytania (in Polish). https://centrumdruku3d.pl/praca-z-filamentem-najczesciej-zadawane-pytania/?amp=1 (accessed on 2023-11-20)
[10] Ilyas R, Zuhri M, Aisyah H, Asyraf M, Hassan S, Zainudin E et al. Natural fiber-reinforced polylactic acid, polylactic acid blends and their composites for advanced applications. Polymers. 2022;14(1):202. https://doi.org/10.3390/polym14010202
[11] Liaw C-Y, Guvendiren M. Current and emerging applications of 3D printing in medicine. Biofabrication. 2017;9(2): 24102. https://doi.org/10.1088/1758-5090/aa7279
[12] Luning-Prak D, Baker B, Cowart J. Engine o-rings produced using additive manufacturing. SAE Technical Paper 2023-01-0893. 2023. https://doi.org/10.4271/2023-01-0893
[13] Marciniak D, Szewczykowski P, Czyżewski P, Sykutera D, Bieliński M. Effect of surface modification by acetone vaporization on the structure of 3D printed acrylonitrilebutadienestyrene elements. Polimery. 2018;63(11-12):785-790. https://doi.org/10.14314/polimery.2018.11.6
[14] MatWeb, LLC https://www.matweb.com/search/datasheet_print.aspx?matguid=4de1c85bb946406a86c52b688e3810d0 (accessed on 2023-11-20).
[15] MatWeb, LLC https://www.matweb.com/search/DataSheet.aspx?MatGUID=3a8afcddac864d4b8f58d40570d2e5aa (accessed on 2023-11-20).
[16] MatWeb, LLC https://www.matweb.com/search/DataSheet.aspx?MatGUID=ab96a4c0655c4018a8785ac4031b9278 (accessed on 2023-11-20).
[17] Mehmood M, Li J, Jaffri Z, Hassan M. Performance evaluation of ABS (acrylonitrile-butadiene styrene) as high voltage insulator in the outdoor environment. 2017 1st International Conference on Electrical Materials and Power Equipment (ICEMPE), 2017:700-702. https://doi.org/10.1109/ICEMPE.2017.7982193
[18] Mitra S, de Castro AR, El Mansori M. On the rapid manufacturing process of functional 3D printed sand molds. J Manuf Process. 2019;42:202-212. https://doi.org/10.1016/j.jmapro.2019.04.034
[19] Mohanavel V, Priyadharshan R, Ravichandran M, Sivanraju R, Velmurugan P, Subbiah R. The role and application of 3D printer in the automobile industry. ECS Trans. 2022; 107(1):12001. https://doi.org/10.1149/10701.12001ecst
[20] Murariu M, Dubois P. PLA composites: from production to properties.. Adv Drug Deliver Rev. 2016;107:17-46. https://doi.org/10.1016/j.addr.2016.04.003
[21] Nofar M, Saçlıgil D, Carreau P, Kamal M, Heuzey M. Poly (lactic acid) blends: processing, properties and applications. Int J Biol Macromol. 2019;125:307-360. https://doi.org/10.1016/j.ijbiomac.2018.12.002
[22] Olivera S, Muralidhara H, Venkatesh K., Gopalakrishna K, Vivek C. Plating on acrylonitrile–butadiene–styrene (ABS) plastic: a review. J Mater Sci. 2016;51:3657-3674. https://doi.org/10.1007/s10853-015-9668-7
[23] Orzeł B, Stecuła K. Comparison of 3D printout quality from FDM and MSLA technology in unit production. Symmetry. 2022;14(5):910. https://doi.org/10.3390/sym14050910
[24] Pogodin VA, Rabinskii LN, Sitnikov SA. 3D printing of components for the gas-discharge chamber of electric rocket engines. Russ Engin Res. 2019;39:797-799. https://doi.org/10.3103/S1068798X19090156
[25] Prusament. Prusament PETG. https://prusament.com/pl/materials/prusament-petg/ (accessed on 2023-11-20).
[26] Prusament. Prusament PLA. https://prusament.com/pl/materials/prusament-pla/ (accessed on 2023-11-20).
[27] Sadeeq MM, Abdulkareem NM, Zeebaree SRM, Ahmed DM, Sami AS, Zebari RR. IoT and cloud computing issues, challenges and opportunities: a review. Qubahan Acad J. 2021;1(2):1-7. https://doi.org/10.48161/qaj.v1n2a36
[28] Satsangi R, Singh H, Satsangee GR, Agrawal S, Sharma S, Gautam G. The concept of viscous material (chocolate) 3D printer/food 3D printer. International Research Journal of Engineering and Technology. 2018;5(2):2144-2148. https://api.semanticscholar.org/CorpusID:222507191
[29] Sava M, Nagy R, Menyhardt K. Characteristics of 3D printable bronze PLA-based filament composites for gaskets. Materials. 2021;14(16):4770. https://doi.org/10.3390/ma14164770
[30] Shaikh S, Jadhav H, Gajinkar A, Khare I, Singh M. Selection of additive manufacturing technology for optimized intake manifold: a review. PalArch's Journal of Archaeology of Egypt/Egyptology. 2020;17(9):4270-4300. https://archives.palarch.nl/index.php/jae/article/view/4602
[31] Stępień Z. Analysis of the prospects for hydrogen-fuelled internal combustion engines. Combustion Engines. 2024; 197(2):32-41. https://doi.org/10.19206/CE-174794
[32] Szczepański E, Jachimowski R, Rudyk T. Simulation studies of fleet vehicle selection in terms of pollutant emissions. Combustion Engines. 2024;196(1):80-88. https://doi.org/10.19206/CE-169802
[33] Tomaszewski S, Grygier D, Dziubek M. Assessment of engine valve materials. Combustion Engines. 2023;194(3): 48-51. https://doi.org/10.19206/CE-166569
[34] Valvez S, Silva A, Reis P. Optimization of Printing Parameters to maximize the mechanical properties of 3D-printed PETG-based parts. Polymers, 2022, 14(13):2564. https://doi.org/10.3390/polym14132564
[35] Woo I, Kim D, Kang H, Lyu M. Cross-section morphology and surface roughness of an article manufactured by material extrusion-type 3D printing according to the thermal conductivity of the material. Elastomers and Composites. 2020; 55:46-50. https://doi.org/10.7473/EC.2020.55.1.46
[36] Xiao J, Ji G, Zhang Y, Ma G, Mechtcherine V, Pan J et al. Large-scale 3D printing concrete technology: current status and future opportunities. Cem Concr Compos. 2021;122: 104115. https://doi.org/10.1016/j.cemconcomp.2021.104115
[37] Zhang X, Xia M, Su X, Yuan P, Li X, Zhou C et al. Photolytic degradation elevated the toxicity of polylactic acid microplastics to developing zebrafish by triggering mitochondrial dysfunction and apoptosis. J Hazard Mater. 2021;413: 125321. https://doi.org/10.1016/j.jhazmat.2021.125321

[38] Devil Design, PET-G Product Card. https://devildesign.com/download/PET-G_-_product_card.pdf (accessed on 2024-04-10).
[39] Devil Design, PLA Product Card. https://devildesign.com/download/PLA_-_product_card.pdf (accessed on 2024-04-10).
[40] Devil Design, ABS+ Product Card. https://devildesign.com/download/ABS+_-_product_card.pdf (accessed on 2024-04-10).

Beniamin Stecuła, MEng. – Faculty of Applied Mathematics, Silesian University of Technology, Poland.
e-mail: *beniamin.stecula@polsl.pl*

Kinga Stecuła, PhD – Faculty of Organization and Management, Silesian University of Technology, Poland.
e-mail: *kinga.stecula@polsl.pl*

Jacek Sitko, DEng. – Faculty of Organization and Management, Silesian University of Technology, Poland.
e-mail: *jacek.sitko@polsl.pl*

Mirosław Witkowski, MEng. – Faculty of Applied Mathematics, Silesian University of Technology, Poland.
e-mail: *miroslaw.witkowski@polsl.pl*

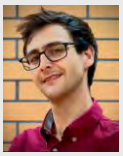

Bartosz Orzeł, MEng. – Faculty of Organization and Management, Silesian University of Technology, Poland.
e-mail: *bartosz.orzeł@polsl.pl*

Article citation info:
Boruc Ł, Kapusta ŁJ, Kindracki J. Selection of the method for determination of ignition delay of hypergolic propellants. Combustion Engines. 2024;199(4):104-111. https://doi.org/10.19206/CE-192420

Łukasz BORUC
Łukasz Jan KAPUSTA
Jan KINDRACKI

Combustion Engines
Polish Scientific Society of Combustion Engines

Selection of the method for determination of ignition delay of hypergolic propellants

ARTICLE INFO

Received: 5 July 2024
Revised: 23 July 2024
Accepted: 18 August 2024
Available online: 20 August 2024

Ignition delay is one of the most important parameters characterising hypergolic propellants. This parameter has a strong impact on thruster operation, especially during the cold start. Ignition delay influences the intensity of pressure rise and its peak values during the start of a thruster. High-pressure levels cause stress inside the chamber wall, which directly affects durability and safety. One of two measurement techniques is usually chosen to determine the ignition delay: visual and pressure-based methods. Visual methods are based on high-speed imaging and subsequent image analysis. In the pressure-based method, the pressure trace is analysed. In this study, both techniques were used together and compared in terms of ignition delay determination of hypergolic propellants igniting during the drop tests. The advantages and disadvantages of both techniques were indicated and described. In the setup used in the study, the visual method was found to be more accurate and reliable.

Key words: *ignition delay, hypergolic ignition, hypergolic propellants, drop test*

1. Introduction

The ignition delay of hypergolic propellants is usually determined by a so-called drop-test method where a drop of oxidiser (or fuel) is dropped into the fuel (or oxidiser) pool [1–5, 7–9, 12, 18, 19, 23–25, 33, 34, 37–39]. In such an arrangement, the ignition delay is determined as the time between the contact of the oxidiser with the fuel and the start of combustion (SOC). In this study, we focus on the determination of SOC.

Alfano et al. [2] used a high-speed camera, two photodiodes and a laser diode to determine the ignition delay and chemical delay in the drop tests. Based on the registered signals, they identified the moment of droplet impact, gas emission near the surface, and light emission from combustion.

Blevins et al. [3] used high-speed photography and Schlieren techniques to determine hypergolic ignition delay between hydrogen peroxide (an oxidiser) and N,N-dimethylbutylamine and N,N-dimethylhexylamine (fuels). The amines were mixed with a catalyst (cobalt II 2-ethylhexanoate) and mineral oil, acting as a stabiliser (prepared as mixtures in a 65% to 35% ratio). The catalyst and stabiliser constituted 5% of the final fuel mixture. The Schlieren imaging enabled the visualisation of enhanced gas-phase generation, which was associated with the decomposition time. Thus, the reported results included both decomposition delay and ignition delay.

Another work utilising the drop test method to measure ignition time delay was conducted by Kang et al. [20]. They tested the ignition of three different fuels with hydrogen peroxide (90%, 95%, and 98%) acting as oxidiser. To measure the ignition delay, they used a high-speed camera with an additional halogen lamp to illuminate falling droplets. Mahakali et al. [24] also used the drop-test method with a high-speed camera to determine the existence of ignition and ignition delay for a group of fuels (triglyme, dimethyl formamide, and dimethyl sulfoxide) with the addition of sodium borohydride (in various concentrations). They used hydrogen peroxide with a concentration between 87.4% and 88.5% as the oxidiser.

McCrary et al. [25] employed the drop test technique with a high-speed camera to measure the ignition delay of synthesised fuels with various oxidisers (99.5% white fuming nitric acid (WFNA), inhibited red fuming nitric acid (IRFNA), and 70% nitric acid (NA). In their setup, the oxidiser drops were dropped onto samples of the fuels. Ramachandran et al. [34] used the drop test technique to measure ignition time delay for WFNA and amine-borane with a high-speed camera and an LED light array to illuminate the fuel sample and the oxidiser.

Wang and Thynell [37] used a similar method to measure the ignition delay of MMH with three different mixtures of nitric acid and water (30% H_2O, 10% H_2O, and WFNA). However, they also measured signals from thermocouples (located at two distances from the fuel pool), photodiodes, and a microphone. They compared the measurements from the photodiode with the signal from the microphone and thermocouples. The signals correlated differently depending on the propellant type, exhibiting sensitivity to the fuel-oxidiser interaction type.

Zarbo et al. [38] studied the effect of humidity and water on the reaction between two pairs of fuel and oxidiser: MMH-RFNA and TEAB (triethylamine borane)-WFNA. The measurements were conducted in a dedicated and developed drop-test stand using a high-speed camera, a piezoelectric sensor to detect droplet impact, and a photodiode to detect the onset of ignition. Zhan and Shreeve [39] also used the drop-test method with a high-speed camera to determine the ignition delay of nine fuels (with three boron-based additives) with WFNA.

Ak et al. [1] used a high-speed camera to measure the ignition delay for 85% hydrogen peroxide and ethanolamine in open-cup drop-test experiments. They assessed the influence of oxidiser and fuel temperature on the ignition time delay. Chambreau et al. [4] applied Fourier-transform

infrared (FTIR) absorption spectroscopy using a rapid-scan spectrometer to observe drop-test experiments for 1-propargyl-3-methyl-imidazolium dicyanamide or MMH with WFNA or RFNA. Chowdhury et al. [5] used the drop test with high-speed photography to observe photodiode signal and laser-induced fluorescence to study the mixing between the liquids. In the drop tests, they used two fuels: 1-ethyl-3-methyl-imidazolium dicyanamide and 1-butyl-3-methyl-imi-dazolium dicyanamide, reacting with 70% and 90% WFNA.

Coil [7] used the drop test to study the ignition of gelled methyl ethyl imidazolium dicyanamide (fuel) with nitric acid (oxidiser). They applied high-speed photography and a photoresistor to determine the ignition delay. Dambach et al. [8] used the drop-test technique with a high-speed camera to observe the ignition process of several selected fuels with RFNA and determine ignition delay. Davis and Yilmaz [9] used a high-speed camera and photodiode to observe the ignition delay of hydrazine and hydrogen peroxide in the drop tests.

Jyoti et al. [18] used the drop-test method with a high-speed camera to measure the ignition delay of gelled ethanol and 90% hydrogen peroxide. Kang et al. [20] also employed the drop test with a high-speed camera for a preliminary approximation of the ignition time delay of a developed fuel with 95% and 98% hydrogen peroxide. Zhao et al. [40] used a high-speed camera in a drop test to observe the ignition and combustion process of specially prepared compounds with HNO_3.

Park et al. [31] utilised a drop-test technique with a laser, photodiode, and fast camera to observe the ignition delay of 95% hydrogen peroxide with $LiNO_3$ and NH_4NO_3. In their tests, the fuels contained different amounts of water (0.5%, 1.0%, 5.0%, and 20%). Several high-speed cameras (infrared, monochrome, and colour) and sensors with a laser and LED lamp were used by Nath et al. [30] in drop tests of hydrogen peroxide and high-density polyethylene mixed with $NaBH_4$. Mota et al. [27] used three high-speed cameras operating in visible, schlieren, and infrared spectra (IR) modes to observe the ignition delay in drop tests of several selected fuels with hydrogen peroxide. Khomik et al. [22] also employed a high-speed camera to observe the ignition time delay in open-cup drop tests.

Pourpoint and Anderson [33] tested the ignition delay of catalytically promoted fuels with highly concentrated hydrogen peroxide (92% to 98%) using an impinging jet apparatus with a high-speed camera. James et al. [16] also used a high-speed camera to observe the ignition delay in impinging-jets tests with gelled hypergolic propellants. Similarly, DeSain et al. [10] used a fast camera to determine the ignition time delay in their experiments. He et al. [14] also employed a high-speed camera to observe the ignition of gelled hydrogen peroxide with various fuels.

As far as ignition delay studies are concerned, there are two main methods that are usually used for the determination of the start of combustion: visual [3, 5, 8, 9, 12, 16, 18, 19, 23, 24] and pressure-based [11, 15, 29, 32]. Visual observation has one strong advantage – one recording can be used for both the determination of the time of contact between an oxidiser and a fuel and the start of combustion [1, 25, 33, 34, 37, 39]. With a known frame rate and a number of frames between these two detected incidents, ignition delay can be calculated. The second method is based on data analysis from a pressure sensor. The pressure inside the chamber increases during combustion in a constant volume chamber. The time, which represents the beginning of combustion, may be defined by the intersection of two lines. The first line represents the average pressure before combustion, while the second is tangent to the pressure curve at its maximum slope. For the detection of the instant contact (between the oxidiser and the fuel), we used high-speed cameras. However, some researchers use photodiodes [9].

The presented literature shows that, in the drop tests, the optical methods are preferred. However, most studies on hypergolic ignition were performed in an open environment. The pressure-based method, in turn, is only applicable in enclosed-volume research devices, such as constant-volume chambers [17, 29], rapid-compression machines [26], or shock tubes [11, 15]. Both of these techniques could be applied in this study, as the drop tests were performed in a constant volume vessel. It should be noted that other methods for estimating ignition delay also exist. Szwaja and Szymanek [35] also used registered pressure trace, but indirectly. First, they calculated heat release, which was then used to determine ignition delay. Chwist [6], in turn, used ANSYS Chemkin Pro for this purpose, which numerically calculates ignition delay.

The goal of the study was to assess and compare both methods in terms of determining the ignition delay of hypergolic propellants by the drop-test method. The data from the pressure sensor and high-speed camera images were taken simultaneously. Thus, both methods were used to determine ignition delay for the same cases, and a direct comparison of these two methods could be made.

For this verification, prospective "green" propellant was chosen, as these kinds of fuels and oxidisers have received much attention recently [28, 36]. Pyridine (with the addition of a catalyst) was used as a fuel, while the HTP (high-test peroxide, also named RGHP – rocket grade hydrogen peroxide [9]) was selected as an oxidiser.

As discussed earlier, most researchers conducted their experiments in an open environment, which means that the reported results were limited to atmospheric conditions [5, 8, 10, 16, 18, 20, 23, 24]. Only a small part of studies have investigated the effect of pressure and temperature on ignition delay [9, 10, 33]. The verification tests presented here were performed for different environmental pressures (0.1, 1, and 2 MPa absolute pressure) and fuel temperatures (295 and 353 K) to make our comparison more universal. In all tests, the oxidiser temperature was 293 K (in a syringe). Ak et al. [1] performed experiments that showed low dependence on ignition delay from oxidiser temperature and high dependence on fuel temperature.

2. Materials and methodology

2.1. Experimental setup

The research was performed using a specially modified constant-volume chamber initially designed for spray tests of marine engine injectors [13]. The chamber was adapted for the drop-test method by providing an oxidiser dosing

unit (Fig. 1) and a fuel pool with a temperature control (Fig. 2). The chamber was pressurised with air. The droplet release and the ignition process were observed through the quartz window by the high-speed camera. The test chamber was also equipped with fast-access entry, which allowed us to refill the fuel after each test.

The dosing system was composed of a high-pressure syringe, a holder for the syringe, which also holds a linear module with a stepper motor (Fig. 1). The stepper motor drives the linear module coupled with the syringe. The holder was designed to eliminate vibrations generated by the stepper motor.

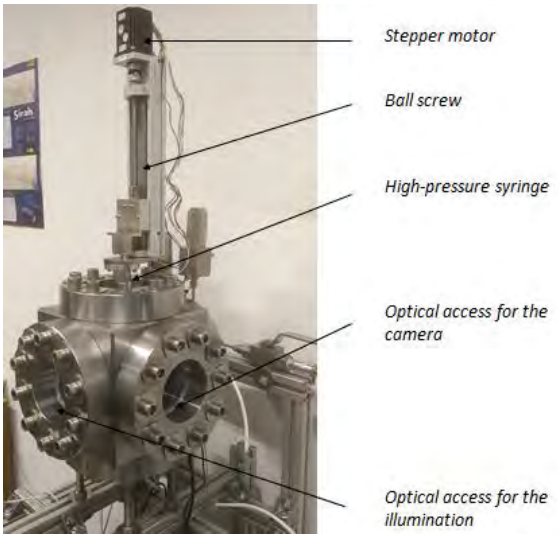

Fig. 1. Modified constant volume chamber for drop-test studies

The vessel was also equipped with a pressurised gas delivery system, an electric heater, and a thermocouple with a temperature controller. The thermocouple was placed one millimetre under the bottom of the fuel pool.

Two holes in the chamber were filled by quartz windows. One window was used to illuminate falling droplets, while the second one provided optical access for a high-speed camera. The fuel pool was made of stainless steel, and it was thermally insulated from the bottom of the chamber. The electric band heater was wrapped around the fuel pool (Fig. 2).

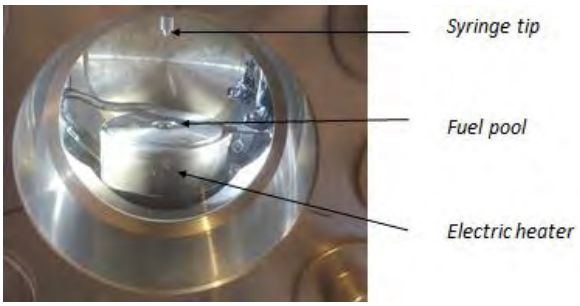

Fig. 2. Fuel pool with a heater for temperature control

The pressure inside the chamber was measured by a piezoelectric pressure transducer (KISTLER 601CA). The pressure and temperature signals were recorded by a data acquisition system (DEWETRON DEWE-50-PCI-16). The pressure signal was recorded at a frequency of 10 kHz. The pressure transducer, charge signal converter and amplifier were configured to measure pressure within the range of 0-5 MPa (absolute). The data acquisition started 1 second before the trigger signal and ended 0.5 seconds after that signal. The trigger signal was generated based on the pressure measurement – when the pressure increase was higher than two kilopascals (above the environmental pressure) for at least three milliseconds.

High-speed camera (Photron SA 1.1) operated at a frame rate of 10 kHz. This frame rate allowed us to determine the moment of self-ignition with an accuracy of 0.1 ms. In order to capture contact of a drop with a pool and the start of combustion, the camera was set to continuous recording and storage mode (operating in a loop limited by the camera memory). The trigger signal was set at the end of the recording. These settings enabled the recording of more than 1 second, which was enough to capture both the moment of contact of the fuel with the oxidiser and the start of combustion.

2.2. Visual analysis

Based on the recorded images, the time of contact between the oxidiser droplet and the fuel, as well as the moment of occurrence of visible effects of the combustion process (identified here as the start of combustion), were determined. Two effects of combustion could be noticed, i.e., increased emission of visible light (Fig. 3) or fast increasing expansion of gases, which caused braking of the fuel surface (Fig. 4).

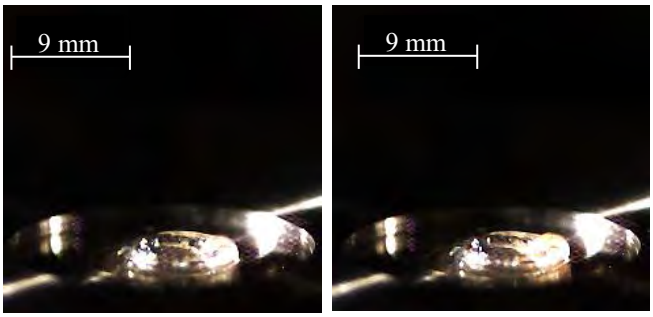

Fig. 3. Beginning of combustion with light emission (two consecutive frames)

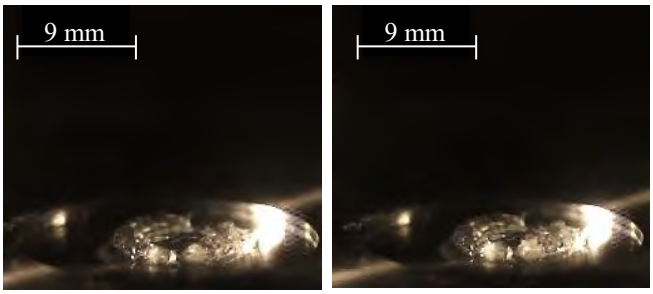

Fig. 4. Beginning of combustion with a brake of the liquid surface caused by decomposition or combustion gases (two consecutive frames)

With determined time of contact and SOC as well as known frame rate, the ignition delay (ID) was calculated according to the equation (1):

$$ID = \frac{n_{ign} - n_{con}}{f} \quad (1)$$

where: n_{ign} – number of the frame with the identified start of the combustion; n_{con} – number of the frame with the identified beginning of contact between the oxidiser drop and the fuel pool; f – frame rate.

2.3. Pressure-trace analysis

In the pressure-based method, SOC is determined based on the analysis of the recorded pressure curve. For this purpose, two lines need to be drawn. The first line corresponds to the average pressure level before combustion. The second one is tangent to the pressure curve at its maximum slope, associated with the fastest pressure increase due to the combustion process. The time at the intersection of these two lines is defined as the start of combustion (Fig. 5).

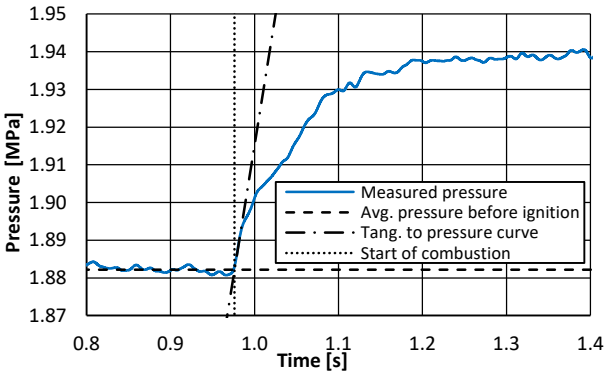

Fig. 5. Example pressure trace in the chamber, with a cross of two lines to determine the start of combustion; time measured from the start of the data acquisition

Note that the time reported in Fig. 5 was measured from the start of the data acquisition. To calculate the ignition delay, the time of contact between the oxidiser and the fuel needs to be determined as well. However, based on pressure trace analysis, it is impossible to determine the moment of contact between oxidiser and fuel. It is necessary to use high-speed imaging anyway. These two measurement methods need to be used together and synchronised in order to combine the data obtained by them. With a known start of combustion and a time of contact of the oxidiser with the fuel, the ignition delay can be determined.

2.4. Measurement procedure

The measurement procedure included the following steps:

1. Setting the temperature of the pool (temperature was measured by type J thermocouple placed 1 mm below the bottom of fuel pool)
2. Opening and cleaning the chamber and windows
3. Filling up the syringe with HTP (if needed)
4. Filling the pool with the fuel
5. Closing and pressurising the chamber
6. Setting up data acquisition and trigger mode
7. Moving the syringe piston for dropping a drop of the oxidiser
8. Saving data (camera recording, pressure data)
9. Scavenging the chamber and releasing the combustion gases into the exhaust-extraction duct.

Steps 2–9 were repeated seven times for each measurement point.

3. Results

3.1. High-speed imaging

Based on recorded images for pyridine and HTP, the ignition delay was calculated. (as described in chapter 2.2). Figure 6 shows the determined ignition delay obtained at three different environmental pressures and for two different fuel temperatures.

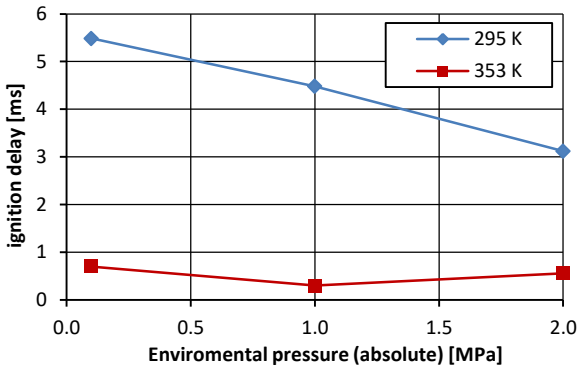

Fig. 6. Ignition delay; calculated using SOC determined by high speed-imaging for two different fuel temperatures

3.2. Pressure-based SOC determination

The ignition delay was also determined using recorded pressure data for the same cases. In this procedure, the ignition delay was calculated by combining two methods. The moment of contact of the oxidiser droplet and fuel in the pool was determined by the high-speed camera, while the SOC was determined based on pressure recording (as described in section 2.2). The results of the calculations for two different fuel temperatures are presented in Fig. 7.

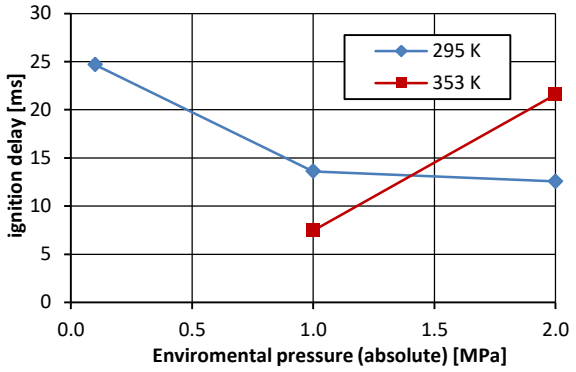

Fig. 7. Ignition delay versus absolute pressure for two different fuel temperatures (SOC determined by pressure-based method)

In the current setup used for drop-test studies, the mass of the fuel was small compared to the volume of the chamber (and thus the mass of the enclosed air). Moreover, energy initially released in one point of the chamber (at the droplet impact point) couldn't rapidly increase temperature and pressure. The whole fuel needed to be consumed until the pressure change was high enough to distinguish it from the noise signal. Thus, the values presented in Fig. 7 are

much higher than those obtained with the visual method (see Fig. 6).

4. Discussion

This section aims to discuss the advantages and disadvantages of the two techniques that were used.

With increasing temperature of the fuel pool, self-ignition delay decreases. This effect could be strengthened by the increasing concentration of catalytic additives in the fuel due to its intensive evaporation at high temperatures. The effect of fuel evaporation at high temperatures leading to an increased concentration of the catalytic additive (manifested by the white colour of the fuel pool) is shown in Fig. 8. The brighter colour of the droplet suggests that the temperature from the pool influenced the oxidiser as well, which supposedly started to decompose already during the free fall.

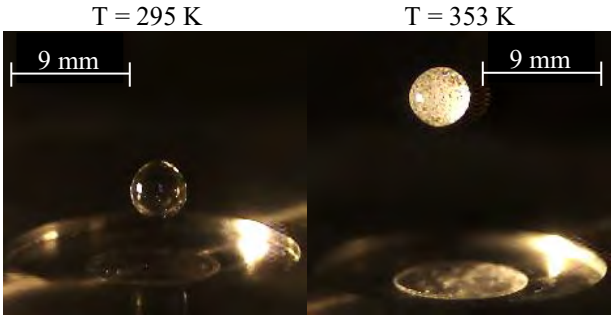

Fig. 8. Droplet of the oxidiser and the fuel pool for different fuel temperatures at 1 MPa absolute pressure

The fuel evaporation seemed to be decreased at increased pressure inside the chamber, which is presented in Fig. 9.

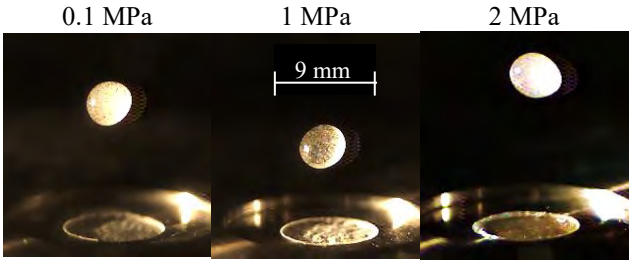

Fig. 9. Droplet of the oxidiser and the fuel pool at different pressures; fuel temperature 353 K

Regardless of these issues, other aspects could also be the reason for the poor repeatability of the results. One of them is the lack of temperature compensation in the pressure transducer. In some cases, droplets splashed from the pool and fell onto the sensor's surface, causing pressure curve breakdown (a sudden pressure drop). This effect is shown in Fig. 10. An additional issue during the estimation of SOC from the pressure curve is the shape of the recorded data. The recorded data was affected by a strong noise signal. Thus, the data from the piezoelectric transducer needed to be filtered. For this purpose, a simple moving average filtering algorithm with five symmetrical points was used. With repeating filtration cycles, filtered curves became smoother, but the large time-scale pressure changes were also affected. These were extended in time. The influence of the number of filtrations on the pressure curve is presented in Fig. 11. Note that time is measured from the beginning of the recording.

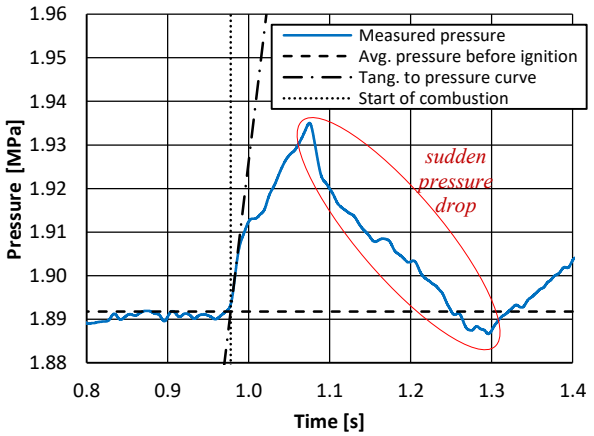

Fig. 10. Pressure curve breakdown caused by the droplet impact onto the sensor's surface

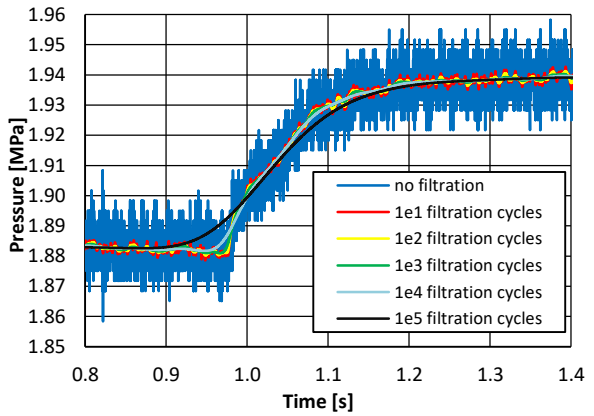

Fig. 11 Example pressure curve – raw data (no filtration) and filtered versions; time measured from the start of the data acquisition

Due to the effects of filtration on the large time-scale pressure features, the ignition delay was also affected. The ignition delay dependence on the number of filtration cycles is shown in Table 1.

Table 1. Ignition delay for different numbers of filtrations calculated from the same pressure curve

No. of filtrations	Ignition delay [ms]
0	18.9
10	46.6
100	51.4
1000	45.9
10000	34.7
100000	16.5
1000000	–80.7

Due to the strong noise signal determination of SOC for non-filtrated data, it is strongly problematic. Increasing the filtration number, in turn, advances the SOC. With an increasing number of filtration over 10^2, the estimated ignition delay decreases even to nonphysical results, as in the case of 10^6 filtration. It might be speculated that the other type of filtration could perform better, and the issue of advancing the SOC could be avoided. However, the Butterworth filter used

in a similar setup also resulted in a delayed start of combustion compared to the visual ignition effects [21].

The other issue affecting the quality of pressure data, specifically the signal-to-noise ratio, was a decreasing combustion intensity with increasing fuel temperature. This was mainly caused by the evaporation of the fuel. This effect had a much lower influence on the optical method than on the pressure-based technique. An example pressure curve (environmental pressure: 1 MPa, fuel temperature 353 K) after 1000 cycles of filtrations is presented in Fig. 12. As one may observe, the shape of the curve is entirely different than that shown in Fig. 11 (environmental pressure: 2 MPa, fuel temperature: 333 K). In that case, the start of combustion could not be appropriately determined using the pressure data.

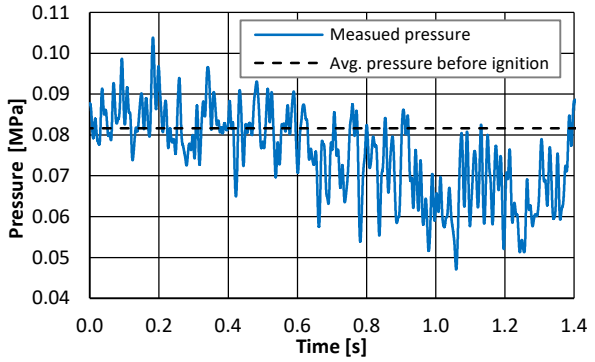

Fig. 12. Determination of SOC for 0.1 MPa absolute pressure and fuel temperature of 353 K

All presented reasons caused low repeatability of the results, especially those obtained using the pressure-based method to determine the start of combustion. The coefficient of variation for both methods is shown in Fig. 13.

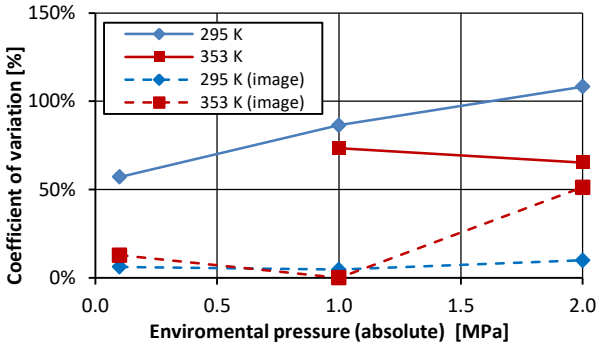

Fig. 13. Coefficient of variation of ignition delay for visual (dashed lines) and pressure-based methods (solid lines)

High-speed imaging-based ignition delay determination provided high repeatability of the results. The cases where the result deviated from the average could be associated with a specific aspect of the measurement, e.g. imprecise impingement point. Table 2. shows the cases when the droplet didn't impinge in the center of the fuel pool and reports the measured ignition delay. It also shows the average ignition delay (for seven repetitions) determined at the corresponding measurement point.

Table 2. Droplet impingement location and the corresponding ignition delay values

Parameters (fuel temperature and pressure in the chamber)	A photograph of droplet impingement	Measured ignition delay	Average ignition delay
T = 295 K p = 2 MPa	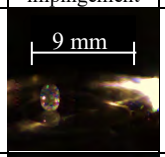	3.1 ms	2.2 ms
T = 333 K p = 1 MPa	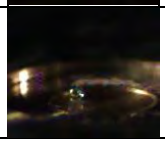	2.2 ms	1.6 ms

An additional issue during the data analysis was related to the droplet oscillation. Figure 14 shows the evolution of the oscillating droplet prior to the impingement. The time displayed in each photograph represents the time remaining to the contact between the oxidiser and fuel.

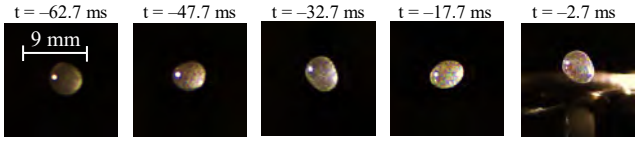

Fig. 14. Evolution of the oscillating droplet prior to the impingement

When using the visual method, the aspect of the oscillating droplet could be evaluated quantitatively by determining the droplet's geometrical features at the instant of the impingement, as was done in our previous study [21]. If the pressure method is applied, high-speed imaging would also be required.

In general, the repeatability of the results obtained using pressure-based SOC determination was much worse than that observed for visual SOC determination. Moreover, the ignition delay values obtained using the pressure-based method are much higher than those obtained by the optical method.

These observations suggest that the pressure-based technique is not acceptable for quantitative ignition delay measurement in the current setup.

5. Conclusions

Simultaneous image acquisition and pressure measurements enabled the direct comparison of two approaches for the start of combustion (and ignition delay) determination. Moreover, the study revealed other aspects which should be addressed when performing drop tests at high temperatures. The crucial aspect is that the delay between the fuel delivery and the test cannot be too long due to fuel evaporation and increasing concentration of the additive.

In terms of the start of combustion and ignition delay determination, the presented analysis allows us to conclude that the visual method is more reliable, accurate and better suited for the setup and propellants used in the study – mainly due to the relatively large volume of the test chamber (compared to the amount of fuel and the size of the fuel-oxidiser contact zone).

The advantages of this method were summarised as follows:

– high repeatability of measurement results
– no need for synchronisation of a high-speed camera with a pressure transducer
– easier evaluation of test quality (size and shape of the droplet, place of droplet impact, amount of fuel in the pool, etc.).

The main disadvantage of this technique is the need for a manually generated trigger signal, which could be overcome by using an additional photodiode triggering system.

The advantages of the pressure-based method are as follows:

– automatic trigger generation based on pressure
– additional information on combustion process dynamics.

In the setup used in the study, the pressure-based method had several disadvantages that make this method useless for ignition delay determination, especially when quantitative measurement is needed:

– high noise signal need for filtration
– sensitivity to droplets splashing onto the pressure sensor surface
– the necessity of using the optical technique for the determination of the time of contact between the fuel and the oxidiser
– low repeatability of results.

Based on the observed features of both techniques, the visual method shall be considered a better and more accurate option for ignition delay determination of hypergolic propellants. The optical method is sufficient to determine the ignition delay without any additional instrumentation. However, even in the visual determination of SOC, the pressure signal can be useful for triggering and data-collecting automation.

Acknowledgements

The paper was prepared as a part of the HIPERGOL project, which is financially supported by the National Centre for Research and Development (NCBiR) under Grant No. DOB-BIO8/07/01/2016.

NCBR
National Centre for Research and Development

Nomenclature

FTIR	Fourier-transform infrared
HTP	high-test peroxide
ID	ignition delay
IRFNA	inhibited red fuming nitric acid
MMH	monomethylhydrazine
NA	nitric acid
RFNA	red fuming nitric acid
RGHP	rocket grade hydrogen peroxide
SOC	start of combustion
TEAB	triethylamine borane
WFNA	white fuming nitric acid

Bibliography

[1] Ak MA, Ulas A, Sümer B, Yazici B, Yildirim C, Gönc LO et al. An experimental study on the hypergolic ignition of hydrogen peroxide and ethanolamine. Fuel. 2011;90(1):395-398. https://doi.org/10.1016/j.fuel.2010.07.048

[2] Alfano AJ, Mills JD, Vaghjiani GL. Highly accurate ignition delay apparatus for hypergolic fuel research. Rev Sci Instrum. 2006;77(4). https://doi.org/10.1063/1.2188909

[3] Blevins JJA, Gostowski R, Chianese S. An experimental investigation of hypergolic ignition delay of hydrogen peroxide with fuel mixtures. 42nd AIAAASMESAEASEE. Jt Propuls Conf Exhib. 2004;1335:1-8. https://doi.org/10.2514/6.2004-1335

[4] Chambreau SD, Schneider S, Rosander M, Hawkins T, Gallegos CJ, Pastewait MF et al. Fourier transform infrared studies in hypergolic ignition of ionic liquids. J Phys Chem A. 2008;112(34):7816-7824. https://doi.org/10.1021/jp8038175

[5] Chowdhury A, Wang S, Thynell S. Ignition behavior of novel hypergolic materials. 45th AIAA/ASME/SAE/ASEE Jt Propuls Conf Exhib. 2009:1-11. https://doi.org/10.2514/6.2009-5352

[6] Chwist M. Comparative analysis of heat release in a reciprocating engine powered by a regular fuel with pyrolysis oil addition. Combustion Engines. 2022;190(3):104-12. https://doi.org/10.19206/CE-146694

[7] Coil M. Hypergolic ignition of a gelled ionic liquid fuel. 46th AIAA/ASME/SAE/ASEE Jt Propuls Conf Exhib. 2010:1-11. https://doi.org/10.2514/6.2010-6901

[8] Dambach E, Cho K, Pourpoint T, Heister S. Ignition of advanced hypergolic propellants. 46th AIAA/ASME/SAE/ASEE Jt Propuls Conf Exhib. 2010.

[9] Davis SM, Yilmaz N. Advances in hypergolic propellants: ignition, hydrazine, and hydrogen peroxide research. Adv Aerosp Eng. 2014;2014(1):1-9. https://doi.org/10.1155/2014/729313

[10] DeSain JD, Curtiss TJ, Metzler KM, Brady BB. Testing hypergolic ignition of paraffin wax/LiAlH4 mixtures – AIAA 2010-6636. 46th AIAAASMESAEASEE Jt Propuls Conf Exhib. 2010;1-19. https://doi.org/doi:10.2514/6.2010-6636

[11] Gauthier BM, Davidson DF, Hanson RK. Shock tube determination of ignition delay times in full-blend and surrogate fuel mixtures. Combust Flame. 2004;139(4):300-311. https://doi.org/10.1016/j.combustflame.2004.08.015

[12] Ghassemi H, Fasih HF. Application of small size cavitating venturi as flow controller and flow meter. Flow Meas Instrum. 2011;22(5):406-412. https://doi.org/10.1016/j.flowmeasinst.2011.05.001

[13] Grochowalska J, Jaworski P, Kapusta ŁJ, Kowalski J. A new model of fuel spray shape at early stage of injection in a marine diesel engine. Int J Numer Method H. 2022;32(7): 2345-2359. https://doi.org/10.1108/HFF-05-2021-0349

[14] He Z, Yang J, Nie Z, Zhou X, Wu J. Preparation, characterization, and thermal decomposition kinetics of high test peroxide gel. Acta Astronaut. 2023;211:510-517. https://doi.org/10.1016/j.actaastro.2023.07.001

[15] Heufer KA, Olivier H. Determination of ignition delay times of different hydrocarbons in a new high pressure shock tube. Shock Waves. 2010;20(4):307-316. https://doi.org/10.1007/s00193-010-0262-2

[16] James MD, Kubal TD, Son SF, Anderson WE, Pourpoint TL. Calibration of an impinging jet injector suitable for liq-

uid and gelled hypergolic propellants. 45th AIAA/ASME/SAE/ASEE Jt Propuls Conf Exhib. 2009:1-13. https://doi.org/10.2514/6.2009-4882
[17] Jaworski A, Kuszewski H, Longwic R, Sander P. Assessment of self-ignition properties of canola oil–n-hexane blends in a constant volume combustion chamber and compression ignition engine. Appl Sci. 2023;13(19):10558. https://doi.org/10.3390/app131910558
[18] Jyoti BVS, Naseem MS, Baek SW. Hypergolicity and ignition delay study of pure and energized ethanol gel fuel with hydrogen peroxide. Combust Flame. 2017;176:318-325. https://doi.org/10.1016/j.combustflame.2016.11.018
[19] Kang H, Jang D, Kwon S. Demonstration of 500 N scale bipropellant thruster using non-toxic hypergolic fuel and hydrogen peroxide. Aerosp Sci Technol. 2016;49:209-214. https://doi.org/10.1016/j.ast.2015.11.038
[20] Kang H, Lee E, Kwon S. Suppression of hard start for non-toxic hypergolic thruster using H_2O_2 oxidizer. J Propul Power. 2017;33(5):1111-1117. https://doi.org/10.2514/1.B36510
[21] Kapusta ŁJ, Boruc Ł, Kindracki J. Pressure and temperature effect on hypergolic ignition delay of triglyme-based fuel with hydrogen peroxide. Fuel. 2021;287:119370. https://doi.org/10.1016/j.fuel.2020.119370
[22] Khomik SV, Usachev SV, Medvedev SP, Ivantsov AN, Stovbun SV, Mikhalkin VN et al. Reasonable testing of hypergolic fuels. Acta Astronaut. 2020;176:695-699. https://doi.org/10.1016/j.actaastro.2020.02.053
[23] Li J, Fan W, Weng X, Tang C, Zhang X, Huang Z et al. Experimental observation of hypergolic ignition of superbase-derived ionic liquids. J Propul Power. 2018;34(1):125-132. https://doi.org/10.2514/1.B36441
[24] Mahakali R, Kuipers FM, Yan AH, Anderson WE. Development of reduced toxicity hypergolic propellants. 47th AIAA/ASME/SAE/ASEE. Jt Propuls Conf Exhib. 2011:1-14. https://doi.org/10.2514/6.2011-5631
[25] McCrary PD, Barber PS, Kelley SP, Rogers RD. Nonaborane and decaborane cluster anions can enhance the ignition delay in hypergolic ionic liquids and induce hypergolicity in molecular solvents. Inorg Chem. 2014;53(9):4770-4776. https://doi.org/10.1021/ic500622f
[26] Merkisz J, Pielecha I, Łęgowik A. The assessment of autoignition of modified jet fuels. Energies. 2021;14(3):633. https://doi.org/10.3390/en14030633
[27] Mota FAS, Fei L, Liu M, Jiang J, Tang C. Novel hypergolic green fuels with hydrogen peroxide for propulsion systems. J Propul Power. 2024;40(2):207-219. https://doi.org/10.2514/1.B39224
[28] Mota FAS, Liu M, Mohsen AAA, Yao X, Mai Z, Tang C. Development of polyamine/alkanolamine-based hypergolics with hydrogen peroxide: a new route to n-methylimidazole with MDEA as a promising green fuel. Fuel. 2024;357:129798. https://doi.org/10.1016/j.fuel.2023.129798
[29] Naber JD, Siebers DL, Di Julio SS, Westbrook CK. Effects of natural gas composition on ignition delay under diesel conditions. Combust Flame. 1994;99(2):192-200. https://doi.org/10.1016/0010-2180(94)90122-8
[30] Nath S, Mallick L, Lefkowitz JK. Hypergolic ignition response to oxidizer droplet properties. Combust Flame. 2023;258:113061. https://doi.org/10.1016/j.combustflame.2023.113061
[31] Park S, Lee K, Kang H, Park Y, Lee J. Effects of oxidizing additives on the physical properties and ignition performance of hydrogen peroxide-based hypergolic propellants. Acta Astronaut. 2022;200:48-55. https://doi.org/10.1016/j.actaastro.2022.07.051
[32] Petersen EL, Kalitan DM, Barrett AB, Reehal SC, Mertens JD, Beerer DJ et al. New syngas/air ignition data at lower temperature and elevated pressure and comparison to current kinetics models. Combust Flame. 2007;149(1-2):244-247. https://doi.org/10.1016/j.combustflame.2006.12.007
[33] Pourpoint T, Anderson W. Hypergolic reaction mechanisms of catalytically promoted fuels with rocket grade hydrogen peroxide. Combust Sci Technol. 2007;179(10):2107-2133. https://doi.org/10.1080/00102200701386149
[34] Ramachandran PV, Kulkarni AS, Pfeil MA, Dennis JD, Willits JD, Heister SD et al. Amine-boranes: green hypergolic fuels with consistently low ignition delays. Chem – Eur J. 2014;20(51):16869-16872. https://doi.org/10.1002/chem.201405224
[35] Szwaja M, Szymanek A. Combustion comparative analysis of pyrolysis oil and diesel fuel under constant-volume conditions. Combustion Engines. 2023;195(4):90-96. https://doi.org/10.19206/CE-169805
[36] Türker L. Hypergolic systems based on hydrogen peroxide oxidizer. Earthline J Chem Sci. 2023;10(1):1-42. https://doi.org/10.34198/ejcs.10123.142
[37] Wang SQ, Thynell ST. An experimental study on the hypergolic interaction between monomethylhydrazine and nitric acid. Combust Flame. 2012;159(1):438-447. https://doi.org/10.1016/j.combustflame.2011.07.009
[38] Zarbo N, Belal H, Pourpoint TL. Effect of water and humidity on hypergolic propellant ignition delay. 51st AIAA/SAE/ASEE Jt Propuls Conf. 2015:1-15. https://doi.org/10.2514/6.2015-3867
[39] Zhang Y, Shreeve JM. Dicyanoborate-based ionic liquids as hypergolic fluids. Angew Chem Int Ed. 2011;50(4):935-937. https://doi.org/10.1002/anie.201005748
[40] Zhao X, Wang Z, Qi X, Song S, Huang S, Wang K et al. Hunting for energetic complexes as hypergolic promoters for green propellants using hydrogen peroxide as oxidizer. Inorg Chem. 2021;60(22):17033-17039. https://doi.org/10.1021/acs.inorgchem.1c02149

Łukasz Boruc, DEng. – Faculty of Power and Aeronautical Engineering, Warsaw University of Technology, Poland.
e-mail: *Lukasz.Boruc@pw.edu.pl*

Łukasz Jan Kapusta, DEng. – Faculty of Power and Aeronautical Engineering, Warsaw University of Technology, Poland.
e-mail: *Lukasz.Kapusta@pw.edu.pl*

Jan Kindracki, DSc., DEng. – Faculty of Power and Aeronautical Engineering, Warsaw University of Technology, Poland.
e-mail: *Jan.Kindracki@pw.edu.pl*

Article citation info:
Sordyl A, Chlopek Z, Merkisz J. Correlation relationships of processes in the combustion engine in the RDE test. Combustion Engines. 2024;199(4):112-125. https://doi.org/10.19206/CE-192877

Adam SORDYL
Zdzislaw CHLOPEK
Jerzy MERKISZ

Combustion Engines
Polish Scientific Society of Combustion Engines

Correlation relationships of processes in the combustion engine in the RDE test

ARTICLE INFO

Received: 22 July 2024
Revised: 26 August 2024
Accepted: 2 September 2024
Available online: 1 October 2024

The article presents considerations on the processes taking place in the combustion engine in the real driving operating conditions of a vehicle performing the RDE (Real Driving Emissions) test. The tests were carried out using a passenger car with a spark-ignition engine. The processes considered in the article were related to the engine operating states, exhaust emissions and fuel mass consumption, and the vehicle velocity, which determines the engine operating conditions. The RDE test was carried out using PEMS (Portable Emissions Measurement System) equipment, and the following variables were recorded: vehicle velocity, control, engine speed, relative torque and relative engine power, emission pollutant intensity of carbon monoxide, hydrocarbons, nitrogen oxides and carbon dioxide, the intensity of particle number and the fuel mass consumption intensity. The recorded signals were digitally processed, and the statistical properties of the variables and the mutual relation between the engine operating states were examined. The properties of the measured variables were investigated in the entire RDE test and in its constituent phases: the first, corresponding to vehicle traffic in cities, the second – outside cities, and the third – on highways and expressways. The pollutant specific distance emission and the particle number specific distance as well as the specific distance fuel mass consumption were determined in relation to the average vehicle velocity, and based on these results, the exhaust emissions and fuel mass consumption characteristics were created. Correlational studies of the considered variables were also performed. Pearson's linear correlation coefficients for the combinations of the measured variables were determined.

Key words: *correlation, Real Driving Emissions test (RDE), pollutant emission, fuel mass consumption, engine operating states*

1. Introduction

The processes occurring in combustion engines, characterizing their exhaust emissions and fuel mass consumption, are among the basic operational properties of engines [11, 12, 17]. These processes are determined by the engine operating states: control, engine speed, load, which can be measured using torque, and the engine's thermal state [11, 12, 17].

The operating states of a vehicle engine are determined by the vehicle's velocity and traffic resistance, which depend on, among others, the type and inclination of the road surface, as well as on the vehicle velocity, environmental conditions and temperature, which primarily influence the time it takes for the engine to reach a thermally stable state after an engine cold start [11, 12, 17].

In dynamic operating conditions, the relationship between the operational properties of combustion engines and their operating states takes the form of operators (or more specifically, the form of functionals) [11, 12, 17], and not as functions with numerical values [7]. For this reason, these properties generally differ under all conditions, making it necessary to test the engines under comparable conditions, in the case of automotive applications, determined by the vehicle velocity. Of course, the actual operating conditions of combustion engines are largely undetermined and, as a consequence, the operational properties in such conditions should be generally treated as random [9, 28, 29]. In such a case, probabilistic characterization of these variables can be assessed, such as probability density [9, 28, 29] or frequency characteristics [9, 28, 29].

This study aimed to assess the following:

- vehicle velocity
- engine steering
- engine speed
- relative engine torque
- relative effective power
- emission pollutant intensity of carbon monoxide, hydrocarbons, nitrogen oxides and carbon dioxide
- particle number intensity
- fuel mass consumption intensity

in the driving conditions of a passenger car in the RDE (Real Driving Emissions) test [20, 39], the phases of which characterize the vehicle's traffic: in cities, outside cities and on highways and expressways.

The nature of vehicle traffic in the RDE test corresponds to typical conditions of vehicle operation. Such conditions are taken into account in the pollutant emission assessment [21], which additionally considers driving in cities separately between driving in cities with traffic congestion and driving in cities without traffic congestion [8].

The aim of this research was to learn about selected properties of the studied processes. These properties were primarily:

- statistical characteristics of the measured variables [9, 25], in particular:
  - average value considering the test phases
  - their distribution characteristics
  - coefficient of variation, enabling the assessment of dynamic properties while taking into account test phases
- characteristics of pollutant specific distance emission, particle number specific distance and specific distance fuel mass consumption of the vehicle depending on the

average velocity in individual test phases and throughout the whole test
- Pearson's linear correlation coefficient [30, 31] of the combination of measured variables.

These properties were examined for the entire test and for individual test phases. Such tests were intended to enable the assessment of the sensitivity of variable properties to changes in vehicle operating conditions.

The innovative aspect of the conducted study is the fact that testing the measured variables properties was possible based on test results in a single test, unlike the commonly used standards for assessing the variable properties, engine operating conditions, exhaust emissions, and fuel mass consumption, which normally require obtaining data from multiple tests, corresponding to the variety of vehicle operating conditions [1, 2, 10, 18, 23].

Of particular note were the correlation studies [13–16] of variables characterizing exhaust emissions and fuel mass consumption, as well as variables of engine operating states and the vehicle velocity that determines them. The goal of these studies was to assess the interdependence of these values, which is particularly important when attempting to reduce the exhaust emissions of all pollutants and fuel mass consumption.

2. Literature review

Research of combustion engines properties in RDE tests has been the subject of many publications [3–6, 12, 22, 26, 33, 38]. The amount of new research increased over the recent years, thanks mainly to the introduction of portable exhaust emission testing equipment [32], which enabled previously unheard-of possibilities for testing vehicles in real operating conditions [36, 37].

Papers [3–5] present the research results of vehicle velocity, the operating states of the internal combustion engine and the processes characterizing the exhaust emissions in the RDE test, carried out in real driving conditions of the vehicle. The engine properties were tested in static and dynamic states. The obtained results confirmed that dynamic states have a greater influence on engine exhaust emissions.

The research results presented in [6] were obtained in the NEDC (New European Driving Cycle) [21, 39] and the Malta test, developed at the Poznan University of Technology. These tests were performed on a chassis dynamometer. The exhaust emission results of carbon monoxide, hydrocarbons and nitrogen oxides were provided relative to the static and dynamic states of the combustion engine. Dynamic states were determined depending on the value of the positive or negative derivative of torque and engine speed with respect to time. It was found that the impact of dynamic states on the exhaust emissions was greater in the Malta test, which was due to the fact that this test was based on a faithful simulation of velocity in the time domain.

Paper [12] concluded that internal combustion engines, as systems described by nonlinear models, do not have any properties that would not depend on their current state. The study contains the test results of a vehicle engine in dynamic states determined by the value of vehicle acceleration in vehicles driving tests simulating the real operation of passenger cars. During the tests, exhaust emissions and fuel mass consumption values were averaged for individual vehicle states. It was found that the investigated processes were very sensitive to both dynamic states and the type of vehicle driving tests performed.

The RDE testing procedure, tested in [22], included: vehicle selection and preparation, route design, route implementation, route verification and calculation of values characterizing the exhaust emissions, pollutant specific distance emission and the particle number specific distance.

Paper [26] presents the results of a four-cylinder turbocharged compression-ignition engine tests, belonging to the Euro 6 category, with a rated power of 126 kW. The tests, conducted on an engine dynamometer, were simulating the engine operating states in a light truck in the RDE test. The emissions of carbon monoxide, hydrocarbons, nitrogen oxides and carbon dioxide were measured. A procedure was developed to test the responsivity of engine properties to engine operating states depending on the driver's behavior.

The aim of [33] was to assess energy consumption and exhaust emissions from passenger cars equipped with various drive systems in real operation. Passenger cars with combustion engines of various emission classes, as well as the latest hybrid vehicles and electric vehicles, were used in the tests. This enabled a comparative assessment of energy consumption in various road traffic conditions, with particular emphasis on the urban phase, as well as the entire RDE test. The test results were analyzed to identify changes in fuel mass consumption and exhaust emissions that could be assigned to the technological progress of the vehicles.

The paper [38] describes the use of the Moving Average Window Method (MAW) and the load-averaging method to process the emission results of a light truck and its combustion engine in the RDE test. Empirical tests were carried out using a fleet of 10 vehicles. The use of both methods of averaging measurement results produced comparable results.

Correlational studies have a very extensive literature covering a wide range of applications, especially in medicine and genetics [19, 24, 27, 35]. Regarding the operational properties of combustion engines, however, the literature is relatively poor [13–16].

Authors of the paper [13] stated their goal was to examine the relationship between the emission of individual exhaust components (carbon monoxide, hydrocarbons, nitrogen oxides and carbon dioxide), fuel mass consumption and various dynamic conditions of engine operation. Empirical data was obtained by testing a passenger car with a spark-ignition engine on a chassis dynamometer in 12 different driving tests, both type approval and special tests. The results indicated that the strongest correlation occurred between carbon dioxide and hydrocarbon emissions and between fuel mass consumption and hydrocarbon and carbon dioxide emissions. The weakest correlation was found between carbon monoxide and nitrogen oxide emissions. The appropriate dimensionless characteristic of dynamic driving conditions turned out to be the average vehicle velocity. The correlation between hydrocarbon emissions and the average vehicle velocity was considered to be the strongest, while the correlation between nitrogen oxide emissions and the average vehicle velocity was found to be the weakest.

The correlation studied in [14] was between the emission pollutant intensity and the operating conditions of A spark-ignition engine in a passenger car was tested on a chassis dynamometer in many dynamic tests, both type approval and special tests. The engine properties were studied in various static and dynamic states.

The general conclusion was that similar relationships and correlations that occur for carbon monoxide emissions were also present for hydrocarbon emissions.

Research results obtained in the paper [15] concern exhaust emissions from the compression-ignition engine of a light truck. The tests were carried out using a vehicle on a chassis dynamometer in the ECE R83 test with a warm engine start. The values of emission pollutant intensity were recorded, followed by a correlation analysis. The theories of Pearson, Spearman, Kendall and Kruskal were used in the study. The analysis showed a clear correlation between the tested variables. The probability of accepting the hypothesis of there being no correlation was zero, with an accuracy of at least six decimal places. The exception was the correlation test between carbon monoxide and carbon dioxide emission pollutant intensity, for which the probability of accepting the no-correlation hypothesis was approximately 5% at most.

Paper [16] presents the exhaust emission test results depending on the engine operating states that determine the emissions. The tests were carried out on an engine dynamometer using a Cummins 6C8.3 compression ignition engine under NRTC (Non-Road Transient Cycle) test conditions. Pearson's linear correlation, Spearman's rank correlation, Kruskal's gamma correlation and Kendall's tau correlation theory were used to analyze the correlation between the studied datasets. The obtained results indicated that it was statistically justified to treat the examined pairs of datasets of physical quantities as strongly correlated. Moreover, it was found that the values of the engine operating states had a similar impact on the emission pollutant intensity of carbon monoxide and hydrocarbons, while their impact on the emission pollutant intensity of nitrogen oxides was completely different. When it comes to carbon monoxide and hydrocarbon emissions, the factor with the greatest influence was found to be the engine speed. The engine torque and useful power had the greatest impact for nitrogen oxide emissions.

The reviewed available literature indicated that so far there was a small number of publications on the study of the properties of vehicle velocity, engine operating states, exhaust emissions and fuel mass consumption due to their statistical properties and mutual correlation relationships, especially in real operating conditions of vehicles.

3. Method

The research method consisted of:

1. Carrying out empirical tests of a passenger car in real driving conditions in the RDE test.
   Measuring and recording the data for:
   – vehicle velocity
   – engine steering
   – engine speed
   – relative engine torque
   – relative effective power
   – emission pollutant intensity: carbon monoxide, hydrocarbons, nitrogen oxides and carbon dioxide
   – particle number intensity
   – fuel mass consumption intensity.
2. Processing the obtained raw results of empirical tests to remove gross errors and reducing the share of high-frequency noise in the recorded signals thanks to the use of low-pass filtering. A second-stage Savitzky-Golay filter was used for filtration [34].
3. Studying the relationships between engine operating states, such as engine steering, engine speed, relative engine torque, and relative effective power, throughout the test and in its individual phases.
4. Determination of the pollutant specific distance emission, the particulate matter number specific distance and the specific distance fuel mass consumption of the vehicle throughout the test and in its individual phases.
5. Correlation studies of the following processes: engine operating states, intensity of emission pollutant, particle number intensity and fuel mass consumption intensity of the vehicle.
6. Formulation conclusions based on research results.

Engine steering in automotive applications is the relative value of the vehicle's engine steering setting, i.e. the engine steering pedal (accelerator pedal).

Relative torque is defined as the ratio of torque and torque on the external characteristic for the same engine speed.

Similarly, the relative effective power is the ratio of the resultant power to the net power on the external characteristic for the same engine speed.

The individual phases of the RDE test are:

– first phase, corresponding to urban driving – labelled – RDE – U
– second phase, corresponding to extra-urban driving – labelled – RDE – R
– third phase, corresponding to driving on motorways and expressways – labelled – RDE – H.

The test vehicle was a passenger car with a four-cylinder turbocharged spark-ignition engine, equipped with an automatic transmission. The engine was of the Euro 6 AP emissions class [20, 39].

Tests in real driving conditions in the RDE test were carried out using PEMS equipment [32]. A Semtech DS analyzer [36] and a TSI 3090 EPSS™ (Engine Exhaust Particle Sizer™ Spectometer) analyzer [37] were used to measure the exhaust emissions.

The equipment used in the tests was in line with the approval procedures requirements.

4. Test results

Figures 1–11 present the results of empirical research filtered with a low-pass filter.

Figure 1 shows the vehicle velocity in the RDE test.

In the first part (0–3732 s), the driving velocity was typical of urban driving. The average velocity was 24.3 km/h, and the maximum velocity was measured at 58.9 km/h. Between the time points 3732 s and 5469 s, the driving conditions resembled those on city outskirts, or suburban

areas. The average velocity of the vehicle was 57.7 km/h and the maximum velocity was measured at 85.1 km/h. The third driving phase corresponded to motorway and expressway driving at (5469 –6000s). The average velocity in the third test phase was 107.2 km/h, and the maximum velocity was measured at 118.9 km/h. The average velocity throughout the test was 41.3 km/h. The variation coefficient of velocity was the highest in the first test phase – and equalled 0.73, in the second phase it was 0.37. In the third it reached 0.13, and the test average was 0.76.

Figure 2 shows the engine steering in the RDE test.

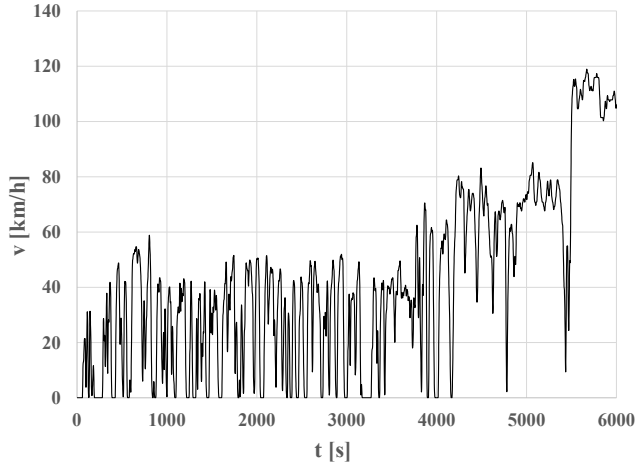

Fig. 1. Vehicle velocity in the RDE test

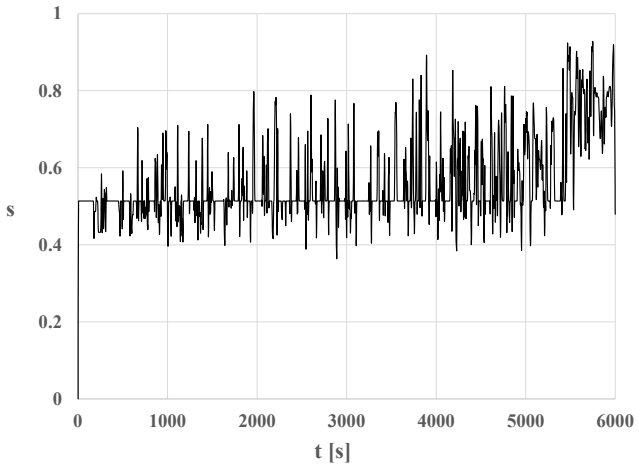

Fig. 2. Engine steering in the RDE test

The average steering value was 0.56, the maximum value was 0.96, and the coefficient of variation was 0.18. The most dynamic properties of the steering process were observed in the second phase of the test – the coefficient of variation was 0.17, while in the first phase it was 0.11, and in the third phase – 0.10.

Figure 3 shows the engine speed in the RDE test.

The engine speed is characterized by high variability. The coefficient of variation of the engine speed in the test was 1.08, in the first phase – 1.39, in the second – 0.79, and in the third – 0.18, so the least dynamic properties of the engine speed could clearly be found in the third test phase.

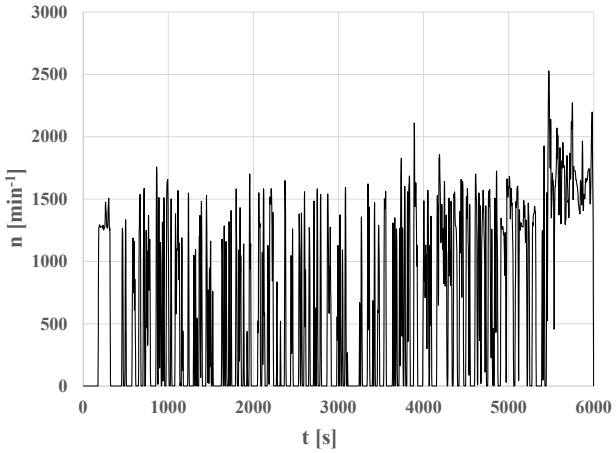

Fig. 3. Engine speed in the RDE test

Figure 4 shows the relative engine torque in the RDE test.

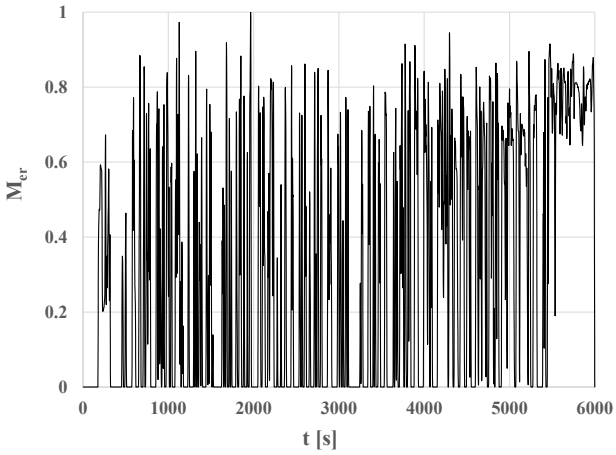

Fig. 4. Relative engine torque in the RDE test

The coefficient of variation of the relative torque in the test was 1.06, in the first phase – 1.38, in the second – 0.79, and in the third – 0.14. By far, the least dynamic properties of the relative torque were observed in phase three of the test.

Figure 5 shows the relative effective engine power in the RDE test.

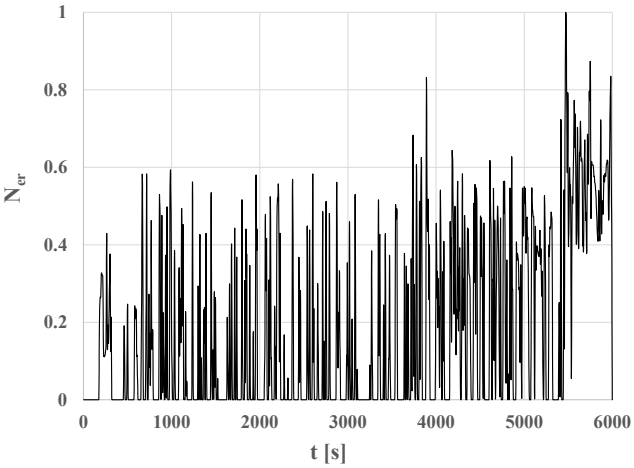

Fig. 5. Relative effective engine power in the RDE test

By far the highest average relative effective engine power was – understandably – in the third phase of the test. The coefficient of variation of the relative effective power in the test was 1.23 in the first phase – 1.59, in the second – 0.89, and in the third – 0.25.

Figures 6–9 present the emission pollutant intensity in the RDE test, and Fig. 10 – the particle number in the RDE test.

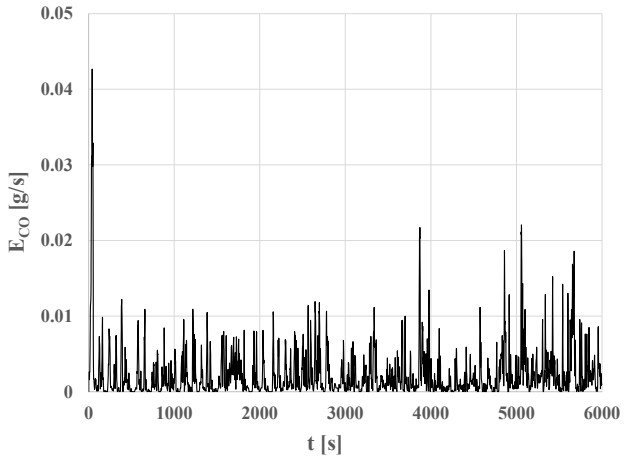

Fig. 6. Carbon monoxide emission pollutant intensity in the RDE test

The average carbon monoxide emission pollutant intensity in the test was 0.0023 g/s, in the first phase of the test – 0.0022 g/s, in the second – 0.0023 g/s, and in the third – 0.0031 g/s. No significant differences were found in the average carbon monoxide emission pollutant intensity value in individual test phases. The coefficient of variation of carbon monoxide emission pollutant intensity in the test was 1.46 in the first phase – 1.57, in the second – 1.33, and in the third – 1.17. The most dynamic properties of the carbon monoxide emission pollutant intensity occurred in the first phase of the test, which was related to the cold start of the engine.

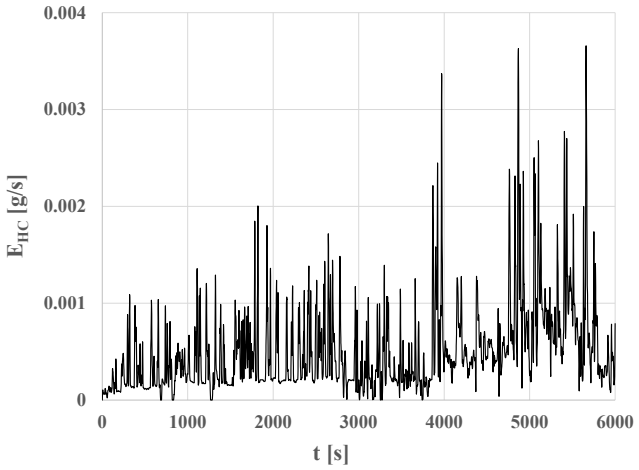

Fig. 7. Hydrocarbon emission pollutant intensity in the RDE test

The average hydrocarbon emission pollutant intensity in the test was 0.00050 g/s, in the first phase of the test – 0.00037 g/s, in the second – 0.00075 g/s, and in the third – 0.00067 g/s. The coefficient of variation of the hydrocarbon emission pollutant intensity in the test was 0.89 in the first phase – 0.82, in the second – 0.74, and in the third – 0.82. No significant differences were found in the coefficient of variation values of the hydrocarbon emission pollutant intensity in individual test phases nor in the test as a whole.

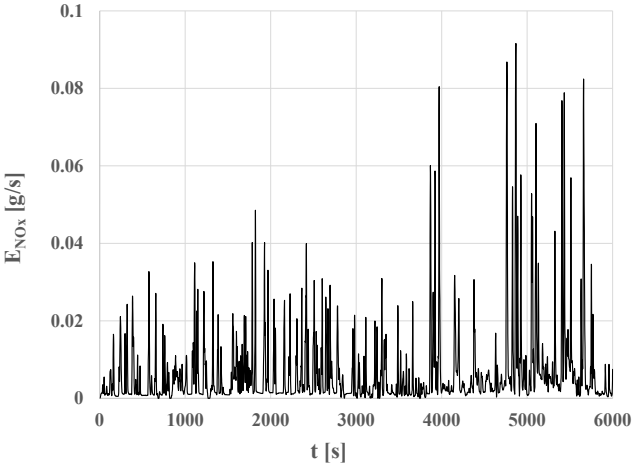

Fig. 8. Nitrogen oxides emission pollutant intensity in the RDE test

The average nitrogen oxide emission pollutant intensity in the test was 0.0067 g/s, in the first phase of the test – 0.0051 g/s, in the second – 0.0096 g/s, and in the third – 0.0074 g/s. The coefficient of variation of nitrogen oxide emission pollutant intensity in the test was 1.57, in the first phase – 1.28, in the second – 1.55, and in the third – 1.66. The lowest average value of the nitrogen oxide emission pollutant intensity was observed in the first phase of the test for the lowest engine load, which was related to the lowest driving velocity in this phase.

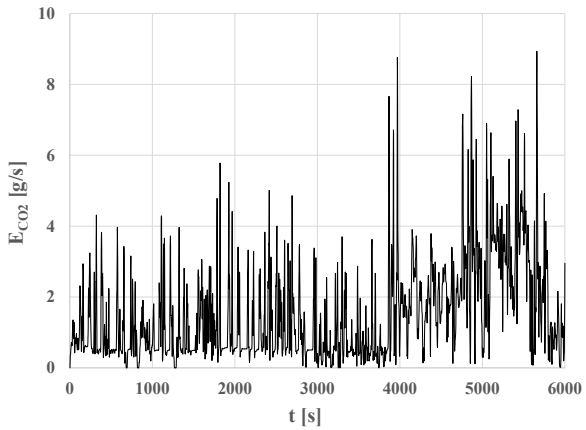

Fig. 9. Carbon dioxide emission pollutant intensity in the RDE test

The average carbon dioxide emission pollutant intensity in the test was 1.51 g/s, in the first phase of the test – 1.00 g/s, in the second – 2.42 g/s, and in the third – 2.07 g/s. The relatively high average value of the carbon dioxide emission pollutant intensity in the first phase of the test was related to the high fuel mass consumption resulting from A cold engine starts. The coefficient of variation of carbon dioxide emission pollutant intensity in the test was 0.89, in the first phase – 0.87, in the second – 0.63, and in the third – 0.80.

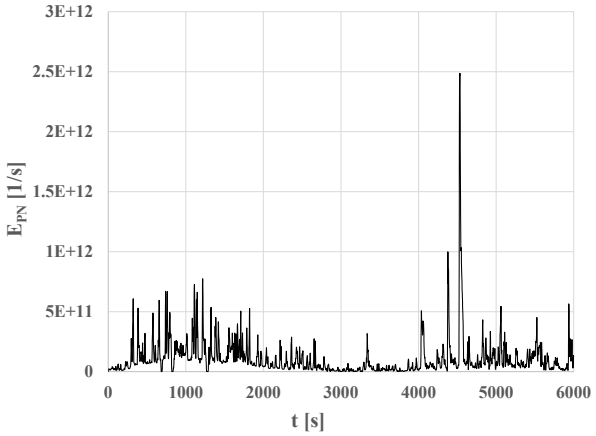

Fig. 10. Particle number intensity in the RDE test

The average particulate number intensity in the test was 1.091E+11 1/s, in the first phase of the test – 1.0044E+11 1/s, in the second phase – 1.313E+11 1/s, and in the third phase – 9.714E+10 1/s. No significant differences in the average particle number intensity values was found in the individual test phases. The coefficient of variation of particulate number intensity in the test was 1.51, in the first phase – 1.31, in the second – 1.91, and in the third – 0.96.

Figure 11 shows the vehicle fuel mass consumption intensity in the RDE test. The average fuel mass consumption intensity of the vehicle in the test was 0.57 g/s, in the first phase of the test – 0.40 g/s, in the second – 0.89 g/s, and in the third – 0.69 g/s. The coefficient of variation of the fuel mass consumption intensity of the vehicle in the test was 0.81 in the first phase – 0.73, in the second – 0.59, and in the third – 0.80.

The carbon dioxide emission pollutant intensity and the fuel mass consumption intensity were approximately linearly related.

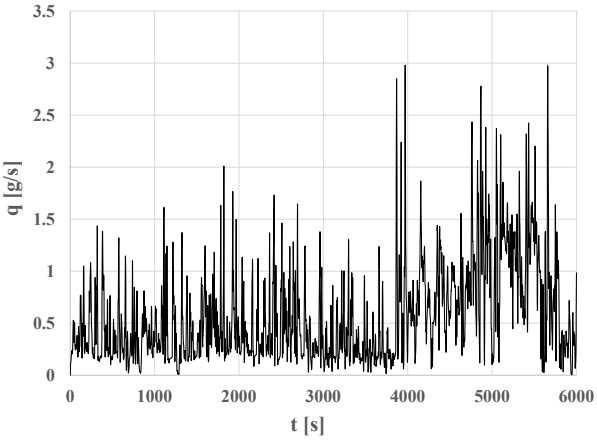

Fig. 11. Fuel mass consumption intensity of the vehicle in the RDE test

5. Results analysis

Figures 12–15 show the relationships between the engine operating states in the RDE test. The average values were marked on the charts: for the whole test the point was labelled as RDE, for the first phase, corresponding to urban driving – RDE – U, for the second phase, corresponding to driving in rural areas – RDE – R, and for the third phase corresponding to motorway and highway driving – RDE – H.

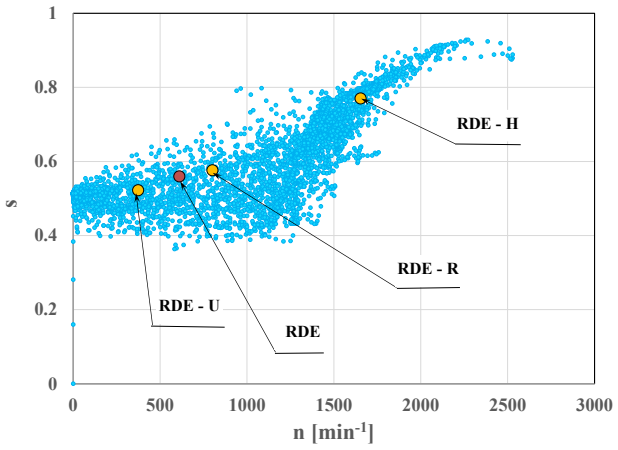

Fig. 12. Relationship between engine steering and engine speed in the RDE test

The relationship between engine operating states in the RDE test and the engine speed was similar for: engine steering, relative torque and relative effective power. The sets of operating states were characterized by significant dispersion, which resulted from the large coefficient of variation, as shown in Fig. 2–5. For all variables in Fig. 12–14, both the independent variables and the dependent variables, their average values were typically the smallest for the first phase, slightly larger for the whole test, even larger for the second phase and the largest for the third phase.

Table 1 presents the statistical characteristics [25] of the vehicle velocity, pollutant specific distance emission, particle number specific distance and specific distance fuel mass consumption for the test as well as for its individual phases. The tables contain the following dimensionless statistical characteristics:

- Min – minimum value
- Max – maximum value
- R – range
- AV – average value
- M – median
- D – standard deviation
- K – kurtosis
- S – skewness
- W – coefficient of variation.

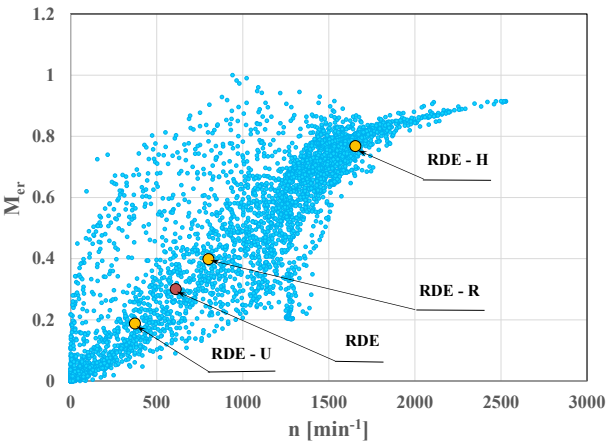

Fig. 13. The relative engine torque vs the engine speed in the RDE test

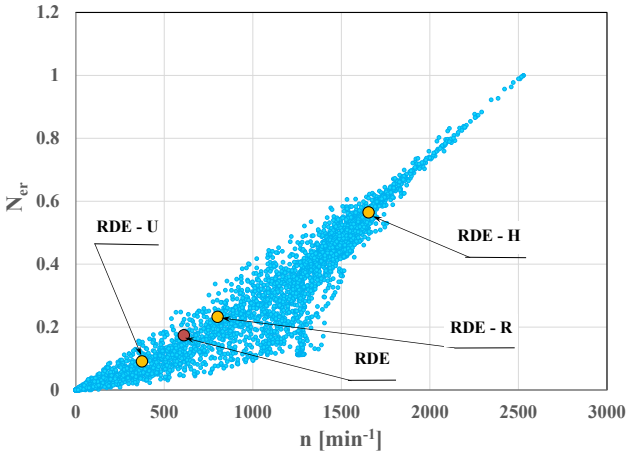

Fig. 14. Relative effective engine power vs engine speed in the RDE test

Very large statistical differences were found in vehicle velocity, engine operating states and emission pollutant intensity, particle number intensity and fuel mass consumption intensity of the vehicle. Significant differences were also noted between the results of the whole test and its individual phases.

It should be noted that:

- the distributions of the emission pollutant intensity and the particle number intensity as well as the fuel mass consumption intensity of the vehicle throughout the test and in its individual phases were viscokurtic
- vehicle velocity distributions were leptokurtic in individual test phases, and their distribution was platykurtic throughout the test as a whole
- the distributions of exhaust emissions, particulate number and fuel mass consumption of the vehicle throughout the test and in its individual phases were characterized by left-sided asymmetry
- in the case of vehicle velocity and internal combustion engine operating states, there was a significant variation in distribution asymmetry throughout the test and in its individual phases
- the coefficients of variation values for the nitrogen oxide emission pollutant intensity and the particle number intensity were the highest, which proves the strongest dynamic properties of these variables

Table 1. the statistical characteristics of the tested variables for the test as well as for its individual phases

	v	s	n	M_{er}	N_{er}	E_{CO}	E_{HC}	E_{NOx}	E_{CO2}	E_{PN}	q_F
	km/h		min^{-1}			g/s	g/s	g/s	g/s	1/s	g/s
RDE											
Min	0	0	0	0	0	0	0	0	0	0	0
Max	118.9	0.93	2529	1	1	0.043	0.0037	0.092	8.93	2.49E+12	2.98
R	118.9	0.93	2529	1	1	0.043	0.0037	0.092	8.93	2.49E+12	2.98
AV	41.3	0.56	611	0.30	0.17	0.002	0.0005	0.007	1.51	1.09E+11	0.57
M	38.6	0.51	312	0.17	0.05	0.001	0.0004	0.003	1.02	6.62E+10	0.42
D	31.4	0.10	659	0.32	0.21	0.003	0.0005	0.010	1.35	1.65E+11	0.46
K	–0.23	1.49	–1.26	–1.43	–0.11	32.68	8.71	18.69	3.05	76.19	2.69
S	0.60	1.35	0.51	0.46	1.00	4.41	2.41	3.82	1.57	6.85	1.49
W	0.76	0.18	1.08	1.06	1.23	1.46	0.90	1.57	0.89	1.51	0.81
RDE – U											
Min	0	0	0	0	0	0	0	0	0	0	0
Max	58.9	0.80	1758	1	1	0.043	0.0020	0.049	5.78	7.74E+11	2.01
R	58.9	0.80	1758	1	1	0.043	0.0020	0.049	5.78	7.74E+11	2.01
AV	41.3	0.56	611	0.30	0.17	0.002	0.0005	0.007	1.51	1.09E+11	0.57
M	66.0	0.53	963	0.49	0.23	0.001	0.0006	0.004	2.25	6.72E+10	0.83
D	21.3	0.10	632	0.31	0.21	0.003	0.0006	0.015	1.52	2.50E+11	0.53
K	0.97	0.10	–1.52	-1.61	–1.03	12.16	4.68	9.21	1.34	45.41	0.86
S	–1.33	0.81	–0.10	-0.14	0.32	3.06	1.97	2.97	0.95	6.06	0.80
W	0.52	0.17	1.04	1.04	1.19	1.35	1.10	2.25	1.01	2.29	0.93
RDE – R											
Min	0	0.38	0	0	0	0	0	0	0	2.09E+07	0.02
Max	85.1	0.92	2460	1	1	0.022	0.0036	0.092	8.76	2.49E+12	2.98
R	85.1	0.54	2460	1	1	0.022	0.0036	0.092	8.76	2.49E+12	2.96
AV	57.7	0.58	801	0.40	0.23	0.002	0.0007	0.010	2.42	1.31E+11	0.89
M	66.0	0.53	963	0.49	0.23	0.001	0.0006	0.004	2.25	6.72E+10	0.83
D	21.3	0.10	632	0.31	0.21	0.003	0.0006	0.015	1.52	2.50E+11	0.53
K	962	923	885	846	808	769	730	692	653	615	24377
S	–1.33	0.81	–0.10	–0.14	0.32	3.06	1.97	2.97	0.95	6.06	0.80
W	0.37	0.17	0.79	0.79	0.89	1.33	0.74	1.55	0.63	1.91	0.59
RDE – H											
Min	24.8	0.5	0	0	0	0	0.0001	0	0.02	1.05E+10	0.01
Max	118.9	0.93	2529	1	1	0.019	0.0037	0.082	8.93	5.65E+11	2.97
R	94.2	0.45	2529	1	1	0.019	0.0036	0.082	8.92	5.54E+11	2.97
AV	107.2	0.77	1654	0.77	0.56	0.003	0.0007	0.007	2.07	9.71E+10	0.69
M	109.8	0.78	1654	0.80	0.57	0.002	0.0005	0.003	1.63	6.77E+10	0.54
D	14.2	0.08	300	0.11	0.14	0.004	0.0006	0.012	1.65	9.28E+10	0.55
K	1.10	0.39	–1.35	–1.60	–0.47	12.18	4.62	9.17	1.23	45.54	0.80
S	–3.80	–0.55	–1.10	–3.58	–0.26	1.96	2.51	3.54	1.16	1.83	1.16
W	0.13	0.10	0.18	0.14	0.25	1.17	0.82	1.66	0.80	0.96	0.80

– the relationship between the mean and median values of individual processes varied throughout the test and in its individual phases.

Such a significant variation in the dimensionless statistical characteristics of the emission pollutant intensity and the particle number intensity as well as the vehicle's fuel mass consumption intensity indicated a significant impact of the engine operating states, determined by the vehicle velocity, on these variables. In the case of the emission pollutant intensity and the particle number intensity, this was due to very low values of these quantities, sometimes near the determination limit.

Table 2 shows the vehicle's average velocity, pollutant specific distance emission, particle number specific distance and specific distance fuel mass consumption of the vehicle throughout the test and in its individual phases.

Table 2. Pollutant specific distance emission, particle number specific distance and specific distance fuel mass consumption of the vehicle throughout the test and in its individual phases

	v_{AV}	b_{CO}	b_{HC}	b_{NOx}	b_{CO2}	b_{PN}	q
	km/h	g/km				1/km	g/km
RDE	41.3	0.195	0.033	0.465	90.2	9.07E+12	36.02
RDE – U	24.3	0.332	0.056	0.789	153.1	1.54E+13	61.16
RDE – R	57.7	0.070	0.023	0.290	73.0	3.95E+12	26.87
RDE – H	107.2	0.015	0.003	0.037	10.2	4.81E+11	3.41

Figures 15–20 present the characteristics of pollutant specific distance emission, particle number specific distance and specific distance fuel mass consumption of the vehicle depending on the average speed in individual test phases and in the test as a whole. The datapoint sets were approximated with an exponential function. The approximating function was chosen due to the small number of points.

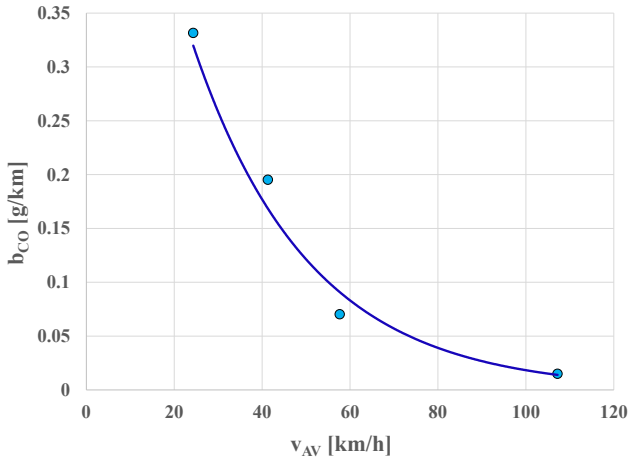

Fig. 15. Carbon monoxide pollutant specific distance emission relative to average velocity

The determined characteristics show a clear regularity, consistent with established knowledge, such as with characteristics created by conducting numerous empirical tests with different average velocity. Similar characteristics of exhaust emissions and fuel mass consumption are also commonly obtained using software such as HBEFA INFRAS [23] or COPERT [18].

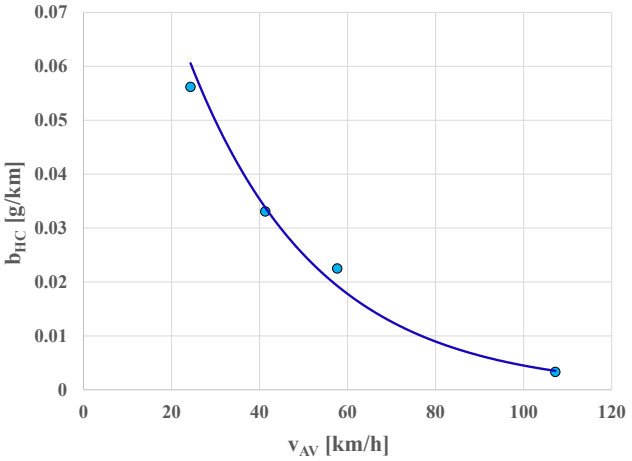

Fig. 16. Hydrocarbons pollutant specific distance emission relative to average velocity

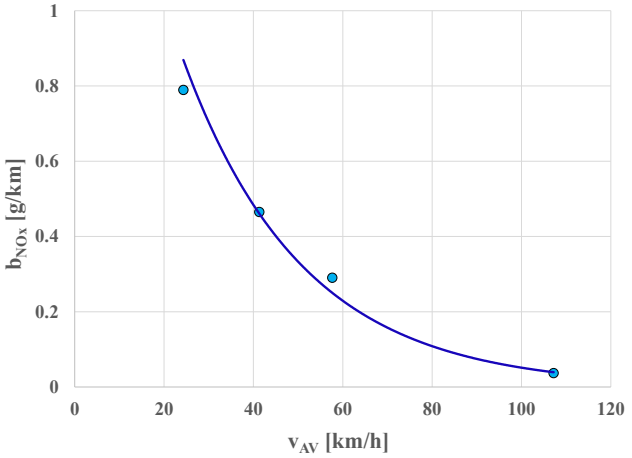

Fig. 17. Nitrogen oxides pollutant specific distance emission relative to average speed

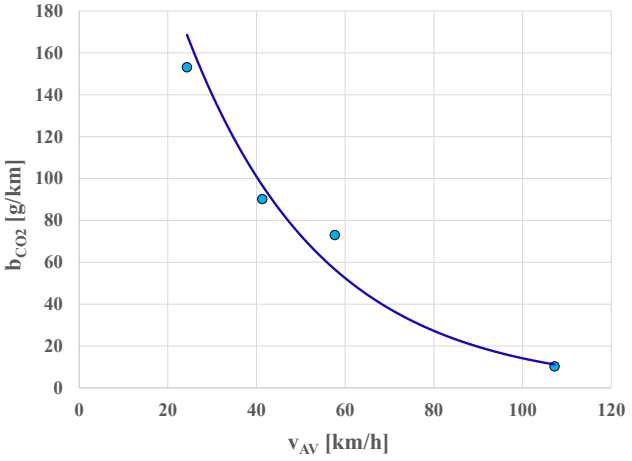

Fig. 18. Carbon dioxide pollutant specific distance emission relative to average velocity

Table 3 presents Pearson's linear correlation coefficients between the measured variables.

Figures 21–31 present Pearson's linear correlation coefficients between the measured variables. Figure 21 shows the correlation coefficient between the vehicle velocity and

the other variables. The Pearson linear correlation coefficient of the vehicle velocity was the greatest, as would be expected, with the engine operating states – the largest value being with the engine steering (0.49).

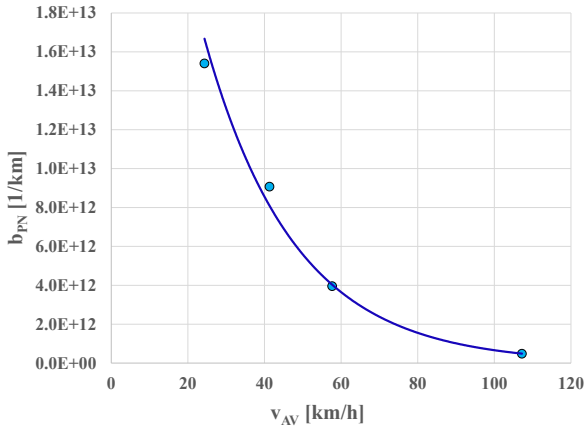

Fig. 19. Particle number specific distance emission relative to the average velocity

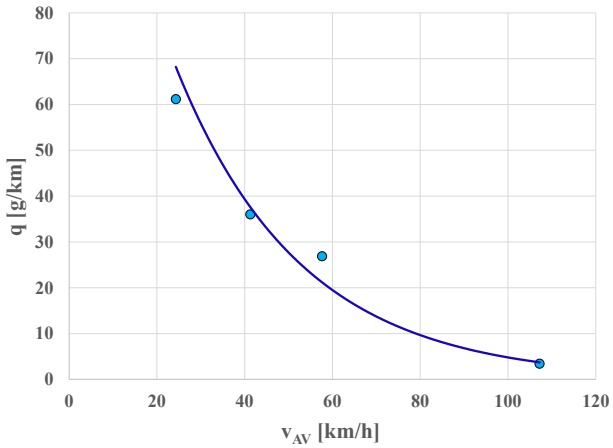

Fig. 20. Specific distance fuel mass consumption relative to average velocity

Figure 22 shows the linear correlation coefficient between engine steering and the other variables. The Pearson linear correlation coefficient values of the vehicle velocity with the emission pollutant intensity of carbon monoxide and nitrogen oxides as well as with the particle number intensity were the smallest – in all these cases the obtained correlation coefficients were less than 0.1.

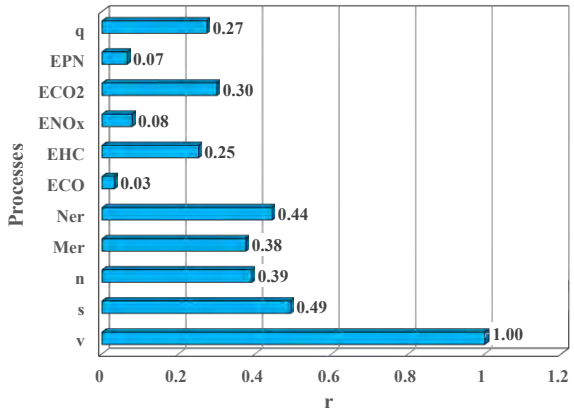

Fig. 21. Pearson's linear correlation coefficient of the vehicle velocity and the following variables: vehicle velocity, engine steering, engine speed, relative engine torque, relative engine effective power, engine fuel mass consumption intensity, emission pollutant intensity of: carbon monoxide, hydrocarbons, nitrogen oxides and carbon dioxide, and particle number intensity

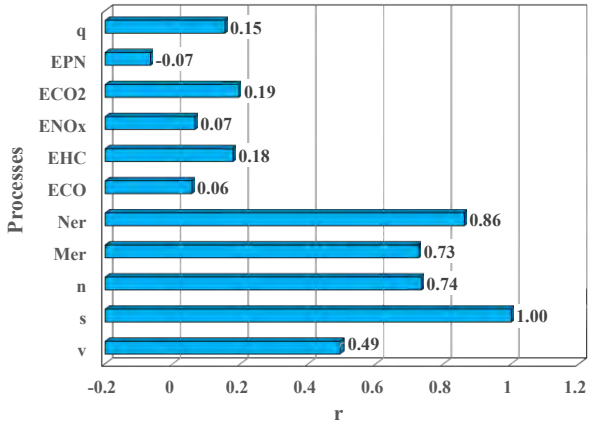

Fig. 22. Pearson's linear correlation coefficient of the engine steering and the following variables: vehicle velocity, engine steering, engine speed, relative engine torque, relative engine effective power, engine fuel mass consumption intensity, emission pollutant intensity of: carbon monoxide, hydrocarbons, nitrogen oxides and carbon dioxide, and particle number intensity

The largest value of the Pearson linear correlation coefficient of the engine steering was for the engine operating states – the value of the correlation coefficient was greater than 0.7, then the value for the engine steering correlation was large also for the vehicle velocity – at almost 0.5. The correlation coefficient of the engine steering with the particle number intensity was the smallest and slightly negative (–0.07).

Table 3. Pearson's linear correlation coefficients between the measured variables

	v	s	n	M_{er}	N_{er}	E_{CO}	E_{HC}	E_{NOx}	E_{CO2}	E_{PN}	q
v	1.00	0.49	0.39	0.38	0.44	0.03	0.25	0.08	0.30	0.07	0.27
s	0.49	1.00	0.74	0.73	0.86	0.06	0.18	0.07	0.19	–0.07	0.15
n	0.39	0.74	1.00	0.94	0.96	–0.02	0.15	0.05	0.19	0.02	0.17
M_{er}	0.38	0.73	0.94	1.00	0.94	–0.02	0.16	0.05	0.19	0.00	0.16
N_{er}	0.44	0.86	0.96	0.94	1.00	0.00	0.17	0.05	0.21	0.00	0.17
E_{CO}	0.03	0.06	–0.02	–0.02	0.00	1.00	0.38	0.37	0.32	0.11	0.30
E_{HC}	0.25	0.18	0.15	0.16	0.17	0.38	1.00	0.91	0.93	0.27	0.90
E_{NOx}	0.08	0.07	0.05	0.05	0.05	0.37	0.91	1.00	0.81	0.25	0.79
E_{CO2}	0.30	0.19	0.19	0.19	0.21	0.32	0.93	0.81	1.00	0.30	0.98
E_{PN}	0.07	–0.07	0.02	0.00	0.00	0.11	0.27	0.25	0.30	1.00	0.30
q	0.27	0.15	0.17	0.16	0.17	0.30	0.90	0.79	0.98	0.30	1.00

Figure 23 shows the linear correlation coefficient between the engine speed and the other variables.

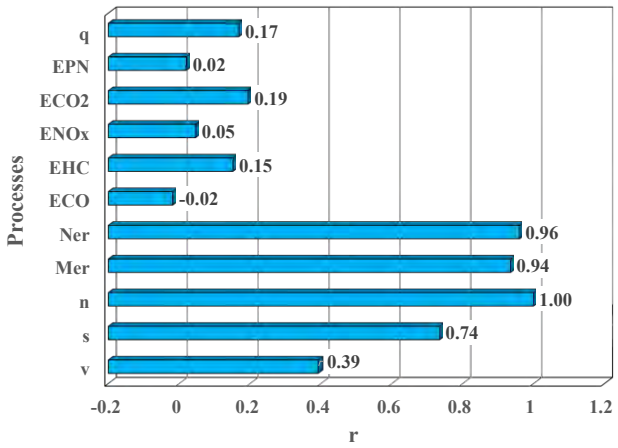

Fig. 23. Pearson's linear correlation coefficient of the engine speed and the following variables: vehicle velocity, engine steering, engine speed, relative engine torque, relative engine effective power, engine fuel mass consumption intensity, emission pollutant intensity of: carbon monoxide, hydrocarbons, nitrogen oxides and carbon dioxide, and particle number intensity

The largest Pearson linear correlation coefficient of the engine speed was found for the engine operating states, primarily for the relative effective power and relative torque – the value of the correlation coefficient for those was greater than 0.9, so the correlation can be considered very strong. The correlation between the engine speed and the engine steering was much weaker – the obtained correlation coefficient was less than 0.75. The weakest correlation was found between the engine speed and the emission pollutant intensity, particle number intensity and fuel mass consumption intensity. For carbon monoxide emission intensity, the correlation coefficient was slightly negative (–0.02).

Figure 24 shows the linear correlation coefficient between the relative engine torque and the other variables.

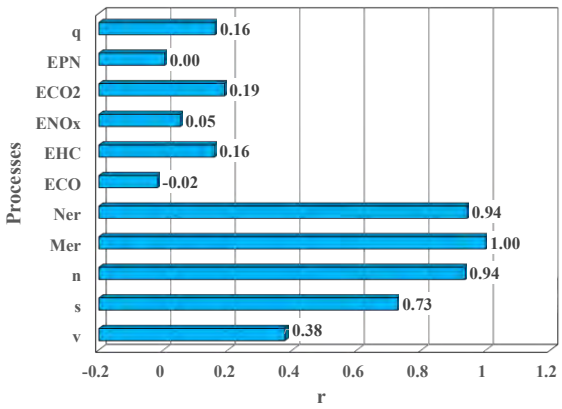

Fig. 24. Pearson's linear correlation coefficient of the engine torque and the following variables: vehicle velocity, engine steering, engine speed, relative engine torque, relative engine effective power, engine fuel mass consumption intensity, emission pollutant intensity of: carbon monoxide, hydrocarbons, nitrogen oxides and carbon dioxide, and particle number intensity

The largest Pearson linear correlation coefficient of the relative engine torque was found for the engine operating states, primarily with the engine speed and relative effective power – the coefficient value was calculated to be 0.94. The value of the correlation coefficient for engine steering was lower – at 0.73. The smallest correlation coefficient was, as in the case of engine speed, with the carbon monoxide emission intensity – in this case the correlation coefficient was slightly negative and reached –0.02.

Figure 25 shows the linear correlation coefficient between the relative effective power of the engine and the other variables.

The nature of the correlation coefficient of the relative effective power with the other variables was very similar to that of engine speed and relative torque.

Figures 26–29 present the linear correlation coefficients of emission intensity of pollutants and the other variables.

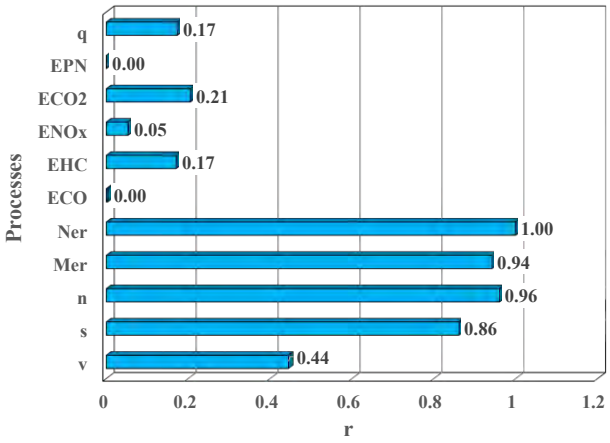

Fig. 25. Pearson's linear correlation coefficient of the engine relative effective power and the following variables: vehicle velocity, engine steering, engine speed, relative engine torque, relative engine effective power, engine fuel mass consumption intensity, emission pollutant intensity of: carbon monoxide, hydrocarbons, nitrogen oxides and carbon dioxide, and particle number intensity

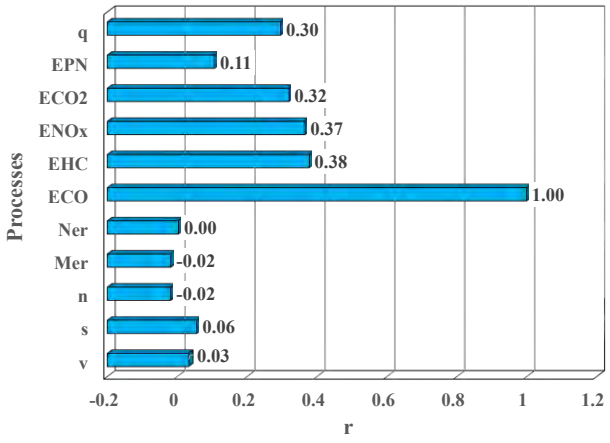

Fig. 26. Pearson's linear correlation coefficient of the carbon monoxide emission pollutant intensity and the following variables: vehicle velocity, engine steering, engine speed, relative engine torque, relative engine effective power, engine fuel mass consumption intensity, emission pollutant intensity of: carbon monoxide, hydrocarbons, nitrogen oxides and carbon dioxide, and particle number intensity

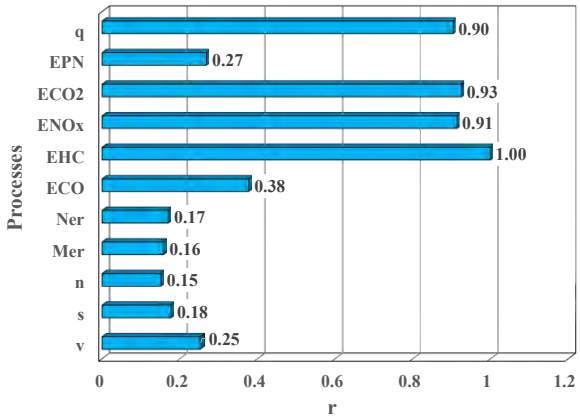

Fig. 27. Pearson's linear correlation coefficient of the hydrocarbon emission pollutant intensity and the following variables: vehicle velocity, engine steering, engine speed, relative engine torque, relative engine effective power, engine fuel mass consumption intensity, emission pollutant intensity of: carbon monoxide, hydrocarbons, nitrogen oxides and carbon dioxide, and particle number intensity

The values of the Pearson's linear correlation coefficients of the carbon monoxide emission pollutant intensity with the emission pollutant intensity of other substances and the fuel mass consumption intensity of the vehicle were similar. All were between 0.3–0.4. The correlation with the particle number intensity was much weaker – the value of the correlation coefficient was only 0.11. Moreover, the correlation between the carbon monoxide emission intensity and the engine operating states and vehicle velocity was very weak.

There was a very strong correlation between the hydrocarbon emission intensity and the emission pollutant intensity of nitrogen oxides, carbon dioxide and fuel mass consumption intensity – the value of the correlation coefficient was found to be greater than 0.9. The correlation with the carbon monoxide emission pollutant intensity was weaker – the correlation coefficient was equal to 0.38, and even weaker with the particle number intensity where the correlation coefficient was 0.27. The correlation of hydrocarbon emission intensity with engine operating states and the vehicle velocity was stronger than in the case of carbon monoxide emission intensity.

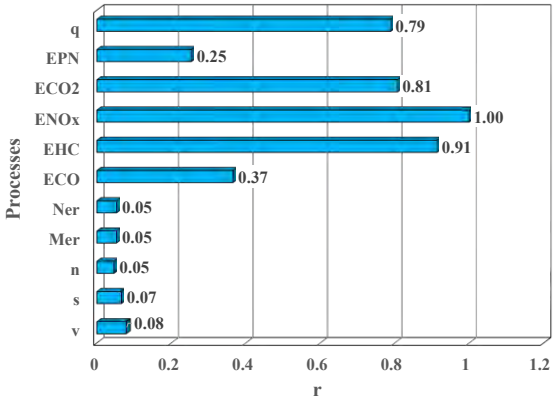

Fig. 28. Pearson's linear correlation coefficient of the nitrogen oxides emission pollutant intensity and the following variables: vehicle velocity, engine steering, engine speed, relative engine torque, relative engine effective power, engine fuel mass consumption intensity, emission pollutant intensity of: carbon monoxide, hydrocarbons, nitrogen oxides and carbon dioxide, and particle number intensity

The strongest correlation was observed between the nitrogen oxide emission intensity and the hydrocarbon and carbon dioxide emission intensity as well as with the fuel mass consumption intensity – the correlation coefficient values were between 0.8–0.9. The correlation of the nitrogen oxide emission intensity was stronger with the carbon monoxide emission intensity – the correlation coefficient value was 0.37 than with the particle number intensity (the correlation coefficient was 0.25).

Predictably, the strongest correlation was between the carbon dioxide emission intensity and the fuel mass consumption intensity of the vehicle – these processes are known to be approximately linearly related.

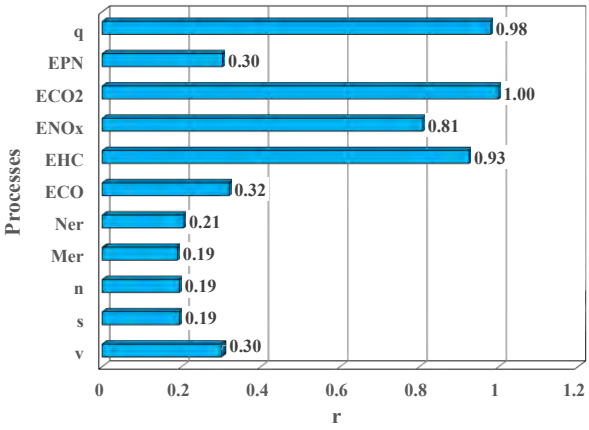

Fig. 29. Pearson's linear correlation coefficient of the carbon dioxide emission pollutant intensity and the following variables: vehicle velocity, engine steering, engine speed, relative engine torque, relative engine effective power, engine fuel mass consumption intensity, emission pollutant intensity of: carbon monoxide, hydrocarbons, nitrogen oxides and carbon dioxide, and particle number intensity

Figure 30 shows the linear correlation coefficient of the particle number intensity and the other variables. There was also a very strong correlation between the carbon dioxide emission intensity and the emission pollutant intensity of hydrocarbons and nitrogen oxides. The value of the correlation coefficient of the carbon dioxide emission intensity with both the carbon monoxide emission intensity and particle number intensity was 0.3. The value of the correlation coefficient of carbon dioxide emission intensity with engine operating states and the vehicle velocity was also similar – in the range of 0.2–0.3.

The value of the correlation coefficient of the particle number intensity with the emission pollutant intensity of carbon dioxide, hydrocarbons and nitrogen oxides, as well as the fuel mass consumption intensity was in the range of 0.25–0.3, lowest among them for the emission intensity of carbon monoxide (0.11). The correlation of the particle number intensity with the engine operating states and the vehicle velocity was very weak.

Figure 31 shows the linear correlation coefficient between the fuel mass consumption intensity and the other variables.

The nature of the correlation between the fuel mass consumption intensity of the vehicle and the other variables was understandably very similar to that of the carbon dioxide emission intensity that was strongly correlated with it.

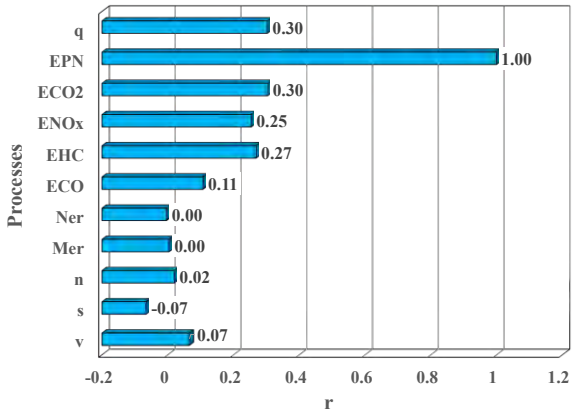

Fig. 30. Pearson's linear correlation coefficient of the particle number intensity and the following variables: vehicle velocity, engine steering, engine speed, relative engine torque, relative engine effective power, engine fuel mass consumption intensity, emission pollutant intensity of: carbon monoxide, hydrocarbons, nitrogen oxides and carbon dioxide, and particle number intensity

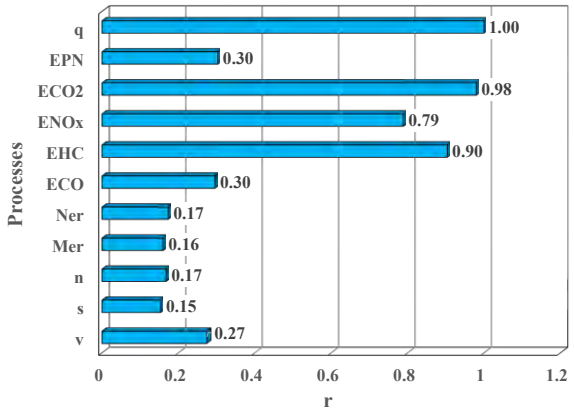

Fig. 31. Pearson's linear correlation coefficient of the engine fuel mass consumption intensity and the following variables: vehicle velocity, engine steering, engine speed, relative engine torque, relative engine effective power, engine fuel mass consumption intensity, emission pollutant intensity of: carbon monoxide, hydrocarbons, nitrogen oxides and carbon dioxide, and particle number intensity

Conclusions

Testing engines of road vehicles in real operating conditions provides the opportunity to obtain information about the engine properties that significantly exceed similar information that could be gained using tests in laboratory conditions. The possibilities of performing such tests were reduced due to technical limitations, especially in the field of exhaust emission tests. However, since the development of portable emission measurement systems (PEMS), these limitations have been significantly reduced. Nevertheless, financial constraints remain, as exhaust emissions and fuel mass consumption testing in real operating conditions tends to be a relatively expensive type of research.

The data obtained from the conducted research was analyzed, leading to the following conclusions:

1. The operating conditions of the combustion engine in the RDE test vary significantly in the phases corresponding to different traffic conditions: in cities, outside cities and on highways and expressways. This applies to all the following processes: engine steering, engine speed, relative torque and relative effective power. The influence of the engine speed on the engine operating states in the RDE test was similar. The sets of operating states were characterized by considerable dispersion, which resulted from their high coefficient of variation. Engine operating states vary greatly. For all engine operating states their average values were typically the smallest for the first test phase, larger for the entire test average, even larger for the second phase, and the largest for the third test phase.
2. There are very large statistical differences in vehicle velocity, engine operating states and emission pollutant intensity, particle number intensity and fuel mass consumption intensity of the vehicle, as well as large differences in the entire test as compared to its individual phases. The large differences in the dimensionless statistical characteristics of the emission pollutant intensity and the particle number intensity as well as the vehicle's fuel mass consumption intensity indicate a significant sensitivity of these values to the changes in engine operating states, which are determined by the vehicle velocity.

   There was a significant difference in the nature of the data points distributions of the studied variables: these were viscometric distributions for the emissions pollutant intensity and the particle number intensity as well as the fuel mass consumption intensity by the vehicle and engine steering. However, for the vehicle velocity, engine speed, relative torque and relative effective power, the distributions were platykurtic in most phases.

   The distribution of the data points of emission pollutant intensity, the particle number intensity and the fuel mass consumption intensity throughout the test and in its individual phases was characterized by left-sided asymmetry. In the remaining cases, the asymmetry of distributions varied.

   The strongest dynamic properties were for the nitrogen oxide emission intensity and particle number intensity, which resulted from the highest value of their coefficient of variation.

   The relationship between the mean and median values of individual variables varied significantly throughout the test and in its individual phases.
3. The vehicle's emission and fuel mass consumption characteristics have shown a clear regularity that is consistent with expectations, e.g., with characteristics determined from empirical studies conducting multiple tests at different average velocities. The characteristics of exhaust emissions and fuel mass consumption determined using software such as HBEFA INFRAS or COPERT were also similar.
4. Significant differences in the correlations of the studied variables were found. The engine operating states and the vehicle velocity were closely correlated with each other and much less correlated with the corresponding values of exhaust emissions. The correlation of variables describing the exhaust emissions also turned out to be varied. The least correlated variable with the emission pollutant intensity of hydrocarbons, nitrogen oxides, carbon dioxide and the fuel mass consumption intensity was the carbon monoxide emission intensity and the particle number intensity. These results were quite

surprising, because previous studies usually showed significant consistency in the results of emission tests with reducing properties: carbon monoxide and hydrocarbons in relation to the results of emission tests of substances with oxidizing properties such as nitrogen oxides, whereas in the case of this study, this regularity was not confirmed.

It would be advisable to consider the possibility of continuing research on the subject of this article. The following activities were proposed:

1. Carrying out empirical test with a larger number of repetitions. This would make it possible to assess the repeatability of research results, and in the case of a significantly larger number of tests, to treat research results in a probabilistic manner.
2. Carrying out studies for various driving test types, determined as a result of empirical tests in various traffic conditions, corresponding to driving in traffic congestion, in urban areas without traffic congestion, outside cities and on highways and expressways.

   It would be particularly useful to perform empirical tests for various vehicle velocity, which would correspond to driving in specific conditions.
3. Performing drive tests for road vehicles of categories other than passenger cars, such as: light trucks, trucks, city buses, long-distance buses and L category vehicles (motorcycles and mopeds, quads and microcars).

Nomenclature

AV	average value operator	Max	maximum value
b	specific distance pollutant emission/specific distance particulate number	M_{er}	relative engine torque
		Min	minimum value
CO	carbon oxide	n	engine speed
CO_2	carbon dioxide	N_{er}	relative engine effective power
COPERT	COmputer Programme to calculate Emissions from Road Transport	NO_x	nitrogen oxides
		PEMS	Portable Emissions Measurement System
D	standard deviation	PN	particle number
E	pollutant emission intensity/particle number intensity	q_F	fuel mass consumption intensity
		R	range/dispersion
EPSS™	Engine Exhaust Particle Sizer™ Spectrometer	RDE	Real Driving Emissions
HBEFA	Handbook Emission Factors for Road Transport	s	engine steering
HC	hydrocarbons	S	skewness
INFRAS	Infrastruktur-, Umwelt- und Wirtschaftsberatung	t	time
K	kurtosis	v	vehicle velocity
M	median	W	coefficient of variation

Bibliography

[1] André M, Joumard R, Vidon R, Tassel P, Perrte P. Real-world European driving cycles, for measuring pollutant emissions from high- and low-powered cars. Atmos Environ. 2006; 40(31):5944-5953. https://doi.org/10.1016/j.atmosenv.2005.12.057

[2] André M. The ARTEMIS European driving cycles for measuring car pollutant emissions. Sci Total Environ. 2004;334-335:73-84. https://doi.org/10.1016/j.scitotenv.2004.04.070

[3] Andrych-Zalewska M, Chłopek Z, Merkisz J, Pielecha J. Analysis of the operation states of internal combustion engine in the Real Driving Emissions test. Archives of Transport. 2022;61(1): 71-88. https://doi.org/10.5604/01.3001.0015.8162

[4] Andrych-Zalewska M, Chłopek Z, Merkisz J, Pielecha J. Exhaust emission from a vehicle engine operating in dynamic states and conditions corresponding to real driving. Combustion Engines. 2019;178(3):99-105. https://doi.org/10.19206/CE-2019-317

[5] Andrych-Zalewska M, Chłopek Z, Merkisz J, Pielecha J. Investigations of exhaust emissions from a combustion engine under simulated actual operating conditions in real driving emissions test. Energies. 2021;14(4):935. https://doi.org/10.3390/en14040935

[6] Andrych-Zalewska M, Chłopek Z, Merkisz J, Pielecha J. Research on exhaust emissions in dynamic operating states of a combustion engine in a Real Driving Emissions test. Energies. 2021, 14(18), 5684. https://doi.org/10.3390/en14185684

[7] Banach S. Théorie des opérations linéaires. Warsaw 1932.

[8] Bebkiewicz K, Chłopek Z, Sar H, Szczepański K, Zimakowska-Laskowska M. Assessment of impact of vehicle traffic conditions: urban, rural and highway, on the results of pollutant emissions inventory. Archives of Transport. 2021;60(4); 57-69. https://doi.org/10.5604/01.3001.0015.5477

[9] Bendat JS, Piersol AG. Random data: analysis and measurement procedures. John Wiley & Sons, 2010. Book Series: Wiley Series in Probability and Statistics. https://doi.org/10.1002/9781118032428

[10] BUWAL (Bundesamt für Umwelt, Wald und Landschaft), INFRAS AG (Infrastruktur-, Umwelt- und Wirtschaftsberatung). Luftschadstoffemissionen des Strassenverkehrs 1950–2010, BUWAL-Bericht 1995; 255.

[11] Chłopek Z, Biedrzycki J, Lasocki J, Wójcik P, Samson-Bręk I. Modelling of motor vehicle operation for the evaluation of pollutant emission and fuel consumption. Combustion Engines. 2017;171(4):156-163. https://doi.org/10.19206/CE-2017-426

[12] Chłopek Z, Biedrzycki J, Lasocki J, Wójcik P. Assessment of the impact of dynamic states of an internal combustion engine on its operational properties. Eksploat Niezawodn. 2015; 17(1):35-41.

[13] Chłopek Z, Biedrzycki J, Lasocki J, Wójcik P. Correlational investigation of air pollutant emissions and fuel consumption of motor vehicle in various dynamic conditions. Global NEST J. 2020;22(2):275-279. https://doi.org/10.30955/gnj.002893

[14] Chłopek Z, Lasocki J. Correlation investigations into pollutant emission and the operational states of compression-ignition engines in dynamic tests. Combustion Engines. 2017;169(2): 87-92. https://doi.org/10.19206/CE-2017-215
[15] Chłopek Z. A correlation analysis of the pollutant emission from a self ignition engine. Silniki Spalinowe – Combustion Engines. 2010;140(1):25-31. https://doi.org/10.19206/CE-117157
[16] Chłopek Z. Analysis of the correlation between pollutant emissions and operation states of a compression ignition engine. The Archives of Automotive Engineering – Archiwum Motoryzacji. 2015;68(2):3-19.
[17] Chłopek Z. Some remarks on engine testing in dynamic states. Combustion Engines. 2010;143(4):60-72. https://doi.org/10.19206/CE-117131
[18] COPERT 5 – Manual. https://copert.emisia.com/manual/ (accessed on 2019.12.01).
[19] Croux C, Dehon C. Influence functions of the Spearman and Kendall correlation measures. Stat Method Appl. 2010;19: 497-515. https://doi.org/10.1007/s10260-010-0142-z
[20] DieselNet: Engine & Emission Technology Online. https://dieselnet.com
[21] EEA/EMEP Emission Inventory Guidebook 2019.
[22] Giechaskiel B, Vlachos T, Riccobono F, Forni F, Colombo R, Montigny F et al. Implementation of Portable Emissions Measurement Systems (PEMS) for the Real-Driving Emissions (RDE) regulation in Europe. JOVE-J Vis Exp. 2016; 118:54753. https://doi.org/10.3791/54753
[23] INFRAS AG. Handbook emission factors for road transport 3.2. Quick reference. Version 3.2. Bern, 2014.
[24] Kendall MG. Rank correlation methods. New York: Hafner Publishing Co, 1955.
[25] Lane D. Introduction to statistics – Open Textbook Library, 2003. https://open.umn.edu/opentextbooks/textbooks/459
[26] Luján J M, Piqueras P, de la Morena J, Redondo F. Experimental characterization of real driving cycles in a light-duty diesel engine under different dynamic conditions. Appl Sci. 2022;12(5):2472. https://doi.org/10.3390/app12052472
[27] Metsämuuronen J. Dimension-corrected Somers' d for the item analysis settings. Int J Educ Method. 2020;6(2):297-317. https://doi.org/10.12973/ijem.6.2.297
[28] Papoulis A, Pillai SU. Probability, random variables, and stochastic processes. Tata McGraw-Hill, 2002;852.
[29] Parzen E. Stochastic processes. Courier Dover Publications. 2015.
[30] Pearson K. Determination of the coefficient of correlation. Science. 1909;30(757):23-25. https://doi.org/10.1126/science.30.757.23
[31] Pearson K. Note on regression and inheritance in the case of two parents. P R Soc London. 1895;58:240-242. https://doi.org/10.1098/rspl.1895.0041
[32] PEMS Testing – Portable Emissions Measurement Systems (horiba.com).
[33] Pielecha J, Skobiej K, Kurtyka K. Exhaust emissions and energy consumption analysis of conventional, hybrid, and electric vehicles in real driving cycles. Energies. 2020;13(23): 6423. https://doi.org/10.3390/en13236423
[34] Savitzky A, Golay MJE. Smoothing and differentiation of data by simplified least squares procedures. Anal Chem. 1964;36(8):1627-1639. https://doi.org/10.1021/ac60214a047
[35] Sedgwick PM. Spearman's rank correlation coefficient. BMJ Brit Med J. 2014;3497327. https://doi.org/10.1136/bmj.g7327
[36] Semtech-DS On Board Vehicle Emissions Analyzer (2010). User Manual. Document: 9510086, Revision: 2.01.
[37] TSI 3090 EEPS™ (Engine Exhaust Particle Sizer™), User Manual (2008).
[38] Wang Z, Wu P, Yu N, Zhang Y, Wang Z. Analysis of the influence of RDE test data processing methods on the emission results of China 6 light duty vehicles. E3S Web Conf. 2021;268:01022. https://doi.org/10.1051/e3sconf/202126801022
[39] Worldwide emission standards (2021/2022). Passenger cars and light duty vehicles. Delphi. Innovation for the real world.

Adam Sordyl, MEng. – researcher in the Engine Research Department, BOSMAL Automotive Research & Development Institute Ltd. in Bielsko-Biała, Poland.
e-mail: *adam.sordyl@bosmal.com.pl*

Prof. Zdzisław Chłopek, DSc., DEng. – Institute of Environmental Protection – National Research Institute, Poland.
e-mail: *zdzislaw.chlopek@kobize.pl*

Prof. Jerzy Merkisz, DSc., DEng. – Faculty of Civil and Transport Engineering, Poznan University of Technology, Poland.
e-mail: *jerzy.merkisz@put.poznan.pl*

Article citation info:
Górzyńska M, Pielecha I. Numerical investigation of pre-chamber holes diameter geometry on combustion parameters in a hydrogen-powered Turbulent Jet Ignition engine. Combustion Engines. 2024;199(4):126-139. https://doi.org/10.19206/CE-193950

Marcelina GÓRZYŃSKA
Ireneusz PIELECHA

Combustion Engines
Polish Scientific Society of Combustion Engines

Numerical investigation of pre-chamber holes diameter geometry on combustion parameters in a hydrogen-powered Turbulent Jet Ignition engine

ARTICLE INFO

Received: 25 June 2024
Revised: 13 September 2024
Accepted: 30 September 2024
Available online: 11 October 2024

The search for substitutes for conventional fuels leads to the use of non-hydrocarbon fuels or synthetic fuels. One of them is hydrogen. The use of hydrogen in combination with a two-stage charge formation system leads to the combustion of lean (λ > 1) or very lean (λ > 3) charges. The simulation tests carried out were aimed at determining the best configuration of the chamber connecting the pre-chamber with the main combustion chamber. Three variants of the diameter of the holes connecting the chambers were selected (d = 0.5; 1.0 and 1.5 mm) in combination with different fuel doses fed to the pre-chamber. A passive chamber (qo_PC = 0 mg) and an active chamber (qo_PC = 0.4 and 1.2 mg) were used with a constant fuel dose to the main chamber (qo_MC = 6 mg). The research was conducted using AVL Fire 2022.1 software using the moving mesh of the LDV engine. Based on the simulation work, the most favourable conditions for conducting the process were determined, taking into account the thermodynamic effects of the process and acceptable levels of nitrogen oxide concentration. The resulting correlation maps of chamber hole sizes and fuel doses supplied to the pre-chamber can serve as a preliminary basis for selecting control options for hydrogen combustion in the TJI system.

Key words: *hydrogen combustion, Turbulent Jet Ignition, pre-chamber, thermodynamic parameters, CFD research*

1. Introduction

In the context of growing environmental concerns and the finite nature of fossil fuel resources, the quest for alternative fuels have become a pivotal focus in the field of automotive and energy engineering. Traditional fossil fuels, while efficient and energy-dense, contribute significantly to greenhouse gas emissions and air pollution, exacerbating climate change and posing serious public health risks. To mitigate these adverse effects, researchers and engineers are increasingly exploring sustainable and cleaner fuel options.

Among the various types of alternative fuels, compressed natural gas (CNG), hydrogen, and ethanol have emerged as prominent contenders. Each of these fuels offers unique advantages and challenges, making them subjects of extensive study and development. CNG, primarily composed of methane, is a cleaner-burning alternative to gasoline and diesel, producing fewer carbon emissions and particulates. Hydrogen, on the other hand, stands out for its potential to produce zero emissions when used in fuel cells or internal combustion engines, emitting only water vapor as a byproduct. Ethanol, derived from biomass, presents a renewable option that can be integrated into existing fuel infrastructures with relative ease.

This study focuses specifically on hydrogen as a fuel, due to its high energy content per unit mass and its potential to significantly reduce the carbon footprint of transportation. The utilization of hydrogen in internal combustion engines (ICEs) and fuel cells represents a promising pathway toward achieving near-zero emissions. However, the adoption of hydrogen-powered engines requires a comprehensive understanding of its combustion characteristics, efficiency, and associated technical challenges.

It is projected [37] that the global market for hydrogen-powered internal combustion engines will reach $35 billion by 2030 and approximately $89 billion by 2040, with a Compound Annual Growth Rate (CAGR) of 9.78% during the forecast period of 2030–2040 (Fig. 1). Hydrogen-powered internal combustion engines (usually modified versions of traditional gasoline engines) will be essential for vehicle propulsion. These engines, utilizing new technologies (e.g., two-stage combustion – TJI), can offer near-zero emissions while simultaneously promoting the development of hydrogen infrastructure worldwide.

The major players operating in the hydrogen combustion engine market are Honda, Toyota, Komatsu, JCB, BMW, MAN and others. The market for hydrogen internal combustion engines is rapidly growing due to swift research and development, as well as the use of hydrogen as a clean fuel. This growth is further driven by an increasing number of government initiatives aimed at promoting the use of fuel cell vehicles, which in turn fuels the market for hydrogen internal combustion engines.

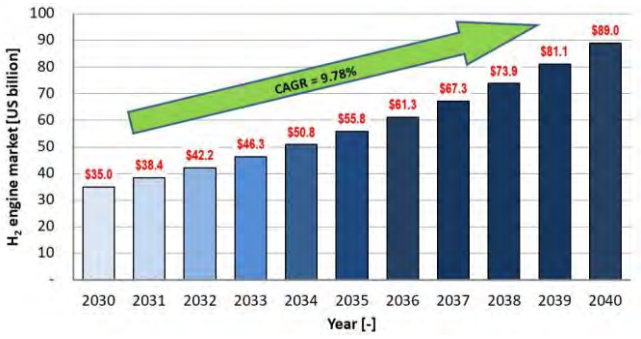

Fig. 1. Hydrogen combustion engine market (US billion) [37]

Due to its geographical position, North America is expected to have a significant share in the market for hydrogen-powered internal combustion engines in the upcoming

timeframes. This is driven by increasing investments in research and development aimed at creating cutting-edge solutions and meeting end-user requirements. Additionally, U.S. government programs promoting eco-friendly energy sources are fostering market expansion across the region. Although hydrogen internal combustion engines are still in the early stages of development, policymakers are encouraged to support their adoption due to the adverse effects of CO_2 emissions in both industrialized and developing countries, such as the United States and China. The European government has called on manufacturers to reduce CO_2 emissions in new road vehicles by approximately 30% starting in 2030. Similar emission reduction targets have been set by the United States and China.

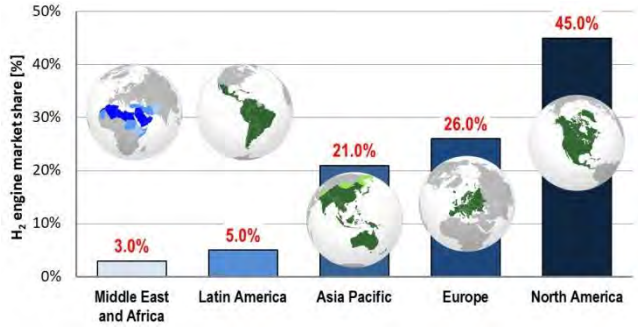

Fig. 2. Hydrogen combustion engine market share by region (in %) [37]

The hydrogen-powered internal combustion engine market is expected to experience the highest growth in the Asia-Pacific region during the forecast period (Fig. 2). This growth is driven by the expansion of key market players in the region and rising fuel prices, which will propel market development in the coming years.

Germany, the Netherlands, Poland, Italy, France, Spain, the United Kingdom, and Belgium are the eight largest hydrogen producers [45] in Europe (Fig. 3). These countries account for 74% of hydrogen produced through reforming processes, 83% of hydrogen generated as a by-product, 65% of hydrogen produced via water electrolysis, and nearly 100% of hydrogen produced through reforming combined with carbon capture.

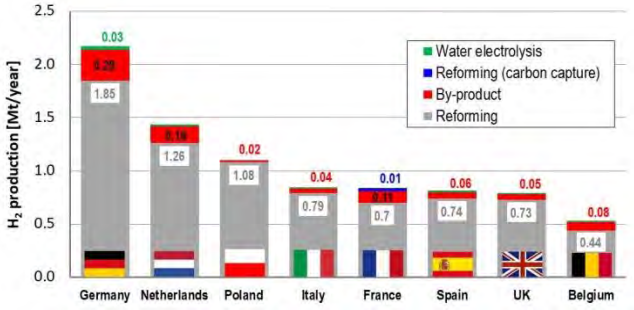

Fig. 3. Top 8 EU countries in terms of hydrogen production capacity by production process [45]

2. Hydrogen combustion engines

2.1. Hydrogen combustion with MPI and DI

The combustion of gaseous fuels (CH_4 and H_2) in internal combustion engines (SI and CI) primarily offers the potential to reduce the emissions of toxic exhaust components (Table 1). Moreover, these fuels can be relatively easily utilized in dual-fuel engine systems, significantly enhancing their potential for combustion or co-combustion. A comprehensive comparison of dual-fuel engines (powered by gasoline or diesel with hydrogen) was presented by Algayyim et al. [1]. Many examples pertain to typical CI engines and the addition of hydrogen up to 100%.

Table 1. Differences in the properties of low- and zero-emission fuels [2, 4, 9, 11, 13, 15, 22, 24, 30, 31, 47, 51]

Parameter	CNG	H_2 (Hydrogen)	Ethanol
Chemical composition and source	The dominant component is methane (CH_4)	The simplest element, produced by electrolysis, steam methane reforming, or biomass gasification	Ethyl alcohol, produced by fermentation of plants (corn, sugarcane)
Emissions and environmental impact	CO_2 emissions are about 53.1 kg/GJ, NO_x emissions are 90% lower than CI engines, and particulate emissions are 98% lower	No CO_2 emissions; emissions during hydrogen production depend on the method (e.g., electrolysis can be zero if renewable energy is used)	CO_2 emissions are about 70% lower than gasoline; NO_x emissions may be higher than gasoline
Calorific value	~50 MJ/kg	~120 MJ/kg	~27 MJ/kg
Efficiency in internal combustion engines	About 20–25% (like gasoline)	FC: about 50–60% ICE: about 30–40%	About 30–35%
Infrastructure cost	Relatively small	High (especially for storage and distribution)	Small (can be mixed with gasoline and use existing infrastructure)
Number of stations	Medium (developing)	Low (developing)	High (in countries with developed biofuel production)
Production cost	~4–5 USD/GJ	2–6 USD/kg (steam methane reforming), 4–5 USD/kg (electrolysis from renewable sources)	0.5–1 USD/dm^3 (biomass)
Operating cost	Relatively low due to lower fuel costs	High due to production and infrastructure costs	Higher than gasoline due to lower calorific value
Safety	Flammable gas under high pressure, requires appropriate tanks and safety systems	Highly flammable, stored under high pressure or cryogenically, requires special precautions	Less flammable than gasoline, but still requires appropriate safety measures
Research comparison of engines	Engines must be specially adapted for natural gas combustion	High material requirements for high temperatures and combustion control	Can operate on ethanol with minor modifications compared to gasoline engines
Combustion process simulation comparison	Indicates lower exhaust emissions compared to conventional CI and SI engines	High energy efficiency and no CO_2 emissions	Better efficiency than gasoline, but higher NO_x emissions

The laminar combustion speeds of methane and gasoline at $\lambda = 1$ obtain quite similar values (about 0.5 m/s) [6]. However, hydrogen under similar conditions achieves a laminar combustion rate approximately 10 times higher. The high flameability range, the very low ignition energy, and the high laminar flame speed make hydrogen produce a fast and short combustion event, fulfilling the requirements of an almost ideal combustion process – the isochoric combustion.

Direct injection of hydrogen increases the possibility of its combustion and at the same time increases the thermal efficiency of the process. Research by Wang et al. [49] indicate an efficiency value of 43.1% (in a turbocharged engine) with a compression ratio of approximately 14.5 (at $\lambda = 1.7$).

2.2. Fuel combustion in TJI

The two-stage combustion process increases the possibility of burning lean charges by using multi-point ignition and the possibility of effective ignition of the charge in the pre-chamber [56]. Positive results of methane combustion in an engine fueled with CH_4 are obtained in the range of lean fuel combustion (up to $\lambda = 2.2$) [35, 55, 58]. The combustion of CH_4 with hydrogen supplied to the pre-chamber causes the combustion of ultra-lean charges with $\lambda = 5.2$ [55] (Table 2).

Hydrogen combustion in engine systems concerns excess air coefficients ranging up to 2.0 (conventional system) [12, 32, 38] and up to 4 (with TJI system) [5, 34].

Ammonia is increasingly used in combustion engines (up to 0.1 m/s at $\lambda = 1.0$) [56]. The limitation of using only ammonia as a fuel is the very low laminar combustion rate. For this reason, dual-fuel systems are becoming more and more common in the TJI system.

There are many solutions for co-combustion of fuels using a two-stage combustion system (PC–MC): hydrogen-methane [26, 55]; hydrogen-ethanol [40, 41]; hydrogen-methanol [33]; hydrogen-diesel fuel [27, 28]; hydrogen-ammonia [17, 50 56, 57] or mixtures [18, 43]. All of them are based on the large flammability range of hydrogen and its high combustion rate, which ultimately leads to the combustion of lean or ultra-lean charges.

2.3. The influence of the geometry of the pre-chamber on fuel combustion

The pre-chamber, which is characterized by a specific volume, number and size of flow channels and their method of connection with the main chamber, has a significant impact on the initial quality of the combustion process (Table 2).

Aoyagi et al. [3], in experimental and simulation studies of CH_4 combustion, indicate that increasing the diameter of the holes reduces the flame outflow speed and, at the same time, increases the flame torch cone angle. Increasing the length/diameter ratio (L/D) also increases the discharge velocity but decreases the flame cone angle. An increase in the number of holes (with an almost unchanged flow surface area) indicates a limitation of the outflow speed with a large number of holes (10 pcs.). Despite such changes, the flame torch cone angle remained practically unchanged (the diameters were 4.0, 3.5, and 3.1 mm, respectively).

Research conducted by Jeelan Basha et al. [20] concerned the process of analyzing CH_4 combustion in RCM with a variable diameter of the single outlet hole of the pre-chamber (up to 1 to 4 mm). It was found that changes in the combustion process (at $\lambda = 2.5$) were observed only with a large hole diameter (4 mm), characterized by a limited combustion pressure. The highest HRR value was observed at d = 3 mm. Increasing the hole diameter resulted in a delay in the pressure increase after ignition. The analysis of flame angles indicates that they increase when the diameter of the holes increases (similar results were obtained in research [3]).

The use of different geometries of pre-chambers (6 variants) was analyzed in experimental engine tests [35] when powered by variable gas. It was found that multi-parameter optimization shows the best effects of using a pre-chamber containing both radial and radial holes (similar hole configurations were also studied in [14]). The research was carried out in terms of exhaust emissions and indicated engine efficiency with a variable fuel dose fed to the pre-chamber. The values of the excess air coefficient were in the range of $\lambda = 1.32–1.65$, at n = 1500 rpm and IMEP ~7 bar.

Simulation studies [25] on methane feeding in the range of changing the hole diameter (from 1.4 to 2.2 mm) indicate that the best solution in terms of combustion pressure and HRR is the value of 1.6 mm.

Guo et al. [14] found that during methane combustion, changing the diameter of the holes from 2.6 to 1.3 almost doubles the flow velocity of the torch (from 220 to 140 m/s) and increases the pressure difference in both chambers from 0.13 to 0.16 MPa.

The diameter of the discharge holes has less impact on the hydrogen combustion process. Research conducted by Liu et al. [26] indicates much greater differences in combustion pressure when using an active or passive chamber than when changing the hole diameter from 2 to 3 mm. When using a passive system, combustion at $\lambda = 3$ and higher causes a slow process. With an active system, this situation occurs only when $\lambda = 5$.

Motor research conducted by Tomić et al. [46] (when powered by gasoline) confirmed that the indicated efficiency data showed that a larger orifice area (OA) or larger orifice diameter at constant pre-chamber volume and orifice number is more favorable regarding the indicated efficiency.

The selection of the ammonia combustion chamber focuses on much smaller differences in the variants of the individual sizes of the pre-chamber. Research by Cui et al. [10] concerned changes in λ the range 1.0–1.4. The influence of the volume of the pre-chamber is significant in the range of lean loads (the greater the leanness, the more delayed combustion in a smaller volume, at a similar level of maximum pressure). Similarly to the combustion of methane, increasing the diameter of the holes when burning ammonia (from 2 to 3 mm) increases the range of the burning torches (by over 100%).

Simulation analysis of the angle of rotation of the discharge holes during gasoline combustion indicates that the degree of charge swirl is very important [16]. Straight channels do not show swirl, but turning the outflow by 30 degrees causes the swirl ratio to reach a value of 10. The tests showed that the highest HRR values were obtained when the holes were turned by an angle of 25 degrees, which resulted in SR = 8.

Table 2. Examples of solutions for the geometry of the initial combustion chamber (with the number of holes greater than 1)

No.	Reference	Volume PC [cm^3/% vol.]	No. × diameter	Fuel	Type of engine	Pre-chamber
1	Brunel University [7] (2019)	1.0/1.27% at TDC	6 × 1.25 mm	gasoline, Et	optical engine	active
2	University of Naples [5] (2024)	1.9/0,3%	6 × 1.15 mm	gasoline	simulation	active
3	University of Zagreb [46] (2023)	2.4/4.07% at TDC	6 × 1.30 mm	gasoline	engine	active
4	Marquette University [54] (2024)	2.0/1.94% at TDC	2 × 2.3 mm	E10-E90	simulation	active
5	Sandia National Laboratories [39] (2021)	4.66	8 × 1.6 mm (angle 130 deg)	Natural gas (95% CH_4)	optical engine	active
6	KAUST [44] (2021)	5.07/2.5% at TDC	2 row × 6 × 1.5 mm (angle 134 deg)	CH_4	optical engine	active
7	ETH [53] (2019)	1.0	4 × 1.2 mm (angle 120 deg)	CH_4	RCEM	passive
8	Shanghai Jiao Tong University [21] (2020)	–	6 × 2.9 mm	CH_4	CVC	active
9	PUT [35] (2019)	1.826/0.35% at TDC	7 × 1.5 mm (radial) + 3 × 1.4 mm (axial)	CH_4	engine	active
10	Kyushu University [3] (2024)	2.3%	10 × 3.1 mm	CH_4	CVC	passive
11	EMPA [43] (2020)	1.8/0.5% at TDC	7 × 1.5 mm	CH_4/HCH_4	engine	active/passive
12	Beijing Institute of Technology [52] (2018)	1.5	6 × 1.0 mm	H_2	CVC	active
13	PUT [36] (2024)	2.29/0.45% at TDC	6 × 1.5 mm	H_2	engine	passive
14	Shanghai Jiao Tong University [57] (2024)	–	6 × 1.4 mm (angle 140 deg)	H_2 (PC) NH_3 (MC)	simulation	active
15	Universidade Federal de Minas Gerais [40] (2019)	0.88/2.2% at TDC	4 × 1 mm (angle 45 deg) + 1 × 2 mm (axial)	H_2 (PC) Et (MC)	engine	active/passive

3. Purpose and scope of engine research work

The aim of the research is to determine the thermodynamics of the hydrogen combustion process, considering geometric changes in the flow channels and the variable fuel dose fed to the pre-chamber. Such control allows (1) to change the use of the pre-chamber from passive to active, (2) to change the thermodynamics of hydrogen combustion, (3) to change the amount of inter-chamber flows of the charge and to simultaneously change the fuel-air ratio in the pre-chamber. The size of the dose administered to the pre-chamber slightly changes the global value of the excess air coefficient, but significantly defines this value in the pre-chamber.

4. Research methodology

4.1. Research object

Simulation tests were carried out using AVL Fire 2022.1 software. A movable combustion chamber mesh was used (Fig. 4) with the parameters presented in Table 3. The mesh represents the combustion chamber of the cylinder with a displacement of 510.7 cm^3. The mesh consists of a pre-chamber, a main chamber, and outflow holes. The mesh is divided into sections that represent the elements of the moving mesh.

The authors used the combustion chamber without considering the engine's intake and exhaust channels due to the simplicity of the model and the implementation of direct fuel injection. This approach appears in many publications [19, 21, 29]. The conditions for starting the compression process correspond to the conditions of the research engine, so the representation of a typical combustion engine has been preserved.

Figure 5a shows the location of the injector. Due to the lack of engine intake and exhaust channels (the model considers only the closed space of the cylinder), fuel injection into the main chamber was carried out by placing the injector

Table 3. Combustion chamber and mesh parameters

Parameter	Unit	Value
S	mm	90
D	mm	85
V_{cyl} (TDC)	cm^3	557
V_{cyl} (BDC)	cm^3	47,2
V_{PC}	cm^3	1.61
Max number of cell (TDC)	–	32 k
Max number of cell (BDC)	–	138 k
Surface cell size (min)	mm	0.2

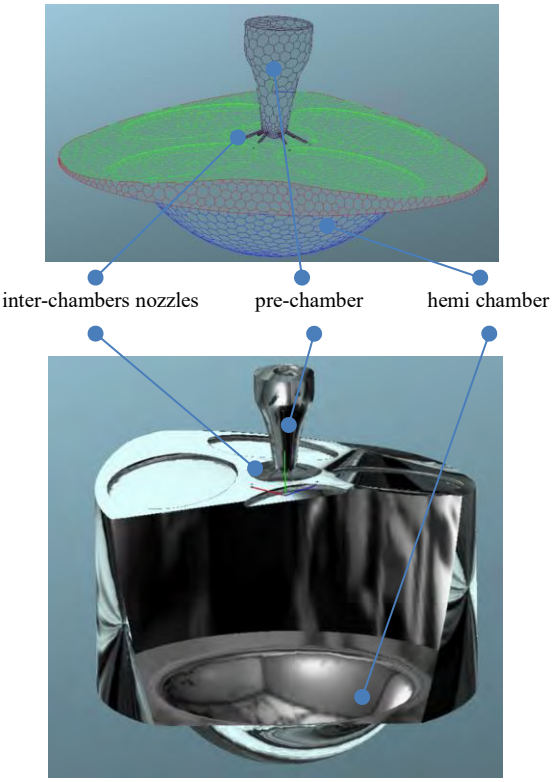

Fig. 4. View of the combustion chamber with elements marked

at an angle between the valves. Fuel was injected into the pre-chamber with a vertically placed injector next to the spark plug (Fig. 5b). This location of the injector may cause some of the gas to enter the main chamber. The angularly placed injector in the main chamber causes the gas to mix with the air, whose Turbulent Kinetic Energy (TKE) is initially 10 m^2/s^2. The fuel injection start time was set at 550 deg. The end of injection was simulated at an angle of 600 deg. An angular time of 50 deg was set for both combustion chambers, primary and main (at n = 1500 rpm, the injection duration is approximately 5.55 ms). The initial values enable fuel injection at low pressure (in the works [32, 36], such injection was carried out at a pressure of 3–7 bar). The ignition angle for all cases was set at 711 deg (9 deg bTDC). This ignition angle prevents the maximum combustion pressure from occurring too early and heat release around 5–10 deg aTDC.

a) b)

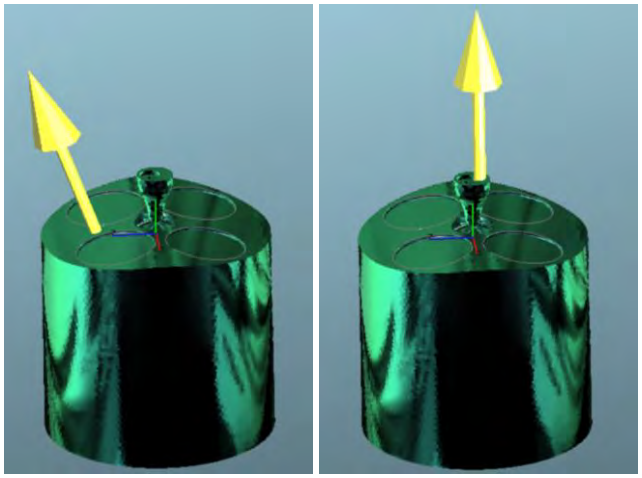

Fig. 5. View of the combustion chamber with the location of the injector marked: a) in the main chamber; b) in the pre-chamber

4.2. Research methodology

Combustion process tests were carried out in the range from 540 to 800 deg CA. It was assumed that the beginning of the cycle begins at an angle of 360 degrees. This is since it is possible to analyze the valve coverage from the previous calculation cycle. For this reason, TDC (hot) is at 720 deg. The boundary conditions are included in Table 4. These conditions apply to low boost pressure (which results from the assumed intake pressure value). It is sufficient to achieve a high charge depletion in the engine's main combustion chamber (MC).

Table 4. Boundary conditions

Parameter	Value
Pressure	100 000 Pa
Density	1.19 kg/m^3
Temperature	293.15 K
Turb. kin. energy (TKE)	0.001 m^2/s^2
Turb. length scale	0.001 m
Turb. diss. rate	0.00519616 m^2/s^3

The combustion process was analyzed using the models included in Table 5. A typical value of rotational speed was assumed (n = 1500 rpm). The combustion module in the form of the Turbulent Flame Speed Closure Model [23] was used. The essence of this model is the determination of the reaction rate based on an approach depending on parameters of turbulence, i.e., turbulence intensity and turbulent length scale, and of flame structure like the flame thickness and flame speed [23, 48].

Model k-epsilon usually yields reasonably realistic predictions of major mean-flow features in most situations. It is particularly recommended for a quick preliminary estimation of the flow field or in situations where modeling other physical phenomena, such as chemical reactions, combustion, radiation, and multi-phase interactions, brings uncertainties that outweigh those inherent in the k-ε turbulence model.

Table 5. Simulation parameters

Run mode	Crank angle
Start angle	540 deg
End angle	800 deg
Engine speed	1500 rpm
Min/max iteration	5/20
Module activation	Species transport
	Combustion (Turbulent Flame Speed Closure Model)
	Emission (Extended Zeldovich)
	Spray
Turbulence model	k-epsilon
Wall treatment	Hybrid Wall Treatment
Heat transfer wall model	Standard Wall Function

The tests were carried out according to a 3 × 3 matrix, including different diameters of the pre-chamber holes (0.5, 1.0, and 1.5 mm) along with different doses of fuel fed to the pre-chamber. Fuel doses with values 0, 0.4, and 1.2 mg were adopted to achieve combustion with a passive chamber (qo_PC = 0 mg) and an active chamber (qo_PC > 0 mg).

5. Analysis of the influence of geometry and fuel dose on the combustion process

5.1. Analysis of fast-varying processes

Cylinder pressure

Tests on the compression pressure and combustion of hydrogen were carried out in a closed combustion chamber (charge exchange was not analyzed). The modeled sections of the moving mesh allowed for the assessment of the pressure in the pre-chamber (PC) and main chamber (MC). Small holes in the pre-chamber (d = 0.5 mm – Fig. 3a) cause significant attenuation of the pressure in the pre-chamber. At the ignition angle (711 deg), the pressure values are 20.7 bar (PC) and 32.0 bar (MC), respectively. In this way, ΔP = 11.3 bar pressure difference is obtained. The significant difference in pressure in PC compared to MC causes the combustion process in PC to be very violent. This means that the charge is close to the stoichiometric charge. The smallest hole diameters cause the maximum pressure in the MC to be the lowest in all analyzed solutions. Despite this, the pressure in PC is higher than in MC and is achieved at a much larger angle. The difference is up to 5 deg (with a passive chamber – Fig. 6a). This means that the small flow holes significantly eliminate the flow of flames into the main chamber. They are probably also ex-

tinguished on the walls of the holes, which may reduce the pressure in the main chamber.

Large hole diameters mean that a larger part of the dose from the main chamber goes to the pre-chamber. This results in increased combustion pressures in the PC in the initial phase of the process.

This is the only case of such changes because increasing the diameter of the holes no longer causes such differences (Fig. 6b and 6c). Additionally, the combustion pressures overlap and are the same at the largest analyzed diameter. With hole diameters d = 1.0 and 1.5 mm, an increase in the combustion pressure in the PC is visible (a characteristic hump of the combustion process). The largest hole diameters result in the highest combustion pressures. This means that holes with a diameter of 1.0 mm and larger do not limit the flow of charge to the PC or the outflow of flames from the PC. Additionally, the flame does not go out, which increases the pressure in the main chamber. In relation to a large dose and large diameter, a characteristic increase in pressure in the PC is observed, indicating the violent nature of combustion (only in the case of the active chamber). Similar tests using alternating gas (d = 2.5; 3.0; 3.5 mm) [3] indicated a large range of burning torches for smaller hole diameters. However, these diameters were not the limit values for extinguishing the methane flame. In the work [46], it was found that increasing the diameter of the holes has a positive effect on the engine's IMEP.

Pre-chamber–main chamber flow characteristic

The magnitudes of the pressure difference in both chambers are shown in Fig. 7 When using holes with the smallest diameter (d = 0.5 mm), the largest pressure differences are observed in both chambers. The first signs of this are visible during fuel injection. This injection takes place in the range of 550–600 deg (in both chambers simultaneously). With minimal hole diameters, a significant pressure build-up in the PC is visible during injection (passive chamber). Increasing the dose to PC reduces the pressure difference (Fig. 7a). Increasing the diameter of the holes increases interchamber flows and at the same time reduces the pressure difference during fuel injection (Fig. 7b). With a diameter of d = 1.5 mm, the pressure difference is below 1 bar (Fig. 7c). Similar interchamber flow relationships are observed with diameters d = 1.0 and 1.5 mm. The course of the pressure difference curves is similar. The larger the holes, the smaller the pressure differences. It is worth noting that the largest differences concern the pressure moments after ignition. The greatest differences were noted at d = 1.5 mm and at a PC dose of 0.4 mg. This may mean that such a dose results in the best composition of the flammable mixture in the pre-chamber.

5.2. Analysis of average thermodynamic quantities

Temperature in the cylinder

The analysis of the temperature distribution in both combustion chambers is presented in Fig. 8. According to the large pressure differences at d = 0.5 mm, similar changes were recorded in terms of temperature changes. Fuel injection into the PC reduces the average temperature value before ignition. Using a passive chamber, 699°C was recorded in the PC before ignition. In the active chamber, this value decreased by over 60°C to 627–633°C. This means that when using small holes in the PC, throttling the flow not only limits the pressure in the main chamber but also greatly limits the temperature (Fig. 8a). No such tempera-

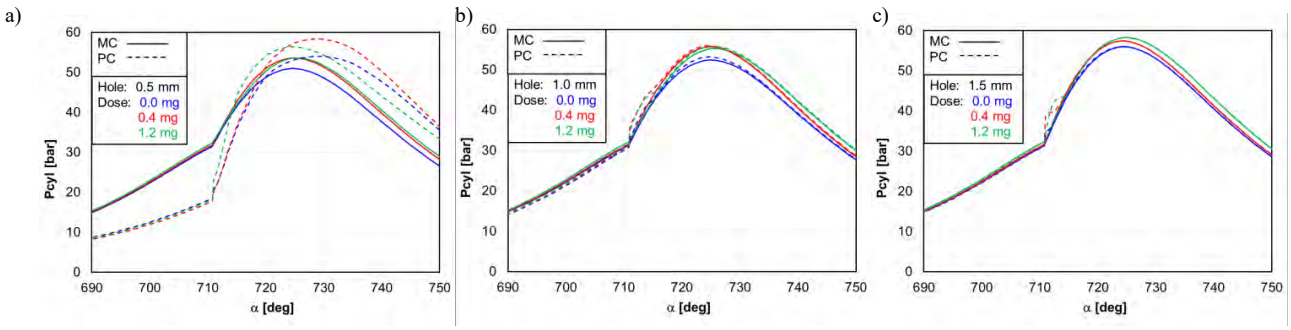

Fig. 6. Analysis of the pressure difference in the pre-chamber and main chamber with different configurations of the diameter of the outflow holes from the pre-chamber: a) 0.5 mm, b) 1.0 mm, c) 1.5 mm and different fuel doses

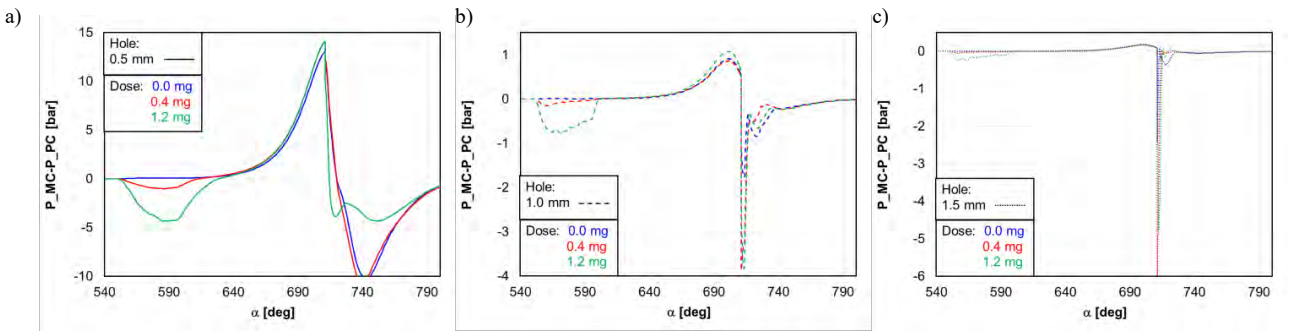

Fig. 7. Analysis of the pressure difference in the pre-chamber and main chamber with different configurations of the diameter of the outflow holes from the pre-chamber: a) 0.5 mm, b) 1.0 mm, c) 1.5 mm and different fuel doses

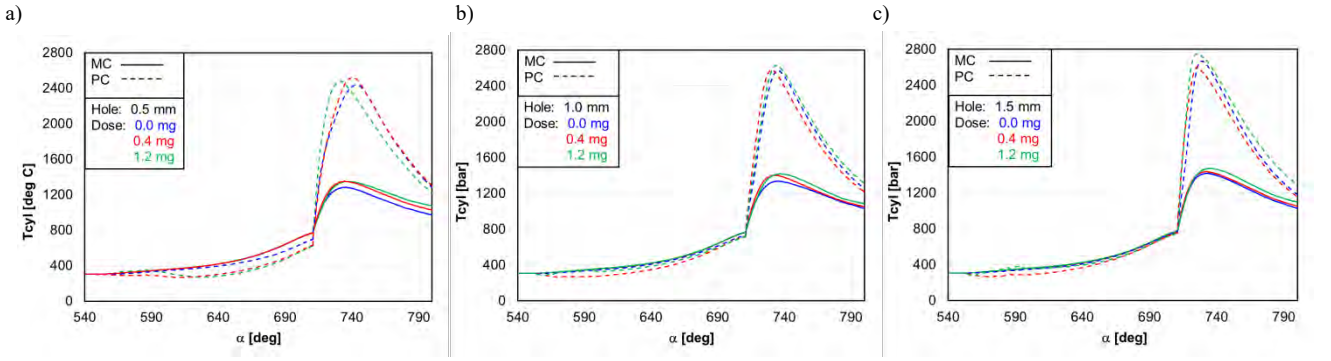

Fig. 8. Analysis of the temperature in the preliminary chamber (dashed line) and main chamber (solid line) with different configurations of the diameter of the outflow holes from the preliminary chamber: a) 0.5 mm, b) 1.0 mm, c) 1.5 mm and different fuel doses

ture changes were recorded for holes with a diameter of 1.0 and 1.5 mm. The differences are only due to fuel injection into the PC, which results in a slight temperature drop. However, until the moment of ignition, these values are equal (changes are below 3°C). As a result of the combustion process, which takes place in the pre-chamber at a much lower value of the excess air coefficient, much higher temperatures are observed. As the diameter of the holes increases, the maximum temperature values in the pre-chamber increase. This means increasing the uniformity of the charge in this chamber. There was also a slight but constant increase in the maximum temperature value in MC. This proves the greater dynamics of the flow of burning fuel flares (Fig. 8b and 8c).

Air-fuel ratio

The previously presented values also depend on the air-fuel ratio in both combustion chambers. The λ values in the pre-chamber are shown in Fig. 9a. The lack of fuel dose (qo_PC = 0 mg) results in significant differences in the formation of this value before ignition. Regardless of the diameter of the holes, the value of λ is approximately 0.4 units different (smaller) in the case of feeding the pre-chamber. Fuel injection into the PC causes λ to reach a value close to zero, which means that almost the entire chamber is filled with fuel. At the ignition angle (711 deg), the value of the excess air coefficient approaches the steady charge (the dose to PC was not previously selected, as a result of which λ = 1 was not obtained in the pre-chamber). The influence of the size of the holes and inter-chamber flows causes those changes in λ and the diameter of the holes do not have a fixed tendency. Analyzing data on Fig. 9a, it can be concluded that an almost stoichiometric charge was obtained at d = 1.0 and the highest dose of fuel to the pre-chamber (1.2 mg). In the absence of fuel fed to the PC, with the hole diameter d = 1.0 mm, the value of λ was also obtained close to the value of 1. Each other research case (regardless of the passive or active chamber caused the value of the excess air coefficient to be less than 1 (which meant the load rich in the pre-chamber). Injection of the fuel dose only into the main chamber resulted in a constant and fixed value of the excess air coefficient equal to 3.1 (regardless of the diameter of the holes (no PC participation in charge formation). With the pre-chamber active, a reduction in the excess air coefficient is observed to 2.9 and 2.6, respectively (Fig. 9b).

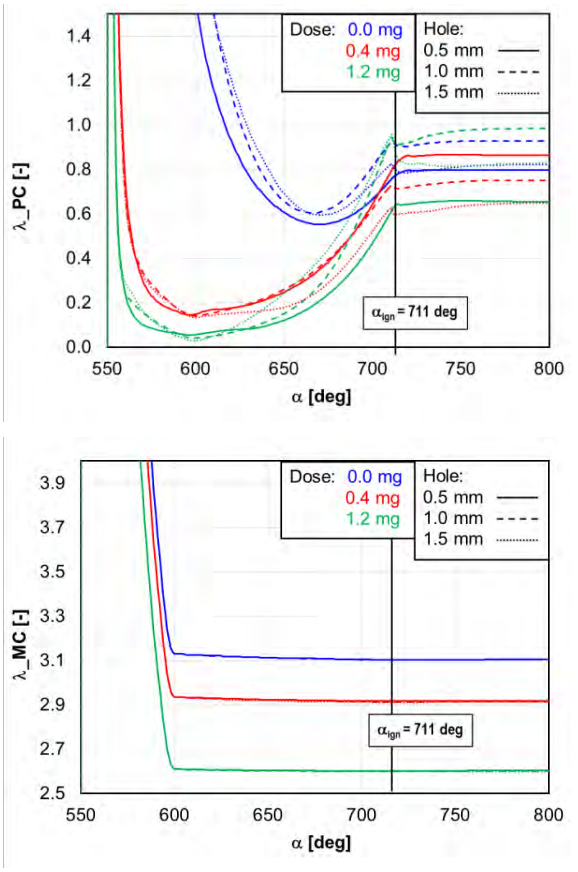

Fig. 9. Analysis of the excess air coefficient in the pre-chamber λ_PC (a) and in main chamber λ_MC (b) with different configurations of the diameter of the outflow holes from the pre-chamber and different fuel doses

As can be seen from the graphs in Fig. 6a, the diameter of the holes is significantly more important than the dose size in creating the final value of the excess air coefficient in the vicinity of the ignition angle. There is no clear relationship between the value of λ and the fuel dose and the diameter of the holes. With a high fuel dose, the lowest λ values were obtained with the average diameter of the holes, and with a dose of 0.4 mg – with the lowest λ. It follows that interventricular flows play an important role in the final value of λ in PC.

Heat release

The amount of released heat was considered separately in the preliminary and main chambers. Passive chambers (qo_PC = 0) with small hole diameters were characterized by a limited heat release rate, which results from the relatively slow growth of the curves (Fig. 10a). The largest amount of heat released in the PC (for a passive chamber) occurs at d = 0.5 mm and a dose of 0.4 mg. The highest Q value for all test cases was obtained with the highest dose to PC and the largest hole diameter. Increasing the dose to PC increases the maximum amount of heat released in this chamber. The decrease in heat in the PC is due to the flow of charge (and heat) into the main chamber. The combustion process in the pre-chamber is partially correlated with the heat release in the main chamber (Fig. 10b). The lowest amount of heat was recorded at d = 0.5 mm and the passive chamber. The highest amounts of heat were recorded with a large dose of fuel for the PC and a large diameter of the holes.

The combustion of fuel in the main chamber causes the amount of heat to increase with the dose to PC. The highest combustion rates in the MC were recorded with a large dose of fuel fed to the PC.

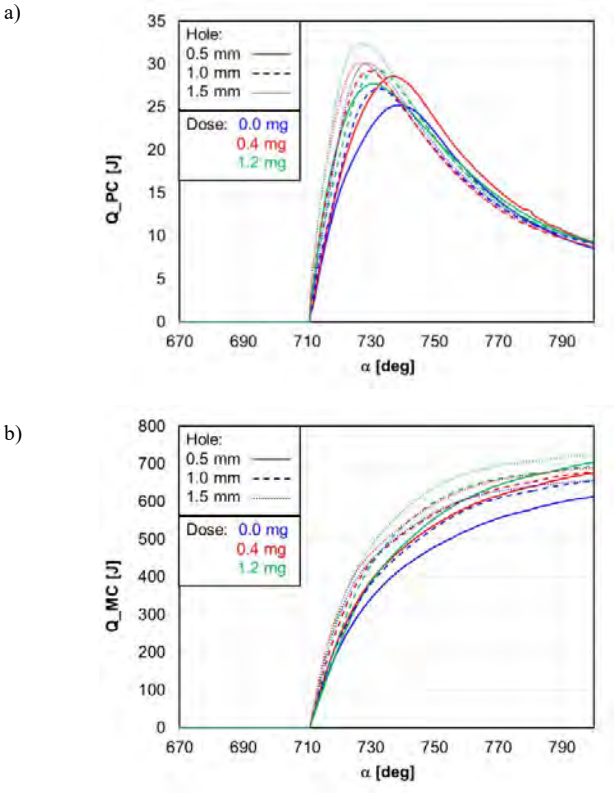

Fig. 10. Analysis of the amount of heat release in the pre-chamber Q_PC (a) and in main chamber Q_MC (b) with different configurations of the diameter of the outflow holes from the pre-chamber and different fuel doses

The increase in the amount of heat when increasing the dose to PC indicates an improvement in the combustion quality in MC and PC. Improving the combustion quality in PC also results in better combustion in MC. This is due to the fact that increasing the dose by 1.2 mg causes a maximum heat to increase of 144 J. The analysis of the best and worst course in Fig. 7b indicates differences of just over 100 J. Large analogies are also observed in the same waveforms in the pre-chamber (the same waveforms reach extremely different values).

NO formation

The amount of nitrogen oxides produced is closely related to the combustion conditions. Even though the maximum temperatures in PC are over 1000 K higher than in MC, the amount of NO produced is an order of magnitude lower than in MC (Fig. 11a and 11b). This is due to the duration of combustion in each chamber. Shorter combustion time in PC generates lower NO values. The lowest amounts of NO were recorded when the engine was powered by passive chambers. The molar fractions of NO in the pre-chamber are closely related to the dose size and the diameter of the holes (the larger the doses and hole diameters, the more NO). Regarding NO production, the diameter of the holes is more important than the amount of fuel dose fed to the PC (the highest initial intensity of NO formation is at large hole diameters). When analyzing the PC and MC chambers, a higher amount of NO was recorded in the main chamber (the difference is exactly 1 order of magnitude: 0.002 and 0.0002, respectively).

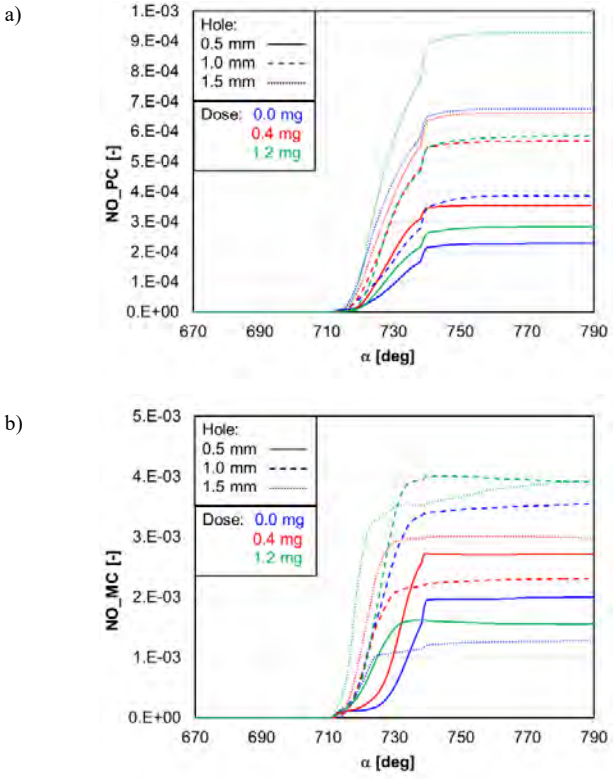

Fig. 11. Analysis of NO in the pre-chamber NO_PC (a) and in main chamber NO_MC (b) with different configurations of the diameter of the outlet holes from the pre-chamber and different fuel doses

5.3. Analysis of thermodynamic quantity distributions

The average values of thermodynamic indicators are now compared with instantaneous values. Hydrogen injection into the main chamber was simulated as direct injection. This has a large impact on the form of the created charge. Analysis of the distribution of the air-fuel ratio (Fig. 12) indicates a significant lack of uniformity of the load.

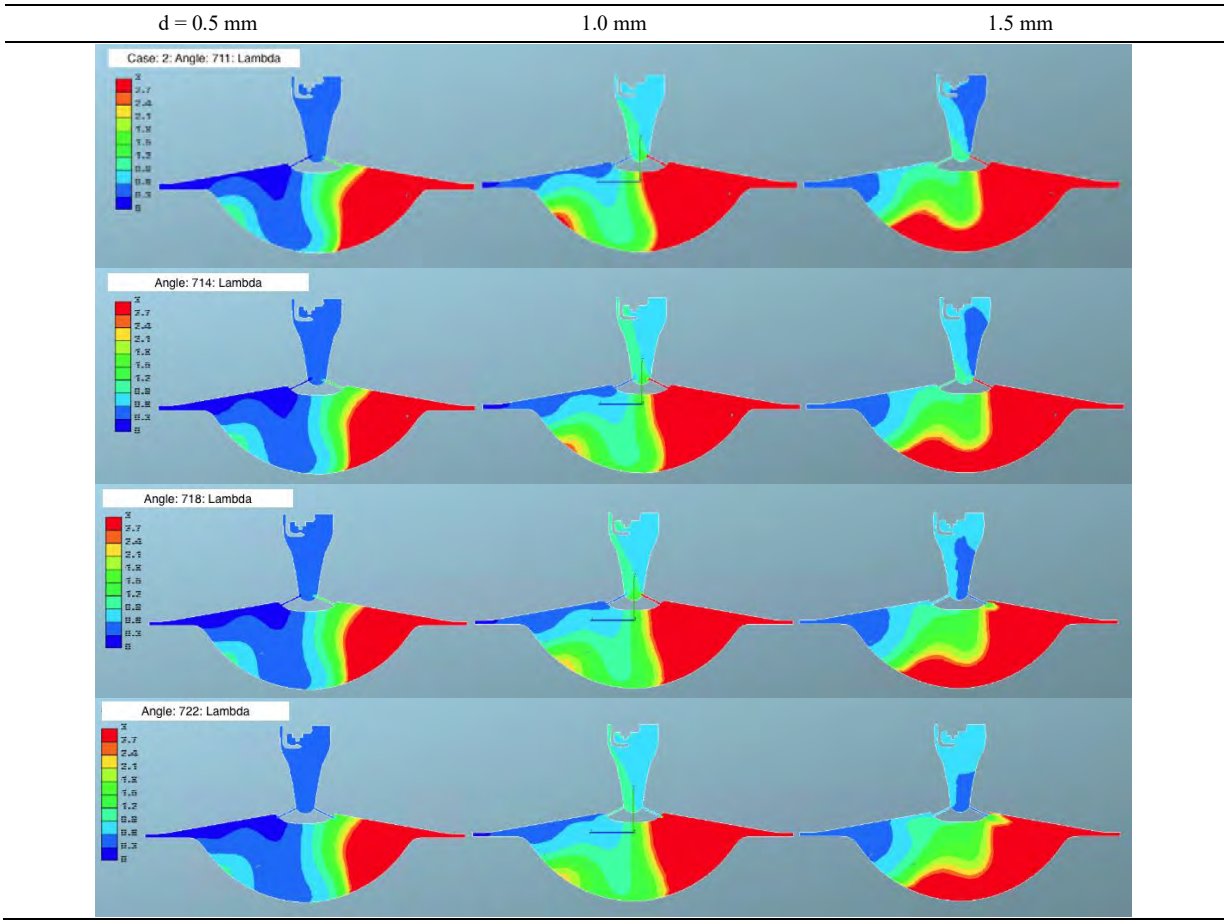

Fig. 12. Analysis of the distribution of the excess air coefficient in the pre-chamber λ_PC and main λ_MC with various configurations of the outflow hole diameter and a constant value of qo_PC = 0.4 mg

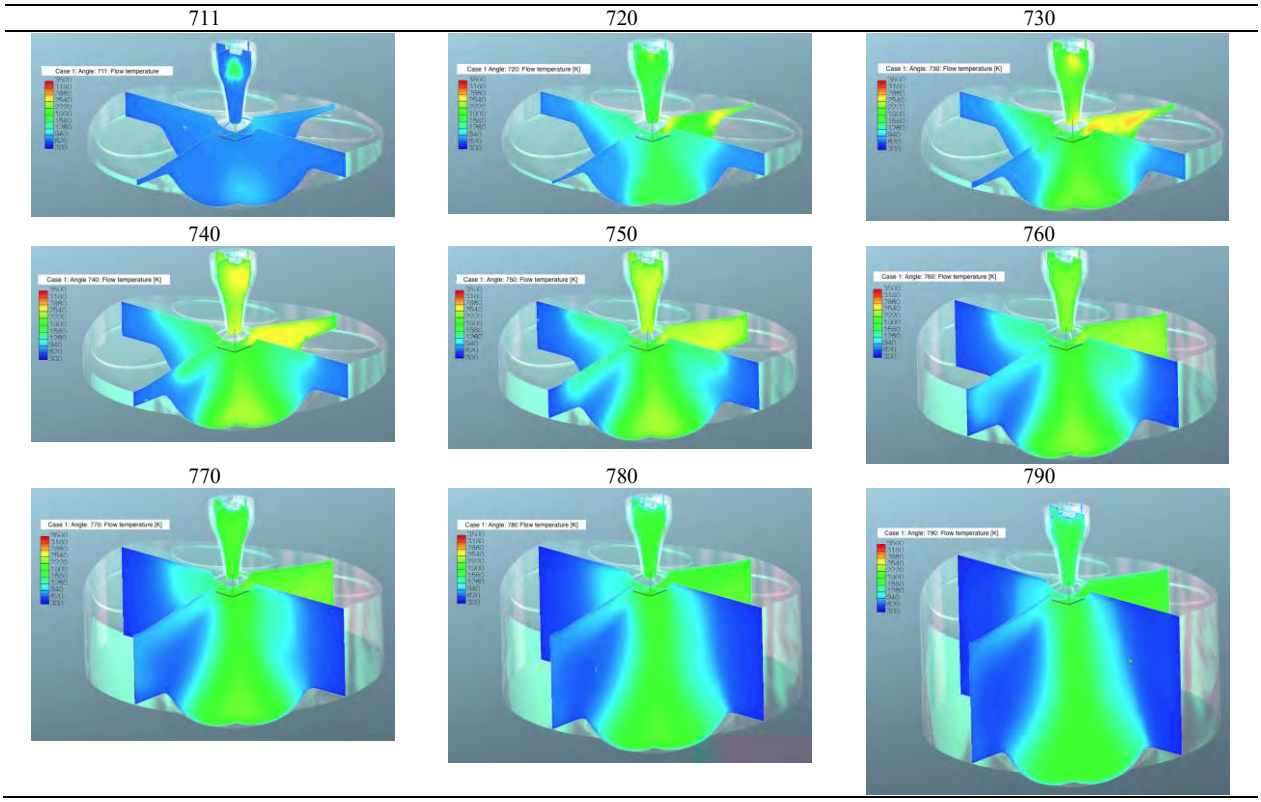

Fig. 13. Analysis of the temperature distribution in the preliminary chamber λ_PC and main λ_MC at d = 0.5 mm and qo_PC = 0 mg (passive chamber)

Due to the injection method (Fig. 5), a characteristic division of the MC chamber into two zones, rich and lean in fuel, was achieved. A similar relationship is observed in the pre-chamber. With a small hole diameter, the tendency of division and zones is dominant in the main chamber, and as the diameter of the holes increases, the division in the main chamber decreases and it increases in the pre-chamber.

Due to the uneven charge formation in both chambers, the combustion temperature distribution is also not the same (Fig. 13). At an angle of 740 deg, the maximum temperature is observed in the PC and MC chambers. These results are consistent with the data presented in Fig. 8, which concerned average values.

The analysis of the temperature distribution with the same dose to the PC (qo = 0.4 ms) is presented in Fig. 14. It shows that the large diameter of the holes facilitates the flow of charge into the PC, causing an increase in the temperature value in a small volume during ignition. The high temperature remains up to 720°C. Despite the large diameter of the holes and the average dose value, a large variation in the charge distribution in the main chamber is observed.

5.4. Maps of thermodynamic quantities

The solutions presented above regarding the analysis of average and instantaneous engine operation indicators enabled the construction of detailed maps. These maps were created in coordinates: hole diameter–fuel dose. Their structure makes it possible to initially determine the tendency of changes in engine operating indicators when one or another parameter is changed.

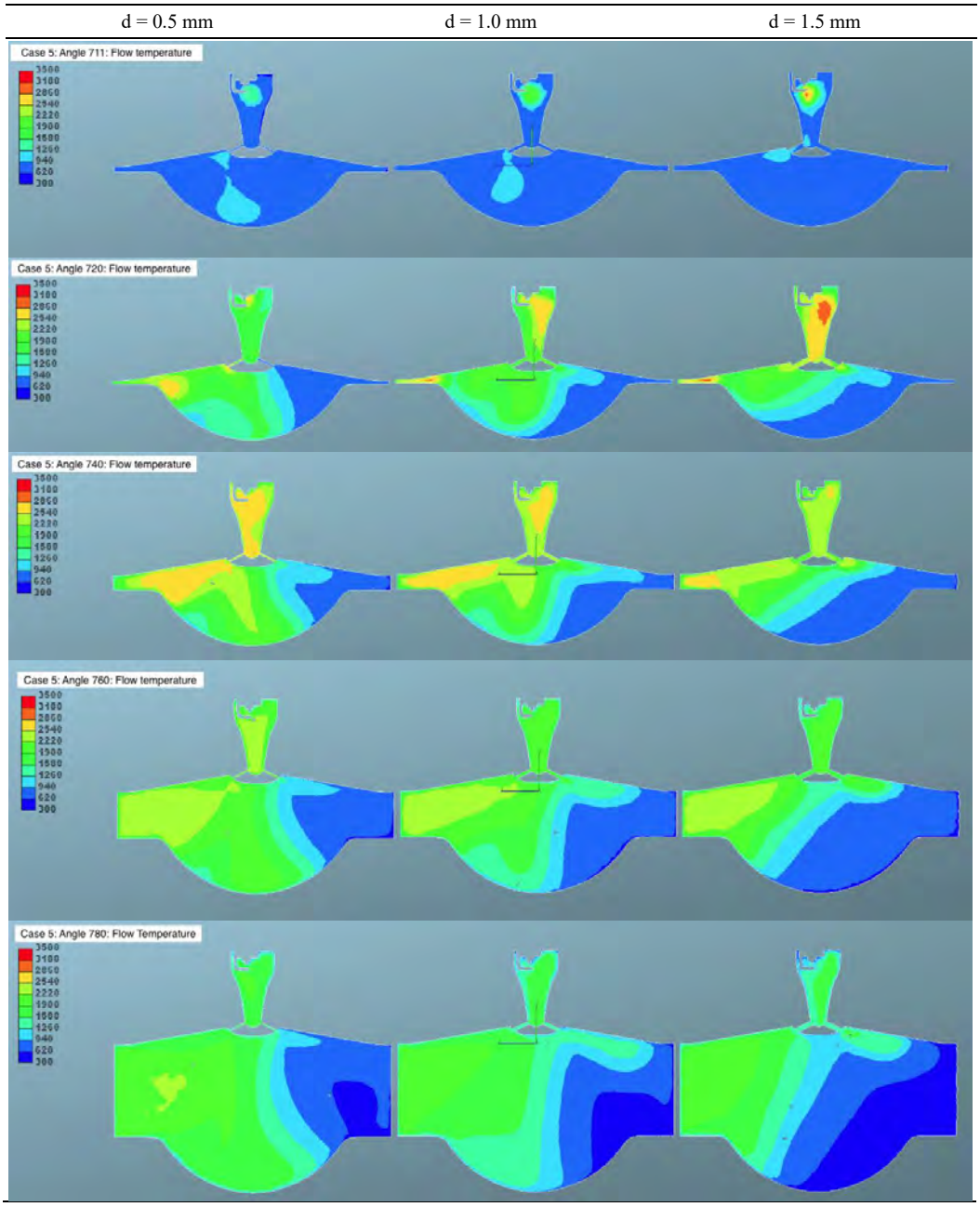

Fig. 14. Analysis of the charge temperature distribution in the cylinder with various hole diameter configurations and a constant fuel dose to the pre-chamber qo_PC = 0.4 mg

The analysis of the pressure distribution in the cylinder in both chambers (Fig. 15) only partially correlates with the amount of released heat. In the pre-chamber, these values are consistent only in the range of large doses to PC and large hole diameters. In the remaining parts of the map, small and medium doses and small hole diameters do not show any correlation. When comparing the main chamber, the correlations are even smaller; this may result primarily from the lack of uniformity of the created charge.

Similar conclusions were obtained when analyzing temperature and NO in both chambers (Fig. 16). In the pre-chamber, a high correlation of temperature and NO formation was obtained in all areas of the d–qo_PC map. The highest NO formation was recorded where the highest temperature was also observed. Unfortunately, this tendency does not occur in the case of the main compartment. As before, it may result from large charge heterogeneity. It follows that fuel injection directly into the cylinder should

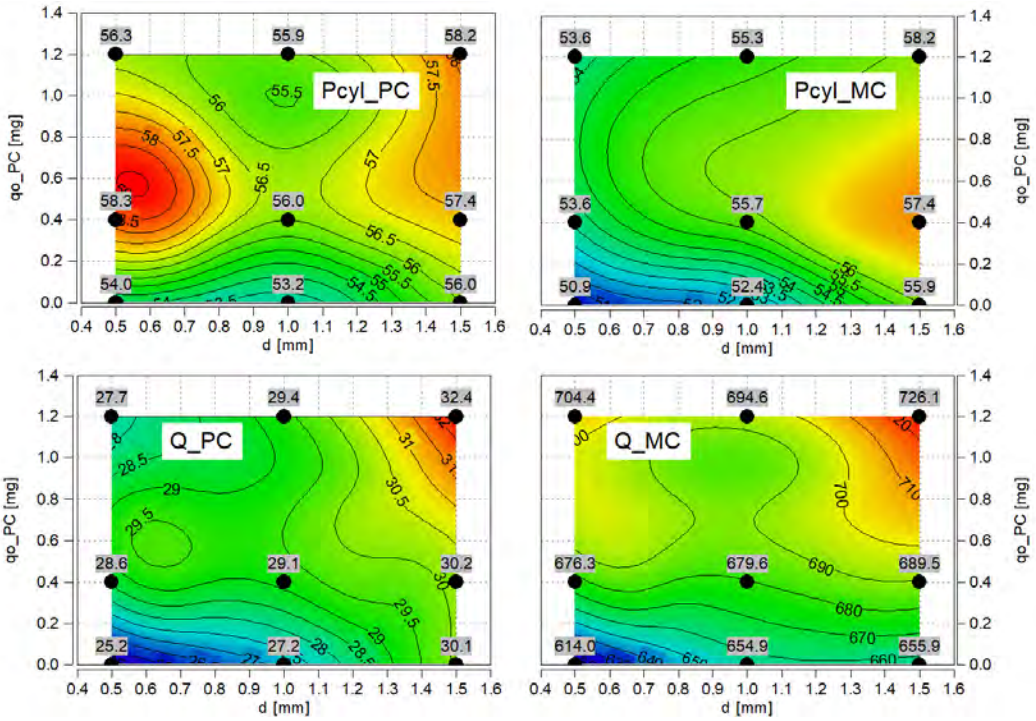

Fig. 15. Map of pressure changes in the cylinder and the amount of heat released in d–qo_PC coordinates: a) in the pre-chamber, b) in the main chamber

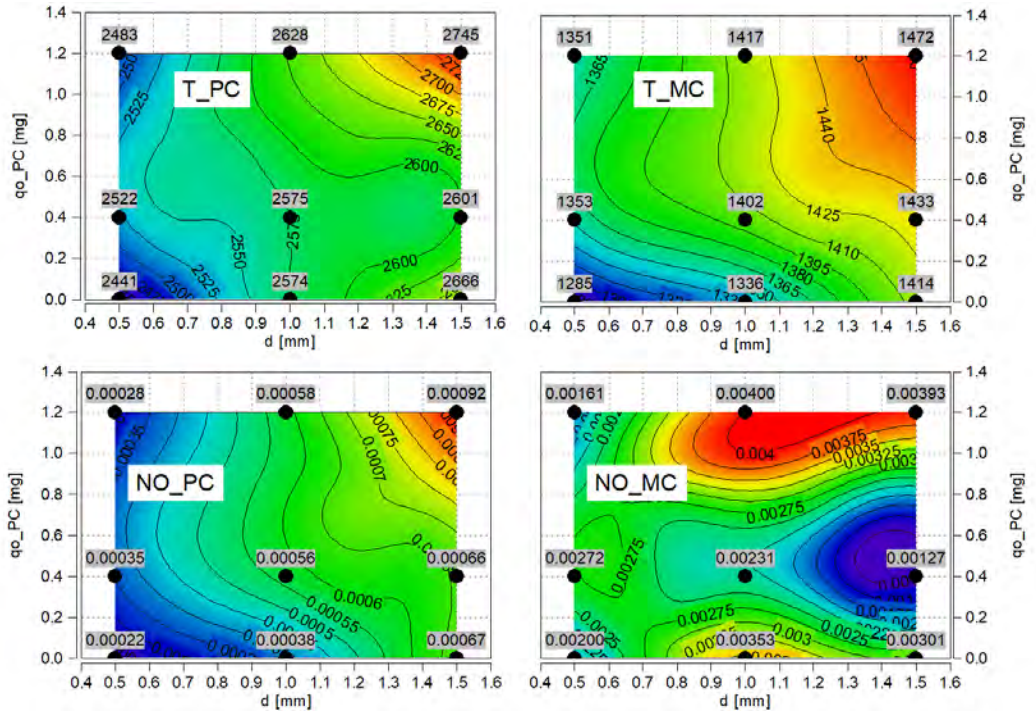

Fig. 16. Map of temperature changes in the cylinder and the amount of NO in d–qo_PC coordinates: a) in the pre-chamber, b) in the main chamber

be performed with a higher injection advance (than 550 deg) or injection should be used with a higher fuel pressure (increasing the range of the gas stream and its atomization in the main chamber). Another possibility may be a different location of the injector or division of the injected fuel dose.

6. Summary

Changing the diameters of the discharge holes significantly changes the combustion process in the TJI engine. Small hole diameters d ≤ 0.5 mm limit the flow of charge into the PC, which results in much lower pressures in the PC. Additionally, the outflow of the flame torches causes their extinction on the channel walls, which results in lower ignitability of the charge in the main chamber. It follows that the quenching distance of 0.6 mm given in the literature is effective [8, 42].

Based on the research work carried out, it was found that:

1. In terms of hole geometry:
   - too small sizes of flow holes (d ≤ 0.5 mm) cause significant throttling of the charge flow into the pre-chamber, which results in large differences in combustion pressure and, consequently, deterioration of the quality of the hydrogen combustion process
   - large diameters of flow holes (d ≥ 1.0 mm) minimize inter-chamber flow conditions, which results in no throttling and higher combustion rates (P_{cyl}, T_{cyl} and Q).
2. In terms of fuel consumption rates:
   - the diameter of the holes is much more important for the proper combustion process than the size of the fuel dose (outside the passive chamber)
   - in the conducted tests in the pre-chamber, an excess air-ratio fuel value close to 1 was obtained in the dose range qo_PC = 0.4 mg
   - increasing the diameter of the holes led to an increase in the maximum pressure in the cylinder and the rate of heat release. The highest values of pressure and heat release were observed with hole diameter d = 1.2 mm
   - the maximum temperature value in the cylinder increased with the increase in the diameter of the holes, which indicates an increase in the importance of inter-chamber flows
   - analysis of the distribution of the excess air-fuel ratio indicates a significant lack of uniformity of the load; Due to the method of fuel injection, a characteristic division of the MC chamber into two zones: rich and lean in fuel, was achieved
   - with a small diameter of the holes, the tendency to divide the zones is dominant in the main chamber, and as the diameter of the holes increases, the division into different spheres in the main chamber decreases, and the disproportion in the pre-chamber increases.

These conclusions constitute a solid basis for further research and experimental work, which may contribute to the development of more effective and ecological drive technologies. Subsequent research stages may be focused on the following issues:

- further optimization of hole diameters and fuel doses in order to determine the best relationship between hydrogen combustion efficiency and nitrogen oxide emissions
- experimental verification to confirm the quality of the simulation work carried out; subsequent work will allow for the calibration of models and a better understanding of the phenomena occurring during hydrogen combustion
- hydrogen injection with other fuels (e.g. NH_3) to increase combustion efficiency.

Nomenclature

BDC	bottom dead center
CFD	computational fluid dynamics
CVC	constant volume chamber
cyl	cylinder
d	diameter
DI	direct injection
dQ	heat release rate
LDV	light duty vehicle
MC	main chamber
MPI	multi point injection
NO	nitrogen oxide
P	pressure
PC	pre-chamber
qo	fuel dose
Q	heat release
RCEM	rapid compression expansion machine
SI	spark ignition
T	temperature
TDC	top dead center
TJI	Turbulent Jet Ignition
TKE	turbulent kinetic energy
λ	air excess ratio

Bibliography

[1] Algayyim SJM, Saleh K, Wandel AP, Fattah IMR, Yusaf T, Alrazen HA. Influence of natural gas and hydrogen properties on internal combustion engine performance, combustion, and emissions: a review. Fuel. 2024;362:130844. https://doi.org/10.1016/j.fuel.2023.130844

[2] Alleman TL, McCormick RL, Yanowitz J. Properties of ethanol fuel blends made with natural gasoline. Energy Fuels. 2015;29(8):5095-5102. https://doi.org/10.1021/acs.energyfuels.5b00818

[3] Aoyagi T, Wakasugi T, Tsuru D, Tashima H. Analysis of effects of pre-chamber orifices on torch flame behaviours in lean-burn gas engines. Combust Engines. 2024;199(4):3-14. https://doi.org/10.19206/CE-188112

[4] Barabás I, Todoruț AI. Key fuel properties of bio-diesel-diesel fuel-ethanol blends. SAE Technical Paper 2009-01-1810. 2009. https://doi.org/10.4271/2009-01-1810

[5] Bozza F, Teodosio L, Krajnović J, Sjerić M, De Bellis V, Malfi E. Extensive validation of a combustion and pollutant

emission model of a pre-chamber engine including different pre-chamber geometries. Fuel. 2024;373:132282. https://doi.org/10.1016/j.fuel.2024.132282

[6] Bucherer S, Rothe P, Sobek F, Gottwald T, Kraljevic I, Vacca A et al. Experimental and numerical investigation of spark plug and passive pre-chamber ignition on a single-cylinder engine with hydrogen port fuel injection for lean operations. SAE Technical Paper 2023-01-1205. 2023. https://doi.org/10.4271/2023-01-1205

[7] Bureshaid K, Shimura R, Feng D, Zhao H, Bunce M. Experimental studies of the effect of ethanol auxiliary fueled turbulent jet ignition in an optical engine. SAE Int J Engines. 2019;12(4):387-399. https://doi.org/10.4271/03-12-04-0026

[8] Butler MS, Moran CW, Sunderland PB, Axelbaum RL. Limits for hydrogen leaks that can support stable flames. Int J Hydrog Energy. 2009;34(12):5174-5182. https://doi.org/10.1016/j.ijhydene.2009.04.012

[9] Crabtree GW, Dresselhaus MS. The hydrogen fuel alternative. MRS Bull. 2008;33(4):421-428. https://doi.org/10.1557/mrs2008.84

[10] Cui Z, Tian J, Zhang X, Yin S, Long W, Song H. Experimental study of the effects of pre-chamber geometry on the combustion characteristics of an ammonia/air pre-mixture ignited by a jet flame. Processes. 2022;10(10):2102. https://doi.org/10.3390/pr10102102

[11] Demirbas A. Fuel properties of hydrogen, liquefied petroleum gas (LPG), and compressed natural gas (CNG) for transportation. Energy Sources. 2002;24(7):601-610. https://doi.org/10.1080/00908312.2002.11877434

[12] Duan Y-h, Sun B-g, Li Q, Wu X-s, Hu T-g, Luo Q-h. Combustion characteristics of a turbocharged direct-injection hydrogen engine. Energy Convers Manag. 2023;291:117267. https://doi.org/10.1016/j.enconman.2023.117267

[13] Fayaz H, Saidur R, Razali N, Anuar FS, Saleman AR, Islam MR. An overview of hydrogen as a vehicle fuel. Renew Sustain Energy Rev. 2012;16(8):5511-5528. https://doi.org/10.1016/j.rser.2012.06.012

[14] Guo X, Li T, Chen R, Huang S, Zhou X, Wang N et al. Effects of the nozzle design parameters on turbulent jet development of active pre-chamber. Energy. 2024;306:132568. https://doi.org/10.1016/j.energy.2024.132568

[15] Hansen A. Ethanol-diesel fuel blends – a review. Bioresour Technol. 2005;96(3):277-285. https://doi.org/10.1016/j.biortech.2004.04.007

[16] Hu J, Pei Y, An Y, Zhao D, Zhang Z, Sun J et al. Study of active pre-chamber jet flames based on the synergy of airflow with different nozzle swirl angle. Energy. 2023;282:128198. https://doi.org/10.1016/j.energy.2023.128198

[17] Huo J, Zhao T, Lin H, Li J, Zhang W, Huang Z et al. Study on lean combustion of ammonia-hydrogen mixtures in a pre-chamber engine. Fuel. 2024;361:130773. https://doi.org/10.1016/j.fuel.2023.130773

[18] Ingo C, Tuuf J, Björklund-Sänkiaho M. Experimental study of the performance of a SI-engine fueled with hydrogen-natural gas mixtures. Int J Hydrog Energy. 2024;63:1036-1043. https://doi.org/10.1016/j.ijhydene.2024.03.252

[19] Jamrozik A, Tutak W, Kociszewski A, Sosnowski M. Numerical simulation of two-stage combustion in SI engine with prechamber. Appl Math Model. 2013;37(5):2961-2982. https://doi.org/10.1016/j.apm.2012.07.040

[20] Jeelan Basha KB, Balasubramani S, Sivasankaralingam V. Effect of pre-chamber geometrical parameters and operating conditions on the combustion characteristics of the hydrogen-air mixtures in a pre-chamber spark ignition system. Int J Hydrog Energy. 2023;48(65):25593-25608. https://doi.org/10.1016/j.ijhydene.2023.03.308

[21] Ju D, Huang Z, Li X, Zhang T, Cai W. Comparison of open chamber and pre-chamber ignition of methane/air mixtures in a large bore constant volume chamber: effect of excess air ratio and pre-mixed pressure. Appl Energy. 2020;260:114319. https://doi.org/10.1016/j.apenergy.2019.114319

[22] Khan MI, Yasmin T, Shakoor A. Technical overview of compressed natural gas (CNG) as a transportation fuel. Renew Sustain Energy Rev. 2015;51:785-797. https://doi.org/10.1016/j.rser.2015.06.053

[23] Kido H, Nakahara M, Hashimoto J. A turbulent burning velocity model taking account of the preferential diffusion effect. In The 4th International Symposium COMODIA; 1998. https://www.jsme.or.jp/esd/laboratory/publishing/comodia/comodia1998/

[24] Li D, Zhen H, Xingcai L, Wu-gao Z, Jian-guang Y. Physico-chemical properties of ethanol–diesel blend fuel and its effect on performance and emissions of diesel engines. Renew Energy. 2005;30(6):967-976. https://doi.org/10.1016/j.renene.2004.07.010

[25] Li J, Wang Y, Xing K, Guo X, Chen K, Huang H. The influence mechanism of pre-combustion chamber orifice structure on natural gas engines: combustion, emissions, and thermofluid analysis. Appl Therm Eng. 2024;236:121654. https://doi.org/10.1016/j.applthermaleng.2023.121654

[26] Liu P, Zhong L, Zhou L, Wei H. The ignition characteristics of the pre-chamber turbulent jet ignition of the hydrogen and methane based on different orifices. Int J Hydrog Energy. 2021;46(74):37083-37097. https://doi.org/10.1016/j.ijhydene.2021.08.201

[27] Liu X, Aljabri H, Panthi N, AlRamadan AS, Cenker E, Alshammari AT et al. Computational study of hydrogen engine combustion strategies: dual-fuel compression ignition with port- and direct-injection, pre-chamber combustion, and spark-ignition. Fuel. 2023;350:128801. https://doi.org/10.1016/j.fuel.2023.128801

[28] Liu X, Aljabri H, Silva M, AlRamadan AS, Ben Houidi M, Cenker E et al. Hydrogen pre-chamber combustion at lean-burn conditions on a heavy-duty diesel engine: a computational study. Fuel. 2023;335:127042. https://doi.org/10.1016/j.fuel.2022.127042

[29] Lu Y, Qian Y, Zhang D, Chen Y, Pei Y. Parameters optimization of prechamber jet disturbance combustion system – effect of prechamber volume and fuel injection mass ratios on performance and exhausts in a diesel engine. Fuel. 2024;373:132360. https://doi.org/10.1016/j.fuel.2024.132360

[30] Molnarne M, Schroeder V. Hazardous properties of hydrogen and hydrogen containing fuel gases. Process Saf Environ Prot. 2019;130:1-5. https://doi.org/10.1016/j.psep.2019.07.012

[31] Momirlan M, Veziroglu T. The properties of hydrogen as fuel tomorrow in sustainable energy system for a cleaner planet. Int J Hydrog Energy. 2005;30(7):795-802. https://doi.org/10.1016/j.ijhydene.2004.10.011

[32] Musy F, Ortiz R, Ortiz I, Ortiz A. Hydrogen-fuelled internal combustion engines: direct injection versus port-fuel injection. Int J Hydrog Energy. 2024; https://doi.org/10.1016/j.ijhydene.2024.07.136

[33] Palombi L, Sharma P, Cenker E, Magnotti G. Effects of engine speed on prechamber-assisted combustion. SAE Technical Paper 2023-24-0020. 2023. https://doi.org/10.4271/2023-24-0020

[34] Peters N, Bunce M. Active pre-chamber as a technology for addressing fuel slip and its associated challenges to lambda estimation in hydrogen ICEs. SAE Technical Paper 2023-32-0041. 2023. https://doi.org/2023-32-0041

[35] Pielecha I, Bueschke W, Skowron M, Fiedkiewicz Ł, Szwajca F, Cieślik W et al. Prechamber optimal selection for a two stage turbulent jet ignition type combustion system in CNG-fuelled engine. Combust Engines. 2019;176(1):16-26. https://doi.org/10.19206/CE-2019-103
[36] Pielecha I, Szwajca F, Skobiej K. Experimental investigation on knock characteristics from pre-chamber gas engine fueled by hydrogen. Energies. 2024;17(4):937. https://doi.org/10.3390/en17040937
[37] Precedence Research. Hydrogen Combustion Engine Market Size, Share, and Trends 2024 to 2034. 2023; https://www.precedenceresearch.com/hydrogen-combustion-engine-market
[38] Qiang Y, Ji C, Wang S, Xin G, Hong C, Wang Z et al. Study on the effect of variable valve timing and spark timing on the performance of the hydrogen-fueled engine with passive pre-chamber ignition under partial load conditions. Energy Convers Manag. 2024;302:118104. https://doi.org/10.1016/j.enconman.2024.118104
[39] Rajasegar R, Niki Y, García-Oliver JM, Li Z, Musculus MPB. Fundamental insights on ignition and combustion of natural gas in an active fueled pre-chamber spark-ignition system. Combust Flame. 2021;232:111561. https://doi.org/10.1016/j.combustflame.2021.111561
[40] Santos NDSA, Alvarez CEC, Roso VR, Baeta JGC, Valle RM. Combustion analysis of a SI engine with stratified and homogeneous pre-chamber ignition system using ethanol and hydrogen. Appl Therm Eng. 2019;160:113985. https://doi.org/10.1016/j.applthermaleng.2019.113985
[41] Santos NDSA, Alvarez CEC, Roso VR, Baeta JGC, Valle RM. Lambda load control in spark ignition engines, a new application of prechamber ignition systems. Energy Convers Manag. 2021;236:114018. https://doi.org/10.1016/j.enconman.2021.114018
[42] Saravanan N, Nagarajan G, Sanjay G, Dhanasekaran C, Kalaiselvan KM. Combustion analysis on a DI diesel engine with hydrogen in dual fuel mode. Fuel. 2008;87(17-18): 3591-3599. https://doi.org/10.1016/j.fuel.2008.07.011
[43] Soltic P, Hilfiker T. Efficiency and raw emission benefits from hydrogen addition to methane in a prechamber–equipped engine. Int J Hydrog Energy. 2020;45(43):23638-23652. https://doi.org/10.1016/j.ijhydene.2020.06.123
[44] Tang Q, Sampath R, Marquez ME, Sharma P, Hlaing P, Houidi MB et al. Optical diagnostics on the pre-chamber jet and main chamber ignition in the active pre-chamber combustion (PCC). Combust Flame. 2021;228:218-235. https://doi.org/10.1016/j.combustflame.2021.02.001
[45] The European Hydrogen Observatory. The European hydrogen market landscape. 2023. https://observatory.clean-hydrogen.europa.eu/
[46] Tomić R, Sjerić M, Krajnović J, Ugrinić S. Influence of pre-chamber volume, orifice diameter and orifice number on performance of pre-chamber SI engine – an experimental and numerical study. Energies. 2023;16(6):2884. https://doi.org/10.3390/en16062884
[47] Torres-Jimenez E, Jerman MS, Gregorc A, Lisec I, Dorado MP, Kegl B. Physical and chemical properties of ethanol–diesel fuel blends. Fuel. 2011;90(2):795-802. https://doi.org/10.1016/j.fuel.2010.09.045
[48] Tutak W, Jamrozik A. Modelling of the thermal cycle of a gas engine using AVL FIRE Software. Combust Engines. 2010;141(2):105-113. https://doi.org/10.19206/CE-117152
[49] Wang K da, Sun B gang, Luo Q he, Li Q, Wu X, Hu T et al. Performance optimization design of direct injection turbocharged hydrogen internal combustion engine. Appl Energy Combust Sci. 2023;16:100204. https://doi.org/10.1016/j.jaecs.2023.100204
[50] Wang Z, Ji C, Wang D, Zhang T, Wang S, Wang H et al. Analysis of the combustion characteristics of ammonia/air ignited by turbulent jet ignition with assisted hydrogen injection in pre-chamber. Fuel. 2024;367:131513. https://doi.org/10.1016/j.fuel.2024.131513
[51] White C, Steeper R, Lutz A. The hydrogen-fueled internal combustion engine: a technical review. Int J Hydrog Energy. 2006;31(10):1292-1305. https://doi.org/10.1016/j.ijhydene.2005.12.001
[52] Wu H, Wang L, Wang X, Sun B, Zhao Z, Lee C et al. The effect of turbulent jet induced by pre-chamber sparkplug on combustion characteristics of hydrogen-air pre-mixture. Int J Hydrog Energy. 2018;43(16):8116-8126. https://doi.org/10.1016/j.ijhydene.2018.02.155
[53] Xu G, Kotzagianni M, Kyrtatos P, Wright YM, Boulouchos K. Experimental and numerical investigations of the unscavenged prechamber combustion in a rapid compression and expansion machine under engine-like conditions. Combust Flame. 2019;204:68-84. https://doi.org/10.1016/j.combustflame.2019.01.025
[54] Zeman J, Dempsey A. Numerical investigation of equivalence ratio effects on flex-fuel mixing controlled combustion enabled by prechamber ignition. Appl Therm Eng. 2024; 249:123445. https://doi.org/10.1016/j.applthermaleng.2024.123445
[55] Zhou L, Liu P, Zhong L, Feng Z, Wei H. Experimental observation of lean flammability limits using turbulent jet ignition with auxiliary hydrogen and methane in pre-chamber. Fuel. 2021;305:121570. https://doi.org/10.1016/j.fuel.2021.121570
[56] Zhou L, Zhong L, Liu Z, Wei H. Toward highly-efficient combustion of ammonia–hydrogen engine: prechamber turbulent jet ignition. Fuel. 2023;352:129009. https://doi.org/10.1016/j.fuel.2023.129009
[57] Zhu J, Liu R, Lin H, Jin Z, Qian Y, Zhou D et al. Computational insights into flame development and emission formation in an ammonia engine with hydrogen-assisted pre-chamber turbulent jet ignition. Energy Convers Manag. 2024;314:118706. https://doi.org/10.1016/j.enconman.2024.118706
[58] Ziyaei S, Mazlan SK, Lappas P, Ziyaei S, Mazlan SK, Lappas P. A review of ultra-lean and stratified charged combustion in natural gas spark ignition engines. Technical Paper 2003-16-0050. 2023. https://doi.org/10.4271/03-16-07-0050

Marcelina Górzyńska, MEng. – Faculty of Civil and Transport Engineering, Poznan University of Technology, Poland.
e-mail: *marcelina.gorzynska@doctorate.put.poznan.pl*

Prof. Ireneusz Pielecha, DSc., DEng. – Faculty of Civil and Transport Engineering, Poznan University of Technology, Poland.
e-mail: *ireneusz.pielecha@put.poznan.pl*

Article citation info:
Bednarek M, Ziółkowski A, Jagielski A, Siedlecki M. The analysis of the operating conditions of a heavy-duty engine of a vehicle designated for timber transport in terms of compliance with the RDE procedures. Combustion Engines. 2024;199(4):140-150. https://doi.org/10.19206/CE-193859

Maciej BEDNAREK
Andrzej ZIÓŁKOWSKI
Aleks JAGIELSKI
Maciej SIEDLECKI

Combustion Engines
Polish Scientific Society of Combustion Engines

The analysis of the operating conditions of a heavy-duty engine of a vehicle designated for timber transport in terms of compliance with the RDE procedures

ARTICLE INFO

Received: 20 August 2024
Revised: 10 September 2024
Accepted: 27 September 2024
Available online: 11 October 2024

According to the data provided by the Polish Central Statistical Office, the years 2000–2020 have seen a general increase in the amount of extracted timber, reaching 43%. The process of obtainment and transport of timber has many stages involving multiple vehicles and machines. The prevailing type of machinery is HDVs (heavy-duty vehicles). Their application is dictated by the fact that high-tonnage-rated vehicles are characterized by the greatest efficiency. The vehicles from this group are homologated under laboratory and actual traffic conditions. It is noteworthy that the transport process of timber takes place under extremely varied conditions – paved urban and rural roads a well as unpaved forest tracks. This renders the mode of operation non-compliant with the conditions set forth in the UE 582/2011 standard. Therefore, the authors decided to carry out an analysis of the operating conditions of a vehicle fitted with an HD engine used in the process of timber transport in terms of its compliance with the RDE (Real Driving Emissions) procedures. The analysis was performed based on investigations carried out under actual traffic conditions with the use of the PEMS equipment. The research object was a tractor-trailer fitted with removable stanchions and a crane used for timber handling. The paper presents, inter alia, the engine operating timeshare characteristics as a function of engine load and speed. The authors also compared the real-world engine operating conditions with the assumptions of the RDE procedures.

Key words: *RDE, PEMS, in-service conformity procedure, HDV*

1. Introduction

Higher traffic congestion, advancement of scientific research on the negative impact of transport related pollution as well as increased sensitivity of the society to health hazards associated with the inhalation of exhaust gases have caused the legislators to continuously introduce legal acts forcing the reduction of the negative environmental impact of the transport sector [19, 4]. The main polluting components of exhaust gas are particulate matter (PM), hydrocarbons (HC), carbon monoxide (CO), nitrogen oxides (NO_x), and carbon dioxide (CO_2) [2]. Multiple research works confirm that these components have a negative impact on human health and the natural environment (the emitted greenhouse gases contribute to the growing greenhouse effect) [12, 36, 40]. Some of the exhaust components, including selected hydrocarbons and particulate matter, are carcinogenic [24, 30].

The pioneer in the emission-reducing legislation is the United States of America. In 1968, the US passed the first legislation on exhaust emissions [38]. In the EU, the first legal standard aiming at a reduction of vehicle exhaust emissions was introduced in 1991. Legislation regarding passenger vehicles (PC) and light-duty vehicles (LDV) evolved throughout the years. More and more chemical components were introduced to the list, and emission limits became more stringent, forming the subsequent Euro 1–Euro 6d standards. This paper discusses vehicles of the GWV (gross vehicle weight) greater than 3500 kg. The standards for this category of vehicles in the EU were introduced a year after such standards had been imposed on PC and LDV vehicles. The standards for heavy-duty vehicles are included in regulations commonly referred to as Euro I–Euro VI. The most recent communications from the EU legislators prompt the introduction of a new Euro 7 standard pertaining to PC, LDV and HDV vehicles [1]. Increasingly stringent emission standards forced the manufacturers to tune their engines and redesign them. The said standards also sparked dynamic technological advancement of aftertreatment systems [15] and, more importantly, dynamic advancement of the alternative powertrain technology. According to the available data, the number of vehicles in the EU fitted with alternative powertrains is growing [6]. In 2022, the European Parliament adopted a resolution that in the European Union, starting in 2035, purchasing a new vehicle fitted with a conventional powertrain would not be possible. Additionally, the European institutions plan that by 2050, all EU member states will become zero-emission ones [7]. It is noteworthy that the market share of passenger vehicles fitted with alternative powertrains – BEV (battery electric vehicle), HEV (hybrid electric vehicle), and PHEV (plug-in hybrid electric vehicle) is still only slightly more than 2% [26]. What is more, these powertrains are widely applied in passenger vehicles only. In the case of HDVs, these powertrains are not as commonplace, even though their technological advancement can only boost the attractiveness of heavy-duty road transport, as has been stressed by the authors in [5].

As the new standards were introduced and the limits of individual exhaust components were changed, the methods of their measurement evolved. HDV vehicles are homologated under laboratory conditions on an engine dynamometer. Pursuant to Regulation 49 of the EEC UN, two research cycles apply – stationary WHSC (World Harmonized Stationary Cycle) and transient WHTC (World Harmonized Transient Cycle). These tests superseded the earlier ESC and ETC ones. The newly designed cycles were made to

better reproduce the actual traffic conditions of heavy-duty vehicles [23]. This aimed to obtain the most reliable exhaust emissions measurement results through an accurate reflection of the engine's operating parameters. It is noteworthy that the said research cycles are also used by research institutions to evaluate the engine operating parameters or determine a variety of relations emission-wise. For example, the authors of [34] used the World Harmonized Stationary Cycle to determine the influence of mixtures of n-butanol and diesel oil on the exhaust emissions and performance of a diesel engine. The investigations were carried out for the entire cycle and for its individual portions. An important component of the analysis presented in the said publication was the discussion related to engine torque and power output. In [4], the authors also used the WHTC procedure in their investigations to assess the influence of the HVO fuel on the engine operation and its performance. In this case, however, a modification of the cycle was necessary because, as the authors indicated, the configuration of the test stand for the investigated engine was inappropriate for the transient stages of the procedure. In [20] the WHTC test was used to investigate the particulate matter emission from a spark ignition engine fueled with CNG and LNG. The World Harmonized Stationary and Transient Cycles were also applied to investigate the emission of nitrogen oxides from a diesel engine fitted with an experimental catalytic converter based on the catalyst combination strategy [37]. Lim [14] et al, based on investigations carried out according to WHSC, generally evaluated a spark ignition engine fueled with synthetic natural gas. The authors of [28], following the results obtained in the World Harmonized Transient Cycle, analyzed the influence of the warm-up phase of an HDV vehicle on the emission of nitrogen oxides.

Laboratory tests do not fully reflect the engine operating conditions, hence, their exhaust emissions. This has been confirmed by multiple research works described in [9, 21, 33, 35]. The advancement of measurement technology has led to a point where the most reliable data are obtained in tests performed under actual traffic conditions. According to many authors, it is the best method of measurement of exhaust emissions and engine operating parameters. It enables very accurate and detailed measurement of the exhaust emissions and engine parameters in stationary, dynamic, and transient conditions [10, 11, 42]. These investigations widely incorporate the use of the PEMS equipment (Portable Emissions Measurement System), particularly when testing emissions according to the RDE (Real Driving Emission) procedures [17, 25]. The equipment is also capable of a detailed analysis of the engine operation [2, 29] and is frequently used to investigate the influence of multiple factors on exhaust emissions. Lee, Junhong, et al. [13] used a portable emission measurement system to investigate the exhaust emissions from construction machinery under actual operating conditions. Mądziel [16] used the data from a PEMS system to model the emission of carbon dioxide from a vehicle fueled with LPG. In [8], the authors presented investigations of energy consumption and exhaust emissions from a plug-in hybrid. One of the measuring instruments in this project was portable emission measurement equipment. It is noteworthy that, aside from the measurement of individual exhaust emissions, through a direct connection to the vehicle OBD system, it can also record the engine operating parameters such as engine torque and speed [27]. For example, the authors of [43] used Semtech D.S. for the research of an HDV vehicle. The aim of their work was to analyze the parameters of the engine fitted to the research object. The authors of [32] also analyzed an HDV vehicle engine operating parameters based on tests performed under actual traffic conditions. The aim of their work was to investigate the performance of an LPG-fueled engine upon a modification of the intake system. [18] analyzes the operating parameters of a farm tractor engine during fieldwork. The possibility of performing research in real-world operating conditions allowed a detailed analysis of the operation of the said engines. For example, research presented in [18], revealed the fact that the operating speed of a farm tractor varies narrowly, which results from the nature of its work.

Many of the above-mentioned research works are performed under real-world operating conditions of the investigated objects. As has been emphasized in [15], the researchers have observed that the homologation procedures do not always fully reflect the actual conditions of operation of the tested objects. In this respect, HDV vehicles are a special case as they are operated under extremely varied conditions (both road and non-road). An example of vehicles whose model is not compliant with the conditions set forth in the standard procedure are those operated in mountain areas, on construction sites, on farms, or in timber transport. Therefore, in this paper, the authors undertook to analyze the actual operating conditions of a vehicle used for the carriage of timber and compare it with the RDE requirements.

2. Research methodology

2.1. Research objects

In the performed investigations, the authors used a heavy-duty truck designated for carriage of timber (Fig. 1). It was composed of a tractor unit coupled with a stanchion trailer and a hydraulic trailer crane fitted for timber handling. The vehicle was fitted with a 6-cylinder (353 kW @1900 rpm) diesel engine. The maximum torque of 2300 Nm was produced at 1200–1500 rpm. The engine displacement was 12.419 dm^3.

Fig. 1. Research object

The vehicle was Euro VI compliant, fitted with an after-treatment system composed of an SCR (selective catalytic reduction), a DPF (diesel particulate filter) and a DOC (diesel oxidation catalyst). The technical specifications of the research object have been presented in Table 1.

Table 1. Specification of research objects

Parameter	Value
Type of engine	Diesel
Engine capacity	12.419 dm^3
Maximum power output	353 kW at 1900 rpm
Maximum torque	2300 Nm at 1050–1400 rpm
Number of cylinders	6 cylinders, straight
Aftertreatment	DOC+DPF, SCR, ASC
Fuel system	Common Rail

2.2. Measuring instruments

For the investigations, the authors utilized Axion RS+, a portable exhaust emission measurement system (Fig. 2a) and TEXA TXT. The first of the devices measures the concentration of individual gaseous exhaust components. The equipment by Global MRV allows the measurement of both gaseous components and particulate matter. Carbon monoxide, carbon dioxide, and hydrocarbons are measured through a non-dispersive infrared method (NDIR – *Nondispersive Infrared Detector*), while nitrogen oxides are analyzed through an electrochemical analyzer. The concentration of particulate matter is measured using the laser scatter method. Axion RS+ can also record the operating parameters of the engine (engine torque and speed). Additionally, the authors used TEXA Navigator TXT (Fig. 2b) whose purpose was to pull the engine operating parameters from the vehicle OBD system.

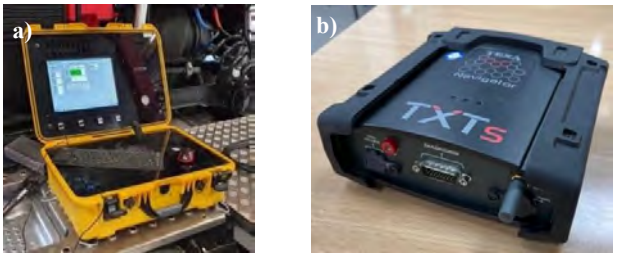

Fig. 2. Axion RS+ (a) and TEXA Navigator TXT (b)

2.3. Research cycle

The tests were carried out under actual conditions of operation of the HDV vehicle. The test procedure was designed to most accurately reproduce the standard process of operation of the research object. The tests were carried out in central Poland. The forests in this region cover ¼ of the area [31]. The test was carried out twice. The first one took place in early autumn. The second took place in more arduous winter conditions. The test reflected the actual model of vehicle operation. This allowed an analysis of the results that pointed to weak spots and non-compliance of the operation model with the homologation conditions for the HDV vehicles. The test routes have been presented in Fig. 4. Each of the research cycles had four stages: a trip to the timber storage with an unloaded truck, timber handling, a trip from the storage facility and unloading. Due to the location of the timber storage area, both the trip to and from the storage facility took place on unpaved forest roads. This is very characteristic of the timber transport process. In the autumn test, the length of the test route was approx. 49 km (paved roads 43.5 km and unpaved roads 5.4. km). The test route in the winter test was a little more than 42 km (paved roads 8.77 km and unpaved roads 33.4 km). The start and end point of the routes was the sawmill.

Fig. 3. Test routes

3. Results of the study

3.1. Speed profile and test routes

The vehicle speed profiles (Fig. 4) were composed based on the obtained results. Due to the nature of the research process, this analysis was carried out in two stages depending on the type of test route. The characteristics clearly indicate three stages of the research process (loading, driving on paved roads and driving on unpaved forest roads). Individual portions of the research cycle vary in terms of dynamics and driving speed. In the autumn portion, the vehicle operated at an average speed of 30 km/h. On the forest roads, it drove at an average speed of 9.5 km/h, while on the paved roads, the average speed was 57 km/h. The winter conditions did not dramatically influence the nature of the test drive. On the paved roads, the vehicle drove with an average speed of 51.7 km/h, and on the forest roads – 13.9 km/h.

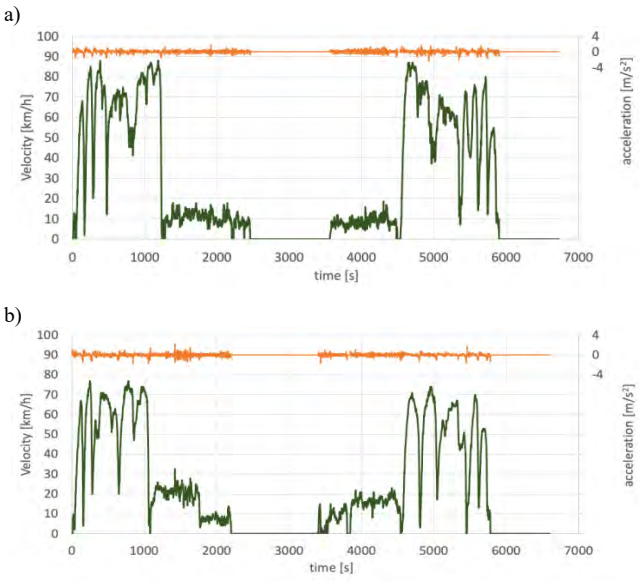

Fig. 4. Speed profiles of the research object: a) the autumn test, b) the winter test

3.2. Operating parameters of the engine

Due to the complexity of the research procedure, the analysis of the HDV's movement parameters in the process of timber transportation will be carried out in sections corresponding to the different stages of the research test, i.e., while driving on paved roads (with and without a load), while driving on unpaved forest roads (also with and without a load), and during loading operations, divided into the autumn and winter test. To present a comprehensive analysis of the performance of the heavy vehicle's drive unit in the process of transporting timber, loading processes were also studied. Because the test vehicle was equipped with a crane, there was no need to engage additional equipment for the loading and unloading of raw timber. During the tests, the vehicle transported approximately 20 tons of timber.

During the tests, instantaneous engine load and speed were recorded. This allowed composing the characteristics of the timeshare of the engine operation in relation to its parameters. The results are presented and discussed below.

The bar graphs have been presented in Fig. 5–7. When comparing the autumn test with the winter one, one may observe that the engine operating areas are similar in individual stages of the test. The tests have shown that, when driving on paved roads, the engine operated in the torque interval of 0–2300 Nm and engine speed interval of 800–1600 rpm for the autumn test and 0–2000 Nm and 800–1600 rpm for the winter test. When driving on the paved roads in the autumn test (Fig. 5a, 5c), a significant share of the speed (1200 rpm; 1600 rpm> and torque (0 Nm; 2400 Nm> intervals were observed. In the winter test, when driving without a load (Fig. 5b), the predominant engine operating area was (0 Nm; 1200 Nm> and (800 rpm; 1800 rpm>. When carrying timber on paved roads in winter conditions (Fig. 5d), the engine operated at the same torque intervals as on the forest roads, but the engine speed interval was 600–1600 rpm. During the winter test, the intervals of the discussed parameters were the same as for the test drives of an empty truck. An increase was observed in the operating timeshare in the (1200 rpm: 1600 rpm> speed interval.

In the second portion of the test covering the forest roads, the engine operated in the same engine speed interval as on the paved roads, but with a much lower load. In the autumn test, during the test drive performed on an empty truck (Fig. 6a), the engine predominantly operated in the load interval of (0 Nm; 800 Nm>. During the winter test (Fig. 6b), the engine predominantly operated in the load interval of (0 Nm; 400 Nm>. In both tests, the transport of timber resulted in an increased engine operation in the torque interval of 400–800 Nm (Fig. 6c and 6d).

The investigations have shown that during timber handling (Fig. 7a–d), the engine operated almost exclusively in the engine speed interval of 800–1200 rpm and torque 0–800 Nm. During the test carried out in the summer-autumn conditions, the load was predominantly 400–800 Nm. During the winter test, a much greater operating timeshare of the engine in the torque interval of 0–400 Nm was recorded.

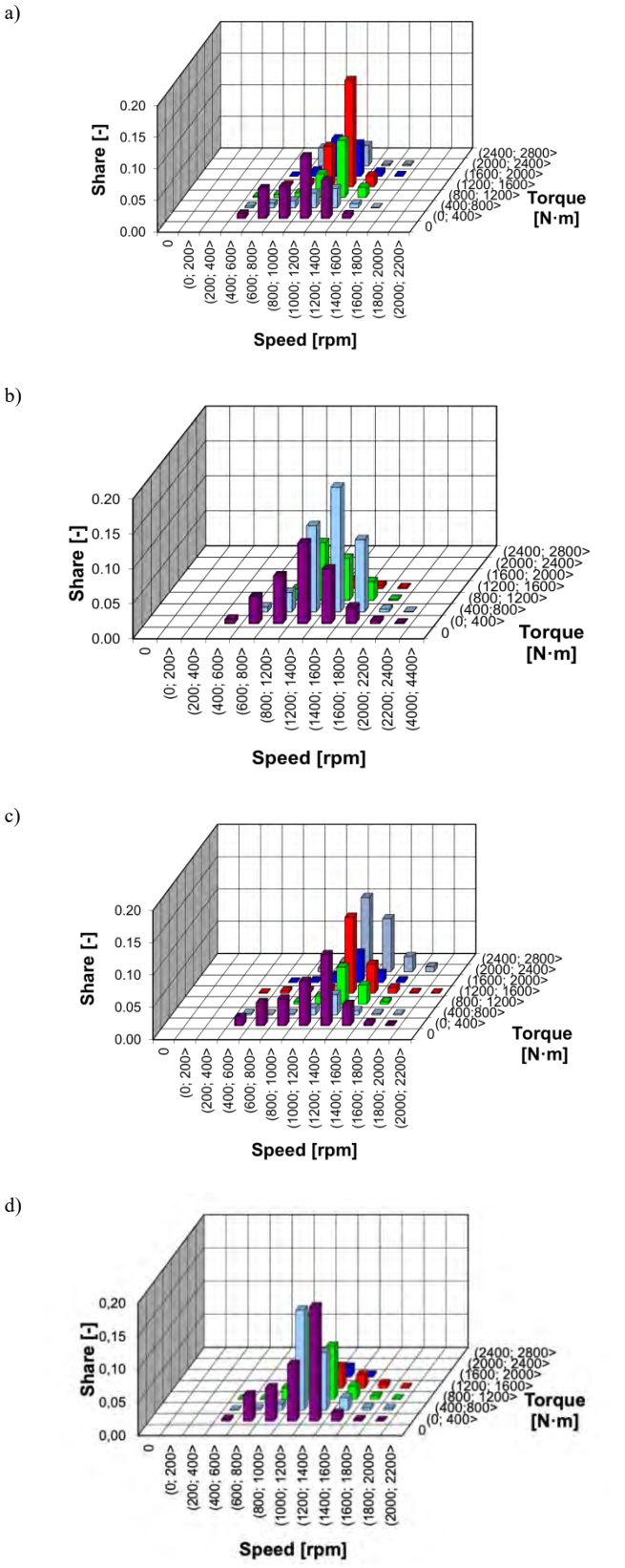

Fig. 5. Engine operating time share as a function of engine torque and speed when driving on paved roads loaded: a) the autumn test, b) the winter test, and loaded c) the autumn test, d) the winter test

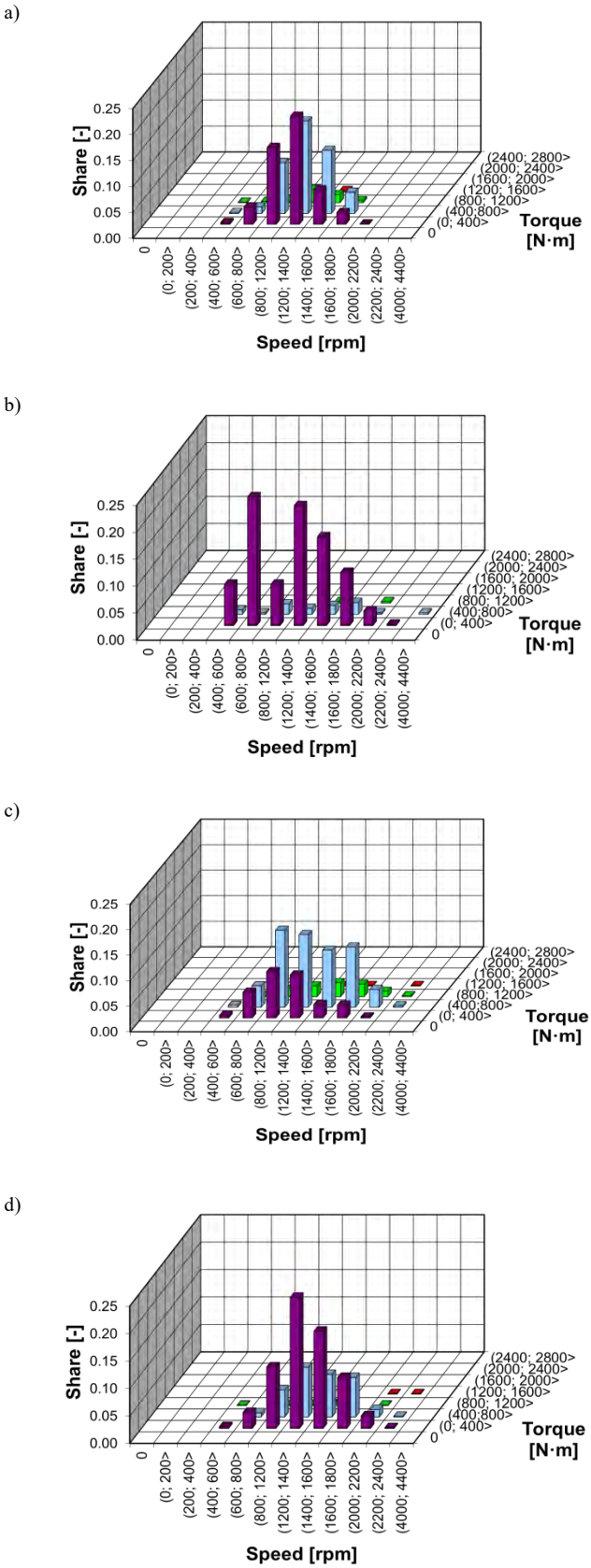

Fig. 6. Engine operating time share as a function of engine torque and speed when driving on unpaved roads (forest) unloaded: a) the autumn test, b) the winter test, and loaded: c) the autumn test, d) the winter test

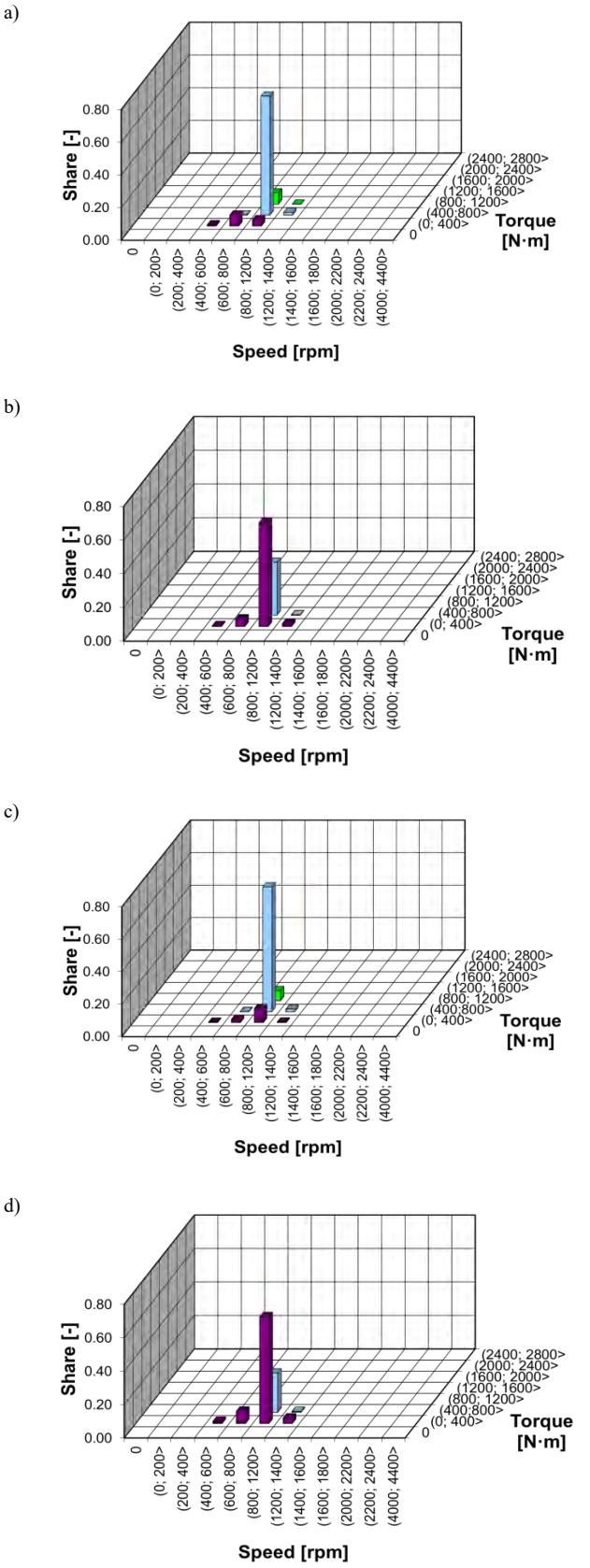

Fig. 7. Engine operating time share as a function of engine torque and speed when loading timber (empty truck): a) the autumn test, b) the winter test, and unloading timber: c) the autumn test, d) the winter test

3.3. Analysis of compliance of the transport cycle with the RDE test procedure

Based on the performed speed profile and engine parameter analysis in both tests, we may confirm that the tests are similar. Therefore, the proposed research cycle is representative of the timber transport process. The research object is subject to standard HDV vehicle homologation procedures. These vehicles or their engines undergo an in-service conformity procedure. precisely defines the procedure of compliance verification, including the conditions of the test drive and operational requirements. Based on the obtained results, the compliance of the homologation procedure with the actual transport cycle was analyzed. The procedure must be composed of three portions whose length (depending on the vehicle category) has been presented in Table 2.

Table 2. Duration of individual test stages in the RDE compliance test

Test portion	M_2 and M_3	N_2	N_3
Urban	45%	45%	20%
Rural	25%	35%	25%
Motorway	30%	30%	55%

Table 3 presents the results of the test drive parameters required by the legislator together with the results obtained during the test performed under actual operating conditions. The obtained values indicate that each of the stages differs from the procedure recommended by the European Commission. It is noteworthy that the procedure does not include the non-road portion, which, in the case of timber carriage, constitutes up to 10–20% of the entire transport cycle. The motorway part of the autumn test constitutes 30% of the transport cycle. In the case of the winter test, this part is a little above 1% of the entire cycle. Such a low value results from the fact that the road conditions render driving at high speeds almost impossible. It is noteworthy that the nature of the process of cutting and extracting timber is dependent on the time of year. For example, timber cut in autumn must be extracted before the vegetation period begins [22, 39]. When analyzing the urban and rural portion of the test, one may observe that the percent values in the real-world test were exceeded compared to the prescribed standard. The exception is the urban portion in the autumn test, in which it was a little above 11% of the entire cycle. This may result from the fact that the test route led through the Czarnków beltway and avoided entering the largest city in the region.

Table 3. Duration of the test drives in individual portions of the test against the requirements of the RDE procedure for heavy-duty vehicles

Test portion	Unpaved roads	City	Rural	Highway
Urban	11%	11.5%	47.2%	30.3%
Rural	20.8%	44%	34%	1.2%
Motorway	–	20%	25%	55%

The regulation also defines the operational requirements. It assumes that the test, as well as the pulling of the data from the OBD system, continues without interruptions. These requirements were fulfilled in both the autumn and the winter tests. The legislation also details the duration of the test. It was described as the time necessary to obtain five times the reference mass of carbon dioxide in kg per cycle from the WHTC test (World Harmonized Transient Cycle) or the time necessary for the tested object to perform five times the work prescribed by the WHTC test procedure. The authors decided to validate the duration of a standard transport cycle in terms of its compliance with the HDV RDE procedure.

The authors calculated the work performed by the engine of the tested object in the WHTC test. Based on the actual torque curve and using a spreadsheet with the appropriate function, the actual torque in Nm was calculated. Based on it, the instantaneous engine power was calculated, which enabled the development of the drive unit's operation in the WHTC test in kWh. The results have been presented in Fig. 8. The obtained results clearly indicate that none of the test drives met this requirement. The work performed by the engine in the autumn test was more than 1.5 times smaller than required, and the one performed in the winter test was almost 2.5 times smaller than required. Based on the previous observations, one may confirm that a standard operational model of the investigated vehicle is non-compliant with the RDE test model.

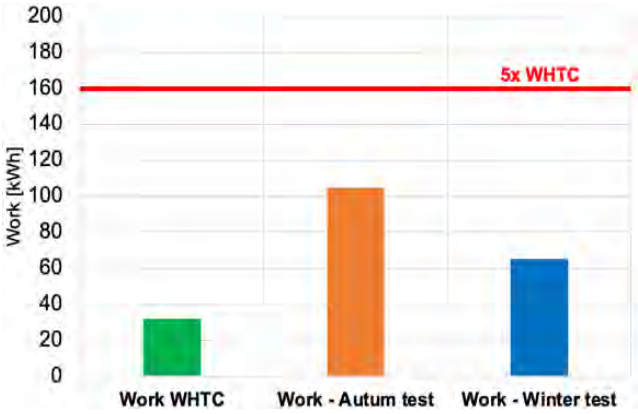

Fig. 8. Work performed by the investigated object in individual tests

The group of vehicles discussed in this article is approved based on procedures that do not consider the impact of unpaved roads on emissions. As confirmed in earlier sections, these roads have a significant impact on the performance of truck power units, which directly affects the number of toxic emissions into the atmosphere. Figure 10 shows a comparison of the emissions of the studied facility. Successively, Fig. 9a shows the results for the test conducted in autumn and Fig. 9b – the results for the winter test. The indicators shown were obtained by comparing the test's gaseous compound emissions with the limits specified in the standard. In both tests, the emission factors did not exceed 1. It is worth noting, however, that they differ significantly from each other. This is due, among other things, to the differences between the two routes – including their length and mainly the difference in the condition of their pavement. These factors significantly affect the operation of the propulsion units, which translates directly into exhaust emissions. Although the values obtained in the test are less than the limit values, it is worth noting that the tests that constitute the actual process of their operation do not meet the requirement of homologation tests, as proven in

the earlier parts of this article. Based on the research test it can be considered that the analysis conducted is representative of the national timber transportation system in which HDVs are used. This can be said because each step of the standard timber transportation process was considered in the analysis.

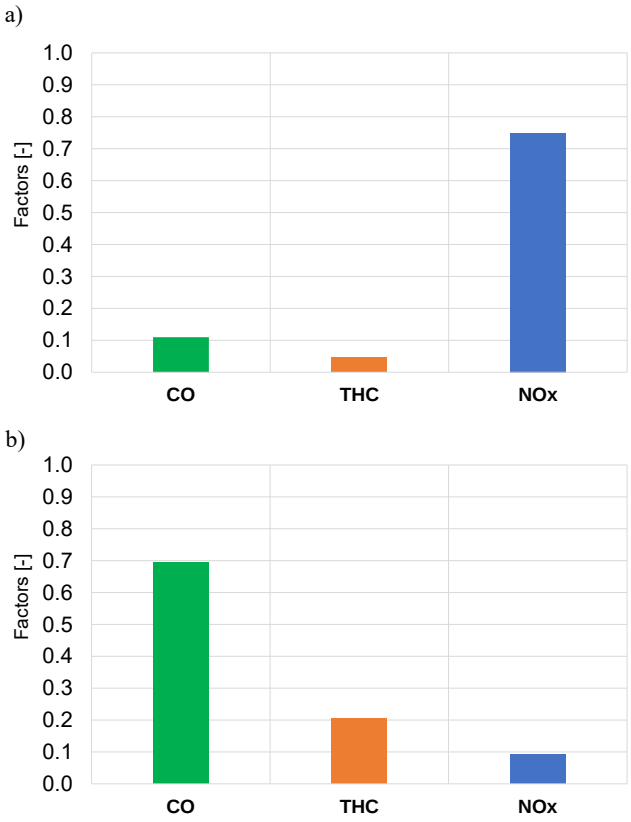

Fig. 9. Compliance factors for exhaust gaseous emissions of tested trucks: a) autumn test, b) winter test

4. Summary

Different climatic conditions, such as low temperatures and rainfall, have a significant impact on truck emissions and fuel consumption. In cold weather, engines take longer to warm up, which increases fuel consumption, especially when starting. In addition, cold weather causes more rolling resistance in tires, which also leads to higher combustion. Rainfall affects the aerodynamics of the vehicle and causes more drag from wheel contact with wet pavement, which further increases fuel consumption. In turn, increased fuel consumption leads to higher emissions, which has a negative impact on the environment. As a result, adverse weather conditions can significantly reduce the energy efficiency of trucks. However, this paper is intended to draw attention to the fact that current approval procedures do not consider the actual operating models of HDVs used in off-highway transportation.

Literature analysis allows a conclusion that heavy-duty vehicles (category N1 in particular) are currently used in the carriage of any type of cargo. The nature of their application can, thus, vary widely. The real-world investigations described in this paper were carried out at different times of the year. Therefore, they varied in terms of road conditions and ambient temperatures. The analysis of the obtained vehicle and engine operating parameters proves that the engines operated in similar intervals irrespective of the ambient conditions. We can, therefore, treat these tests as representative of the discussed timber transport process. The performed research leads to a conclusion that the operational model of heavy-duty vehicles operating under variable conditions does not reflect the model specified in the RDE procedure. The analysis of the engine operating conditions in terms of RDE compliance has shown that the main assumptions as to the test drive conditions and operational requirements are inadequate. Vehicles carrying timber operate on paved as well as unpaved roads (these are not included in the procedure). Individual stages of the RDE test (urban, rural, motorway portions) did not comply during the tests either. Additionally, the test duration criterion was not met (it is noteworthy that the research object was a truck designed to carry timber). Heavy-duty vehicles are used in different transport processes that are also composed of portions involving non-road operation. An example of such could be HDV machinery operating in farm fields, construction sites or open cast mines. Therefore, it is important to further investigate a greater number of research objects and perform detailed analyses of the compliance of their operational model with the legislative assumptions related to RDE testing.

Acknowledgements

The study presented in this article was performed within the statutory research (contract No. 0415/SBAD/0326).

Nomenclature

CO carbon monoxide
CO_2 carbon dioxide
NO_x nitrogen oxides
SI spark ignition
THC hydrocarbons
RDE real driving emission
PEMS portable emission measurement system
ASC ammonia slip catalyst
DOC diesel Oxicat
DPF diesel particular filter
SCR selective catalytic reduction

Bibliography

[1] AVL List. https://www.avl.com/en (accessed on 06.06. 2023).

[2] Biswal A, Singh V, Malik L, Tiwari G, Ravindra K, Mor S. Spatially resolved hourly traffic emission over megacity

Delhi using advanced traffic flow data. Earth Syst Sci Data. 2023;15;661-680. https://doi.org/10.5194/essd-15-661-2023
[3] Borken-Kleefeld J, Dallmann T. Remote sensing of motor vehicle exhaust emissions. International Council on Clean Transportation. 2018.
[4] Bortel I, Vávra J, Takáts M, Effect of HVO fuel mixtures on emissions and performance of a passenger car size diesel engine. Renew Energ. 2019;140:680-691. https://doi.org/10.1016/j.renene.2019.03.067
[5] Brach J. Konkurencyjność współczesnego ciężarowego transportu samochodowego. Zeszyty Naukowe Uniwersytetu Szczecińskiego Problemy Transportu i Logistyki (in Polish). 2015;319-344. https://doi.org/10.18276/ptl.2015.29-23
[6] European Environment Agency. EEA Report No 2/2022. Decarbonizing road transport — the role of vehicles, fuels and transport demand. https://doi.org/10.2800/68902
[7] European Parliament. https://www.europarl.europa.eu/portal/en (accessed on 6.06. 2023).
[8] Frey HC, Zheng X, Hu J. Variability in measured real-world operational energy use and emission rates of a plug-in hybrid electric vehicle. Energies. 2020;13;1140. https://doi.org/10.3390/en13051140
[9] Giechaskiel B, Clairotte M, Valverde V, Bonnel P. On-road emissions of passenger cars beyond the boundary conditions of the real-driving emissions test. Environ Res. 2019;176: 108572. https://doi.org/10.1016/j.envres.2019.108572
[10] Jaworski A, Mądziel M, Lew K, Campisi T, Woś P, Kuszewski H et al. Evaluation of the effect of chassis dynamometer load setting on CO_2 emissions and energy demand of a full hybrid vehicle. Energies. 2022;15;122. https://doi.org/10.3390/en15010122
[11] Kurtyka, K, Pielecha J. The evaluation of exhaust emission in RDE tests including dynamic driving conditions. Transp Res Proc. 2019;40:338-345. https://doi.org/10.1016/j.trpro.2019.07.050
[12] Lave LB, Seskin EP. Air pollution and human health. Science. 1970;169:723-733. https://doi.org/10.1126/science.169.3947.723
[13] Lee DI, Park J, Shin M, Lee J, Park S. Characteristics of real-world gaseous emissions from construction machinery. Energies. 2022;15;9543. https://doi.org/10.3390/en15249543
[14] Lim G, Lee S, Park C, Kim C, Choi Y. Combustion and emission characteristics of heavy-duty SI engine fueled with synthetic natural gas (SNG). SAE Technical Paper 2013-01-0026. 2013. https://doi.org/10.4271/2013-01-0026
[15] Mazanek A. An overview of engine and exploitation research methods taking into account the current and future quality requirements on motor fuels. Nafta-Gaz. 2014;8:534-540.
[16] Mądziel M. Liquified petroleum gas-fuelled vehicle CO_2 emission modelling based on portable emission measurement system, on-board diagnostics data, and gradient-boosting machine learning. Energies. 2023;16:2754. https://doi.org/10.3390/en16062754
[17] Mądziel M. Vehicle emission models and traffic simulators: a review. Energies. 2023;16;3941. https://doi.org/10.3390/en16093941
[18] Merkisz J, Lijewski P, Pielecha J. PEMS-based investigations into exhaust emissions from non-road and rail vehicles. Combustion Engines. 2016;166(3);46-53 https://doi.org/10.19206/CE-2016-339
[19] Merkisz J, Pielecha J, Fuć P. Badania i analizy zużycia energii i emisji zanieczyszczeń przez pojazdy w sieci drogowej (in Polish). Komitet Inżynierii Lądowej i Wodnej PAN. 2013;84.
[20] Napolitano P, Alfè M, Guido C, Gargiulo V, Fraioli V, Beatrice C. Particle emissions from a HD SI gas engine fueled with LPG and CNG. Fuel. 2020;269;117439. https://doi.org/10.1016/j.fuel.2020.117439
[21] Pelkmans L, Debal P. Comparison of on-road emissions with emissions measured on chassis dynamometer test cycles. Transport Res D-Tr E. 2006;11;233-241. https://doi.org/10.1016/j.trd.2006.04.001
[22] Porter B. Analysis of the timber transportation efficiency (in Polish). Technika Rolnicza Ogrodnicza Leśna. 2012;1. https://tech-rol.eu/index.php/pl/archiwum-2/2012
[23] Rahman SMA, Fattah IMR, Ong HC, Ashik FR, Hassan MM, Murshed MT et al. State-of-the-art of establishing test procedures for real driving gaseous emissions from light- and heavy-duty vehicles. Energies. 2021;14;4195. https://doi.org/10.3390/en14144195
[24] Ravanbakhsh M, Yousefi H, Lak E, Javed Ansari M, Suksatan W, Qasim QA et. al. Effect of polycyclic aromatic hydrocarbons (PAHs) on respiratory diseases and the risk factors related to cancer. Polycycl Aromat Comp. 2023; 43(9): 8371-8387. https://doi.org/10.1080/10406638.2022.2149569
[25] Real driving emissions: 2017 assessment of Portable Emissions Measurement Systems (PEMS) measurement uncertainty. JRC Technical Reports. 2018. https://doi.org/10.2760/127122
[26] Report European Automobile Manufacturers Association: Vehicles in use. Europe 2022.
[27] Rymaniak Ł, Kamińska M, Szymlet N, Grzeszczyk R. Analysis of harmful exhaust gas concentrations in cloud behind a vehicle with a spark ignition engine. Energies. 2021;14;1769. https://doi.org/10.3390/en14061769
[28] Sala R, Krasowski J, Dzida J. The influence of engine warm-up phase on nitrogen oxides emission for heavy-duty Euro VI diesel engine. MATEC Web Conf. 2017;118; 00035. https://doi.org/10.1051/matecconf/201711800035
[29] Siedlecki M, Fuć P, Sokolnicka B, Szymlet N. Analysis of the effect of exhaust aftertreatment systems configurations on the temperature measured in the exhaust system of a spark-ignition engine. Autobusy – Technika, Eksploatacja, Systemy Transportowe (in Polish). 2019;231. https://doi.org/10.24136/atest.2019.161
[30] Singh V, Biswal A, Kesarkar AP, Mor S, Ravindra K. High resolution vehicular PM10 emissions over megacity Delhi: relative contributions of exhaust and non-exhaust sources. Sci Total Environ. 2020;699;134273. https://doi.org/10.1016/j.scitotenv.2019.134273
[31] State Forest of Poland. https://www.lasy.gov.pl/en (accessed on 8.06.2024).
[32] Tang Q, Fu J, Liu J, Zhou F, Yuan Z, Xu Z. Performance improvement of liquefied natural gas (LNG) engine through intake air supply. Appl Therm Eng. 2016;103:1351-1361. https://doi.org/10.1016/j.applthermaleng.2016.05.031
[33] Thomas D, Li H, Wang X, Song B, Ge Y, Yu W et al. Comparison of tailpipe gaseous emissions for RDE and WLTC using SI passenger cars. SAE Technical Paper 2017-01-2391. 2017. https://doi.org/10.4271/2017-01-2391
[34] Tipanluisa J, Fonseca N, Casanova J, López J. Effect of n-butanol/diesel blends on performance and emissions of a heavy-duty diesel engine tested under the World Harmonized Steady-State cycle. Fuel. 2021;302;121-204. https://doi.org/10.1016/j.fuel.2021.121204
[35] Tzirakis E, Pitsas K, Zannikos F, Stournas S. Vehicle emissions and driving cycles: comparison of the Athens Driving

Cycle (ADC) with ECE-15 and European Driving Cycle (EDC). Global NEST J. 2006;8(3):282-290. https://doi.org/10.30955/gnj.000376
[36] Walendzik M, Łepkowski M, Nowacki G. Influence of road transport on the natural environment and threats involved in road goods transport (in Polish). Autobusy: Technika, eksploatacja, systemy transportowe. 2016;6.
[37] Wang X, Yan Y, Zhang C. Study of NH_3-SCR catalyst combinations based on diesel engine exhaust emission mechanisms. J Phys: Conf Ser. 2022;2329:012042. https://doi.org/10.1088/1742-6596/2329/1/012042
[38] Watson AY, Bates RR, Kennedy D. (ed.) Air pollution, the automobile, and public health. National Academies Press, Washington 1988. https://doi.org/10.17226/1033
[39] Więsik J. Technical equipment in forestry production. Machines and equipment for logging and transport of timber (vol. 2). Publishing House SGGW, Warsaw 2015.
[40] Xie J, Teng J, Fan Y, Xie R, Shen A. The short-term effects of air pollutants on hospitalizations for respiratory disease in Hefei, China. Int J Biometeorol. 2019;63(3):315-326. https://doi.org/10.1007/s00484-018-01665-y
[41] Zimkowska-Laskowska M, Laskowski P. Comparison of pollutant emissions from various types of vehicles. Combustion Engines. 2024,197(2), 139-145. https://doi.org/10.19206/CE-181193
[42] Ziółkowski A, Daszkiewicz P, Rymaniak Ł, Fuć P, Ukleja P. Analysis of the exhaust emissions from hybrid vehicle during RDE test. MATEC Web Conf. 2019;294:02002. https://doi.org/10.1051/matecconf/201929402002
[43] Ziółkowski A, Fuć P, Lijewski P, Rymaniak Ł, Daszkiewicz P, Kamińska M et al. Analysis of RDE emission measurements in rural conditions from heavy-duty vehicle. Combustion Engines. 2020;182(3):54-58. https://doi.org/10.19206/CE-2020-309

Maciej Bednarek, MEng. – Faculty of Civil and Transport Engineering, Poznan University of Technology, Poland.
e-mail: *maciej.bednarek@doctorate.put.poznan.pl*

Aleks Jagielski, MEng. – Faculty of Civil and Transport Engineering, Poznan University of Technology, Poland.
e-mail: *aleks.jagielski@doctorate.put.poznan.pl*

Andrzej Ziółkowski, DSc., DEng. – Faculty of Civil and Transport Engineering, Poznan University of Technology, Poland.
e-mail: *andrzej.j.ziolkowski@put.poznan.pl*

Maciej Siedlecki, DEng. – Faculty of Civil and Transport Engineering, Poznan University of Technology, Poland.
e-mail: *maciej.siedlecki@put.poznan.pl*

Łukasiewicz
Poznański Instytut Technologiczny

Łukasiewicz – Poznański Instytut Technologiczny

to jednostka realizująca krajowe i międzynarodowe projekty badawczo-rozwojowe dla biznesu. Instytut wyróżniają wieloletnie tradycje sięgające 1945 roku, profesjonalna kadra i know-how.

Na podstawie połączenia unikalnych kompetencji zostały stworzone cztery centra badawcze, które realizują projekty B+R oraz usługi komercyjne w zakresie nowoczesnej mobilności, zrównoważonej gospodarki i transformacji cyfrowej. Instytut dysponuje również akredytowaną i nowoczesną bazą laboratoryjną.

Centrum Nowoczesnej Mobilności

oferuje innowacyjne rozwiązania i technologie w obszarze:

- taboru kolejowego,
- maszyn rolniczych i leśnych,
- logistyki,
- elektrotechniki, automatyki i robotyki,
- modelowania i badań symulacyjnych.

Centrum Transformacji Cyfrowej

adaptuje oraz wdraża inteligentne technologie cyfrowe dla optymalizacji procesów i systemów biznesowych. W skład centrum wchodzą grupy badawcze zajmujące się:

- rozwojem oprogramowania, platform cyfrowych i sztucznej inteligencji,
- urządzeniami elektronicznymi,
- transformacją procesów biznesowych.

Centrum Zrównoważonej Gospodarki

zajmuje się badaniami, rozwojem oraz wdrażaniem technologii przyjaznych środowisku. Oferuje usługi z zakresu:

- inżynierii materiałowej,
- inżynierii mechanicznej,
- technologii chemicznej i ochrony środowiska.

Centrum Badań Laboratoryjnych

wykonuje badania akredytowane zgodnie z normami branżowymi. Składa się z:

- Laboratorium Badań Materiałowych,
- Laboratorium Badań Elektrotechnicznych,
- Laboratorium Badań Środowiskowych,
- Laboratorium Metrologicznego,
- Laboratorium Obróbki Cieplnej.

Sieć Badawcza Łukasiewicz – Poznański Instytut Technologiczny
ul. Estkowskiego 6, 61-755 Poznań, Polska

company/lukasiewiczpit lukasiewiczpit @lukasiewiczpit

pit.lukasiewicz.gov.pl

Ergonomics and automation

Compliance: UE regulations 2017/1151, EN 12341:2014,
US EPA 40CFR 1065, 40CFR part 50

- Automation of measurement procedures
- On-line measurement data analysis
- Air buoyancy correction
- Dynamic analysis of the quality of weighing
- Environmental conditions module

Research and development centres

National laboratories monitoring air quality (NAAQS)

Automotive laboratories

Registration of filter mass changes during chemical and physical processes

RADWAG Wagi Elektroniczne
26-600 Radom, ul. Toruńska 5
tel. 48 386 60 00, e-mail: radom@radwag.pl

radwag.com

Czołowy producent agregatów prądotwórczych w Polsce

FOGO®

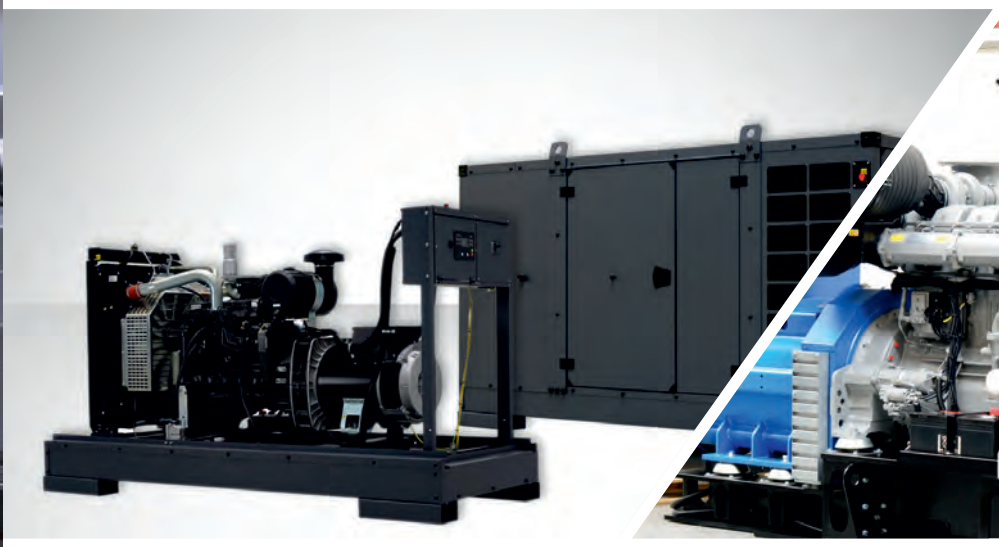

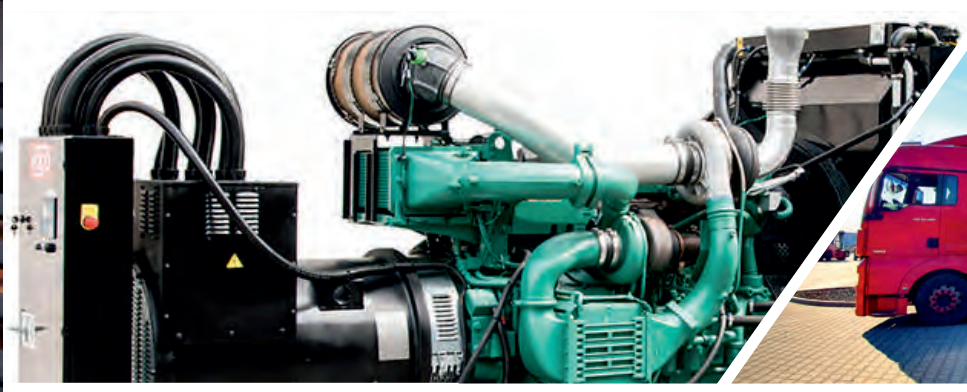

pewna **ENERGIA**

www.fogo.pl

Poznan University of Technology

Faculty of Civil and Transport Engineering

Institute of Powertrains and Aviation

- Emissions of combustion engines and hybrid powertrains
- Energy consumption of HEV, FCHEV, EV
- Hydrogen and multi-fuel combustion engines
- Maintenance of aircraft propulsion
- Vehicle and aircraft simulators
- Unmanned aerial vehicles
- Combustion systems
- Fuel cells

Division of Powertrains
Division of Aircarft
Institute of Powertrains and Aviation

Piotrowo 3 street, 60-965 Poznan, Poland
Phone: +48 61 665-2207
e-mail: office_ice@put.poznan.pl

AIR FORCE INSTITUTE OF TECHNOLOGY
INSTYTUT TECHNICZNY WOJSK LOTNICZYCH

ul. Księcia Bolesława 6, 01-494 Warszawa, Poland
tel.: +48 261 851 300; fax: +48 261 851 313
www.itwl.pl e-mail: poczta@itwl.pl

SUPPORTING OPERATIONS & MAINTENANCE OF AERONAUTICAL ENGINEERING:

- tribological diagnostics of lubrication systems in power units and hydraulic systems
- endoscopic examinations of power units
- measurements of operation parameters of power units using one's own and company systems and their analysis

DEVISING AND DEVELOPING NEW DIAGNOSTIC METHODS:

- CT examinations – V/tome/X CT system
- blade vibration measurements using the tip-timing method

NEW TECHNOLOGIES FOR UNMANNED AERIAL VEHICLES:

- technical condition monitoring system of mini jet engine
- hybrid drive of unmanned aerial vehicle

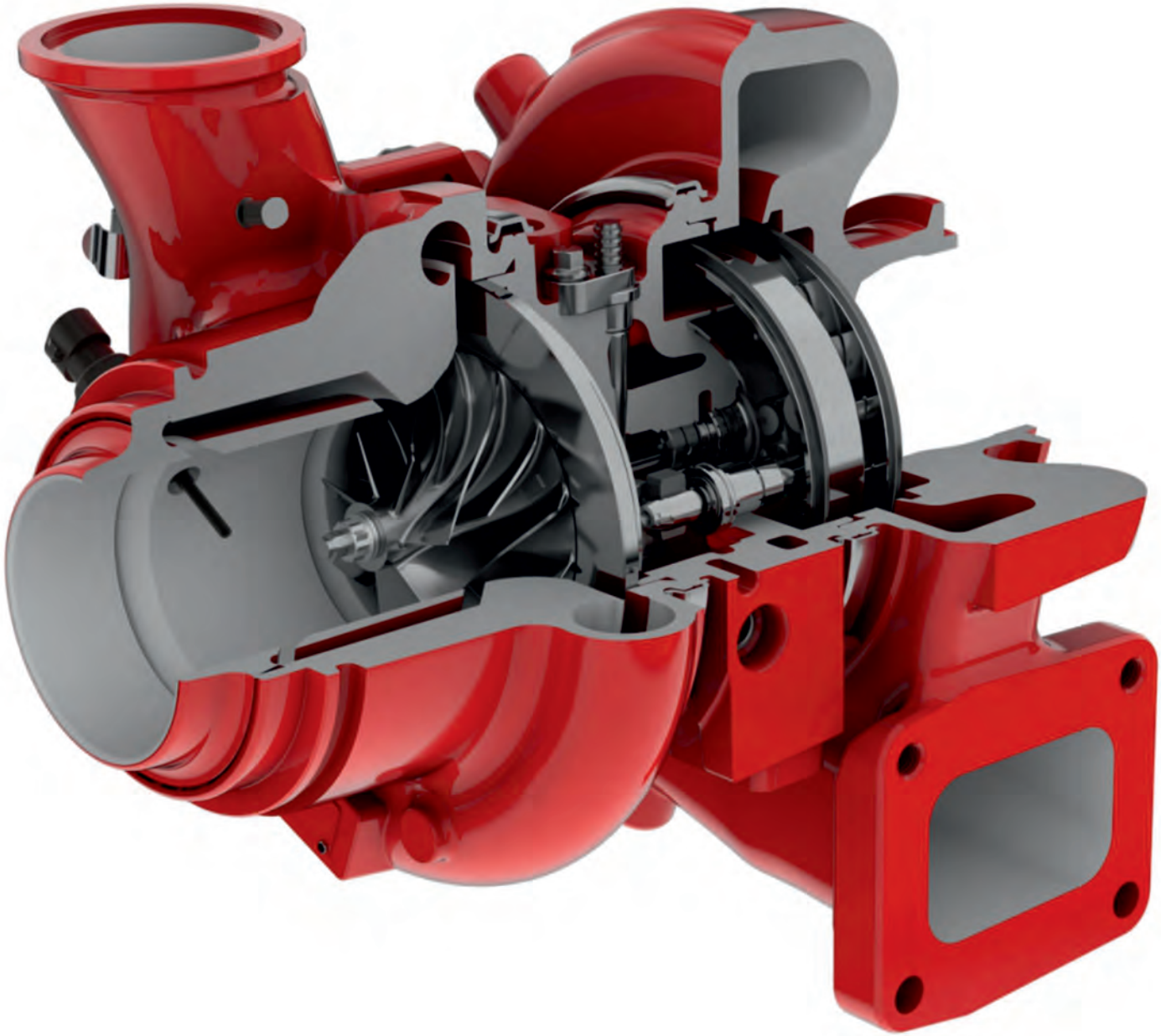

Publisher:

Polish Scientific Society of Combustion Engines

ISSN: 2300-9896
eISSN: 2658-1442

Combustion Engines

Polskie Towarzystwo Naukowe Silników Spalinowych

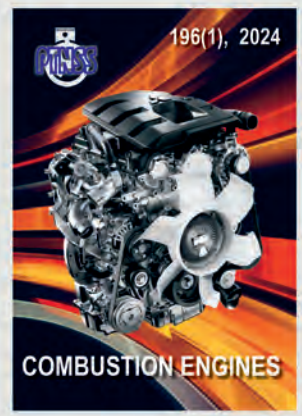

www.combustion-engines.eu